Thermal stability of warm-rolled tungsten

Alfonso, Angel

Publication date:
2015

Document Version
Publisher's PDF, also known as Version of record

Citation (APA):
Alfonso, A. (2015). *Thermal stability of warm-rolled tungsten*. DTU Mechanical Engineering.

Thermal stability of warm-rolled tungsten

PhD Thesis

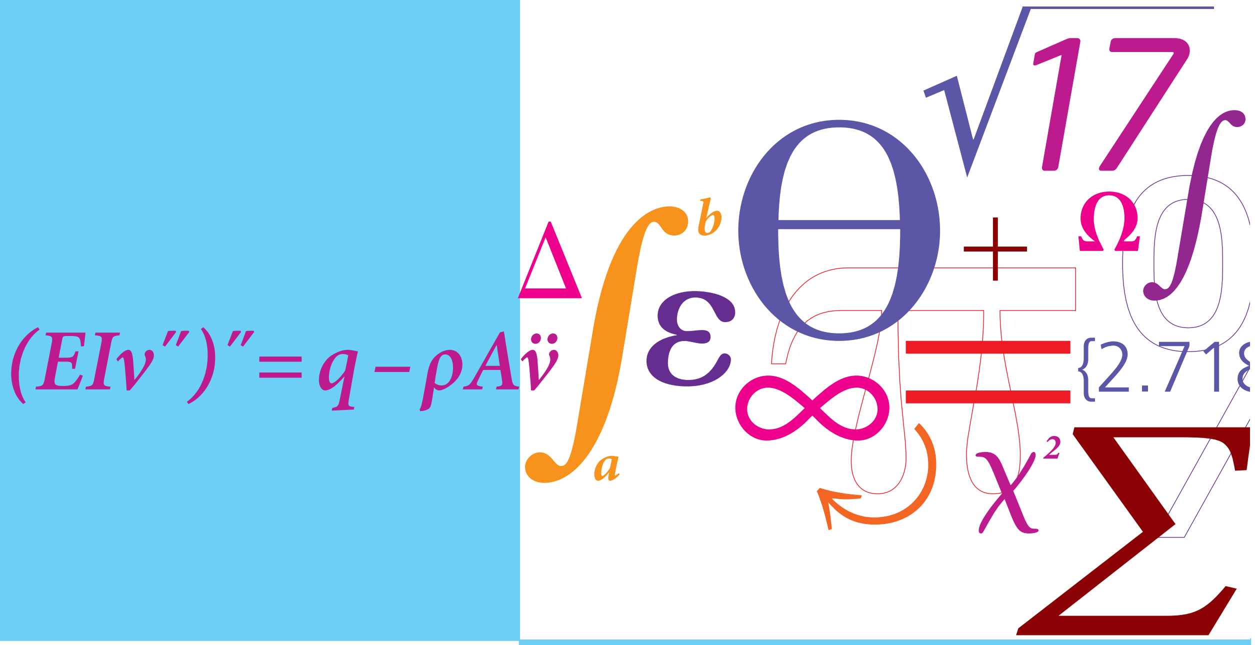

Angel Alfonso Lopez
June 2015

DTU Mechanical Engineering
Department of Mechanical Engineering

Author: Angel Alfonso Lopez
Title: Thermal stability of warm-rolled tungsten
Division: Section of Materials and Surface Engineering, Department of Mechanical Engineering
Submission date: June 2015
Sponsorship: Sino-Danish Centre for Research and Education (SDC)
Main Supervisor: Wolfgang Pantleon
Co-supervisors: Dorte Juul Jensen, Guangnan Luo

This thesis is submitted in partial fulfillment of the requirements for the Ph.D. degree at the Technical University of Denmark.

Abstract:

Pure tungsten is considered as armor material for the most critical parts of fusion reactors (the divertor and the blanket first wall), mainly due to its high melting point (3422 °C). This is because both the divertor and the first wall have to withstand high temperatures during service which may alter the microstructure of the material by recovery, recrystallization and grain growth, and may cause degradation in material properties as a loss in mechanical strength and embrittlement.

For this reason, this project aims towards establishing the temperature and time regime under which recovery and recrystallization occur in tungsten, and quantifying the kinetics and microstructural aspects of these restoration processes. Two warm-rolled tungsten plates are annealed at temperatures between 1100 °C and 1350 °C, under vacuum conditions or argon atmosphere. The effects of annealing on the microstructure are characterized microstrucurally by Optical Microscopy (OM) and Electron Back-Scattered Diffraction (EBSD), and mechanically by Vickers hardness.

Deformation to different strains will affect the deformation microstructure, and hence the mechanical strength and recrystallization behavior during subsequent annealing. In the present work, the annealing behavior is investigated after introducing different deformation structures by rolling to moderate (67% thickness reduction) and high (90% thickness reduction) rolling reductions. The deformation-induced microstructures after rolling are characterized by the aforementioned techniques to assess the effect of the processing parameters. Characterization of the annealed state reveals the effect of the degree of deformation on the recovery and recrystallization annealing phenomena. This allowed comparing recrystallization kinetics (in terms of nucleation and growth) in dependence on initial strain and annealing temperature. The long-term annealing kinetics were fully characterized at a wide range of annealing times and temperatures comparable to those during operation in fusion reactors.

Using Vickers hardness characterization, recovery could be fitted to classical Kuhlmann recovery kinetics, and recrystallization fitted to JMAK recrystallization kinetics, which in turn allowed the calculation of recrystallization activation energies. Much faster recovery and recrystallization kinetics were found for the plate warm-rolled to 90% thickness reduction, as compared to the plate warm-rolled to 67% thickness reduction. An initial incubation time before recrystallization was found for both plates warm-rolled to 67% and 90% thickness reductions. The different Avrami exponents found for the two plates were explained microstructurally in terms of nucleation.

The microstructural evolution during recovery and recrystallization was in good agreement with the mechanical characterization. The recrystallized grains were equiaxed and coarser than the grains of the starting microstructure. Vickers hardness measurements indicated that no considerable grain growth occurred after full recrystallization. The typical bcc rolling texture of the as-received plates was replaced by an almost-random texture in the fully-recrystallized state, with a slight preference for cube components, especially in the plate warm-rolled to 90% thickness reduction. This was explained in terms of oriented nucleation of cube nuclei. The nucleation regime showed a tendency for site-saturation for the plate warm-rolled to 67% thickness reduction and a constant nucleation rate for the plate warm-rolled to 90% thickness reduction. During nuclei growth, it was found that the deformation texture component $\{111\}<1\bar{1}0>$ was less consumed by the recrystallizing grains than the other main deformation texture components. Its higher stability was explained by the lower stored energy of this deformed texture component. Grain sizes are observed to increase linearly with time during recrystallization, until grain impingement occurs. The growth rates are found to be faster for higher annealing temperatures and higher deformation.

Considerably different activation energies were found for the plates W67 and W90, comparable to the activation energies of bulk diffusion and grain boundary diffusion respectively. The extrapolation of the recrystallization kinetics (based on these activation energies) to lower annealing temperatures allows predicting the lifespan of these tungsten plates under fusion reactor conditions. A much longer lifetime at normal operating temperatures was found for the plate W67 (e.g. at least 1 million years at 800 °C) as compared to the plate W90 (e.g 71 years at 800 °C). It is therefore concluded that high rolling reductions lead to severe degradation of the material at high temperatures and shall be avoided. It is suggested that the microstructural reason for the different lifetime of both plates lies in the much higher density of low angle boundaries present in the plate W90, as compared to the plate W67. The higher presence of low angle boundaries might aid diffusion at the interface between recovered matrix – recrystallized nuclei, and hence reduce the activation energy required for the migration of tungsten atoms towards the recrystallizing nuclei during recrystallization.

Thermal stability of warm-rolled tungsten

TERMISKE STABILITET AF VARM-VALSET WOLFRAM
钨温轧的热稳定性

Author: Angel Alfonso Lopez

Main supervisor: Wolfgang Pantleon

Co- Supervisors: Dorte Juul Jensen, Guangnan Luo

Section of Materials and Surface Engineering

Department of Mechanical Engineering

Technical University of Denmark

June 2015

List of publications

I. A. Alfonso, D. Juul Jensen, G.-N. Luo, W. Pantleon, **”Recrystallization kinetics of warm-rolled tungsten in the temperature range 1150 °C to 1350 °C”**. Journal of Nuclear Materials (**JNM**), 455 (2014) pp. 591-594.

II. A. Alfonso, W. Pantleon, G.-N. Luo, D. Juul Jensen, **“Microstructural investigation of the recrystallization of warm-rolled tungsten**”. Presented at 35th Risø International Symposium on Materials Science and Published in: **Proceedings 35th Risoe Symposium**. New frontiers in Nanometals, DTU, Roskilde, Denmark 2014, pp. 193-200.

III. A. Alfonso, D. Juul Jensen, G.-N. Luo, W. Pantleon, **“Thermal stability of a highly-deformed warm-rolled tungsten plate in the temperature range 1100 °C - 1250 °C”.** Fusion Engineering and Design **(FED)**, 98-99 (2015) pp. 1924-1928.

IV. A. Alfonso, D. Juul Jensen, G.-N. Luo, W. Pantleon, **“Microstructural characterization of recrystallization in warm-rolled tungsten to different strains".** In preparation and planned to be sent to a peer-reviewed journal.

Abbreviations

AR	Aspect Ratio
bcc	Body-centered cubic
EAST	Experimental Advanced Superconductive Tokamak
EBSD	Electron Back-Scattered Diffraction
EDS	Energy Dispersive X-ray Spectroscopy
fcc	Face-centered cubic
GB	Grain Boundary
GDOES	Glow Discharge Optical Emission Spectroscopy
HAB	High Angle Boundary
ITER	International Thermonuclear Experimental Reactor
IPF	Inverse Pole Figure
LAB	Low Angle Boundary
ND	Normal Direction
OM	Optical Micrograph
PFC	Plasma Facing Component
PM	Powder Metallurgy
RD	Rolling Direction
SFE	Stacking Fault Energy
TD	Transverse Direction
W67	Tungsten plate warm-rolled to 67% thickness reduction
W90	Tungsten plate warm-rolled to 90% thickness reduction

CONTENTS

Preface

This thesis is submitted as partial fulfillment of the requirements for the PhD degree at the Technical University of Denmark (DTU). This research work was mainly done at DTU mechanical Engineering (Section of Materials and Surface Engineering) during the period December 2011 – June 2015. This work was supervised by Wolfgang Pantleon, Guangnan Luo and Dorte Juul Jensen. The project was funded by the Sino-Danish Centre for Research and Education (SDC).

Lyngby, June 2015

Angel Alfonso Lopez

Acknowledgements

I give special consideration to my Supervisors, Wolfgang Pantleon, Guangnan Luo and Dorte Juul Jensen, for their constructive advice, patience, sharing of knowledge and guidance during my research work, as well as for their close supervision.

At DTU/MEK, I thank Marcel Somers as head of Section for his openness to PhD students, his care about their satisfaction and performance, and for trying to improve the working environment at MEK. I thank metallographer Steffen S. Munch for his assessment regarding good operation of equipment and habits in the metallography laboratory at MEK.

At DTU/Wind, I thank the technician Johannes Steen Bang for his complete laboratory introduction and teaching on how to operate equipment, as well as for his advice regarding good habits in the lab. I am also grateful to Preben Olesen for his close teaching of good EBSD equipment usage, Lars Lorentzen for guidance in operating furnaces, as well as for his encapsulation of samples in ampoules and annealing of samples. Yubin Zhang for his advice regarding EBSD data software treatment, Yue Zhao for openly letting me use their group´s furnace, and my PhD colleague Zhenbo Zhang for scientific advice and fellow companion support.

At DTU/CEN, I want to thank them for letting me use their facilities. I especially thank laboratory technician Zoltan Imre for his close and affable teaching of microscopy operation as well as researcher Hossein Alimadadi for his willingness to help in technical problems and in giving advice on crystallography.

I also thank the Department of Materials Science and Engineering, Laboratory of Advanced Materials, Tsinghua University (Beijing, China) for letting me use their facilities during my research stays at their institutions. Here, I want to especially thank Professor Wei Liu for his welcoming invitation to stay at his department and use their facilities, Professor Ben Xu for his invaluable help in finding accommodation and regulating my stay in Beijing, and fellow PhD students Qu Shilian, Lingkang Wu, Haiyan Xu and Jia Yuzhen for scientific discussions, as well as for arranging accommodation and helping me to get acquainted with Tsinghua University and Beijing city.

At the Institute of Plasma Physics, from the Chinese Academy of Sciences (ASIPP, Hefei, China), I want thank Prof. Guangnan Luo for warmly welcoming me into their group, introducing me to their facilities, and arranging accommodation for me in Hefei. I also thank fellow PhD students Zhao Si-Xiang and Yuping Xu for their scientific discussions as well as invaluable help in arranging and regulating my stay in Hefei.

I also want to thank the company Advanced Technology & Materials (AT&M) in Beijing, China, for sintering the tungsten raw material and applying the required rolling deformation in their facilities. I am also very grateful to the Sino-Danish Research Center for funding support regarding salary, material, equipment and travelling expenses for this project.

CHAPTER 1

Introduction

Pure tungsten is a potential candidate material for the plasma-facing first wall and the divertor of fusion reactors. In fact, tungsten has been chosen as the first-wall and divertor material for the International Thermonuclear Experimental Reactor (ITER). Both parts have to withstand high temperatures during service, which may alter the microstructure of the material by recovery and recrystallization.

Recovery summarizes a set of thermally activated processes that reorganize the microstructure of a metal by reducing its stored energy. These processes entail mutual annihilation of dislocations and reorganization of dislocations into fewer Low Angle Boundaries (LABs) with a higher misorientation across them, leading to subgrain growth.

Recrystallization is a thermally activated process by which almost defect-free grains are first nucleated inside a deformed or recovered matrix and will later on grow by grain boundary migration consuming the matrix. These free nuclei are fully or partially surrounded by High Angle Boundaries (HABs) and may present new orientations different from that of the deformed metal. The driving force for recrystallization is the energy stored in the deformed and recovered matrix which is consumed during recrystallization.

Recrystallization of tungsten will cause degradation of the material properties, such as a loss in mechanical strength, or (being most critical) embrittlement due to recrystallization. Although recrystallization of fusion reactor tungsten components has a detrimental effect on the mechanical properties and therefore must be avoided, it may still occur due to the presence of thermal shocks due to plasma instabilities. In order to understand the possible degradation of tungsten under fusion reactor conditions, it is paramount to characterize the kinetics of these restoration phenomena (recovery and recrystallization) at temperatures close to the service temperature in fusion reactors. Although a lot of work has been done on recovery and particularly on recrystallization, there is considerable lack of experimental data on tungsten, especially on the long-term annealing recrystallization kinetics, despite its importance for understanding and quantifying the degradation of tungsten components.

For this reason, the aim of this thesis is to experimentally quantify and characterize the long-term recovery and recrystallization kinetics of tungsten, both mechanically and microstructurally. This is done by obtaining Vickers hardness data and fitting them to theoretical models for recovery and recrystallization, and by characterizing the recrystallization of tungsten microstructurally with optical microscopy (OM) and Electron backscattered diffraction (EBSD). Two tungsten plates reduced to different thickness reductions by warm-rolling (67% and 90%, named W67 and W90 respectively) were studied. A wide range of experimental annealing times and temperatures were used for characterization, providing detailed data on the microstructural evolution and the change of mechanical properties during annealing.

Chapter 2 provides an introduction to the application of tungsten in fusion reactors, its production route, the characteristics of deformed metals and the annealing phenomena. Chapter 3 provides the experimental details of this work and gives an insight into the techniques that are used to characterize the studied tungsten plates, justifying the reason of their choice. Chapter 4 provides and explains the results of the Vickers hardness measurements. Chapter 5 provides and discusses the results of the microstructural characterization. Chapter 6 discusses the relationships and differences observed between both plates, W67 and W90, and attempts to compare some findings to previously reported studies in literature. Finally, Chapter 7 presents the outlook and the main conclusions which can be drawn from this study.

CHAPTER 2

Background

In this chapter, tungsten and its application in fusion reactors are introduced, followed by the synthesis method used to produce the tungsten plates at AT&M. Finally, the theoretical background is provided about deformation structures and the annealing phenomena of recovery and recrystallization.

2.1 Tungsten in Fusion reactors

Tungsten is the most promising candidate for the first wall material and the divertor in fusion reactors (see Fig. 1), which will be subjected to high heat peak loads up to 10-20 MW/m² and temperature gradients [1], causing thermal shock and fatigue that would damage most materials [2], [3]. These parts of the fusion reactor form the material interface with the plasma. While the first wall has a containment purpose, the divertor serves as an exhaust channel from which the energy of highly charged α particles can be dissipated (15% of the total thermal energy inside the reactor is dissipated in this way) [4], [5]. The requirements that materials for fusion reactors as the ITER (International Thermo-nuclear Experimental Reactor) must meet are very stringent. Among them, high thermal conductivity [6], low sputtering yield [7], good thermo-mechanical properties (e.g. creep resistance) [8], resilience to thermal shocks [5] and resistance to radiation damage [9] are the most critical. Tungsten can meet the aforementioned requirements during operation and can also offer high stability under such conditions (i.e. the highest melting point of all metals, 3695 K, and therefore the highest recrystallization temperature), excellent mechanical properties (i.e. the highest strength of all metals at high temperature), stability of mechanical properties at high temperatures, high heat conductivity at high temperature (98 W/m·K at 2000 K), relative chemical inertness, good radiation damage resistance, low tritium retention and excellent erosion resistance [4], [10].

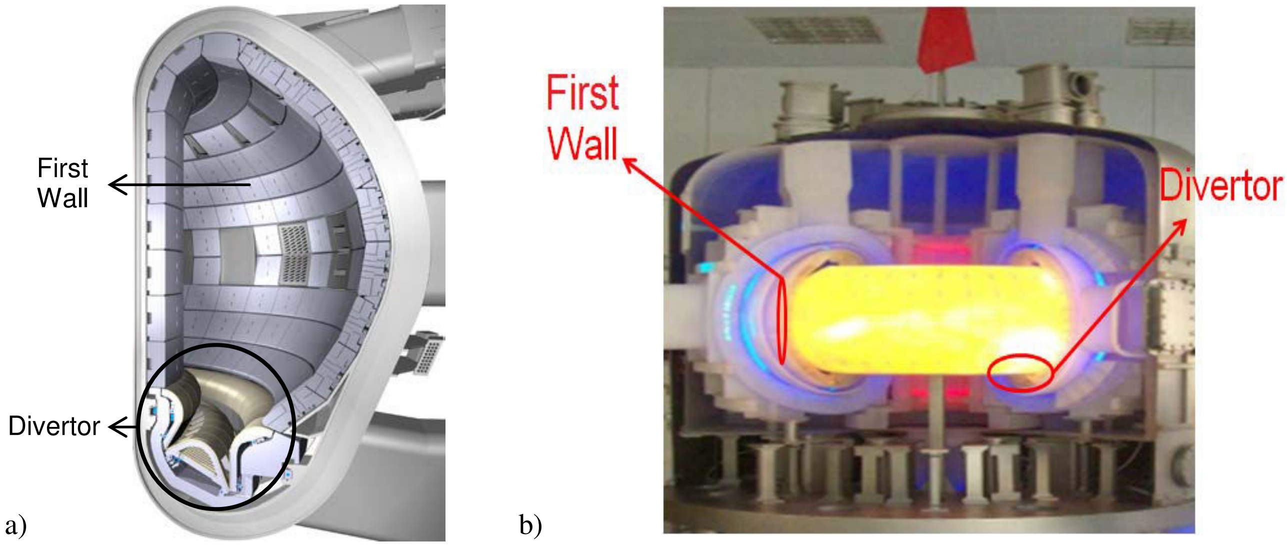

Fig. 1. a) A cut-away of the ITER vacuum vessel showing the inner wall (first-wall) attached to its blanket modules, and the divertor at the bottom, both planned to be made entirely of tungsten. ITER is currently under construction in Cadarache, France (from www.iter.org).
b) Model of EAST (Experimental Advanced Superconnductive Tokamak) vacuum vessel, located in Hefei, China. The divertor and first-wall of the fusion reactor are highlighted in red (from own Photograph of an EAST model taken at ASIPP (Hefei, China)).

In pure tungsten, microstructural changes during recrystallization cause considerable degradation of the mechanical properties, including High Angle Boundary (HAB) embrittlement [11], [12]. Although brittleness is an intrinsic property of tungsten said to be caused by the high activation energy required for screw dislocation glide [1], the brittleness of tungsten becomes even more pronounced in the recrystallized state. Although precipitation or segregation of brittle impurities at HABs is a cause of embrittlement in pure tungsten [13], explanations for embrittlement during recrystallization are also given in terms of HAB weakening [12]. When such stresses reach the tensile strength of the material, irreversible cracking at the grain boundaries occurs in order to relax the stresses in the matrix [12]. The cracking mode tends to be intergranular in the recrystallized state [12], [14]. When grain growth occurs, fracture is dominated by transgranular cleavage, also initiated at HABs [14].

The use of tungsten alloys is currently not feasible, as temperature and hence diffusion is so high under fusion reactor conditions that diluted impurities in oversaturated solid solution may segregate as new phases, mainly at the grain boundaries, weakening their strength [15]. Such precipitates have an embrittling effect on tungsten. Even strengthening by dispersed oxides or carbides (oxide dispersion strengthening or carbide dispersion strengthening; ODS or CDS respectively) has an embrittling effect on tungsten [13]. Recent studies show that control of the spatial distribution of very small (nano-sized) precipitates can provide an improvement of mechanical properties, as observed in CDS tungsten [16], [17]. However, this is an ongoing research topic which is not within the scope of this research work.

2.2 Synthesis of tungsten

The studied pure tungsten plates of this work were sintered from tungsten powders and warm-rolled to 67% and 90% thickness reduction after powder metallurgy treatment. This was done by the company Advanced Technology & Materials (AT&M), Beijing, China.

2.2.1 Powder metallurgy

Sintered tungsten metallic material is made from tungsten metal powder, produced through pressing and high temperature diffusion sintering processes. These 2 processes are called compacting and sintering respectively.

Powder compaction is used to produce the required shapes with reduced porosity. Cold-isostatic pressing is a compaction technique in which a metal powder is sealed inside a flexible mould and pressed uniformly using a fluid (especially a liquid) at room temperature. A uniform distribution of pressure over the powder is achieved. This method provides tungsten with high strength, rigidity, good and uniform permeability, and high purity with low oxygen impurity content [18]. For the production of the tungsten plates of this work, tungsten powder was cold-isostatically compacted (at room temperature) with 19.6 kPa of pressure. The final density of the powder is directly proportional to the applied pressure which normally ranges from 19.6 to 98 kPa. At this stage, the powder still needs to be sintered.

Powder sintering is the process by which the powder still compacted in the mold is heated up at high temperature for a long period of time. This process creates uniform solid products from the powder, increasing their density and enhancing the product properties. Powder sintering is the process of choice for metals with high melting points such as tungsten, for which easier processes such as metal casting cannot be used. Powder sintering is based on atomic diffusion, which takes place faster at high temperatures. The heat helps the powder particles to bond together, which eliminates porosity and increases compactness. The sintering process can be divided into three stages; during the 1st stage, the initial powder particles grow into bigger particles. In the 2nd stage, recrystallization and high diffusion are the dominating mechanisms, both leading to densification of the product by particle coalescence. During the 3rd stage, the pores become spherical and are eliminated at a much lower speed.

In the case of the tungsten material of this study, the tungsten powder was sintered (after compaction) in an electrical furnace at 2300 °C for 6 hours, in a hydrogen atmosphere. Using hydrogen during sintering presents two main advantages; on the one hand, by flowing pure hydrogen through the tungsten material, the oxygen that may be previously absorbed reacts with hydrogen to create water, thus removing detrimental oxygen impurities. On the other hand, the solubility of hydrogen in tungsten is low, ensuring that little hydrogen will be absorbed in solid solution.

2.2.2 Rolling

In rolling, a metal piece is forced to pass through a set of rolls which apply pressure on it, reducing its thickness with every pass (see Fig. 2). Rolling allows shaping by deformation up to high strain levels. Depending on whether the operation temperature is below or above the recrystallization temperature, the process is called cold-rolling or hot-rolling respectively. The term warm-rolling, in contrast to hot-rolling, will refer in this work to rolling done at high temperatures which are still below the recrystallization temperature of the rolled material.

Pure tungsten is hard and brittle at ambient temperature, making it difficult to deform. It is reasonable to expect that, in practice, tungsten components of fusion reactors will be worked at high temperatures by processes such as warm-rolling.

In order to obtain a dense tungsten material from powder with the desired shape and mechanical properties, a good approach is to apply warm-rolling and cold-rolling in several stages. Warm-rolling is required to induce ductility for better shaping of tungsten into rods or sheets. The reason for the low workability of W at low temperatures is its lack of mobile dislocations, which induces cracking and breakage [10]. Ductility at room temperature is only achieved by extensive wire drawing, when a long-filamentary microstructure is developed. Rolling of tungsten is usually carried out at quite high temperatures, as tungsten shows a very high ductile to brittle transition temperature (DBTT) [19]. However, warm-rolling must be carried out below the recrystallization temperature, because otherwise dynamic recrystallization would take place, which leads to grain boundary embrittlement [15], [20]. On the other hand, if worked at a too low temperature, cracks will easily build up. Intermediate stress-relief annealing is also necessary to relieve internal stresses, avoiding cracking.

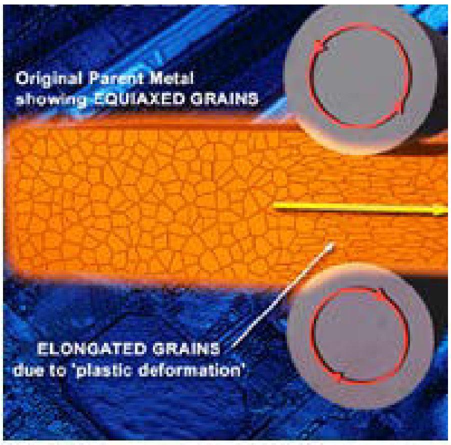

Fig. 2. Sketch of warm-rolling procedure which creates elongated grains along the rolling direction RD. The thickness of the rolled plate is decreased after rolling (from http://bsbcorp.vn/knowledge-center/thep-can-nong?lang=en).

2.3 Deformation structures

During deformation, most of the mechanical energy is released as heat, but a very small fraction (around 1%) is stored inside the material in the form of point defects and to a major extent as dislocations [21]. For worked tungsten, the dislocation density varies between 10^{12} m^{-2} and 10^{16} m^{-2} [15]. This dislocation density accounts for the strengthening of the metal during deformation, by accumulation of dislocations which become an obstacle to dislocation motion. The dislocation accumulation introduced after deformation represents most of the stored energy in the material. Dislocation density increases by generation of new dislocations. Mainly, dislocations are trapped inside the increased grain boundary area resulting from the grain shape change, due to accommodation to the macroscopic strain during deformation. The high mobility of point defects (vacancies and interstitials) renders their stored energy negligible at normal operating temperatures, as they annihilate easily even below room temperature. Since the fraction of the energy stored during deformation is present as dislocations, the stored energy is usually discussed in terms of dislocation density. The arrangement and distribution of the dislocations in the material also must be taken into account for the calculation of stored energies. Dislocations are stored in microstructural features characteristic of the deformed state.

Stored energies are usually estimated using calorimetry or by measuring related changes in the physical or mechanical properties of the material, such as the increase of hardness with deformation, process known as work hardening. As an example, the stored energies for lightly deformed aluminum (5% thickness reduction) and highly deformed aluminum (90% thickness reduction) were found to be 32.6 kJ/m^3 and 1390 kJ/m^3 respectively. These values were estimated by Godfrey et al. [22] from Transmission Electron Microscopy (TEM) measurements of dislocation boundary spacing and misorientation angles in cold-rolled aluminum. This is an example of stored energy calculations from subgrain boundaries, the energy being stored in the Low Angle Boundaries (LAB) that make up the subgrain boundaries, which consist of dislocation arrays. The magnitude of the stored energies in the subgrain boundaries of deformed metals (even deformed severely) is much lower than the energies related to phase transformations (e.g. 129.3 MJ/m^3 for the $\alpha-\gamma$ transformation in iron).

The microstructure of the metal also undergoes several changes during deformation; first of all, the grain shapes are modified from the macroscopic straining. Secondly, an internal microstructure consisting of cells or subgrains appears within the grains, caused by dislocation accumulation and rearrangement. Some of these cell or subgrain boundaries develop high angles, making them indistinguishable from HABs. The grain shapes are dependent on the type of deformation; rolled sheets present grains with lath shapes, compressed sheets show disc-like grains, and drawn wires develop needle-like grains. Moreover, the microstructures of rolled and compressed metals present higher grain boundary area than those which were deformed by wire-drawing or torsion, with their corresponding higher stored energy [23]. The stored energy is higher for microstructures with smaller grains and subgrains.

Tungsten, as a body-centered cubic (bcc) metal, generally undergoes slip upon deformation. Tungsten presents a very high stacking fault energy (γ_{SFE} = 0.23eV/Å^2 or γ_{SFE} = 3.68J/m^2), and its preferred deformation method is slip and cross-slip [15]. Due to this high stacking fault energy (*SFE*), twinning is a much less frequent deformation mechanism, and is only observed in high purity tungsten, occurring only on the {112} <111> system [15]. Also, the *SFE* is too high for dislocations to be able to dissociate into stacking faults (even though impurity segregation in tungsten may cause a lowering of this *SFE* and allow the creation of small stacking faults [24]). Nevertheless, screw dislocations dissociate in bcc metals at low temperatures, making the dislocations immobile, which induces brittleness into the material.

Slip in bcc metals takes place in the most densely packed directions <111>, and mostly in any of the 3 plane families containing this direction; namely {110}, {122} and {123}. Deformation occurs by glide of the most favorably oriented slip systems with the higher resolved shear stress. In fact, slip can take place on any {hkl}<111> system [25]. The number and selection of operating slip systems depends on the applied strain and the constraint imposed on the grain boundaries by the surrounding grains. This will affect the resulting microstructure as well as the resulting deformation texture.

In metals of medium to high *SFE* deforming by slip (e.g. tungsten) a deformation microstructure comprised of low dislocation density regions surrounded by walls of high dislocation density evolves. These structures are referred to as cells or subgrains, depending on whether the walls are made up of dislocation dipoles (cells) or sharp and ordered dislocation arrays (subgrains) [26]. Subgrains form as a result of recovery, which can be triggered by annealing (static recovery) or occur concurrently with straining (dynamic recovery). Cell structures form by dislocation movement during deformation, and are a result of self-organization of dislocations. Cells are usually equiaxed and range from 0.5 to 2 µm [19], [27]. At low strains, the cell walls are made up of dislocation dipoles. At higher strains, the cell walls become sharper due to dynamic recovery and the cell interiors show even lower dislocation density. Generally, the orientation difference between cells is usually smaller than 2°. This misorientation tends to increase with increasing strain. In contrast, in metals with low *SFE* (e.g. brass), dislocations dissociate into stacking faults and a cell structure does not form.

For polycrystalline tungsten, the thermal activation of dislocation motion marks the difference between brittle behavior at room temperature and improved ductility at higher temperatures, being necessary therefore to deform the metal at high temperatures (e.g. by warm-rolling). An increase in ductility at higher temperatures can be observed in tungsten for both single crystals and polycrystals (see Fig. 3) [15]. The much lower ductility for polycrystals at room temperature, as compared to single crystals (see Fig. 3), indicates that the presence of grain boundaries in polycrystalline tungsten has an embrittling effect at room temperature.

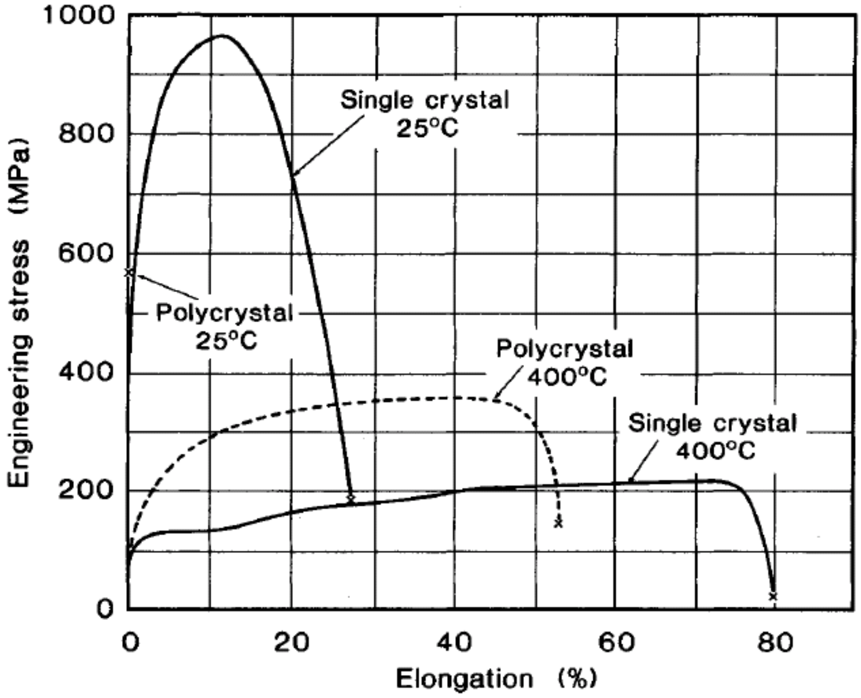

Fig. 3. Stress/strain curves for high purity single crystal and polycrystalline annealed tungsten (swaged and annealed for 1 h at 2000 °C). Tensile testing carried out at 25°C and 400°C. Improved ductility can be observed at higher temperatures, although the ductility of polycrystalline tungsten is lower than the ductility of single crystals. (from [15]).

When a polycrystalline metal is deformed, the grains change their orientation and the metal acquires preferred orientation (i.e. it develops a texture). The new orientations are related to the nature and direction of the applied stress, as deformation occurs on the most favorably oriented slip systems. Therefore, as the degree of deformation increases, certain orientations of the grains become more predominant, and the material develops a texture. The reorientation of grains by plastic deformation in tungsten is less severe than it is for low *SFE* metals (e.g. silver). In the case of bcc metals, the rolling textures are unaffected by alloying elements (i.e. impurities) and rolling temperature, and become sharper with increasing deformation [25].

In this work, Miller indices $\{hkl\} < uvw >$ will be used to represent orientations (texture) with respect to a reference frame. For rolling, the first indices $\{hkl\}$ refer to the crystallographic plane which is parallel to the rolling plane (or axis parallel to the normal direction), whereas the second set of indices $< uvw >$ represents the crystallographic direction parallel to the rolling direction. The rolling texture of bcc metals is usually composed by a range of orientations from $\{100\} < 001 >$ through $\{111\} < 1\bar{1}0 >$ to $\{111\} < 11\bar{2} >$ [25]. In other words, rolling textures of bcc metals show components of the α fiber $\{hkl\} < 110 >$ and the γ fiber $\{111\} < uvw >$. However, at thickness reductions higher than 70% the two components $\{112\} < 110 >$ and $\{111\} < 110 >$ usually become more pronounced [25].

A common way to represent textures is using pole figures. A more complete yet more complex representation of texture is achieved by orientation distribution functions (ODFs).

Microstructural investigations of rolled tungsten published in literature report well-defined and nearly-equiaxed subgrain structures (e.g. [19], [27], [28], [29]). Well-defined subgrain structures are observed after rolling to strains up to 98% thickness reduction at rolling temperatures between 1000-1700 °C. Subgrain sizes reported for moderately deformed and severely deformed tungsten are in the range 1.5-3 µm and 1-1.5 µm respectively. The subgrain size is directly related to the stored energy, which is the driving force for both recovery and recrystallization.

2.4 Annealing phenomena

When a deformed metal is annealed, thermal energy is provided to the material that allows reducing its stored energy, thereby restoring its microstructure. It is the stored energy that provides the driving force for the annealing phenomena of recovery and recrystallization.

2.4.1 Recovery

Recovery refers to the set of microstructural processes by which dislocations annihilate and rearrange themselves into more thermodynamically stable configurations (i.e. of lower stored energy), without long range motion of grain boundaries. Both dislocation annihilation and rearrangement are achieved through dislocation climb, glide and cross-slip [21], [22], [24], [25]. It is worth noting that point defects may also recover, although this process occurs below room temperature without the need of annealing.

Annihilation of dislocations occurs between dipoles (i.e. two parallel dislocations of opposite Burgers vector). For instance, edge dislocations can annihilate by glide or a combination of glide and climb. Screw dislocations can annihilate by cross-slip, more easily or at lower temperatures in metals with high stacking fault energy, aided by the lack of stacking faults [21].

If the amount of dislocations with opposite Burgers vector is uneven or dislocations cannot meet their opposite counterpart, total annihilation is not possible and these dislocations of same sign rearrange themselves into low energy boundaries or low angle boundaries (LABs). This process is known as polygonization and its simplest case (where finally only dislocations of one sign of the Burgers vector exist) is shown schematically in Fig. 4. Although the associated energy of these LABs increases with increasing misorientation, the amount of dislocations in the LABs is also higher for higher misorientations, which leads to a reduction in the energy per dislocation. Therefore, polygonization is a successful mechanism in lowering the stored energy by formation of misoriented LABs during recovery.

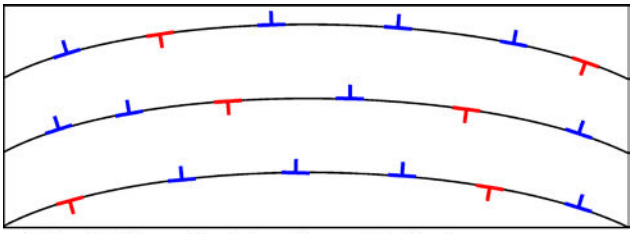

a) Bent lattice with dislocations of both sign

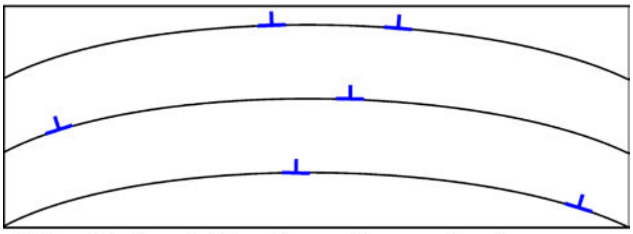

b) Annihilation of dislocations with opposite sign

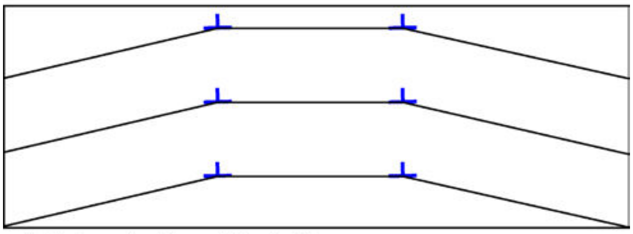

c) Polygonization of the lattice

Fig. 4. (a) Crystal with only dislocations of Burgers vectors of opposite sign (b) Resulting configuration after dipole annihilation where only dislocations of one sign are left. (c) Rearrangement of dislocations into LABs or polygonization (from http://upload.wikimedia.org/wikipedia/en/b/b6/Polygonization.png).

The term recovery refers to a set of microstructural changes, rather than a single mechanism. These processes take place gradually over time, so that there is no clear identification of a beginning or an end of recovery. Recovery occurs upon annealing of deformed metals, but also in any metal which is not in an equilibrium state, namely in metals with high concentrations of point and line defects, such as irradiated or quenched metals. These microstructural changes affect the properties of the metal, restoring them partially to their values prior to deformation. When recovery is occurring simultaneously with plastic deformation it is called dynamic recovery [21]**.**

Recovery competes with recrystallization since both are driven by the stored energy of deformation. In other words, recovery of the deformed grains will affect the recrystallization kinetics, affecting especially the nucleation process but also decreasing the speed of the migrating boundaries during growth. Moreover, recrystallized regions are defect free and can no longer recover.

Cell structures surrounded by high density dislocation walls are found right after deformation, in the case of metals of medium to high-stacking fault energies (e.g. tungsten). Recovery leads to the decrease of dislocation density of the cell interiors, while the cell walls evolve towards more sharply defined low angle boundaries. A subgrain structure has been formed at this stage. A subgrain structure can also be found right after deformation, especially for metals and alloys with high stacking fault energy and low solute content, which have been deformed to large strains at high deformation temperature. On the other hand, subgrains are not observed in low stacking fault energy metals (e.g. silver) deformed at high temperatures, because recrystallization sets in and eliminates the deformation structure before subgrain formation, unless recrystallization is inhibited (e.g. as it happens in particle-containing alloys) [21].

Upon further annealing, the subgrains tend to coarsen in order to decrease the low-angle grain boundary area and therefore its associated subgrain boundary energy. This process is known as **subgrain growth**, and occurs via subgrain boundary migration.

Another mechanism which might lead to subgrain growth is rotation and coalescence of subgrains, being driven by the reduction in subgrain boundary area too.

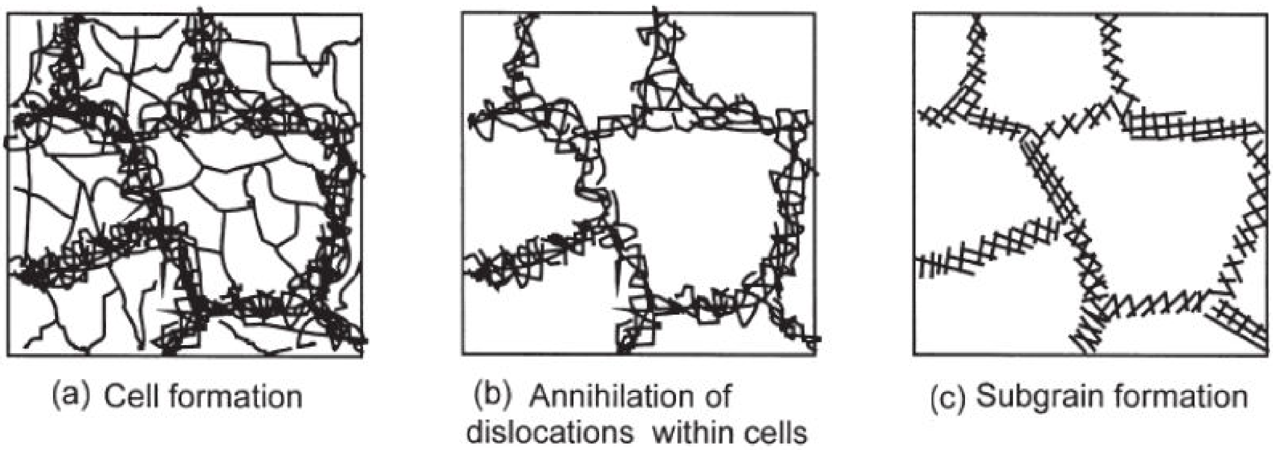

Fig. 5. Recovery stages. (a) Loose dislocations arranged into a cell structure; (b) These tangles furtherly evolve by dislocation annihilation and rearrangement in the cell interiors and walls; (c) resulting in a more sharply defined subgrain structure. Finally, these subgrains can grow in size driven by the corresponding reduction in stored energy (from [21]).

All these recovery stages do not necessarily take place during annealing. Some recovery stages might have already occurred during plastic deformation due to dynamic recovery (e.g. cell formation). Also, their occurrence and kinetics depends on factors such as strain, deformation mode and annealing temperatures, material and purity: more highly strained materials recover faster. Higher annealing temperatures will more readily provide the thermal energy required to activate recovery, leading to faster and more complete recovery with increased annealing temperature. Solutes have a pinning effect on dislocations and retard recovery by dislocation rearrangement and annihilation. Solutes might even retard dynamic recovery during deformation, which might lead to faster recovery kinetics during subsequent annealing, due to the higher stored energy after deformation [21].

Recovery kinetics

The microstructural changes induced by recovery are difficult to observe, and hence recovery is usually quantified indirectly by measuring the material property changes it induces. This approach only works for recovery kinetics as a whole, since it does not allow differentiating among the different set of atomistic mechanisms taking place during recovery. Indirect approaches include the measurement of the released stored energy during recovery (using calorimetry), and the decrease in electrical resistivity or mechanical properties (e.g. hardness, yield stress) over time during isothermal annealing. A microstructural yet more complex approach is also possible by measuring subgrain growth during recovery via electron microscopy. For any property X, its rate of change will be expressed as dX/dt. The most common types of empirical relationships to describe recovery kinetics are known as **type 1** and **type 2**.

Type 1 or Kuhlmann recovery kinetics:

This empirical relationship and mainly states that a recovery-related property change is inversely proportional to annealing time [cf. 21],

$$\frac{dX_R}{dt} = -\frac{c_1}{t} \rightarrow X_R = c_2 - c_1 \cdot \ln t \qquad (2.1)$$

where c_2 is an integration constant and c_1 is a constant directly related to the recovery kinetics. This expression only fails to describe the early stages of recovery ($t \rightarrow 0$) and the last stages ($t \rightarrow \infty$) [21].

Type 1 recovery kinetics are controlled by thermally activated dislocation glide and cross-slip. Type 1 kinetics usually describes recovery of polycrystals, which allows calculating the activation energy for recovery from the Arrhenius temperature dependence (e.g. [30]). However, since recovery is a combination of micromechanisms, it is usually found that the activation energy itself will vary during the different stages of recovery. Therefore, the activation energy for recovery cannot be defined unless the physical processes occurring at a certain stage of recovery are clearly understood.

A physical explanation for the kinetic logarithmic dependence of recrystallization kinetics (Eq. 2.1) was developed by D. Kuhlmann [31]. According to this explanation, recovery kinetics are related to how far a trapped dislocation (which is released by an external applied stress) can move away until becoming trapped by another obstacle (e.g. another dislocation). The area on which the dislocation moves freely can be defined as an activation area or activation volume V .

The relationship between an external stress applied on a dislocation and the activation energy required to release a trapped dislocation and move it an area V can be described as Eq. 2.2 (from Eq. 5 of reference [31]),

$$\frac{d\sigma}{dt} = -A \cdot \exp\left(-(\frac{Q - \sigma V}{kT}) \right) \qquad (2.2)$$

where σ is the applied true stress on the dislocation (equivalent to the recovery-related property X_R of Eq. 2.1), Q is the activation energy required to move the dislocation, k is the Boltzman constant and T is the temperature in K. Mathematically, Eq. 2.2 can be converted into an equation of the type Eq. 2.1 (namely Eq. 2.3) for the Vickers hardness (mechanical property measured during recovery in this work), which in turn allows to reflect the physical meaning of the recovery kinetics constant c_1 of Eq. 2.1 (notice that stress and Vickers hardness show an approximate relationship $HV = 3\sigma$ as deduced in [32], [33]:

$$\frac{d\sigma}{dt} = -A \cdot \exp\left(-(\frac{Q - \sigma V}{kT}) \right) \xrightarrow{\int_{\sigma_0}^{\sigma}} \sigma = \sigma_0^* - \frac{kT}{V} \ln t \xrightarrow{HV=3\sigma} \boxed{HV = HV_0^* - \frac{3kT}{V} \ln t} \qquad (2.3)$$

Comparison of Eq. 2.3 with Eq. 2.1 allows to elucidate the values for the kinetic constant c_1 and the activation volume V (Eq. 2.4). In Eq. 2.4, $b = 2.74 \cdot 10^{-10}\,\mathrm{m}$ is the burgers vector for the tungsten crystal lattice, while A is the activation area and n is a proportionality constant. These values will be discussed in the discussion section (6.1 recovery). Notice that the activation volume V is defined as the area swept by the dislocation times the Burger's vector.

$$c_1 = \frac{3kT}{V} \rightarrow V = \frac{3k}{c_1 / T} \rightarrow V = b \cdot A = n \cdot b^3 \qquad (2.4)$$

Type 2 recovery kinetics or power law kinetics:

Other times, recovery kinetics are properly described by a power law (Type 2 recovery kinetics) of the type [cf.21]:

$$\frac{dX_R}{dt} = -c_1 \cdot X_R^m \qquad (2.5)$$

Some literature studies report logarithmic recovery kinetics (Kuhlmann recovery kinetics) based on measurements of electrical resistivity [34], [35] for recovery of cold-worked tungsten during annealing. Additionally, in literature [36] it was found that during recovery the reduction of the strength of tungsten followed the changes observed in subgrain coarsening according to follow a Hall-Petch relationship. Given that recovery kinetics also affect recrystallization kinetics, recovery kinetics are determined in detail in the current study.

2.4.2 Recrystallization

Recrystallization is the process by which defect-free regions (nuclei) are generated in the deformed matrix and grow into it. The driving force for this process is the internal energy difference between the highly strained deformed material and the recrystallized grains with quite low dislocation content. The thermal energy required to activate this process is provided during annealing of the metal [37], [38], [39].

A partly-recrystallized microstructure is comprised at any time of a mixture of recrystallized and recovered matrix, mathematically represented by the recrystallized fraction (X) which varies from 0 to 1 while recrystallization proceeds. The recrystallization temperature is usually defined as the temperature at which 50% recrystallization ($X = 0.5$) is reached after annealing for a constant time (e.g. 1 h).

Recrystallization has 2 different stages: nucleation characterized by the formation of new defect-free regions, and growth of these nuclei. The recrystallizing nuclei grow into the recovered matrix until they impinge on other nuclei and stop growing in the impinged directions. Nucleation and growth usually occur simultaneously during annealing.

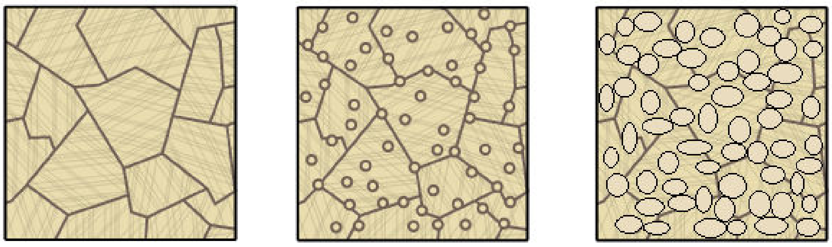

a) Deformed structure

b) Nucleation of defect-free grains

c) Partly recrystallized

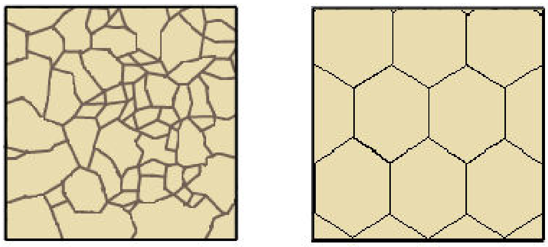

d) Fully recrystallized

e) Grain Growth

Fig. 6. a) Deformed structure with its corresponding stored energy. b) Nucleation of almost defect-free grains at favoured sites (i.e. mainly at GBs and triple junctions). c) Partly-recrystallized state where the initial nuclei (represented as eliptical nuclei) have grown. Some of the recrystallizing nuclei already impinge upon each other. d) Nuclei growth up to full recrystallization. e) Grain growth after recrystallization, leading to hexagonally-shaped grains.
(edited from:http://commons.wikimedia.org/wiki/File:Ricristallizzazione_e_accrescimento.svg#/media/File:Ricristallizzazione_e_accrescimento.svg).

Nucleation describes the formation of defect free regions of low internal energy separated by a HAB from the recovered matrix in which they appeared and shall grow into. The driving energy for nucleation is provided by the defects accumulated in the recovered microstructure. Nuclei will be viable only when they are thermodynamically favourable. On the one hand, there is a stored energy reduction Δu from creating a defect-free region by eliminating the dislocation density (ρ). On the other hand, new HABs separating these nuclei from the recovered matrix will have a high boundary energy (γ_b). The balance between these two energies establishes the minimum nucleus radius R required for a viable recrystallization nucleus [37], [40].

$$R = \frac{2\gamma_b}{\Delta u} \approx 1\,\mu\text{m} \qquad (2.6)$$

Therefore, deformed regions of high stored energy (or high local strain) will be the favorable nucleation sites. These regions may be grain boundaries, triple junctions, or deformation induced bands (i.e. transition bands, shear bands…) presenting short-range orientation gradients which favor nucleation. Nucleation in the strict sense of phase transformations is not likely, since the gain in energy by the formation of a nucleus is much lower than that of standard phase transformations. As a consequence, recrystallized nuclei will not form randomly distributed, but at the aforementioned nucleation sites [21]. Also in the case of phase transformations, nuclei often form non-randomly distributed.

Nucleation can occur at the beginning of recrystallization (site-saturated nucleation), in which case the nuclei density N will be an important parameter, or happen throughout recrystallization, in which case the definition of a nucleation rate $\dot{N} = (dN/dt)$ becomes useful. This nucleation rate $\dot{N}$ can in turn be constant or vary during recrystallization. The nucleation process is important, as it will determine the final grain size as well as the orientations of the grains of the recrystallized microstructure [21].

Growth is the process by which the boundaries surrounding the defect-free nuclei migrate through the neighboring recovered matrix while consuming it. Nuclei will grow into the recovered matrix until they impinge other recrystallized grains. At this point, nuclei growth will stop given the lack of stored energy in the neighboring grain [21].

The velocity at which a boundary moves is given by Eq. 2.7,

$$v = MP \quad ; \text{(where } P = P_d - P_c\text{)} \qquad (2.7)$$

The driving pressure for recrystallization (P_d) will be the stored energy corresponding to the dislocation density of the recovered matrix,

$$P_d = \alpha \rho G B^2 \qquad (2.8)$$

where α is a constant with a value close to 0.5, ρ is the dislocation density, G the shear modulus and b the Burgers vector of the dislocations.

An opposing force to nuclei growth (P_c) is also present whose driving force is the boundary energy related to the boundaries of the nucleus,

$$P_c = \frac{2\gamma_b}{R_n} \qquad (2.9)$$

where γ_b is the boundary energy and R_n is the radius of the recrystallized nucleus. The balance between these opposing forces $(P_d - P_c)$ will determine the velocity of the migrating grain boundary during growth. Given this balance of forces, it can be noted that the velocity or growth rate v will be faster with higher initial stored energy and will slow down during annealing due to recovery and the consequent reduction of the stored energy of the recovered matrix [41]. Although the mobility M may be orientation dependent, the main reason for growth rate changes during recrystallization is considered to be the variation in overall driving pressure. This variation in driving pressure over time is due to decreasing dislocation densities (due to on-going recovery), and also due to local heterogeneities which the moving boundary meets.

Grain growth is a stage occurring after full-recrystallization is complete, and leads to a state of lower associated internal energy. The internal energy of the metal is decreased by a reduction of grain boundary area. The stored energy in the HABs is the driving force for grain growth. Since the order of magnitude in energy for grain growth is two times lower than that of recrystallization, grain growth typically starts after full recrystallization. During normal grain growth, the bigger grains tend to expand at the expense of the smaller grains. When a boundary pinning effect is present (e.g. particles, LABs with low mobility) some grains may grow abnormally large with respect to the rest, being therefore noted as abnormal grain growth [42].

Recrystallization as a whole is a thermally activated process and as such presents a relationship between the time t to reach recrystallization and the annealing temperature T, which allows to obtain an activation energy for the process as a whole. The relation can be described by an Arrhenius relationship (Eq. 2.10),

$$t = t_o \exp(E / RT) \qquad (2.10)$$

where t_o is a pre-exponential factor, R is the universal gas constant, E is the activation energy required during annealing for both nucleation and growth, and T is the annealing temperature.

A typical example of recrystallization kinetics is shown in Fig. 7. The study of recrystallization kinetics considers both recrystallization processes altogether (nucleation and growth), as they are difficult to study individually. A model usually used to fit recrystallization kinetics was proposed by Johnson-Mehl-Avrami-Kolmogorov (JMAK), which describes the recrystallized fraction (X) as a function of the annealing time t (cf. [21]),

$$X = 1 - \exp(-Bt^n) \qquad (2.11)$$

where B is a coefficient describing thermal activation and n is known as the Avrami exponent, being related to the nature of nucleation and dimensionality of the growth process [21].

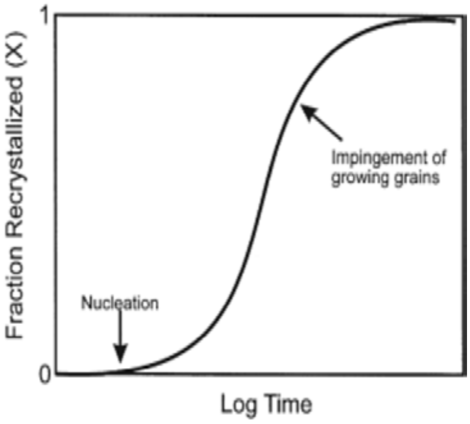

Fig. 7. Recrystallization kinetics typical of isothermal annealing. One can see that at the early stages of nucleation the recrystallized fraction is low and it increases exponentially over time as the nuclei grow into the recovered matrix. When the growing nuclei impinge one another, the recrystallization kinetics decrease until full recrystallization is achieved (from [21]).

The plastic strain, the initial grain size and the annealing temperature can be related to the recrystallization rate and the final grain size after recrystallization as follows (cf. [21]):

1) A minimum amount of deformation is needed (usually around 5-15% strain), to make the formation of a nucleus energetically favorable and guarantee its growth.
2) Deformation to higher strains brings about faster recrystallization, as the higher stored energy in the deformed matrix is the driving force for recrystallization.
3) Deformation at high temperatures and/or low strain rates decreases the recrystallization velocity due to the lower stored energy in the deformed matrix.
4) Higher annealing temperatures bring about faster recrystallization, since the required activation energy for recrystallization can be reached more easily (Arrhenius relationship).
5) The initial texture before deformation and the deformation texture influences the recrystallization kinetics, as the active slip systems of the grains of the starting texture, as well as the interaction between the grains, will affect the orientation gradients and stored energy in the deformed microstructure.
6) Recrystallization in single crystals is retarded compared to polycrystals, due to the lack of high angle boundaries and triple junctions serving as nucleation sites.
7) More highly-strained materials produce a finer recrystallized microstructure, since more nucleation sites become active.

8) Recrystallization will be retarded for bigger starting grain sizes (as there are fewer HABs which are favorable nucleation sites) and for metals deformed at higher temperatures (since recovery will decrease its stored energy).

9) Alloying elements or impurities (as solutes or small dispersoids) decrease recrystallization rates, as they have a pinning effect on the sweeping boundaries of the recrystallized grains.

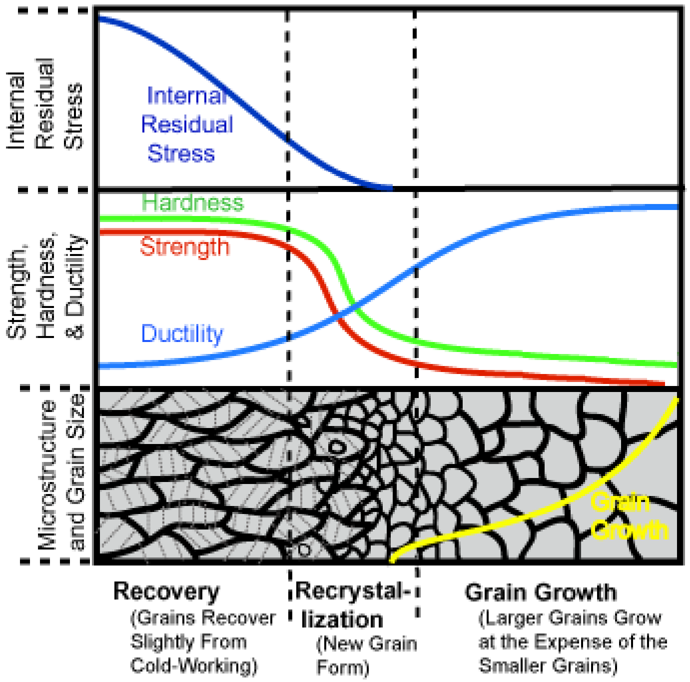

Fig. 8. Scheme showing the softening or loss of strength typical of recovery and recrystallization during annealing. Two different stages, namely recovery and recrystallization, can be clearly distinguished by their different slopes. Recrystallization is the 2nd stage, and entails a large decrease in hardness and strength. (edited from:https://www.nde-ed.org/EducationResources/CommunityCollege/Materials/Graphics/Recovery.gif)

Regarding static annealing, as seen in Fig. 8, recrystallization is (to a higher extent than recovery) related to degradation of the material properties, expressed as softening or loss of strength. Additionally, in the case of tungsten, recrystallization brings about an embrittling effect during deformation, due to accumulation of internal stresses at the grain boundaries. In fact, recrystallization embrittlement makes the study of the recrystallization of tungsten a critical asset for high temperature applications such as fusion reactor components.

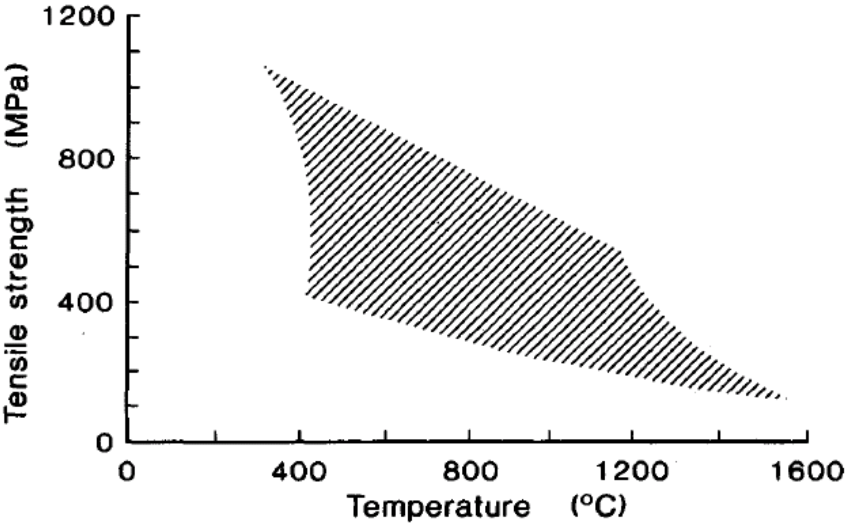

Fig. 9. Tensile strength of tungsten sheets deformed to different strains as a function of testing temperature (from [15]).

Fig. 9 graphically showcases the degradation of the properties of tungsten during recrystallization. The upper strength limit corresponds to a stress-relieved sheet after deformation to high strain, whereas the lower strength values around 400 °C correspond to sheets deformed to low strains. As the tensile testing temperature is increased above 1200 °C, the material recrystallizes and loses its strength. At about 1500 °C, there is a lower strength limit characteristic of the fully recrystallized state. Below 1200 °C, the degradation of the properties is only due to recovery.

2.4.3 Texture evolution

The microstructural and textural changes induced by recrystallization are relevant for the application of tungsten in fusion reactors because they are expected to affect the behavior of tungsten under irradiation conditions [43], as well as its mechanical properties [25]. For example, refinement of the grain size may lead to improved radiation resistance [44]. It has also been observed that the crystallographic orientations of the grains are critical in determining the amount and structure of blistering on the surface when exposed to a high flux plasma [45]. It has also been observed that the <001> orientation exhibits the highest deuterium blistering resistance [46]. Orientation dependence is also shown for He trapping in radiation-induced defects in W during fusion operation, which can seriously affect the PFC robustness [47].

The mechanical properties are also affected by the material texture. As an example, slip, the basic mechanism for plastic deformation of pure tungsten, occurs along {110} and {112} planes, in the most densely packed [111] direction [15]. Additionally, slip occurs in the {111} plane at high temperature, and both twinning and cleavage are affected by texture [15].

The texture of rolled tungsten and other bcc transition metals is accepted to present a "typical bcc rolling texture"; a texture comprised of a γ fiber {111}<uvw> and a α fiber {hkl}<110> ([48], [49]). The fibers are usually heterogeneous, and some studies find the γ fiber to be more predominant

[48]. The heterogeneity in the fibers is inherited from warm-rolling. Along with the α and γ fibers, a predominant rotated cube component {001}<110> has also been found in rolled tungsten ([50], [47]) and in other bcc metals like ferritic steel ([51], [52]).

The recrystallization texture of tungsten is widely found to be weak or quite close to random (e.g. [46], [50]). This weak recrystallization texture is rationalized in [50], in terms of the recrystallization of (001)<110> components into various components related to <110> rotations, based on the elastic isotropy of tungsten.

2.4.4 Activation energies

2.4.4.1 Activation energies of recrystallization

The recrystallization activation energy can be defined as the energy barrier that needs to be overcome (or the energy that needs to be provided externally) for recrystallization to occur. This is a very important parameter because it will determine the lifetime of a tungsten component during high temperature operation, since recrystallization degrades the material. Few literature studies on tungsten recrystallization provide recrystallization activation energies comparable to bulk diffusion in tungsten (586-628 kJ/mol). For example, comparably high activation energies for recrystallization include an activation energy of 544 kJ/mol reported for recrystallization of a drawn wire of high purity tungsten [53], and recrystallization activation energies of 502 kJ/mol and 573 kJ/mol for recrystallization of heavily-drawn wires annealed under vacuum or Argon atmosphere, respectively [54]. Usually, lower recrystallization activation energy values are found in literature (e.g. [55], [53], [56], [57], [58], [59]). The reason for these lower recrystallization activation energies is said to remain in the additional contribution of grain boundary diffusion, which depends on the microstructure in polycrystalline tungsten [15].

2.4.4.2 Activation energies of bulk-diffusion

Tungsten bulk self-diffusion is relevant especially in coarse-grained material where the contribution of grain boundary diffusion is less dominant [15]. For this reason, the activation energies for bulk self-diffusion of tungsten were compiled from literature. Literature reference [15], a book on tungsten properties, presents a compilation of literature data for activation energies of bulk self-diffusion ranging from 586 to 628kJ/mol. Direct measurements of bulk self-diffusion activation energies from diffusion of tungsten radiotracers include 526-666 kJ/mol [60], 568 kJ/mol [61], 504 kJ/mol [62], 640kJ/mol [63], 669kJ/mol ([64],[65]). Other indirect measurements provide 523kJ/mol [66], 582 kJ/mol [67] and 594kJ/mol [68]. Some theoretically predicted values found in literature are 586 kJ/mol and 611 kJ/mol, as estimated in [69] and [70].

2.4.4.3 Activation energies of grain boundary-diffusion

Grain boundary diffusion becomes more important with decreasing grain boundary spacing [15]. Literature reference [15] quantifies the activation energy for grain boundary diffusion to be 377-460 kJ/mol. Other reported values in individual literature references include 210.7 kJ/mol [71] (at 1500-1900 °C), 294 kJ/mol [72] (at 887-1050°C) and 380.7 kJ/mol [73].

As an example for the calculation of activation energies of grain boundary diffusion, Rühle & Almanstötter [71] determined the activation energy for grain boundary diffusion in the temperature range 1500-1900 °C experimentally, for severely-deformed pure tungsten wire. The calculation is based on the estimation of grain growth after recrystallization at different annealing time and temperature. The activation energy for GB migration is calculated to be $G_{gb} = 210.7 \pm 13.2$ kJ/mol using an Arrhenius relationship for the grain size with annealing temperature.

For clarity purposes, the range of activation energies for bulk self-diffusion and grain boundary diffusion are summarizedd in Table 1.

Table 1. Ranges of the activation energies for bulk self-diffusion and grain boundary diffusion (from reference [15]).

Bulk self-diffusion activation energy	Grain boundary diffusion activation energy
586 – 628 kJ/mol	377 – 460 kJ/mol

In this background chapter, it was described that recovery and recrystallization will cause degradation in material properties as softening and loss in mechanical strength, being most critical for tungsten the embrittlement due to recrystallization. In order to characterize the possible degradation of tungsten under service conditions, it is paramount to characterize the kinetics of these restoration phenomena (recovery and recrystallization), as well as to understand the microstructural evolution during recrystallization, at temperatures close to the service temperature in fusion reactors. Although a lot of work has been done on recovery and particularly on recrystallization, there is considerable lack of experimental data on tungsten, especially on the long-term annealing recrystallization kinetics, despite its importance in understanding and quantifying the degradation of tungsten components. For this reason, the long-term recovery and recrystallization kinetics of tungsten are experimentally quantified and characterized in this work, both mechanically and microstructurally.

Chapter 3

Experimental Method

In this chapter, the experimental procedures followed in this thesis are described. Apart from the experimental details, a few results on Optical Microscopy and impurity measurements (GDOES) are also provided. Moreover, the theoretical background of the most widely used techniques of this work, namely Vickers hardness testing and Electron Backscattered Diffraction (EBSD), is explained in detail.

3.1 Experimental details

Two tungsten plates warm-rolled to 67% and 90% thickness reduction (and with 99.95% purity according to the material supplier) were received from Advanced Technology & Materials Co., Ltd., Beijing. The plates had been manufactured from tungsten powder by cold-isostatic pressing and sintering under a hydrogen atmosphere at 2300 °C for 6 h. The tungsten product was pre-annealed at 1200 °C for 15 minutes before rolling in order to relieve internal stresses. After pre-annealing, the tungsten plates were warm-rolled 10 times by reverse rolling (i.e. the plate was turned over after each rolling pass), starting at a temperature of 1550 °C and the last pass being carried out at 1100 °C. No protective atmosphere was used during rolling. The initial and final thicknesses of the tungsten plate warm-rolled to 67% thickness reduction were 36 mm and 12 mm respectively. The initial and final thicknesses of the tungsten plate warm-rolled to 90% thickness reduction were 39 and 4mm respectively. The final dimensions of the warm-rolled plates were 180x100x12 mm^3 and 210x130x4 mm^3 respectively. From now on, the plates warm-rolled to 67% and 90% thickness reduction will be referred to as W67 and W90 respectively.

The homogeneity of the plates after rolling was checked by testing the rolling surface of the plates with Vickers hardness measurements, using a load of 10 kg and a dwell time of 10 s. The as-received plates and the Vickers hardness profiles obtained on their rolling surfaces are shown, for both plates W67 and W90, in Fig. 10 and Fig. 11 respectively. 10 hardness measurements were done and averaged within each of the squared areas of the plates indicated in Fig. 10b and Fig. 11b. The maximum observed standard deviations of the average among the 10 hardness indents for the individual indented areas were $HV_{W67} \pm \frac{\sigma_{W67}}{\sqrt{10}} = 445 \pm 3HV_{10}$ and $HV_{W90} \pm \frac{\sigma_{W90}}{\sqrt{10}} = 440 \pm 2HV_{10}$ for the plates W67 and W90 respectively. This means that these maximum deviations correspond to the squared areas with average Vickers hardness $HV_{W67} = 445HV_{10}$ for the plate W67 (see Fig. 10b) and $HV_{W90} = 440HV_{10}$ for the plate W90 (see Fig. 11b). The maximum difference in Vickers hardness from indented area to indented area was $HV_{W67\max} - HV_{W67\min} = 17HV_{10}$ and $HV_{W90\max} - HV_{W90\min} = 12HV_{10}$ for the plates W67 and W90 respectively. It was concluded that both plates presented a reasonably homogeneous hardness distribution throughout the plate.

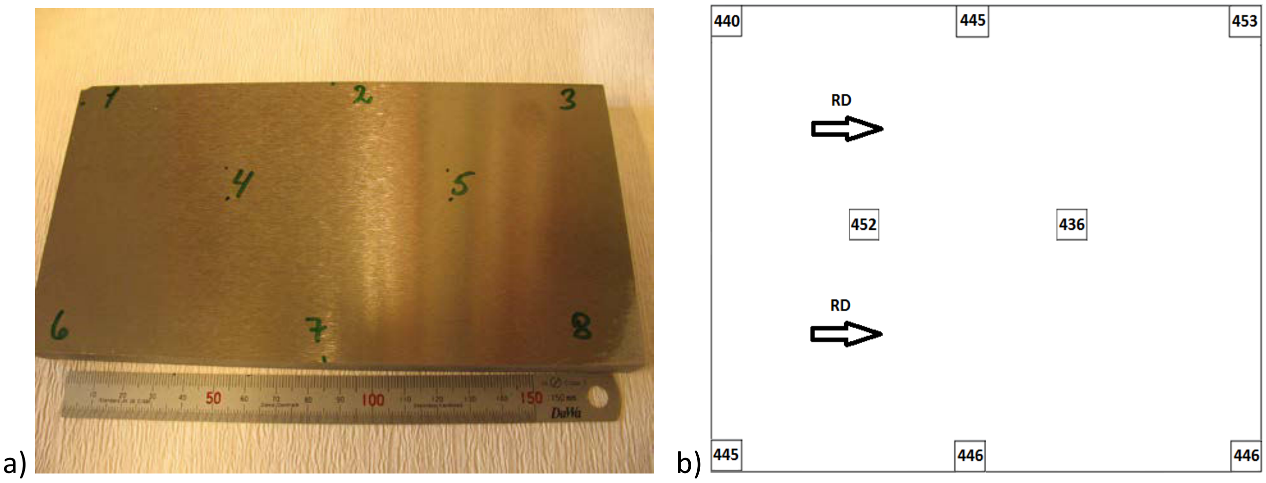

Fig. 10. Plate W67. a) Picture of the plate with the indented areas (in order to check homogeneity in hardness) numbered 1 to 8. The rolling direction is shown horizontally and the transversal direction vertically. b) Sketch showing the position of the areas where the hardness values are obtained for each area (HV_{10} as measured on the RD/TD surface and averaged over 10 indents). The values are measured on the surface which has been in direct contact with the rolls.

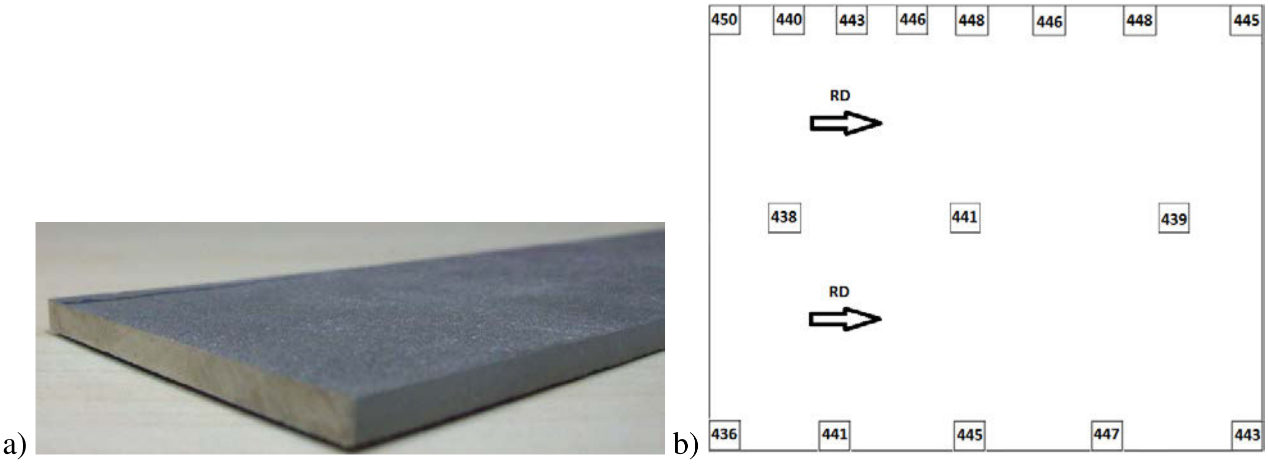

Fig. 11. Plate W90. a) Picture of the plate, with RD being the longest direction, TD representing the width of the plate, and ND representing its thickness. b) Sketch showing the position of the areas where the hardness values are obtained (HV_{10} as measured on the RD/TD surface and averaged over 10 indents). The values are measured on the surface which has been in direct contact with the rolls.

For both plates W67 and W90, the hardness on the RD/ND surface was also checked, showing a considerably lower value as compared to the outer RD/TD plane. For the plate W67, the hardness for individual as-received samples was also checked at the middle of the RD/TD plane (at a depth of approximately 6mm), and the hardness of the internal RD/TD plane was comparable to that of the RD/ND plane. It was concluded that the higher hardness value of the outer RD/TD surface was due to the overstraining due to the direct contact with the surface of the rolls. Therefore, it was ensured that the hardness and microstructural characterization was done far from the surface with direct contact with rolls (outer RD/TD surface).

In contrast, a third plate warm-rolled to 50% thickness reduction had to be discarded after checking that its hardness distribution turned out to be very heterogeneous. Optical microscopy revealed that the plate also had cracks which developed along the GBs. The cracking and the heterogeneous hardness distribution suggest that the plate underwent brittle fracture during rolling, which led to heterogeneous straining. The fact that an intermediate annealing step (at 1350 °C for 24 h) was introduced to achieve a fully-recrystallized state before rolling (for this plate only, in order to be certain of the initial state before deformation) could explain this behavior; the inherent brittle behavior of tungsten becomes more pronounced in the recrystallized state; a process known as “recrystallization embrittlement” in tungsten ([15], [13]). Therefore, rolling this plate in the recrystallized state to 50% thickness reduction might have led to cracking and heterogeneous straining. The rest of the plates (W67 and W90) did not undergo this intermediate recrystallization annealing step before rolling.

A chemical analysis of the as-received plates (W67 and W90) was carried out, as impurities can strongly affect the recrystallization kinetics. EDS (Energy-dispersive X-ray Spectroscopy) and GDOES (Glow Discharge Optical Emission Spectroscopy) were used to measure impurity contents.

Energy-dispersive X-ray Spectroscopy (EDS) is a technique that detects and analyzes X-rays emitted from a sample in order to determine the chemical composition of its constituent elements [74]. It consists of an X-ray detector attached to a Scanning Electron Microscope (SEM) or a Transmission Electron Microscope (TEM). The X-rays are generated from the interaction of the electrons from the electron beam with the different atoms of the sample. The advantages of this technique are its capability to do non-destructive and quick measurements, and the lack of need of specimen preparation. The EDS equipment used in this work could detect elements with an atomic number Z above 6, with a detection limit of approximately 1% wt.

Glow Discharge Optical Emission Spectroscopy (GDOES) is a technique that can measure the chemical concentration and depth profiles of constituent elements in a solid sample ([75], [76], [77]). The technique relies on sputtering the surface of the specimen and detecting the emission of the constituent elements with photon detectors. The sputtering is carried out using low energy Argon or Neon ions, which cause damage to the sample. The main advantages of GDOES are high measurement speed (faster than EDS), the lack of need of ultra-high vacuum and specimen preparation, and the possibility to measure big specimens. Other advantages are the possibility to detect all kind of chemical elements (regardless of their atomic number) and the high sensitivity of GDOES measurements (e.g. compositions as low as 0.1% wt. could be detected for P and S in white cast iron AS2027 [77], given that good calibration curves from standard samples are available. This information is given as an example, understanding that lower detection limits are also possible with GDOES). These specifications are particularly suitable for Plasma Facing Components (e.g. parts of the tungsten divertor). Impurities in Plasma Facing Components (PFCs) have an effect in plasma-surface interactions and recrystallization kinetics (e.g. interstitial impurities like boron, oxygen, nitrogen, phosphorus, silicon, hydrogen and carbon pin the grain boundaries, hampering their mobility during recrystallization and therefore having a retarding effect on recrystallization [15]).

GDOES allows to measure these big parts without introducing any modifications that might affect the performance of the PFCs during service.

The chemical analysis of the plates W67 and W90 by EDS did not detect any impurities. However, as mentioned earlier, the sensitivity for impurity detection with this EDS equipment was around 1% wt., which is why GDOES was additionally used for higher sensitivity. Very low impurity concentrations can affect recrystallization kinetics. The chemical composition of the elements present in both tungsten plates (W67 and W90) were measured with GDOES and compared. The chemical concentrations for all detected elements are shown in Table 2. The purity of the tungsten plates was determined to be 98% wt. with these GDOES measurements. However, the GDOES equipment used at DTU/MEK was not calibrated for measurement of high W concentrations, and therefore these purity values cannot be considered as absolute values. Similar concentrations of impurity elements were detected in both plates. Only the elements Sr, Ge and Mg might have a slightly higher concentration in the plate W67, as compared to the plate W90. The GDOES results suggest that there was no significant impurity concentration difference between the plates. It was therefore assumed that the low impurity levels found would affect recrystallization kinetics in a similar way for both plates. For this reason, the chemical impurity of the plates will not be dealt with from now on in this work.

Table 2. Chemical concentrations determined by the GDOES element analysis carried out on both warm-rolled plates W67 and W90. The comparison of both plates in terms of impurity elements shows that there is no considerable impurity difference between the plates. The displayed concentrations in Table 2 are averaged from 3 GDOES measurements for each plate. The standard deviations for the concentrations of all elements of each plate are also listed as σ_{67} and σ_{90} respectively.

Element	Element wt. % W67 plate	σ_{67}	Element wt.% W90 plate	σ_{90}	Difference between both plates
W	*97.986*	*±0.01152*	*98.040*	*±0.01713*	*0.054*
Fe	0	±0	0	±0	0
Ti	0	±0	0	±0	0
Al	0.01295	±0.00126	0.01462	±0.00104	0.00166
C	0	±0	0.00003	±0.00002	0.00003
O	0.00013	±0.00005	0.00143	±0.00202	0.00130
N	0.01177	±0.00097	0.00827	±0.00038	0.00349
P	0	±0	0	±0	0
S	0	±0	0	±0	0

Ni	0	±0	0	±0	0
Cr	0	±0	0	±0	0
Mn	0.26127	±0.00327	0.25983	±0.00690	0.00143
Si	0.70820	±0.00672	0.73310	±0.01066	0.02490
V	0.82540	±0.00434	0.81810	±0.00014	0.00730
Co	0	±0	0	±0	0
Cu	0	±0	0	±0	0
Nb	0.12567	±0.00164	0.12283	±0.00196	0.00283
Mo	0.00233	±0.00017	0.00139	±0.00056	0.00094
B	0	±0	0	±0	0
Pb	0	±0	0	±0	0
Bi	0.00013	±0.00005	0.00011	±0.00009	0.00002
Sn	0	±0	0	±0	0
H	0	±0	0	±0	0
Cl	0.00002	±0.00001	0.00001	±0	0.00001
Ta	0.00068	±0.00004	0.00078	±0.00003	0.00010
Be	0.00334	±0.00010	0.00362	±0.00027	0.00029
Ag	0.00040	±0.00001	0.00039	±0.00001	0.00001
Pd	0.00044	±0.00003	0.00047	±0.00001	0.00003
Zr	0	±0	0	0	0
Ca	0.00112	±0.00005	0.00100	±0.00003	0.00012
Sr	0.01777	±0.00045	0.00191	±0.00005	0.01586
Ga	0.00433	±0.00018	0.00373	±0.00015	0.00060
In	0.00042	±0.00001	0.00042	±0.00005	0
Zn	0.00172	±0.00011	0.00131	±0.00004	0.00041

Au	0.00163	±0.00028	0.00220	±0.00006	0.00057
Sb	0.00254	±0.00007	0.00223	±0.00008	0.00031
Pt	0.00579	±0.00029	0.00610	±0.00022	0.00031
Ge	0.00112	±0.00005	0.00238	±0.00007	0.00126
Mg	0.02763	±0.00151	0.02864	±0.00061	0.00101
Na	0.00050	±0.00008	0.00061	±0.00009	0.00011
Li	0.00051	±0.00006	0.00066	±0.00012	0.00015
K	0.00038	±0.00004	0.00042	±0.00002	0.00004

For annealing, small specimens of about 8x3x6 mm^3 and 8x3x4 mm^3 (RDxTDxND) were cut from the plates W67 and W90 respectively using a diamond saw. These specimens were isothermally annealed for different times at five different temperatures between 1150 °C and 1350 °C (namely 1150 °C, 1175 °C, 1200 °C, 1250 °C and 1350 °C) in the case of the plate W67. Annealing was carried out at six different temperatures between 1000 °C and 1250 °C for the plate W90 (namely 1100 °C, 1150 °C, 1175 °C, 1200 °C, 1225 °C and 1250 °C).

A mirror furnace (FTTF250 from Scandiaovnen A/S) which could provide a protection gas atmosphere (argon) was available for annealing at the highest temperature of 1350 °C only. Annealing at lower temperatures was done in conventional furnaces (as Nabertherm RHTC 80-230/15), where protection of the specimen against oxidation was required. In order to avoid the formation of the volatile WO_3, individual specimens were encapsulated in glass ampoules. The ampoules each containing a single specimen were flushed with argon, evacuated and finally sealed. The specimens were put in the pre-heated furnace, removed after the desired annealing time and cooled to room temperature by air-cooling. Specimens which by optical microscopy showed any indication of oxidation after heat treatment were discarded. The annealing furnace Nabertherm RHTC 80-230/15 and the encapsulated samples inside quartz ampoules and set up for annealing are shown in Fig. 12.

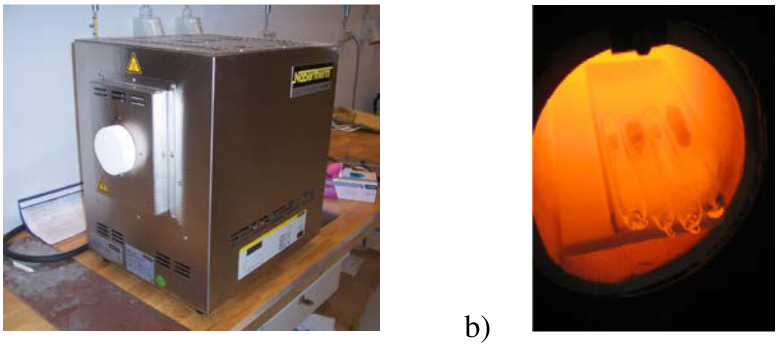

a) b)

Fig. 12. a) Tube furnace Nabertherm RHTC 80-230/15 used for annealing of tungsten samples. b) Setting of the encapsulated tungsten samples in quartz ampoules during annealing inside the tube furnace.

Optical Microscopy (OM) was used to reveal the microstructure at different stages of recrystallization. Initially, two etching solutions were tried out; namely 3% wt. hydrogen peroxide (H_2O_2) and Murakami´s reagent (10 g: 10 g: 100 ml; $K_3Fe(CN)_6$: NaOH: H_2O). These etching solutions are among the recommended etchants for tungsten in [78]. The optimal etching times with these two reagents were found by trial and error. Etching for 20 minutes with 3% wt. H_2O_2 provided good enough grain boundary enhancement without over-etching the material (see Fig. 13 and Fig. 14). The same effect was achieved with the more aggressive Murakami´s reagent much faster; after just 1 minute. However, out of the two solutions, hydrogen peroxide (H_2O_2) 3% wt. was chosen as the best option on practical and safety grounds. Although both etchants can achieve good etching, use of Murakami´s reagent can be hazardous. This is due to the fact that it contains dissolved cyanide anions (CN^-), an extremely lethal chemical species for humans [79]. Skin contact with the solution might lead to cyanide poisoning. Moreover, although NaOH provides a strong alkaline solution in Murakami´s reagent, accidental exposure to oxidizing agents can lead to the formation of hydrogen cyanide (HCN), a potentially lethal gas when inhaled [79]).

Examples of Optical Micrographs (OMs) for the plates W67 and W90 (etched with 3% wt. H_2O_2) are presented in Fig. 13 and Fig. 14 respectively. The different tonality of both figures is only due to different microscope tonality settings during image acquisition.

Fig. 13 presents the transversal (RD/ND) and rolling (RD/TD) planes for the plate W67 in the as-received condition (Fig. 13a and Fig. 13b respectively). Fig. 13c presents the microstructure after annealing for 24 h at 1350 °C (fully-recrystallized condition according to hardness data) Fig. 13 clearly reveals that the deformation structure with elongated grains after warm-rolling gets replaced by a fully recrystallized structure with equiaxed grains during the heat treatment. Moreover, a higher elongation (or higher aspect ratio) is observed on the (RD/ND) surface (Fig. 13a), as compared to the (RD/TD) surface (Fig. 13b). This is expected since grain elongation along RD and contraction along ND are expected after rolling, while no significant changes are expected in grain shape along TD.

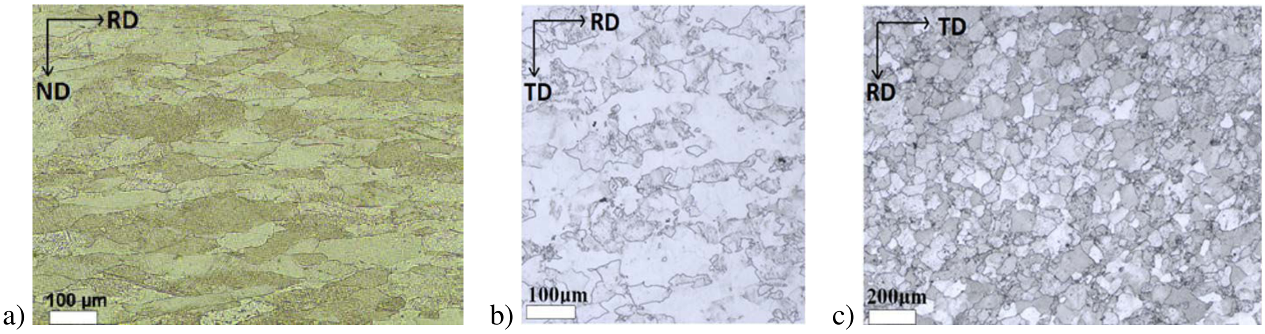

Fig. 13. Optical micrographs (OMs) for the plate W67: a) RD/ND section from the as-received state, with RD horizontal b) RD/TD section from the as-received state, with RD horizontal c) RD/TD section of the fully recrystallized sample annealed for 24 h at 1350 °C. All observed surfaces were located in the center of the plate, away from the surface in contact with the rolls.

Fig. 14 presents the plate W90 in the warm-rolled condition, a partially recrystallized state (*X*=0.38), and the fully recrystallized state after annealing at 1175 °C. The micrographs showcase that the deformation structure with elongated grains along the rolling direction after warm-rolling (Fig. 14a) becomes replaced by recrystallizing grains (Fig. 14b) until a fully recrystallized structure with equiaxed grains is achieved (Fig. 14c).

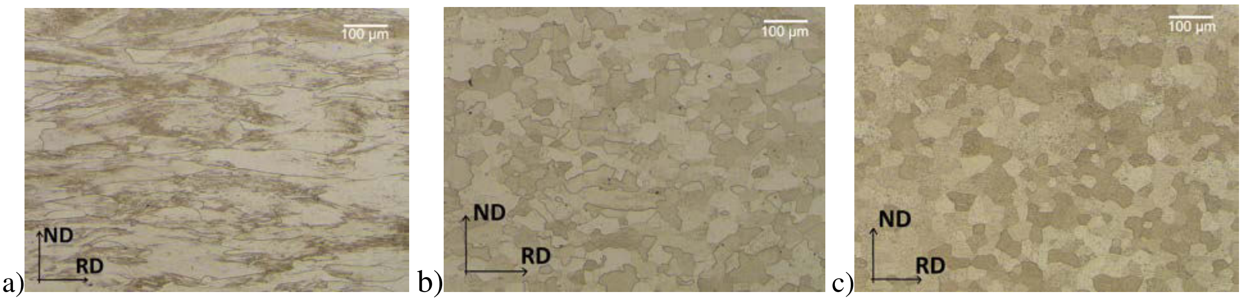

Fig. 14. Optical micrographs for the plate W90: a) as-received condition with elongated grains along RD, b) partially recrystallized sample (*X*=0.38) annealed for 20 h at 1175 °C, where a mixture of equiaxed recrystallized grains and recovered elongated grains is observed, c) fully recrystallized sample annealed for 50 h at 1175 °C showing only equiaxed recrystallized grains. All sections represent the transversal plane containing the rolling and the normal direction, RD and ND, respectively; RD being horizontal. Source: own work.

For Electron Backscattering Diffraction (EBSD), four different scanning electron microscopes were utilized: a Zeiss Supra 35 (at DTU Risø Campus) and a Tescan Mira 3 LHM (at Tsinghua University) with a Nordlys II EBSD detector using the program Flamenco of HKL Channel 5 for indexing, a FEI Helios Nanolab™ 600 (at DTU CEN) with a EDAX Hikari Camera using OIM 5TMsoftware from EDAX TSL, and a JEOL JSM-840 (at DTU Risø Campus) with a phosphor screen as detector using CROMATIC v.2.10 software to index the measured bands (Fig. 18 in subchapter 3.3.2). Orientations were gathered at individual positions on regular square grids on the prepared surfaces with step sizes ranging from 0.2 µm to 20 µm. Boundaries in the EBSD maps were identified based on the misorientation between adjacent pixels: high angle boundaries (HABs) were defined as those with misorientation angles above 15°, whereas boundaries with misorientation angles between 2° and 15° were defined as low angle boundaries (LABs). Misorientation angles below 2° were ignored due to the limited angular accuracy of the orientation determination by EBSD.

In order to achieve the surface quality required for electron backscatter diffraction investigations, the samples were grinded, polished and electropolished. After grinding (the final step being 4000 grit paper), the samples were polished with diamond suspensions of 3 µm and 1 µm size respectively. The final polishing steps were chemical polishing with an oxide particle suspension (OPS with 0.02 µm particles), and electropolishing using a steel anode. Electropolishing was carried out with 3% wt. NaOH at room temperature, and a constant voltage of 12 V in DC at an intensity of approximately 2 A for a time between 40-100 s.

Initially, electropolishing was performed at room temperature with NaOH (30% wt.) at 12V DC, according to [80]. Although [80] recommends the use of KOH, the similar reactant NaOH was used as it was more readily available. However, the tungsten material became over-etched at these electropolishing conditions. For this reason, the optimal electropolishing concentrations and times required for a good surface finish were found out by trial and error. Finally, the electropolishing conditions were optimized using NaOH (3% wt.) for 40-100 s. It was experimentally observed that required electropolishing times for optimal EBSD pattern acquisition were longer for samples with higher deformation. At least 40 seconds were required to obtain high-indexing in partly-recrystallized material (as high as 98% indexing), whereas the as-deformed tungsten plate required around 100 seconds for reasonable indexing, (only a maximum of 96% indexed points could be obtained in the best case). Electropolishing was required to eliminate remaining deformation still present after polishing, in order to obtain good EBSD indexing. Note that EBSD patterns are obtained from 10-50 nm in-depth from the measured surface, and even slight surface deformation can have a detrimental effect on the pattern quality. The quality of the patterns decreases by introduction of defects and is very sensitive to sample preparation [81].

The orientation data gathered on square grids of different step sizes were analyzed using HKL Channel 5 software. The presented orientation maps are RD/TD and RD/ND sections colored according to the crystallographic direction aligned with RD. {100}, {110} and {111} pole figures were contoured using a Gaussian spread function with 10° half width and a cluster size of 17°. Orientation distribution functions (ODFs) were calculated from the individual orientations using a Gaussian spread function with 5° half width by series expansion in generalized spherical harmonics truncated at order 22.

Table 3 provides all the annealing conditions for which EBSD orientation maps were gathered on the plates W67 and W90.

Table 3. List of annealing conditions for which EBSD orientation data were collected. A wide range of annealing times were covered at three temperatures (1150 °C, 1200 °C, 1250 °C) for the plate W67, and at two temperatures (1200 °C and 1250 °C) for the plate W90.

Plate W67 Temperature 1150 °C Annealing time	Plate W67 Temperature 1200 °C Annealing time	Plate W67 Temperature 1250 °C Annealing time	Plate W90 Temperature 1200 °C Annealing time	Plate W90 Temperature 1250 °C Annealing time
750 h	240 h	6 h	5.5 h	1 h
950 h	300 h	12 h	7 h	2 h
1213 h	320 h	24 h	8 h	3 h
1373 h	359 h	36 h	8.5 h	4 h
1582 h	480 h	48 h	9 h	5.5 h
1900 h	600 h	72 h	10 h	6 h
2200 h		110 h	11 h	7.5 h
			13 h	11 h
			15 h	12 h
			20 h	18 h
			25 h	30 h

It shall be noted that the samples from the W90 plate after annealing at 1250 °C showed a heterogeneous recrystallization behavior which, because of a large scatter, did not correlate well with the hardness data. For this reason, the EBSD orientation data from the W90 plate after annealing at 1250 °C were not used in this study. An exception is the EBSD orientation data from the sample annealed for 1 h at 1250 °C, which is used to study nucleation orientation relationships in subchapter 5.5.3. For this type of investigation, the heterogeneous recrystallization does not represent a problem. In this sample, many small nuclei developed, which facilitates this analysis.

Below, the two characterization techniques used most extensively in this work (namely Vickers Hardness and Electron Backscatter Diffraction) are explained in greater detail.

3.2 Vickers Hardness

3.2.1 Definition

Vickers hardness is a hardness test that uses a small diamond pyramidal indenter to create a small indentation in the surface of a material. This small indentation can be measured using an Optical Microscope and a Vickers hardness value deduced from the indent using standardized information (see below). Accurate measurements of the indent can nowadays be provided in an automated way, as was the case for the equipment used in this work to measure Vickers hardness (see Fig. 15a). The hard diamond indenter keeps its shape even at high loads, so that the measurements on hard metals are reliable. The indenter forms a 136° angle with the indented surface of the sample (see Fig. 15b), [37], [82].

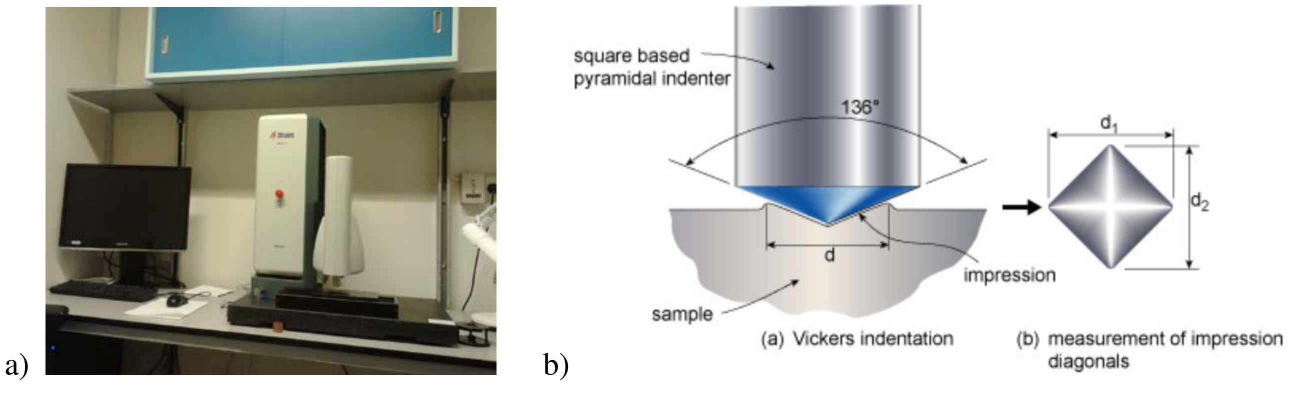
a) b)

Fig. 15. a) Equipment Struers Duracsan-70 used to measure Vickers Hardness. b) Square based pyramidal Vickers indenter making an indent in a sample of diagonals d_1 by d_2. (from http://www.twi-global.com/technical-knowledge/job-knowledge/hardness-testing-part-1-074/).

The Vickers hardness can be determined from the indent diagonals d_1 and d_2, and the load applied, according to the formula:

$$HV_w = 2F\sin\frac{136^\circ}{2}\cdot\left(\frac{2}{d_1+d_2}\right)^2 \qquad (3.1)$$

Vickers Hardness values are usually expressed as HV_w in (kgf/mm^2), for an applied load of w kg. In this work, Vickers hardness values HV_{10} are reported, which represent measurements with 10 kg load for a dwelling time of 10 s.

Vickers hardness measurements represent an average of flow stress related to the induced strain [83]. If a material were perfectly elastic, no indent would be left and the hardness could not be measured. Nevertheless, during deformation, most materials plastically work-harden after the initial breakdown of elasticity. Recovery and recrystallization of the material leads to a characteristic decrease in hardness. For this reason, Vickers hardness can be used to track the recovery kinetics of tungsten at the initial stages of annealing, and also to elucidate the recrystallized fraction of material (X) at any stage of recrystallization annealing, by using the rule of mixtures,

$$HV = X\ HV_{rex} + \left(1 - X\right) HV_{rec} \qquad \text{or} \qquad X = \frac{HV_{rec} - HV}{HV_{rec} - HV_{rex}} \tag{3.2}$$

where HV_{rex} is the hardness of the recrystallized volume fraction and HV_{rec} the hardness of the deformed or recovered matrix.

The factors that mostly affect the reliability of the measurements are flatness and a good surface finish; the indented surface is acceptable within a maximum 1° angle tolerance. For this reason, grinding or machining is required for a flat surface finish. Statistically, Vickers hardness measurements are highly reliable as long as the number of measurements taken does not exceed a minimum spread of the hardness [84].

3.2.2 Experimental details

In this work, Vickers hardness tests were carried out in order to determine the mechanical strength at different annealing stages (as hardness values relate to yield strength [11]), and the recrystallization fraction during annealing. Vickers hardness measurements were performed with a fully automatic hardness tester Struers Duracsan-70 (Fig. 15) on mechanically polished surfaces using a load of 10 kg and a dwell time of 10 s. The surfaces were prepared metallographically by subsequent mechanical grinding and polishing with silicon carbide paper, the final step being 4000 grit paper. The indents were made on the rolling plane (RD/TD) for the plate W67 on a fresh surface well inside the material, in order to avoid the extra deformation that might have been induced by direct contact with the rolls. In contrast, in the case of the plate W90, the indents were made on the transversal plane (RD/ND), because otherwise the effect of the extra deformation on the rolling plane might have been present at all depths, considering the low thickness of the plate W90 (4 mm). It was found that, for the as-received material, hardness values tended to be higher at the surface as compared to the bulk. For example, in the case of the plate W67, an average hardness value of 445 HV_{10} was found at the outer surface in contact with the rolls. When the measurements were made deep in the material bulk, the average hardness value decreased to 423 HV_{10}. Obviously, the latter average hardness value (423 HV_{10}) was used in this study. All reported hardness values in chapter 4 of this work are averages over 20 indents.

3.3 Electron backscattered diffraction (EBSD)

Electron backscatter diffraction (EBSD) is an add-on technique to a Scanning Electron Microscope (SEM) used to examine the crystallographic texture or orientation of crystalline materials. EBSD offers the ability of fast and automated diffraction analysis in order to obtain crystallographic data and maps with nanometric scale resolution [85], [86].

3.3.1 EBSD Components

The most essential accessories for an operative EBSD system are a Scanning Electron Microscope (SEM) equipped with an EBSD detector (Fig. 18), a phosphor screen where the pattern is diffracted, a low light CCD camera to detect the diffraction pattern on the phosphor screen, and a software that allows communication between the different components, as well as capability of EBSD data treatment [81],[86],[87]. The components of an EBSD system are shown in Fig. 16 and Fig. 17.

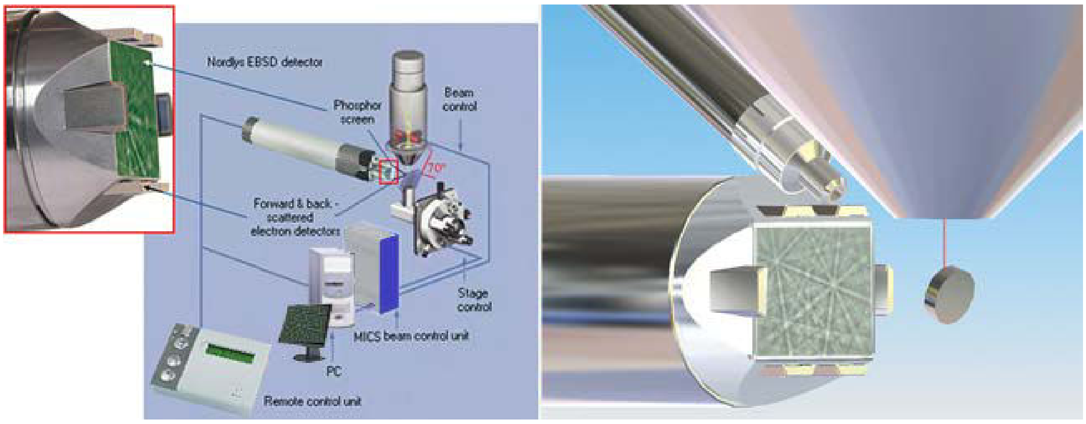

Fig. 16. Experimental set-up for EBSD. Left: Necessary hardware and interconnection among its components. Right: Close-up of the specimen chamber with the Electron Beam, the EBSD detector and the phosphor screen on which the diffraction pattern is captured. (from http://www.ebsd.com/ebsd-explained/basics-of-ebsd/principal-system-components).

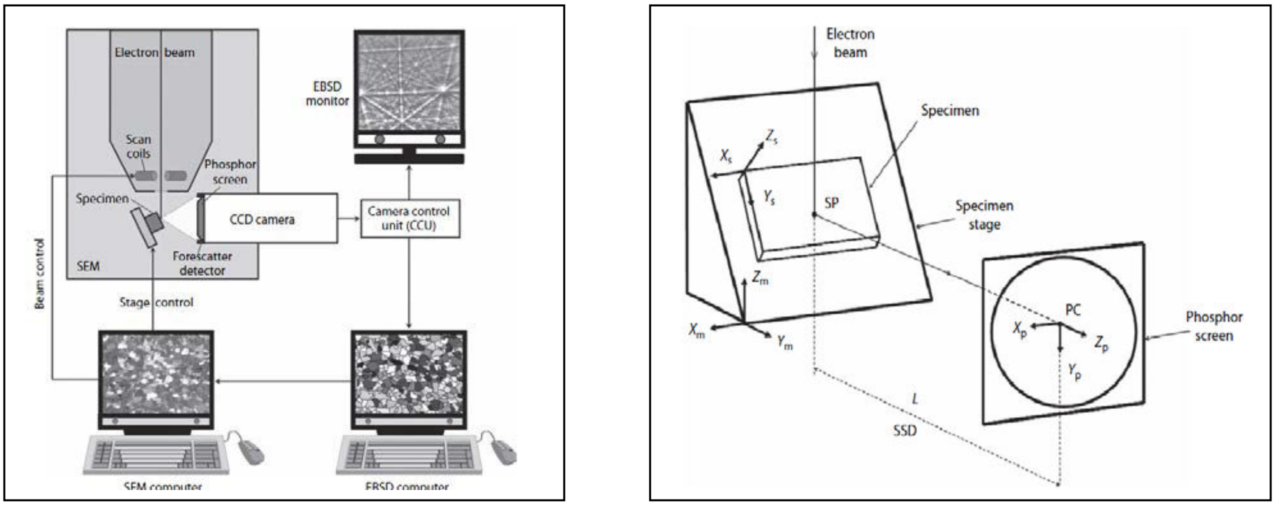

Fig. 17. Left: Diagram showing the formation of the diffraction patterns and the processed maps from such data, as well as the better-defined microstructure obtained using EBSD as compared to conventional SEM imaging. Right: Diagram showing the specimen mounting and the diffraction of the electron beam generated radiation onto the phosphor screen; the parameters required for EBSD orientation measurements such as specimen-to-screen distance L, x y z (screen/pattern axes), X_s Y_s Z_s (specimen coordinates), and X_m Y_m Z_m (microscope coordinates) are also shown (from [81]).

Fig. 18. One of the SEMs with an EBSD detector used for the EBSD analysis of this work: a JEOL JSM-840 with a phosphor screen as detector using CROMATIC v.2.10 software to index the measured bands (at DTU Risø campus).

3.3.2 Collection and Analysis of Diffraction patterns

The basis for EBSD is the collection and analysis of diffraction patterns from the surface of bulk samples in the SEM. In the early stages of EBSD, pattern recognition was done manually and was time-consuming. Nowadays, the process is automated or semi-automated. This allows the diffraction pattern to be captured and analyzed in real time, and computer algorithms allow the orientation of each diffraction pattern to be obtained and stored automatically.

In order to collect the diffraction pattern, the specimen is positioned within the SEM sample chamber and an angle of 20° is kept between the incident electron beam and the specimen surface. This sample tilting increases the amount of backscattered electrons that diffract from the specimen surface and leave the specimen. Some of the inelastically scattered electrons hit the atomic planes of the sample at angles which satisfy Bragg's law (Eq. 3.3),

$$n\lambda = 2d\sin\theta \qquad (3.3)$$

where n is an integral number, λ is the electron wavelength, d is the spacing between diffracting planes and θ is the angle of incidence of the inelastically scattered electrons on the diffracting plane.

As diffraction occurs in all directions which form the incident angle θ with the diffracting plane, each family of planes produces a set of paired electron cones; cones that are used to form an image onto the phosphor screen. The intersection of this cone with a big enough phosphor screen would result in the formation of a circle of large radius. Since the radius of this circle is considerably large and the phosphor screen has a limited size, only an almost straight segment of this circle intersects with the screen. This intersection forms the almost parallel Kikuchi lines on the phosphor screen.

The cones diffracted from parallel planes of the same crystallographic orientations form pairs of parallel Kikuchi lines that define Kikuchi bands. Each Kikuchi band has width proportional to the interplanar spacings. Different planes lead to different bands, resulting in the formation of countless overlapping Kikuchi bands [86], [81]. This is sketched in Fig. 19.

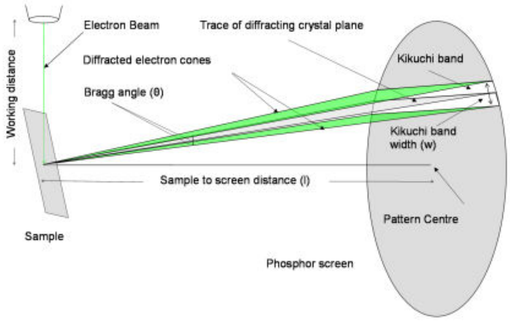

Fig. 19. Scheme showing how the diffraction cone generates the Kikuchi bands onto the phosphor screen. (from (http://www.ebsd.com/ebsd-explained/basics-of-ebsd/interpreting-the-diffraction-pattern).

Once the pattern has been collected, the determination of the crystallographic orientation of the sampled volume is performed in two consecutive steps:

1) First, the pattern is indexed by identifying the crystallographic indices of the poles and bands/lines in the pattern (pattern indexing). The poles (or zone axis) are the points where Kikuchi bands intersect, and physically correspond to a shared direction by two intersecting planes (see Fig. 20). The Kikuchi bands, as mentioned earlier, are formed by a pair of Kikuchi lines. The identification of the position of the bands and poles in the diffraction pattern is done using the Hough transform algorithm. The Hough transform detects each line in the phosphor screen projection and transforms it into a point in the Hough space. What the Hough transform does it to convert the x and y directions of the pixels of the phosphor screen (namely x_i and y_i, where i refers to the pixel index in the image) into the new parameters θ and ρ. In this fashion, the Hough space is constructed by using the parameters θ and ρ as the x and y axis of the Hough space, covering an area $\Delta\theta \cdot \Delta\rho$. The result of this conversion is that each original pixel is transformed into a sinusoidal curve with intensity proportional to that of the original pixel. The addition of sinusoidal curves at the intersection of Kikuchi lines provides peaks of highest intensity, which are identified as points of higher intensity in Hough space. Finally, the peak detection algorithm selects the highest intensity peaks (which correspond to the Kikuchi lines and poles), while disregarding other false or weaker peaks.

2) Secondly, the relative position of the Kikuchi bands/lines and poles with respect to the chosen external axes is determined (orientation determination).

As to pattern indexing, each Kikuchi band was formed by the projection of a crystallographic plane and can therefore be indexed with the Miller indices of the plane which formed it. The Kikuchi bands are sorted according to their intensities and widths. Indexing is based on the comparison of measured interplanar angles (which correspond to the angles between the Kikuchi bands) and interplanar spacings (which are represented by the band widths) with theoretically known values of different crystal structures, until a match is made. It is the positions of the narrower and brighter bands that are used for such indexing (5 to 10 bands). In the case of high-symmetry crystals (cubic and hexagonal) 3-4 families of {hkl} planes are enough to solve the Kikuchi pattern, whereas for lower symmetry crystals the use of more bands and plane families is required for pattern indexing.

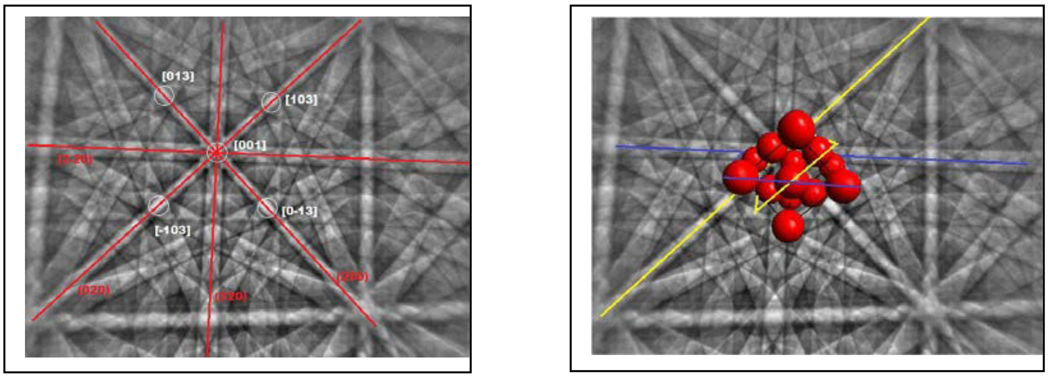

Fig. 20. Left: Kikuchi diffraction pattern showing plane Miller indices (red) and zones axis (white). Right: A nickel crystal unit cell on top of the diffraction pattern which it generates. The blue and yellow highlighted planes correspond to the same Kikuchi bands, and so does the zone axis from their intersection. Source: (from http://www.ebsd.com/ebsd-explained/basics-of-ebsd/interpreting-the-diffraction-pattern).

In order to determine crystallographic orientations, first the angles between the indexed bands or poles and the sample normal or beam normal (α_1, α_2, α_3) must be determined. This is done by measuring the distance from the bands or poles to the beam normal. Distances are therefore transformed into angles using the distance between two indexed poles or from the bandwidth of a Kikuchi band, which is related to its indices through 2θ (angle of incidence of the electron beam onto the plane), as shown in Fig. 21.

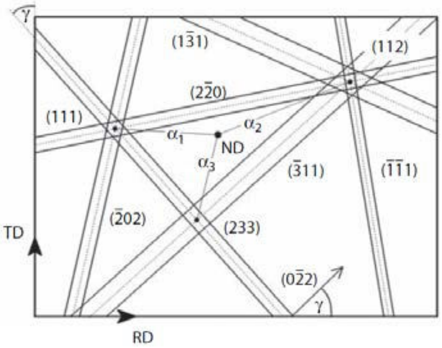

Fig. 21. Indexed Kikuchi pattern showing the angles (α_1, α_2, α_3) from which the crystal orientation is determined, corresponding to the distance between ND (beam normal) and the poles (from [81]).

The relation between the crystallographic indices q_i (of each band or pole, where i is the identified number of bands and poles), and α_i (the corresponding angle between each band or pole and ND), yields the axis of the crystal in terms of its crystallographic indices (hkl) through Eq. 3.4:

$$\begin{pmatrix} q_1^i \\ q_2^i \\ q_3^i \end{pmatrix} \cdot \begin{pmatrix} h \\ k \\ l \end{pmatrix} = \cos\alpha_i \cdot \sqrt{\left(q_1^i\right)^2 + \left(q_2^i\right)^2 + \left(q_3^i\right)^2} \qquad (3.4)$$

Eq. 3.4. represents the indexing of three bands or poles; the minimum necessary for orientation determination. The root in this equation normalizes the obtained orientation vector (hkl) to unity.

To derive the full orientation matrix with respect to the specimen, the indices of one further reference axis (TD or RD) have to be determined as well. Once this is accomplished, the crystallographic orientation of the grain can be finally described either in (hkl)[uvw] notation, or by its orientation matrix g. Euler angles, Rodrigues vectors, or misorientation parameters can be computed according to standard algorithms, and the results can be stored for further evaluation and representation of the data. As a final result, each pixel can be assigned a certain crystallographic orientation, which allow the reconstruction of orientation maps of the microstructure from which a wealth of microstructural information can be obtained.

3.3.3 Advantages of EBSD

- EBSD allows quantitative and automated analysis of grains/subgrains more accurately than other imaging techniques (except for TEM) [88]. In fact, using Field Emission GUN SEM (FEGSEM) grains as small as 0.2 µm can be characterized [88].
- Subgrain/cell measurements are easier than in the TEM, although the limited angular resolution of EBSD may be problematic [86].
- X-ray methods can also determine bulk texture. However, EBSD allows spatial location of texture distributions and correlations with grain or subgrain size, shape and position in the sample [81].
- The fact that EBSD uses misorientations to elucidate the microstructure, enables the distribution and nature of boundaries present in the sample to be determined [81].
- EBSD is an optimal technique to measure the spatial distribution of stored energy in subgrain boundaries and the recrystallized fraction in a sample, both relevant parameters in this work.

3.4 Applications of EBSD

In materials science, EBSD is mainly used to index and identify the seven crystal systems. In terms of crystallography, it can offer crystal orientation mapping, defect studies, phase identification, grain boundary and morphology studies, regional heterogeneity investigations, material discrimination and microstrain mapping. Using complementary techniques, it can also offer physicochemical identification of the different crystallographic components. For example, in-situ chemical analysis of certain texture components or phases is possible by combining EBSD with another add-on package to a SEM: Energy-dispersive X-Ray spectroscopy (EDS). In the present work, EBSD is mainly used to determine the evolution of the recrystallized fraction and the texture evolution during recrystallization. An in-depth analysis of nucleation and growth during recrystallization is also done with EBSD. The most relevant data to be obtained using EBSD analysis for this work, mainly on recrystallization of pure tungsten, will be furtherly explained [86], [81], [89], [90], [88].

3.4.1 Misorientation, IPF coloring and crystal symmetry

Misorientation is defined as the orientation difference between two crystals. The definition of an orientation in EBSD is refers to the misorientation between the crystal in question and a reference axis (i.e. sample axis). The EBSD data analysis can easily work out the misorientation between two crystals from their corresponding orientations defined in Euler angles. Misorientations or angular relationships between crystals can be described in a variety of ways (e.g. Rotation matrix, Rodrigues vector, angle/axis pair…). Cubic crystals (as in bcc tungsten) present symmetry along all its three axis ($a=b=c$) and along all its interaxial angles ($\alpha=\beta=\gamma=90°$) [37]. As a consequence of this high crystalline symmetry, there are 24 equivalent descriptions for the orientation of each cubic crystal [81]. Misorientation angles above 62.8° between cubic crystals can be equivalently described using lower misorientation angles due to the cubic symmetry. Also, it is standard practice in angle/axis pair notation to use of all 24 possibilities the rotation axis more closely aligned with <110> [81].

Misorientations can also be described in Inverse Pole Figure (IPF) space. In the current work, all EBSD orientation maps are presented with IPF coloring along the rolling direction. Each pixel is represented in one color which is directly related to the orientation of the crystallite in that pixel. What the IPF coloring represents is the orientation axis that, for that crystallite in particular, would align with the reference direction [86], [81]. The reference direction was chosen as RD in this work. The colors used for the different axes are standardized; red for the [001] axis, green for the [011] axis and blue for the [111] axis. Intermediate directions are represented by the combination of these standardized axis, in a way directly related to the equivalent combination of their corresponding colors (e.g. the orientation axis in between [001] (red) and [011] (green) is displayed in yellow; see Fig 22). The advantage of representing misorientations in IPF space is that, since this space is relatively large, it allows differentiating a wide range of misorientations by subtle color tonalities [81]. IPF coloring is especially useful to show fiber orientations, as they are aligned along an axis and appear in that specific color, or whenever there is a textural preference aligned along an axis [33].

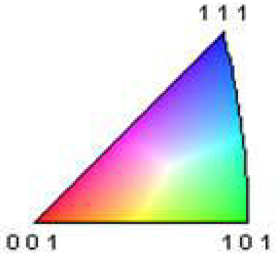

Fig. 22. Inverse Pole figure legend where all the spectra of colors related to the orientation axis parallel to a certain reference axis is displayed (from [86]).

3.4.2 Boundary character

Boundaries possess 5 degrees of freedom; 3 related to the misorientation across the boundary and 2 related to the inclination of the boundary plane. Through these parameters, EBSD allows to determine the nature of the boundaries.

The orientation of the crystals (3 degrees of freedom for each crystal) is related to the boundary between the 2 crystals through their misorientation. Boundaries in EBSD maps are classified according to their misorientation angle as low angle boundaries (LABs) for misorientation angles between 2° and 15° and high angle boundaries (HABSs) for misorientation angles above 15°. However, it is not usually possible to determine the boundary plane using EBSD. Coincident site lattice (CSL) boundaries are also a type of boundaries detectable by EBSD.

3.4.3 Calculation of stored energy

Given a microstructure consisting of well-defined subgrains, the stored energy in the dislocation structure can be calculated as a function of the subgrain size, the misorientation of the boundaries, and the boundary energy [88]. A way to calculate the stored energy in the microstructure from these parameters is presented in Eq. 3.5 [21],

$$\left\{\begin{array}{l} \Delta u_{LAB} = S_{v(LAB)} \cdot \gamma_{B(LAB)} \\ \Delta u_{HAB} = S_{v(HAB)} \cdot \gamma_{B(HAB)} \\ \gamma_{B(LAB)} = \gamma_{B(HAB)} \cdot \dfrac{\theta_{av}}{\theta_m} \cdot (1 - \ln \dfrac{\theta_{av}}{\theta_m}) \end{array}\right\} \Delta u = \Delta u_{LAB} + \Delta u_{HAB} \qquad (3.5)$$

where Δu_{LAB} , Δu_{HAB} and Δu are the stored energies in the LABs, HABs and all boundaries. $\gamma_{B(HAB)}$ is the boundary energy. $S_{v(LAB)}$ and $S_{v(HAB)}$ are the specific surface densities for LABs and HABs (or the inverse of the chord lengths), θ_{av} refers to the average misorientation for LABs between 2° and

15°, and θ_m is the misorientation at which the boundary energy shows a maxima ($\theta_m = 15°$). Note that both LABs and HABs contribute to the stored energy of the material. For tungsten, the surface boundary energy for HABs is $\gamma_{B(HAB)} = 0.869\ \text{J/m}^2$ [91].

EBSD data treatment allows to calculate these parameters from grain and subgrain chord length measurements and misorientation measurements from grain boundary maps (e.g. see Fig. 23).

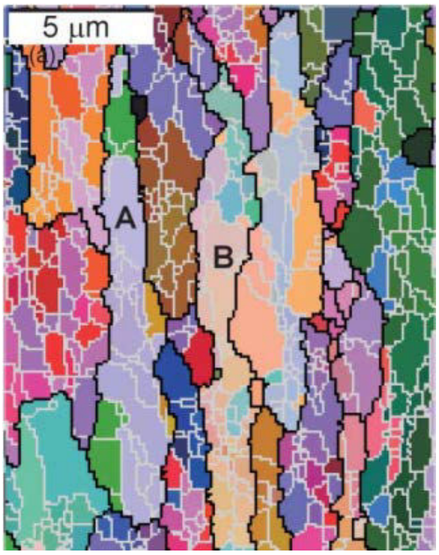

Fig. 23. Grain boundary map of a cold rolled aluminum alloy obtained by EBSD. Euler contrast was used for the coloring of the grain pixels. High Angle Boundaries (HABs) are represented as black lines, and low angle boundaries as grey lines. The map corresponds to an RD/ND section, with RD vertical. (from [92]).

3.4.4 Characterization of Recrystallization

The recrystallized fraction is estimated from EBSD by separating different areas of the microstructure as recrystallized or non-recrystallized according to certain criteria. For this purpose, recrystallized regions are defined as areas surrounded at least partly by HABs that meet a minimum size and have a minimum internal misorientation. In this thesis, recrystallized regions were determined from the orientation data using the in-house software DRG [93] based on three criteria: i) the internal misorientation within a recrystallized nucleus/grain is less than 1°, ii) the area of a nucleus/grain is larger than 8 pixels corresponding to 72 μm^2 or 200 μm^2 (for maps obtained with 3 µm or 5 µm step size respectively) and iii) the nucleus/grain is at least partially surrounded by high angle boundaries with misorientations larger than 15°. The volume fraction X of recrystallized material is therefore determined as the area fraction of all recrystallized areas detected in the orientation map.

This last method can also be used for subgrain detection, defined as regions surrounded by LABS of a minimum size. Summing up, EBSD data allows for grain and subgrain reconstruction, which in turn allows quantifying the recrystallized fraction X. Examples of partly-recrystallized tungsten material are presented in Fig. 24.

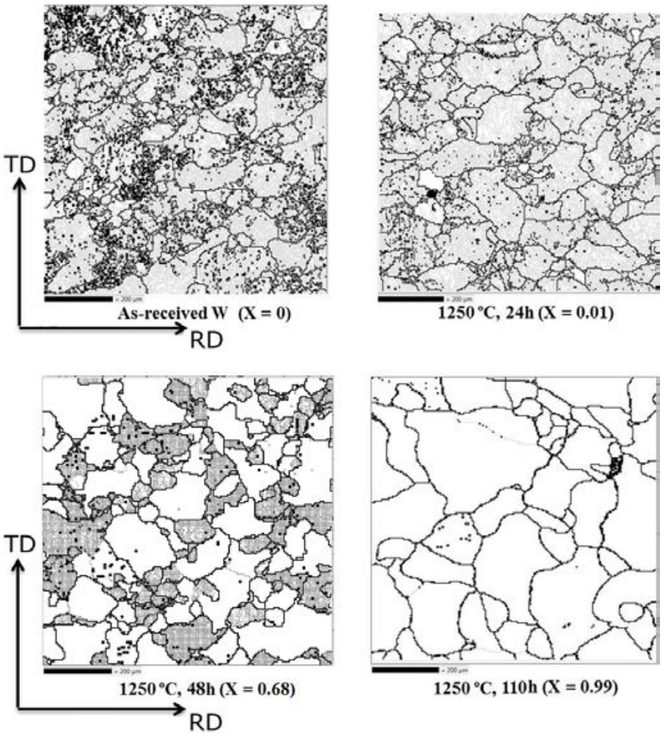

Fig. 24. Boundary maps for tungsten in the warm-rolled state (top-left), at the beginning of recrystallization (top-right), in a 68% recrystallized state (bottom-left) and in the fully-recrystallized state (bottom-right). High angle boundaries (>15°) appear as black lines and low angle boundaries (2-15°) as grey lines. Black dots correspond to non-indexed pixels. Clean white regions correspond to recrystallized grains, whereas the greyish grains correspond to the recovered matrix. All maps are obtained on the plate W67.

Chapter 4

Characterization based on hardness measurements

In this chapter, the characterization of recovery and recrystallization kinetics from Vickers hardness measurements is done for both moderately-deformed (W67) and highly-deformed (W90) warm-rolled tungsten plates. The combination of both recovery kinetics and recrystallization kinetics provides a good description of the annealing kinetics at all studied annealing temperatures and times. This characterization allows determination of the corresponding activation energies. The different activation energies obtained for both plates are discussed. The activation energies of recrystallization allowed to extrapolate lifespans of these tungsten plates at different operation temperatures. The lifespans for both plates are presented and discussed in chapter 6.

4.1 Moderately-rolled plate (W67)

4.1.1 Hardness evolution

Vickers hardness measurements were done on isothermally annealed samples at five different temperatures; namely 1150 °C, 1175 °C, 1200 °C, 1250 °C and 1350 °C (see Table 4). Fig. 25 provides the hardness evolution during annealing at these temperatures.

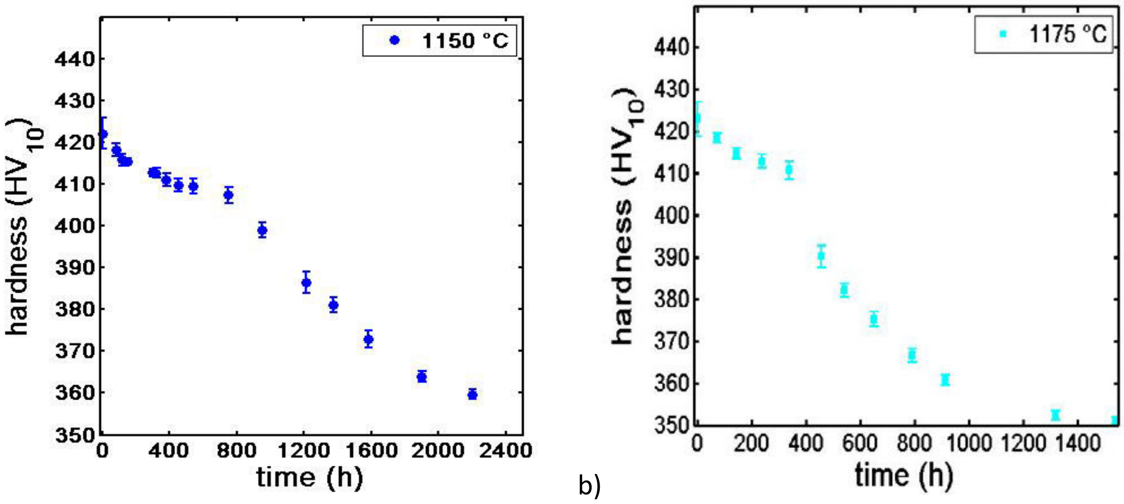

a) b)

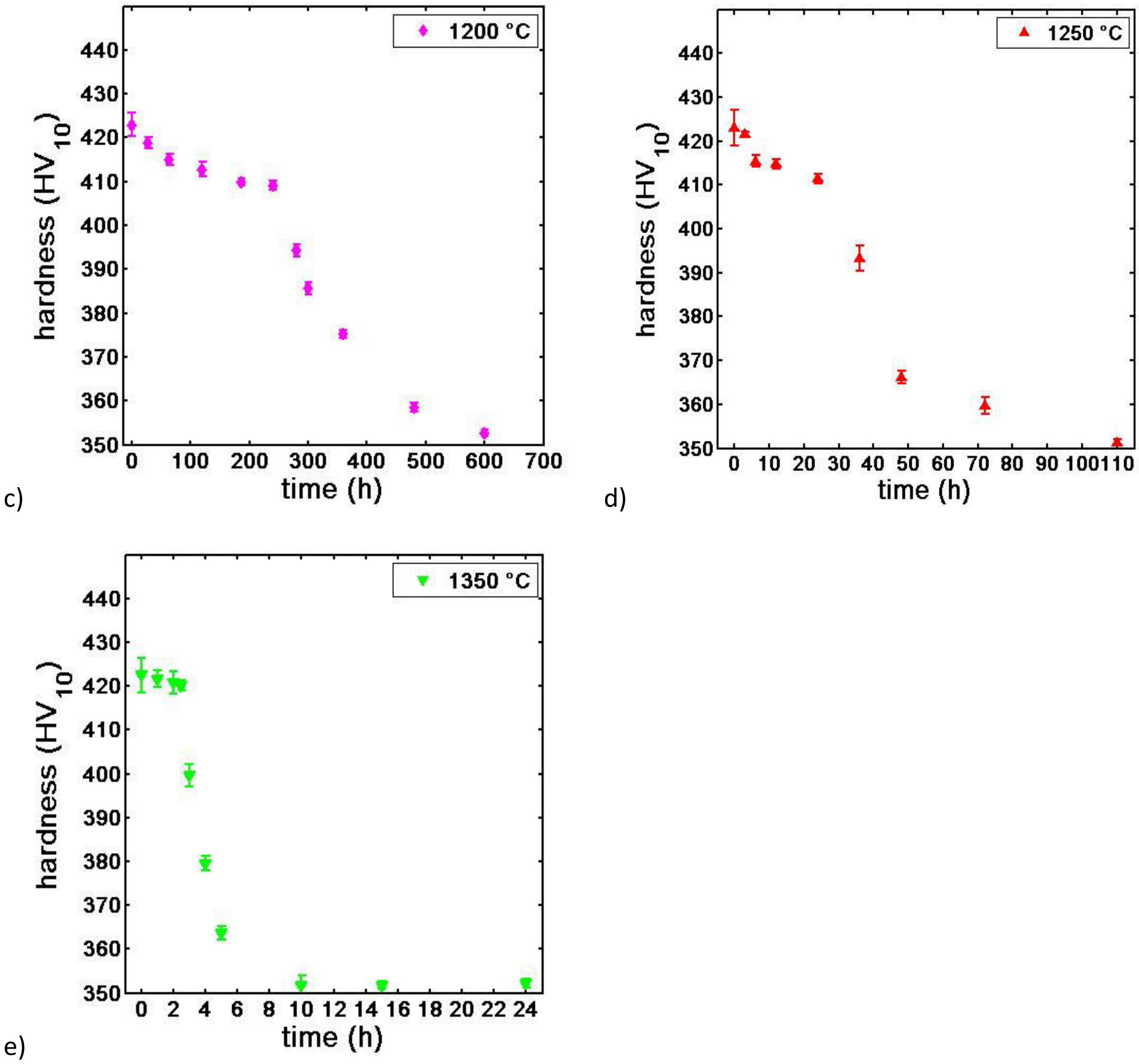

c)

d)

e)

Fig. 25. Hardness evolution at different annealing times during annealing at 1150 °C (a), 1175 °C (b), 1200 °C (c), 1250 °C (d) and 1350 °C (e). Vickers hardness measurements were performed on the mechanically polished RD/TD surfaces using a load of 10 kg and a dwell time of 10 s. The reported hardness values $HV_{10} \pm \Delta HV_{10}$ are averages over 20 indents with the standard deviation ΔHV_{10} of the average; error bars in graphs represent $\pm \Delta HV_{10}$ as well.

The standard deviation of the average (plotted error bars in Fig. 25) is defined by Eq. 4.1,

$$\Delta x = \frac{\sigma}{\sqrt{N}} \qquad (4.1)$$

where σ is the standard deviation and N the number of hardness measurements per sample $(N = 20)$

During annealing, the Vickers hardness decreases from $HV_{def} = 423 \pm 4\, HV_{10}$ in the as-received condition, to $HV_{rex} = 351 \pm 1\, HV_{10}$ in the fully recrystallized condition. All five annealing temperatures showed a common HV_{rex} value which did not decrease for longer annealing times, indicating that no grain growth occurred after recrystallization. This hardness value for the recrystallized state is comparable to hardness values reported in literature for the recrystallized state in tungsten [3].

In Fig. 25 it can be seen that the annealing temperature (as expected) has a large influence on the required annealing time; the annealing times $t_{\Delta HV/2}$ required to attain half of the hardness loss or, formulated differently, to reach half-hardness $\left(HV_{def} + HV_{rex}\right)/2 = 387\, HV_{10}$, are reported in Table 4.

Table 4. Times to reach half-hardness loss at the different annealing temperatures. The annealing times at 1175 °C and 1350 °C were not directly available from hardness measurements, and were estimated using linear interpolation between the two closest hardness values.

T (°C)	$t_{\Delta HV/2}(h)$
1150	1213
1175	482
1200	300
1250	36
1350	3.58

Inspection of the hardness decrease of Fig. 25 allows distinguishing two clearly identifiable stages from their different slopes. During the first stage, the initial rapid decrease of the Vickers hardness is slowing down considerably with increasing annealing time. After some time, a significantly faster decrease in the hardness is observed marking the occurrence of a second stage. The behavior in the second stage is attributed to recrystallization by nucleation and grain boundary migration, whereas the first stage is characteristic for recovery. The driving force for both processes is the stored energy in the deformation structure and the associated defects (i.e. dislocations) [21]. For a full analysis of the annealing kinetics, a full description of both recovery and recrystallization kinetics is required.

4.1.2 Recovery kinetics

During the recovery stage (first stage of Fig. 25), the decrease of hardness with annealing time was successfully described by logarithmic recovery kinetics (Eq. 4.2),

$$HV_{rec} = HV_0^* - C \ln t \,. \tag{4.2}$$

where HV_{rec} is the hardness of the recovered state after the annealing time. Such a dependence has been rationalized by Kuhlmann [94] for intermediate annealing times as consequence of the reduction in strength (caused by dislocation rearrangement and removal) due to thermally activated processes during recovery. Eq. 4.2 allows a fitting of the hardness data during the recovery hardness drop, as it is shown in Fig. 26 for temperatures between 1150 °C and 1250 °C (for 1350 °C not enough data were available to reliably fit this first recovery stage). A good description of the hardness decrease is achieved by Eq. 4.2 for all temperatures.

As it can be noticed in Fig. 26, the slope of the linear fits represents how fast recovery kinetics are. Such slope is mathematically described by the coefficient C. As expected, recovery kinetics become faster with increasing annealing temperature (see Table 5, where the coefficient C increases with increasing annealing temperature). Normalization of this coefficient C by the annealing temperature leads to an average constant value $C/T = 3.1\cdot10^{-3}\ (1\pm8\%)\ \text{kgf K}^{-1}\text{mm}^{-2}$. The reason for the constant ratio C/T is related to the ability of the dislocations to move further away with increasing temperature (activation volume). The physical interpretation of the ratio C/T will be explained in more detail in the discussion section (6.1 recovery) for both plates W67 and W90.

Table 5. Values of the slope C of the linear fit of recovery kinetics at different annealing temperatures T (°C), leading to a constant average value for the coefficient $C/T = 3.1\cdot10^{-3}(1\pm8\%)\ \text{kgf K}^{-1}\text{mm}^{-2}$

$C\left(\text{kgf mm}^{-2}\right)$	$T\left(°\text{C}\right)$	$C/T\left(\text{kgf K}^{-1}\text{mm}^{-2}\right)$
4.45	1150	0.00313
4.61	1175	0.00318
4.68	1200	0.00317
4.83	1250	0.00317

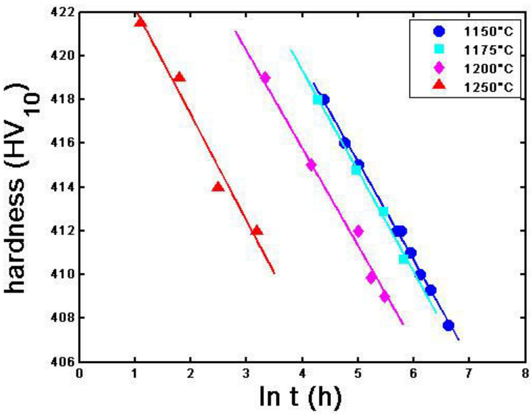

Fig. 26: Semi-logarithmic plot of the Vickers hardness of the tungsten plate W67, in dependence on the annealing time for different temperatures.

4.1.3 Recrystallization kinetics

Considering that a partly recrystallized sample will consist of both recovered regions (with hardness HV_{rec} characterized in the previous subchapter 4.1.2) and recrystallized regions (with hardness $HV_{rex} = 351 \pm 1\, HV_{10}$), the recrystallized fraction X at any time can be easily calculated by applying the classical rule of mixtures (Eq. 3.2).

The recrystallized fraction X can be worked out from hardness measurements. HV represents the experimental value of the hardness measured at any time. HV_{rec} corresponds to the hardness value that the recovered matrix (non-recrystallized matrix) is expected to present at any annealing time. This HV_{rec} value has been fitted by Eq. 4.2, and can be extrapolated to longer times. This means that, for the shorter annealing times, the hardness values HV_{rec} are those of the samples of Fig. 26. For longer annealing times, the hardness values HV_{rec} correspond to those that the extrapolation of Eq.2 at that particular annealing time would yield for each temperature. (note that for 1350 °C the value after 2.5 h is used for HV_{rec} due to the lack of data during the recovery stage, which does not allow a fit to Eq. 4.2. As an example, the results of these extrapolations for the lowest annealing temperature (1150 °C) are presented in Table 6. Use of Eq. 3.2 allowed the calculation of the recrystallized fraction X presented in Table 6.

Table 6. Relevant values for recrystallization during annealing at 1150 °C; annealing time (first column); extrapolated HV_{rec} values from the recovery kinetics model of Eq. 4.2 (second column); the recrystallized fraction X calculated according to the rule of mixtures of Eq. 3.2 (third column).

Annealing time at 1150 °C	HV_{rec}	X
80h	417.9	0
117h	416.2	0
150h	415.1	0
300h	412.0	0
320h	411.6	0
380h	410.9	0
450h	410.1	0
540h	409.3	0
750h	407.8	0
950h	406.7	0.14
1213h	405.7	0.36
1373h	405.1	0.44
1582h	404.4	0.61
1900h	403.6	0.76
2200h	403.0	0.85

Recrystallization occurs by thermally activated nucleation and growth of new and almost defect-free grains. The evolution of the recrystallized fraction follows in general Johnson-Mehl-Avrami-Kolmogorov kinetics (cf. [21]), whose mathematical expression was already described in Eq. 2.11. A modified form of Eq. 2.11 is used in this chapter as Eq. 4.3,

$$X = 1 - \exp\left(-b^n t^n\right) \tag{4.3}$$

where the former coefficient B is equivalent to b^n. With Eq. 4.3, a fair description of the experimental data can be obtained as shown by the dashed line in Fig. 27, but only for the later stages where both recovery and recrystallization occur. From Fig. 27, it becomes obvious that especially at the beginning of the annealing treatment (e.g. up to 750 h for annealing at 1150 °C) Eq. 4.3 overestimates the recrystallized volume fraction by far. Recrystallization apparently does not occur during the initial stage of annealing. This can be reflected by introducing an incubation time t_{inc} before the onset of recrystallization [95] in Eq. 4.4.

$$X = 1 - \exp\left(-b^n \left(t - t_{inc}\right)^n\right). \tag{4.4}$$

By fitting an incubation time (e.g. 887 h for annealing at 1150 °C), a much better description of the hardness evolution during recrystallization at 1150 °C is obtained by Eq. 4.4 as shown by the solid line in Fig. 27.

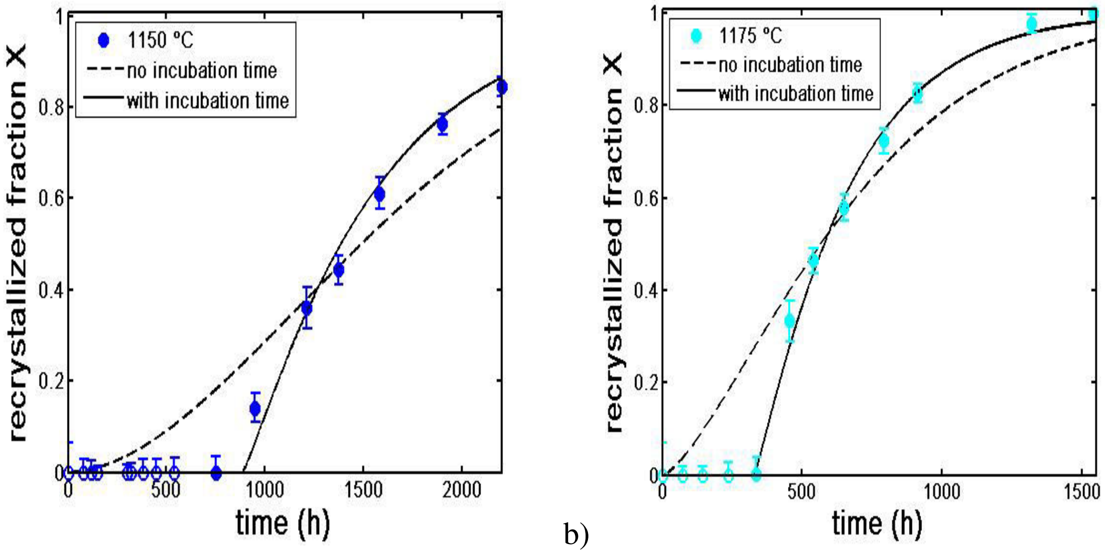

a) b)

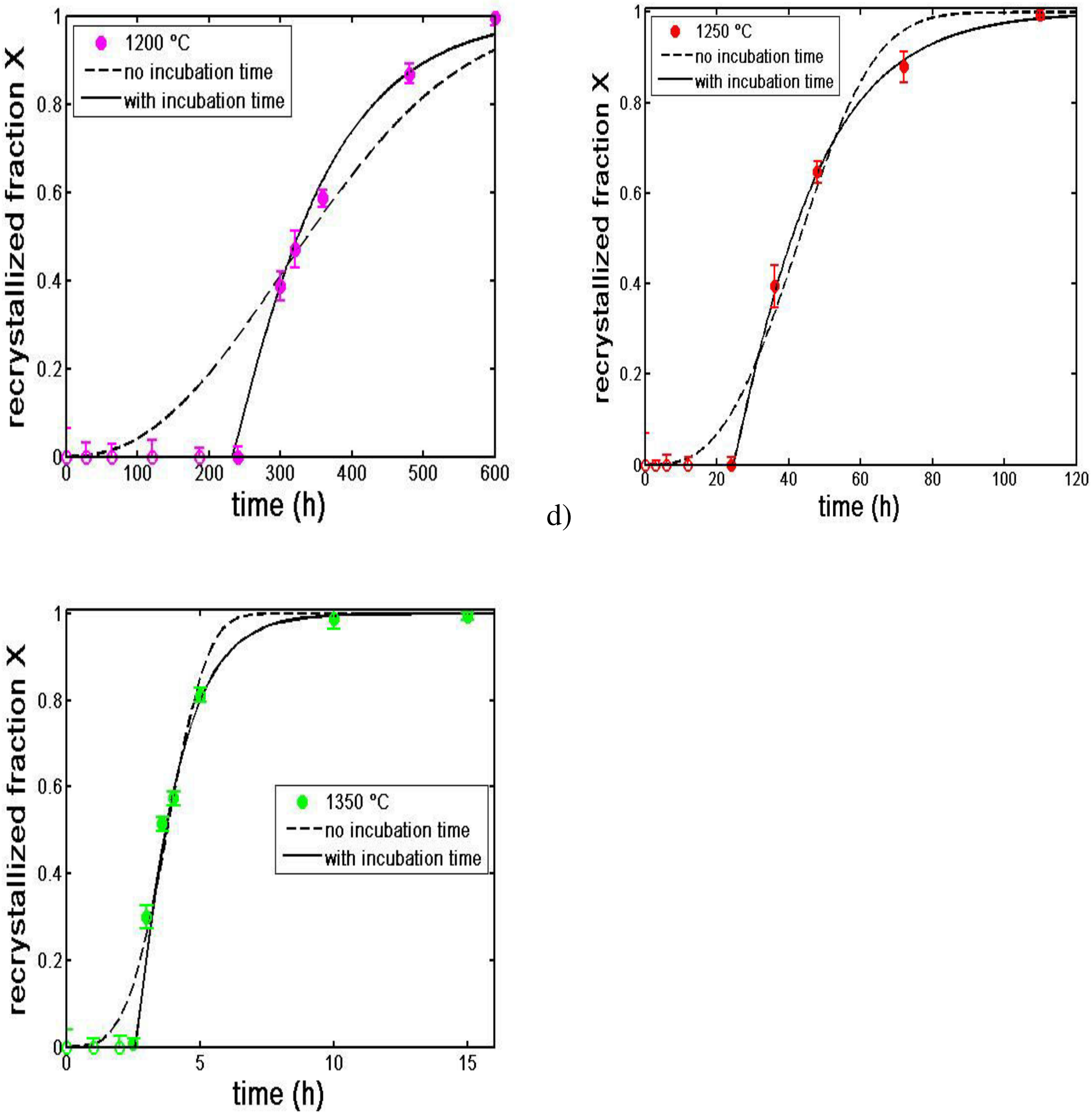

c) d) e)

Fig. 27. Recrystallized volume fraction X of warm-rolled tungsten W67 as a function of annealing time at 1150 °C (a), 1175 °C (b), 1200 °C (c), 1250 °C (d) and 1350 °C (e). Open symbols mark values where only recovery is expected to occur, whereas filled symbols mark values where recovery and recrystallization occur simultaneously. The lines are fits of Eq. 4.3 (dashed line) to all values and of Eq. 4.4 (solid line) only to those values where recrystallization is expected to occur (filled symbols).

Comparing all five investigated temperatures (Fig. 27), it was found that both, the coefficient b and the incubation time t_{inc}, are strongly depending on temperature, whereas the exponent n shows only minor deviations from an average value 1.1. Despite theoretical expectations of much larger values up to 4 (which are related to the nucleation mode and the growth dimensionality [21]) such a low value for the Avrami exponent n is typically found in literature, e.g. ([96], [97], [98], [99]). This low values of the Avrami exponent n have been explained to be due to the inability of the JMAK model to account for the heterogeneity of the recrystallization process [21]; the heterogeneous microstructure will lead to a non-random distribution of nuclei (due to the heterogeneous distribution of nucleation sites) and to different growth rates for the different individual grains (due to the stored energy of the surrounding recovered matrix and the recovered matrix-nucleus orientation relationship).

The addition of an incubation time is justified microstructurally. The approach was to measure microstructurally the recrystallized fraction for a sample annealed for a time close to the estimated incubation time with Eq. 4.4. A very low recrystallized fraction should be observed at this annealing stage to justify the introduction of an incubation time. An EBSD grain boundary map for a sample annealed at 1250 °C for a shorter period (24 h) than the obtained incubation time $t_{inc}(1250\ °C) = 24.5\ \text{h}$ is provided in Fig. 28. It shows that only very few nuclei (covering a recrystallized fraction of 1%) are present after annealing for 24 h at 1250 °C. Had there not been an incubation time, a much larger recrystallized fraction X would have been observed at this relatively advanced annealing stage. Therefore, there is microstructural evidence for the existence of an incubation time before recrystallization.

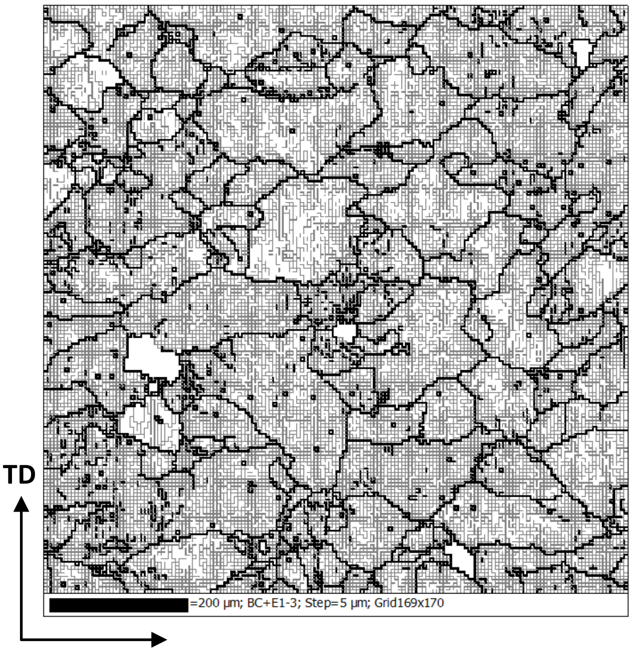

Fig. 28. Plate W67. Boundary map obtained by EBSD with a 5 µm step size on the rolling plane (RD/TD) of a sample annealed for 24 h at 1250 °C, covering an area $845\times 850\ \mu m^2$. A few nuclei shown in white are identified. Nuclei were defined as regions with internal misorientations below 1°, partially surrounded by high angle boundaries and at least 225 μm^2 large. The recrystallized fraction corresponds to $X = 0.01$. Grey lines represent LABs (2°-15°), whereas black lines represent HABs (>15°).

Fig. 29 finally compares the evolution of the hardness during annealing at all temperatures (except 1350 °C, where no recovery model was available). Recrystallization and recovery kinetics are expressed in Fig. 29 as functions of the hardness decrease over annealing time they induce. The Kuhlmann recovery model (Eq. 4.2, expressed as a dashed line in Fig. 29) directly provides the expected decrease in hardness at any annealing time. The recrystallization model of Johnsson-Mehl-Avrami-Kolmogorov with an incubation time (Eq. 4.4, plotted as a solid line in Fig. 29) provides the expected recrystallized fraction at any time. By using the rule of mixtures of Eq.3.2, the recrystallized fraction can directly be converted into the modelled hardness. Obviously, as the recrystallized fraction increases with annealing time, the hardness decreases.

A good description of the entire annealing behavior is obtained by the combined models, as observed by the good fit to the experimental data at all temperatures. In Fig. 29, the experimentally measured hardness values fit the recovery model up to the incubation time of recrystallization. Once recrystallization sets in, the experimentally-measured hardness values perfectly fit the recrystallization model. Obviously, the extrapolation of the recovery model to longer annealing times (dashed line) does not fit the experimental data, since the additional effect of recrystallization must also be taken into account (solid line).

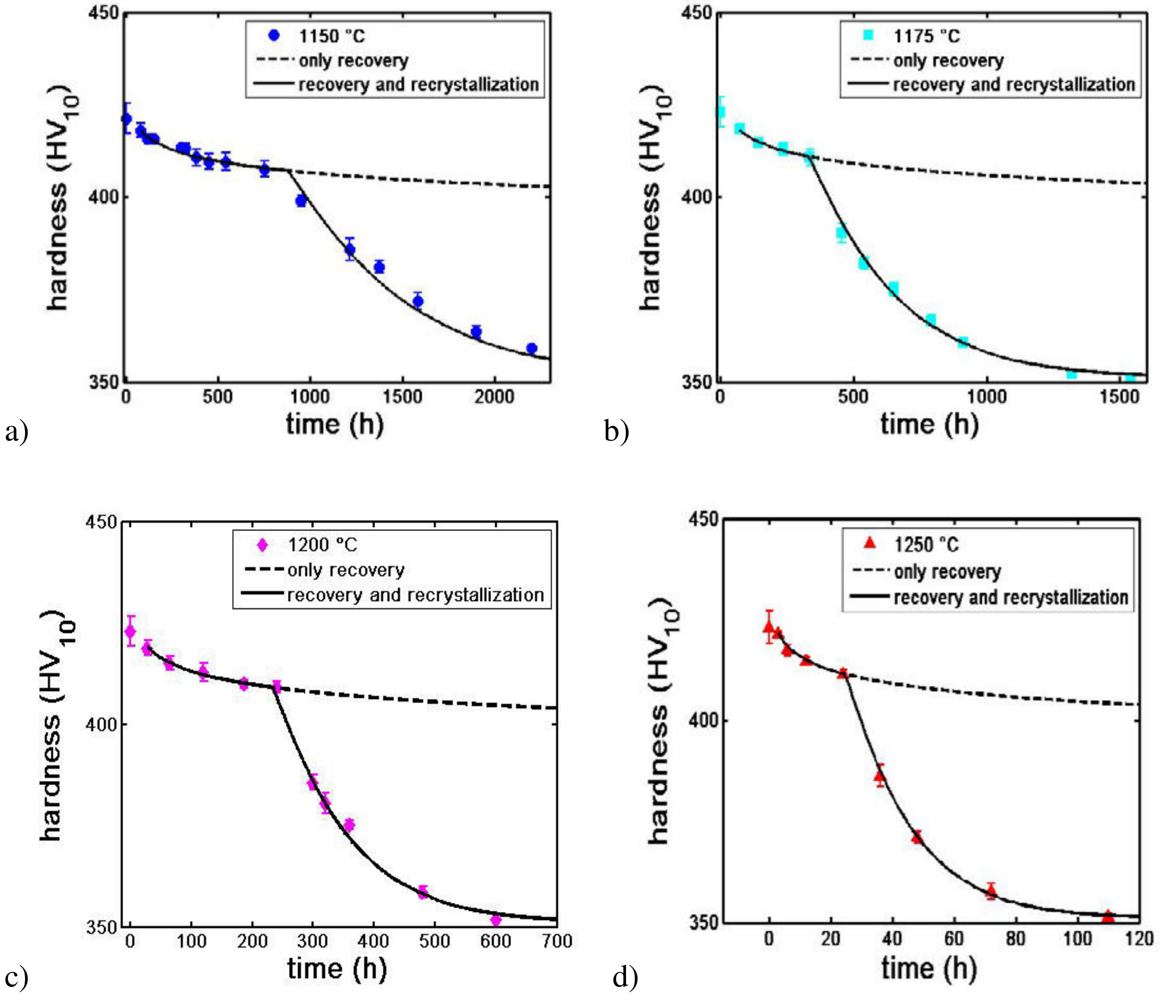

a) b) c) d)

Fig. 29. Evolution of the Vickers hardness of warm-rolled tungsten W67 measured in the rolling plane with time during annealing at 1150 °C (a), 1175 °C (b), 1200 °C (c) and 1250 °C (d). Experimental values (symbols) versus predictions by solely the recovery model according to Eq. 4.2 (dashed line) and additionally the recrystallization model of Eqs. 3.2 and 4.4 (solid line).

4.1.4) Activation energies

An easy and first approach to characterize the activation energy for recrystallization is to assume that the half-recrystallized state $(X = 0.5)$ corresponds to the state where half of the hardness loss has occurred or, formulated differently, the average hardness $\left(HV_{def} + HV_{rex}\right)/2 = 387\ HV_{10}$. A reason for this choice is that the half-recrystallized state is the stage where the material shows faster recrystallization kinetics. A number of literature references make use of the half hardness loss for the calculation of the activation energy for recrystallization (e.g. [100], [101], [99]). In this manner, the annealing time $t_{\Delta HV/2}$ required to reach a hardness $\mathrm{HV} = 387\ \mathrm{HV}_{10}$ at all temperatures allows an initial estimation of the activation energy for recrystallization. These times $t_{\Delta HV/2}$ are estimated from Fig. 25 by linear interpolation between the two closest hardness values to $\mathrm{HV} = 387\ \mathrm{HV}_{10}$, and shown in dependence on the annealing temperature T in Fig. 30. As indicated by the straight line, they can be approximated by an Arrhenius relationship,

$$t_{\Delta HV/2} = t^{*}_{\Delta HV/2} \exp\left(E_{\Delta HV/2}/RT\right) \tag{4.5}$$

with the universal gas constant R. Having obtained a proper description of the recrystallization kinetics (subchapter 4.1.3), one can (analogously to the time for attaining half the hardness loss) identify the proper time $t_{X=0.5}$ for half recrystallization, the incubation time t_{inc}, and the value of the thermal coefficient b at all temperatures, and analyze their temperature dependence. This allows the calculation of the activation energy for half-hardness loss ($E_{\Delta HV/2}$), half-recrystallization ($E_{X=0.5}$), nucleation ($E_{t_{inc}}$) and recrystallization as a whole including both nucleation and growth (E_b), from the slopes of Fig. 30. The values of all the obtained activation energies are presented in Table 7.

It shall be noted that the values t_{inc} and b were obtained from the fitting of the recrystallization kinetics expressed in Eq. 4.4 at all temperatures. $E_{t_{inc}}$ defines the activation energy that shall be provided to the sample to initiate recrystallization. On the other hand, the coefficient B from Eq. 2.11 is a kinetic parameter depending on the annealing temperature, nucleation rate and growth rate. By the new approach of using the re-formulation of Johnson-Mehl-Avrami-Kolmogorov kinetics of Eq. 4.4, the coefficient b should now describe thermal activation of recrystallization as a whole, including both nucleation and growth, and without a dependence on the exponent n. Therefore, an activation energy for recrystallization (E_b) can also be directly calculated from the dependence of the coefficient b on annealing temperature, using the Arrhenius relationship (Eq. 4.5).

Table 7. Activation energies for the plate W67 calculated using the Arrhenius relationship for different parameters: time to reach half of the total hardness loss $t_{\Delta HV/2}$, time to reach half-recrystallization $t_{X=0.5}$, incubation time for initiation of recrystallization t_{inc}, and kinetic parameter b.

Process	Activation energy (kJ/mol)
Half-hardness loss ($E_{\Delta HV/2}$)	$568\ (1 \pm 6\%)$
Half-recrystallization ($E_{X=0.5}$)	$579\ (1 \pm 7\%)$
Incubation time before recrystallization ($E_{t_{inc}}$)	$568\ (1 \pm 11\%)$
Thermal activation of nucleation and growth (E_b)	$599.5\ (1 \pm 7\%)$

An activation energy $E_{\Delta HV/2} = 568\ (1 \pm 6\%)$ kJ/mol for half-hardness loss was obtained from the slope of Fig. 30 (red line). A slightly higher apparent activation energy of $E_{X=0.5} = 579\ (1 \pm 7\%)$ kJ/mol for half-recrystallization is obtained from the slope of Fig. 30 (blue line) using this more elaborate approach, which takes into account that part of the hardness loss is due to recovery. For this reason, the values $t_{X=0.5}$ are slightly higher than the values $t_{\Delta HV/2}$ (see Fig. 30). For all activation energies, $(1 \pm X\%)$ represents the error progressed through the calculation using the Arrhenius relationship of Eq. 4.5, as extrapolated from the standard deviations of the 20 hardness measurements for each sample. All activation energies are within the same range.

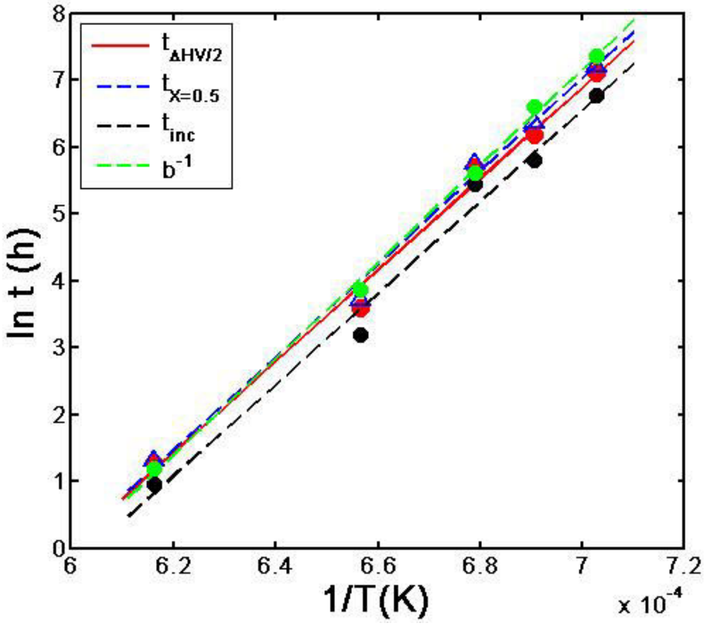

Fig. 30. Activation parameters of the plate W67. Arrhenius plot of: time to reach half of the total hardness loss $t_{\Delta HV/2}$; time to reach half-recrystallization $t_{X=0.5}$; incubation time for initiation of recrystallization t_{inc}; and b parameter.

It is worth noting that all the activation energies of Table 7 are within the range of the activation energy of volume self-diffusion $E_{SD.vol} = 586 - 628\ \text{kJ/mol}$ for polycrystalline tungsten as reported by the literature compilation of Lassner et al. [15]; values as low as $E_{SD.vol} = 526\ \text{kJ/mol}$ are reported in literature for bulk self-diffusion [60]. The calculated recrystallization activation energies indicate that recrystallization of this plate W67 is a thermally activated process governed by jumps of individual tungsten atoms, similar to the jumps in the bulk self-diffusion process.

4.2 Highly-rolled plate (W90)

4.2.1 Hardness evolution

Vickers hardness measurements were done on isothermally annealed samples from the plate W90 at six different temperatures; namely 1110 °C, 1150 °C, 1175 °C, 1200 °C, 1225°C and 1250 °C. Fig. 31 shows the experimental hardness values measured on samples annealed at these six different temperatures.

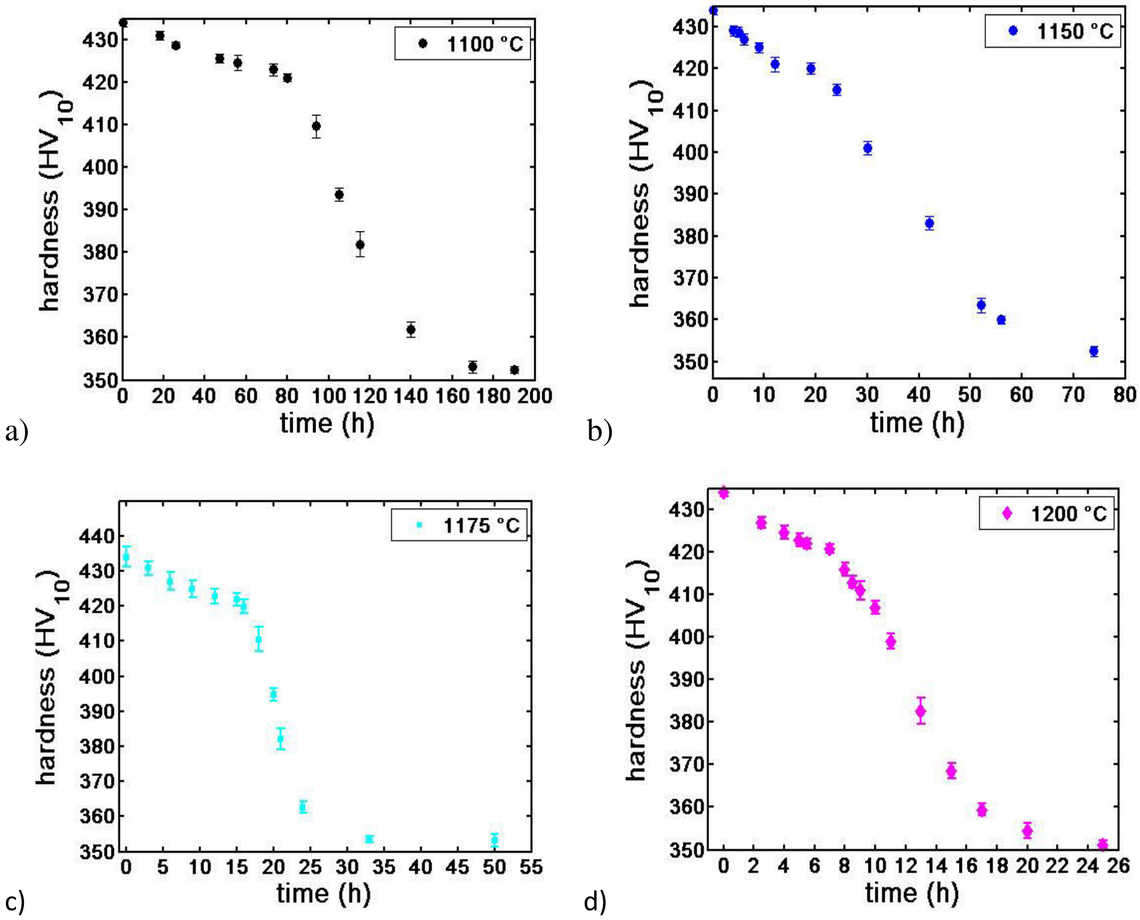

a)

b)

c)

d)

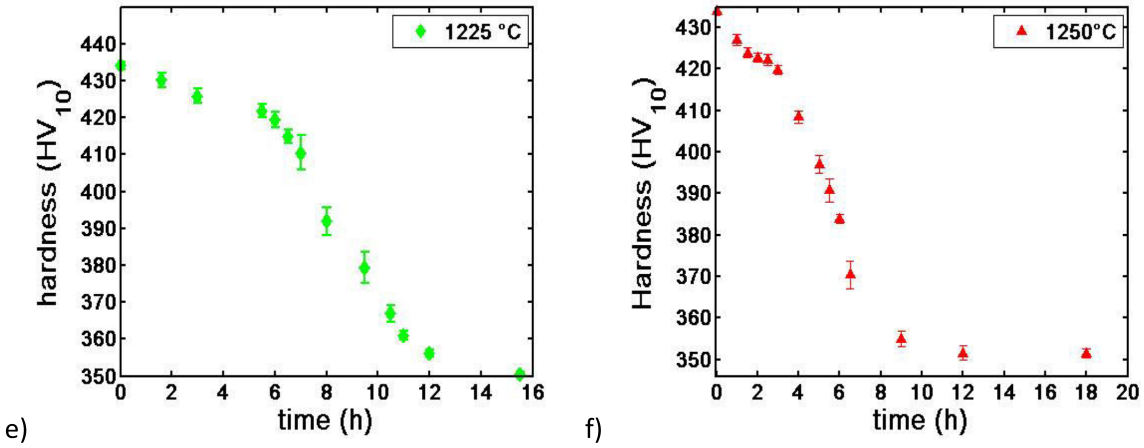

Fig. 31. Hardness evolution at different annealing times during annealing at 1100 °C (a), 1150 °C (b), 1175 °C (c), 1200 °C (d), 1225 °C (e) and 1250 °C (f). Vickers hardness measurements were performed on the mechanically polished surfaces RD/ND using a load of 10 kg and a dwell time of 10 s. The reported hardness values $HV_{10} \pm \Delta HV_{10}$ are averages over 20 indents with the standard deviation ΔHV_{10}; error bars in graphs represent $\pm\Delta HV_{10}$.

The standard deviation of the average (plotted as error bars in Fig. 31) was calculated using Eq. 4.1. For the plate W90, a decrease in hardness is observed from the value $HV_{def} = 434 \pm 2\,HV_{10}$ of the deformed state to the value $HV_{rex} = 351 \pm 2\,HV_{10}$ of the fully recrystallized state. This value did not decrease anymore with increasing annealing time, indicating that grain growth did not occur after recrystallization.

Analogously to the plate W67, the annealing kinetics and the activation energy for this plate W90 were obtained by the time to reach a half-hardness $\left(HV_{def} + HV_{rex}\right)/2 = 392.5\ HV_{10}$. The annealing times to reach half of the hardness loss for the plate W90 were estimated by interpolation from Fig. 31. The results are shown in Table 8.

Table 8. Estimated times to reach half-hardness loss at the different annealing temperatures. The annealing times were determined using linear interpolation between the two nearest hardness values.

T (°C)	$t_{\Delta HV/2}(h)$
1100	106.3
1150	36
1175	20.2
1200	11.9
1225	8
1250	5.35

The recrystallization kinetics are clearly much faster for this plate W90 (Table 8), as compared to the plate W67 (Table 4). This is expected due to its higher strain and its corresponding higher stored energy. Similarly to the plate W67, two different softening stages can be distinguished in Fig. 31 during annealing. The first stage corresponds to recovery, whereas the second stage occurring at longer annealing times corresponds to recrystallization.

4.2.2 Recovery kinetics

Analogously to the analysis of recovery done for the plate W67, the plate W90 was also fitted to the logarithmic dependence elucidated by D. Kuhlmann (Eq. 4.2)

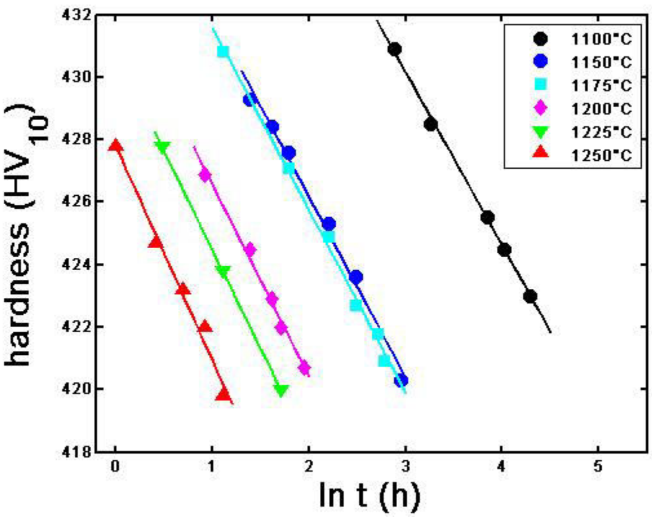

Fig. 32. Semi-logarithmic plot of the Vickers hardness for the tungsten plate W90, in dependence on the annealing time for different temperatures.

A good description of the hardness decrease is achieved by Eq. 4.2 for the plate W90 at all temperatures for the initial annealing stages (see Fig. 32), as was previously observed for the plate W67 (see Fig. 26). The slope of these linear fits, mathematically described by the coefficient C (see Table 9), also depends linearly on temperature, leading to an average constant value $C/T = 4.2 \cdot 10^{-3}\ (1 \pm 4\%)\ \mathrm{kgf\,K^{-1}mm^{-2}}$. The reason for this dependence is explained in the discussion section (6.1 Recovery).

Table 9. Values of the slope C of the linear recovery kinetics fit at different annealing temperatures T (°C), leading to a constant average value for the coefficient $C/T = 4.2\cdot10^{-3}\ (1\pm4\%)\ \mathrm{kgf\,K^{-1}mm^{-2}}$.

$T\left(°\mathrm{C}\right)$	$C\left(\mathrm{kgf\,mm^{-2}}\right)$	$C/T\left(\mathrm{kgf\,K^{-1}mm^{-2}}\right)$
1100	5.60	0.00408
1150	5.81	0.00408
1175	5.95	0.00411
1200	6.15	0.00418
1225	6.32	0.00422
1250	6.65	0.00437

By using D. Kuhlmann recovery kinetics (expression of Eq. 4.2), the coefficients $C/T = 3.1\cdot10^{-3}\ (1\pm8\%)\ \mathrm{kgf\,K^{-1}mm^{-2}}$ and $C/T = 4.2\cdot10^{-3}\ (1\pm4\%)\ \mathrm{kgf\,K^{-1}mm^{-2}}$ were obtained respectively for the plates W67 and W90. Comparison of both coefficients reveals faster recovery kinetics for the most highly-deformed plate (W90). The same recovery model of Eq. 4.2 is also used in literature (e.g. near grain boundaries of polycrystalline aluminum to fit recovery kinetics in [102]). The reasons for the faster recovery kinetics for the most highly-deformed plate W90 seem to be microstructural and will be discussed in the discussion chapter (6.1 recovery).

4.2.3 Recrystallization kinetics

As was done for the plate W67, the recrystallized fraction of the plate W90 can be estimated from hardness data using the rule of mixtures (Eq. 3.2), accounting also for the decrease of hardness induced by recovery (Eq. 4.2), and finally fitted to classical Johnson-Mehl-Avrami-Kolmogorov recrystallization kinetics with an incubation time t_{inc} (Eq. 4.4):

The obtained Avrami exponent n shows only minor deviations from a common average value of 2; The lower exponent n obtained for the plate W67 $(n = 1.1)$ as compared to that of the plate W90 $(n = 2)$ will be explained by microstructural considerations of nucleation in subchapter 5.5.1.

Analogously to the plate W67, a much better description of the hardness evolution during recrystallization of this plate W90 is obtained by considering an incubation time (e.g. 19 h for annealing at 1150 °C), in Eq. 4.4. This is reflected by the solid line of Fig. 33 at all temperatures.

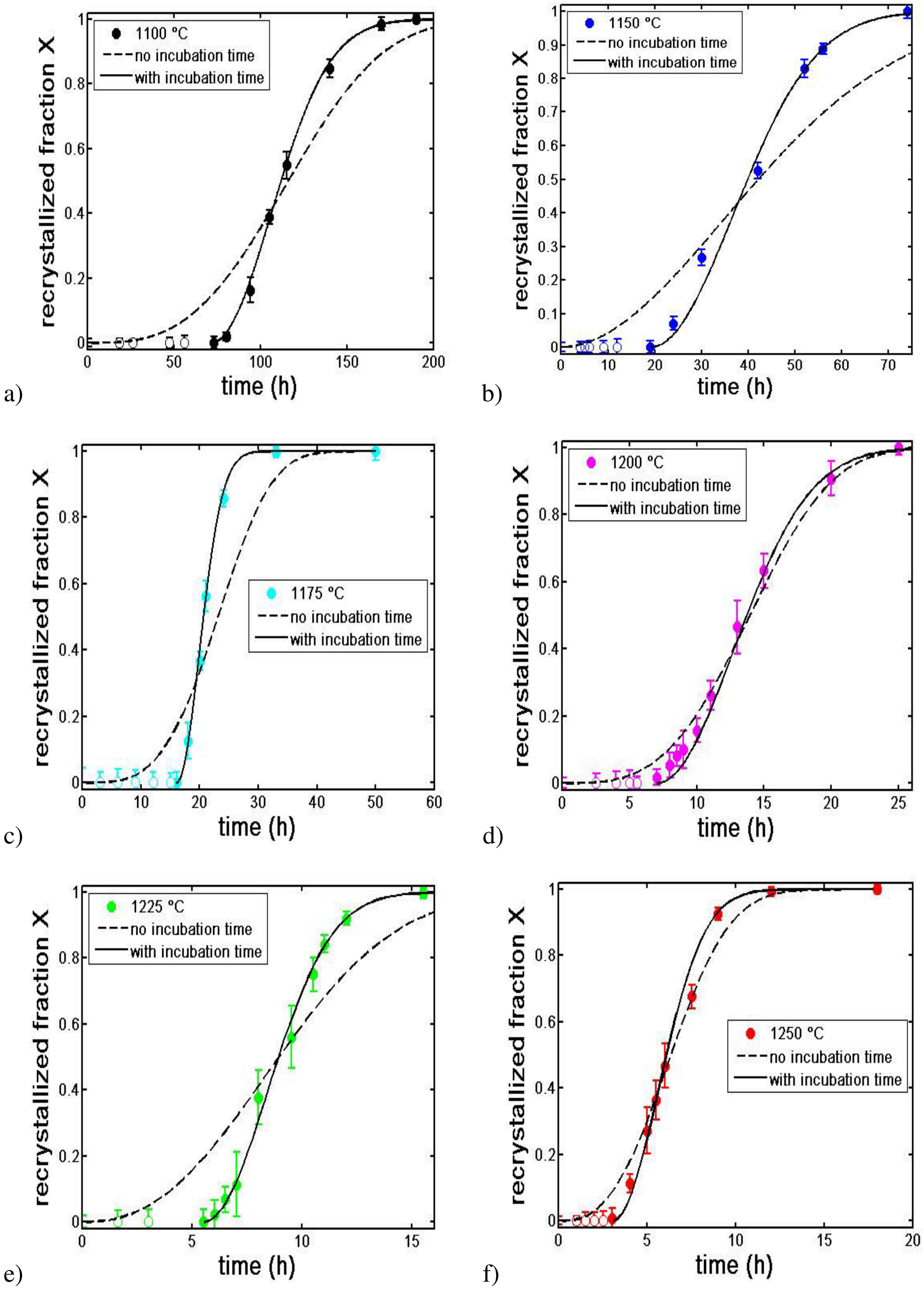

Fig. 33. Recrystallized volume fraction X of warm-rolled tungsten plate W90 as a function of annealing time at 1100 °C (a), 1150 °C (b), 1175 °C (c), 1200 °C (d), 1225 °C (e) and 1250 °C (f). Open symbols mark

values where only recovery is expected to occur, whereas filled symbols mark values where recovery and recrystallization occur simultaneously. The lines are fits of Eq. 4.3 (dashed line) to all values and of Eq. 4.4 (solid line) only to those values where recrystallization is expected to occur (filled symbols).

The addition of an incubation time is also justified microstructurally. As previously done for the plate W67, an EBSD grain boundary map for a sample annealed at 1175 °C (from the plate W90) for a shorter period (15 h) than the obtained incubation time $t_{inc}(1175\ °C) = 16$ h is provided in Fig. 34. In Fig. 34, only very few nuclei (covering a recrystallized fraction of 2%) are present after annealing for 15 h at 1175 °C. Had there not been an incubation time, a much larger recrystallized fraction X would have been observed at this relatively advanced annealing stage in the plate W90. It seems therefore that an incubation time for recrystallization exists for both plates W67 and W90.

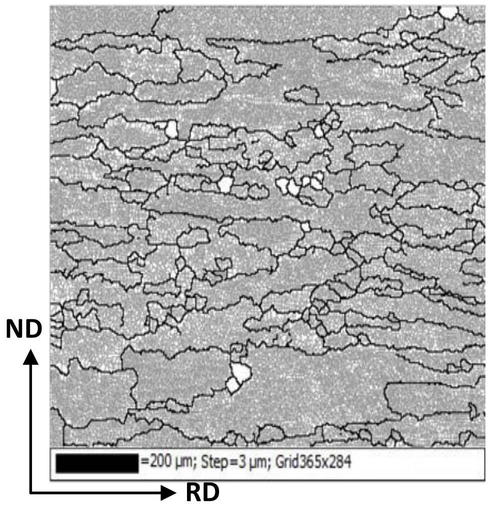

Fig. 34. Plate W90. Boundary map obtained by EBSD with a 3 µm step size on the transversal section (RD/ND) of a sample annealed for 15 h at 1175 °C, covering an area 1095× 852 µm^2. A few nuclei shown in white are identified. Nuclei were defined as regions with internal misorientations below 1°, partially surrounded by high angle boundaries and at least 81 µm^2 large. The recrystallized fraction corresponds to $X = 0.02$. Grey lines represent LABs (2°-15°), whereas black lines represent HABs (>15°).

Once the recovery and recrystallization kinetics have been described, combining the Kuhlmann model for recovery with the Johnson-Mehl-Avrami-Kolmogorov model for recrystallization allows the entire annealing kinetics to be described successfully for all temperatures as illustrated in Fig. 35.

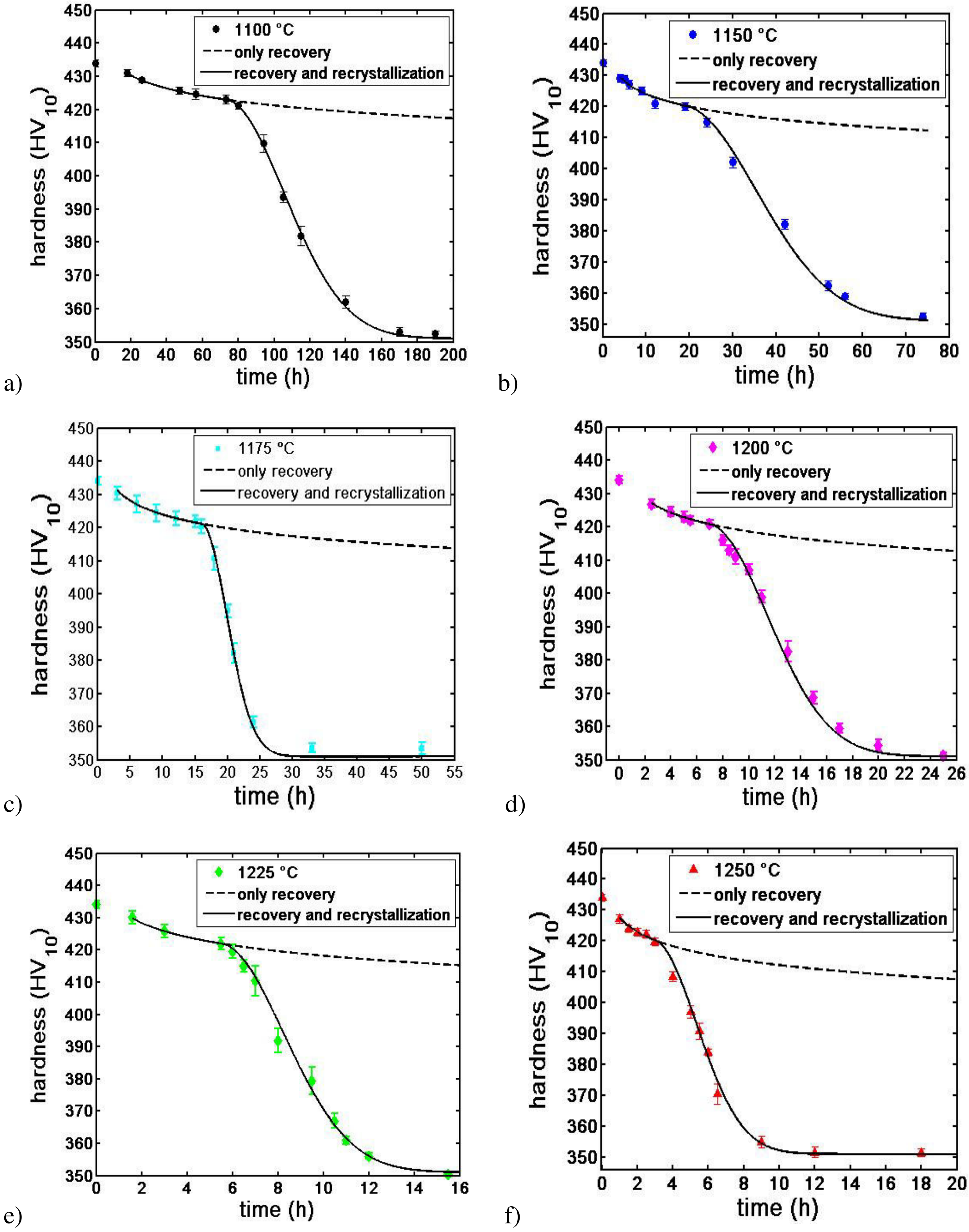

Fig. 35. Evolution of the Vickers hardness of warm-rolled tungsten W90 measured in the rolling plane with time during annealing at 1100 °C (a), 1150 °C (b), 1175 °C (c), 1200 °C (d), 1225 °C (e) and 1250 °C (f). Experimental values (symbols) versus predictions by solely the recovery model according to Eq. 4.2 (dashed line) and additionally the recrystallization model of Eqs. 3.2 and 4.4 (solid line).

4.2.4) Activation energies

Analogously to the plate W67, the parameters $t_{\Delta HV/2}$, $t_{X=0.5}$, t_{inc} and b obtained for the plate W90 allow the calculation of the activation energy for half-hardness loss ($E_{\Delta HV/2}$), half-recrystallization ($E_{X=0.5}$), nucleation ($E_{t_{inc}}$) and recrystallization as a whole including both nucleation and growth (E_b), from the slopes of the linear fits of Fig. 36. The values of all activation energies for the plate W90 are within the same range, indicating similar activation energies for all recrystallization processes (values presented in Table 10). In fact, all calculated activation energies for the plate W90 are within the range of the activation energy of grain boundary diffusion in tungsten $E_{GbD.vol} = 377 - 460$ kJ/mol. The activation energies for the plate W90 are also lower than the activation energies previously calculated for the plate W67, which were comparable to the activation energy for bulk diffusion $E_{SD.vol} = 586 - 628$ kJ/mol (see Table 7). Lower activation energies within the range $E_{GbD.vol} = 377 - 460$ kJ/mol are more frequently reported; for instance, an activation energy of 396 kJ/mol has been found for grain growth after recrystallization of a similar plate (manufactured by the same company; AT&M) warm-rolled to 75% thickness reduction [56].

Moreover, Table 10 shows that the activation energy calculated from the coefficient b for recrystallization as a whole including both nucleation and growth (E_b) seems slightly lower than the rest for the plate W90. The lower value of E_b could be explained by a possible change in atomic jump mechanism from one with activation energy close to that of bulk diffusion to one with activation energy close to that of grain boundary diffusion. It must be noted that the change in atomic jump mechanism has not been proved and we mainly introduce this concept as a possibility. It is suggested for the plate W90, that an atomic jump mechanism with activation energy close to grain boundary diffusion, requiring a lower activation energy, is the dominating mechanism during the growth of the recrystallizing grains of the plate W90 and facilitates it. In other words, the easier jumps of tungsten atoms across the boundary from the recovered matrix towards the recrystallizing grains reduce the activation energy for growth. Since (E_b) also includes growth during recrystallization, it seems reasonable that the apparent lower activation energy for growth could decrease the activation energy for recrystallization as a whole expressed by E_b (which includes both nucleation and growth). This is also in good agreement with the fact that the parameter b shows considerable higher values than the other parameters for the plate W90, which was not the case for the plate W67 (compare Fig. 36 with Fig. 30). As discussed earlier, it is suggested that the change to an atomic jump mechanism with lower activation energy (close to that for grain boundary diffusion) for the plate W90 would lead to faster nuclei growth and therefore to higher values of the parameter b which is also related to the kinetics of the growth process.

Table 10. Activation energies for the plate W90 calculated using the Arrhenius relationship for different parameters: time to reach half of the total hardness loss $t_{\Delta HV/2}$, time to reach half-recrystallization $t_{X=0.5}$, incubation time for initiation of recrystallization t_{inc}, and kinetics parameter b.

Process	Activation energy (kJ/mol)
Half-hardness loss ($E_{\Delta HV/2}$)	$357\ (1 \pm 2\%)$
Half-recrystallization ($E_{X=0.5}$)	$352\ (1 \pm 4\%)$
Incubation time before recrystallization ($E_{t_{inc}}$)	$369\ (1 \pm 7\%)$
Thermal activation of nucleation and growth (E_b)	$328\ (1 \pm 5\%)$

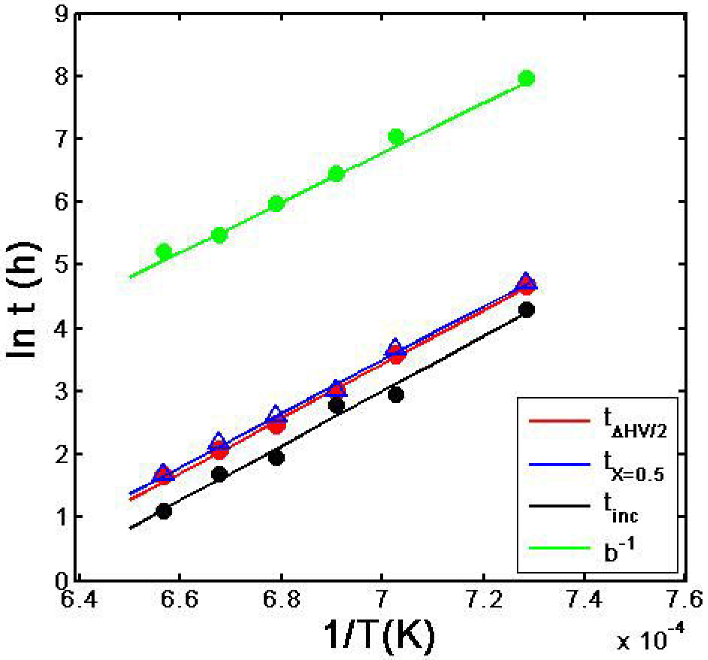

Fig. 36. Activation parameters of the plate W90. Arrhenius plot of: time to reach half of the total hardness loss $t_{\Delta HV/2}$; time to reach half-recrystallization $t_{X=0.5}$; incubation time for initiation of recrystallization t_{inc}; and b parameter.

From Fig. 36, one can observe that both the times for half hardness loss and half recrystallization (as calculated from JMAK kinetics of Eq. 4.4) are almost equivalent, with $t_{\Delta HV/2}$ being slightly smaller. As one would expect, the incubation times before recrystallization t_{inc} are shorter than the times to half-recrystallization $t_{X=0.5}$ (t_{inc} is expected to be approximately half the time to reach half-recrystallization $t_{X=0.5}$). All characteristic times also show a similar activation energy (see Table 10).

Comparison of the parameters $t_{\Delta HV/2}$, $t_{X=0.5}$, t_{inc} and b for the plates W67 and W90 shows lower recrystallization activation energies and faster recrystallization kinetics for the plate W90. The microstructural reasons for these lower activation energies and faster recrystallization kinetics, as well as for the possible dominance of different diffusion mechanisms for the plates W67 and W90, will be provided in the discussion section (chapter 6). The extrapolation of the recrystallization kinetics to elucidate lifespans at different operation temperatures is also presented and discussed in chapter 6.

4.3 Summary of Chapter 4

The long-term annealing behavior of two warm-rolled tungsten plates (namely W67 and W90) has been quantified via Vickers hardness characterization in the temperature range from 1150 °C to 1350 °C for the plate W67 and in the temperature range from 1100 °C to 1250 °C for the plate W90. From the loss in hardness, two characteristic annealing stages (corresponding to recovery and recrystallization) are identified. These stages are perfectly described by theoretical models at all annealing temperatures and for both plates.

The hardness loss during recovery can be nicely fitted by the logarithmic time dependence rationalized by Kuhlmann. A direct relationship is found between the the recovery kinetics and the annealing temperature, as indicated by the constant coefficient C/T found for both plates, since recovery is a thermally activated process. The coefficients $C/T = 3.1 \cdot 10^{-3}\ \left(1 \pm 8\%\right)$ kgf $\mathrm{K}^{-1}\mathrm{mm}^{-2}$ and $C/T = 4.2 \cdot 10^{-3}\ \left(1 \pm 4\%\right)$ kgf $\mathrm{K}^{-1}\mathrm{mm}^{-2}$ obtained for the plates W67 and W90 respectively show much faster recovery kinetics for the plate W90. The physical meaning of these coefficients as well as the reasons for the faster recovery kinetics for the plate W90 will be discussed in the discussion section (6.1 recovery).

A proper description of the recrystallization behavior was obtained by the Johnson-Mehl-Avrami-Kolmogorov kinetics model, accounting for an incubation time for recrystallization. Microstructural examination of samples annealed to annealing times shorter than the fitted incubation times supports the existence of an incubation time before recrystallization. An Avrami exponent 1 unit higher ($n = 2$) was obtained for the more highly-strained plate W90, as compared to the moderately-strained plate W67 ($n = 1.1$). This difference in Avrami exponent seems to be microstructural and is dealt with in chapter 5.

From the annealing kinetics, the activation energies for half-hardness loss, recrystallization, nucleation, and nucleation and growth as a whole (as obtained from the kinetic exponent b) were elucidated for both plates. All calculated activation energies for a particular plate were within the same range. The obtained activation energies were comparable to the activation energy of self-diffusion for the plate W67 $(E_{SD.vol} = 586 - 628\ \text{kJ/mol})$, and to the activation energy of grain boundary diffusion for the plate W90 $(E_{GbD.vol} = 377 - 460\ \text{kJ/mol})$. Much faster recrystallization kinetics are observed for the most highly-strained plate W90 due to its higher stored energy and its lower recrystallization activation energies. The reason for the considerably lower activation energies of the plate W90 seems to lie in the as-received microstructure and is provided in chapter 5. From the values of the activation energies for recrystallization, the lifetime of these tungsten components could be extrapolated to lower temperatures, indicating a much higher thermal stability for the plate W67 at the studied temperatures. These lifetimes are presented in the discussion section of chapter 6.

CHAPTER 5

Microstructural characterization

In this chapter, Electron Backscattered Diffraction (EBSD) is used in order to study recovery and recrystallization. A thorough EBSD analysis of samples annealed at different temperatures and covering a wide range of annealing times is carried out. This chapter also includes a detailed study of nucleation and growth during recrystallization. Both the moderately-rolled (W67) and the highly-rolled (W90) plates are studied and compared. Additionally, the EBSD data also complement the hardness data in tracking recovery and recrystallization kinetics.

5.1 As-received state

5.1.1 General microstructure and texture

The microstructure of the as-received states is illustrated by EBSD orientation maps in Fig. 37 for the plates W67 (a) and W90 (b). Both maps represent the rolling plane (RD/TD). High angle boundaries (HABs) with misorientations above 15° (black lines) delineate a coarse-grained microstructure slightly elongated along RD. Corresponding maps obtained with smaller step size 0.5 µm, (a) and 0.2 µm (b) are presented in Fig. 41 in subchapter 5.1.2.

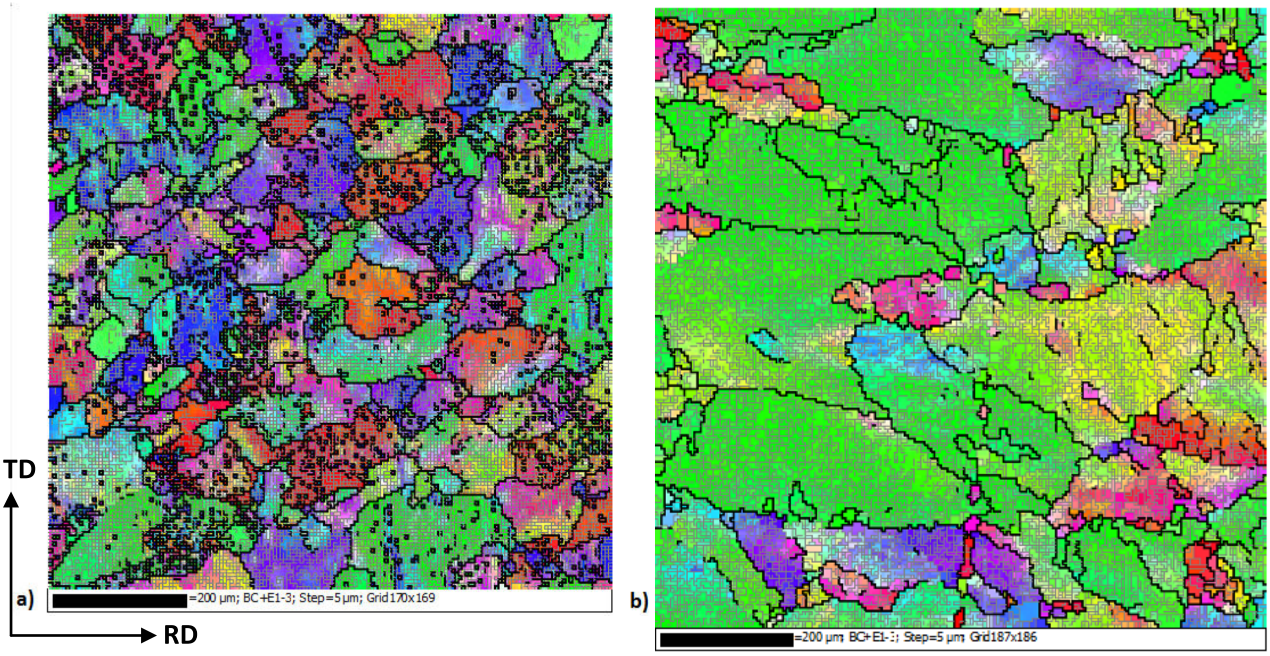

Fig. 37. Orientation maps obtained by EBSD: a) tungsten plate W67, b) tungsten plate W90. The observed sections correspond to the rolling plane RD/TD, with RD being horizontal in both maps. IPF coloring of the rolling direction is used. The maps were obtained with 5 µm step size, covering an area of 850x850 μm^2 and 930x930 μm^2 respectively. Black lines represent HABs (>15°) and grey lines LABs (2-15°). The maps are presented on the same scale for comparison purposes. Non-indexed points are represented as black pixels.

From the maps, the mean chord lengths of the grains ($\lambda_{HAB,RD}$, $\lambda_{HAB,TD}$) for the plates W67 (Fig. 37a) and W90 (Fig. 37b), the experimentally calculated average grain aspect ratio $AR_{\exp}$ (from Fig. 37), and the theoretically expected grain aspect ratio AR_{Theo} after rolling (as estimated from the thickness reduction, and ignoring any possible dynamic recrystallization), are summarized in Table 11. The mean chord length of the grains refers to the length of the grains along a specific direction. The mean chord length is calculated by plotting 50 intercept lengths that measure lengths in the grain boundary map until a critical misorientation is met (15° in this case).

Table 11 also provides the specific surface density of HABs (Eq. 5.1), as calculated from the mean chord lengths between HABs.

$$S_{V,HAB} = \frac{1}{\lambda_{HAB,RD}} + \frac{1}{\lambda_{HAB,TD}} \qquad (5.1)$$

A considerably bigger average grain size is observed for the plate W90 as compared to the plate W67. This difference can only be explained by a different initial microstructure before rolling for the plates W67 and W90. Higher rolling strains are expected to lead to smaller grain sizes, and the fact that the contrary relationship is found here seems to indicate that the plate W90 already possessed a coarser microstructure than the plate W67 before rolling.

Regarding the aspect ratio of the grains of both plates, although the most highly-strained plate W90 (Fig. 37b) shows a slightly higher aspect ratio $(AR_{\exp} = 1.3)$, both plates (W67 and W90) present nearly-equiaxed grains $(AR_{\exp} \approx 1)$. However, for both plates, the experimentally determined aspect ratios $AR_{\exp}$ are much lower than the expected theoretical aspect ratios AR_{Theo} that would result from rolling to the different rolling reductions (especially for the most highly-deformed plate). An equiaxed microstructure was assumed after powder sintering $(AR_{Theo} = 1)$, so that AR_{Theo} reflects the expected change in the aspect ratio entirely due to warm-rolling. The difference between $AR_{\exp}$ and AR_{Theo} is most likely caused by dynamic recrystallization during warm-rolling; recrystallization would lead to the formation and growth of new grains during the several rolling passes, resulting in more equiaxed grains (with lower aspect ratio) than would have otherwise been expected, had dynamic recrystallization not occurred. Dynamic recrystallization could also explain the bigger grain size for the plate W90. Nevertheless, the abundance of LABs in the as-received structure (see Fig. 41c, d) excludes the possibility of dynamic recrystallization during the last rolling passes.

Table 11: Microstructural parameters obtained from Fig. 37 for the warm-rolled plates W67 and W90: mean chord lengths of grains along the rolling and transversal direction, specific surface density of High Angle Boundaries $(S_{V,HAB})$ and experimental $(AR_{\exp})$ and theoretical (AR_{Theo}) aspect ratios. For the plate W67, the grain elongation after rolling is expected to increase 3 times along RD and remain constant along TD, leading to an expected $AR_{Theo} = 3$. For the plate W90, the grain elongation after rolling is expected to increase 10 times along RD and remain constant along TD, leading to an expected $AR_{Theo} = 10$.

Condition	$\lambda_{HAB,RD}$ (μm)	$\lambda_{HAB,TD}$ (μm)	$S_{V,HAB}$ (μm^{-1})	$AR_{\exp} = \frac{\lambda_{HAB,RD}}{\lambda_{HAB,TD}}$	AR_{Theo}
Warm-rolled W67 (RD/TD)	36	37	0.055	1	3
Warm-rolled W90 (RD/TD)	62	47	0.037	1.3	10

The textures of the plates are presented as {100}, {110} and {111} pole figures in Fig. 38a and Fig. 38b respectively, and as inverse pole figures in Fig 38c and Fig 38d.

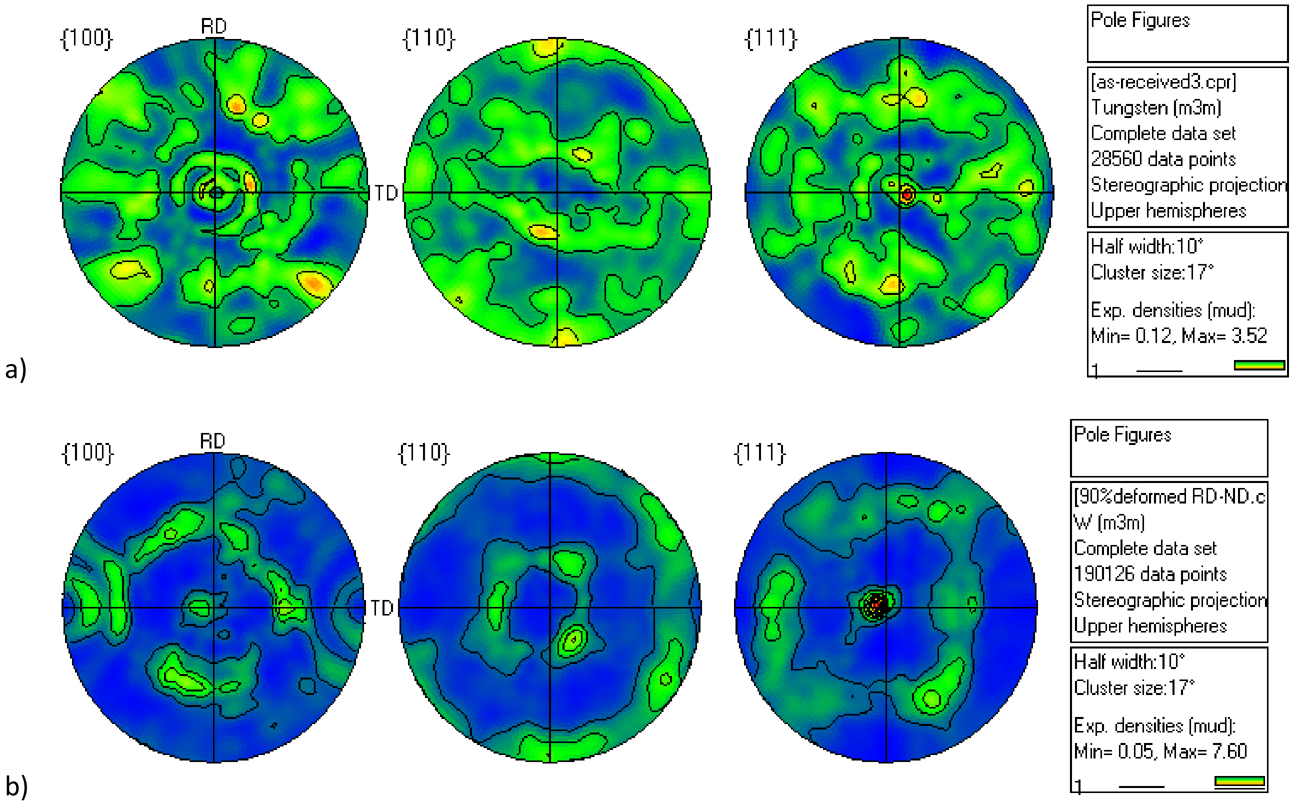

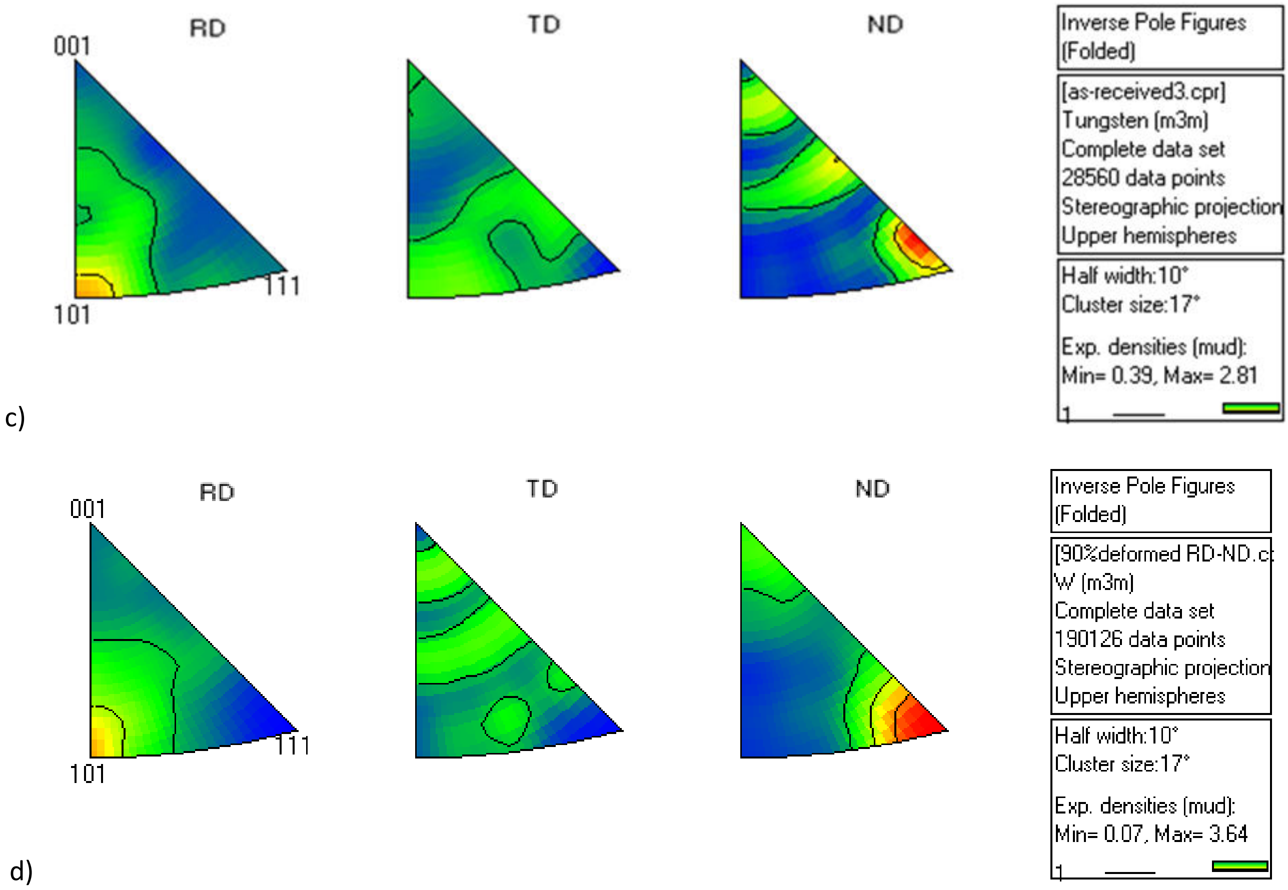

Fig. 38. {100}, {110} and {111} pole figures contoured using a Gaussian spread function with 10° half width and a cluster size of 17°. a) Plate W67, showing a maximum density 4 times above random for the {111} orientation parallel to ND, b) Plate W90, showing a maximum density 7.6 times above random for the {111} orientation parallel to ND. Inverse pole figure for the plate W67 (c) and the plate W90 (d).

The pole figures of the plate W67 were calculated from the map of Fig.37a, while the pole figures for the plate W90 were calculated from the following orientation map (Fig. 39). This is because the map of Fig. 37b did not cover enough grains for a statistically reliable description of the texture (note that more grains are mapped in the as-rolled microstructure for the plate W90 of Fig. 39).

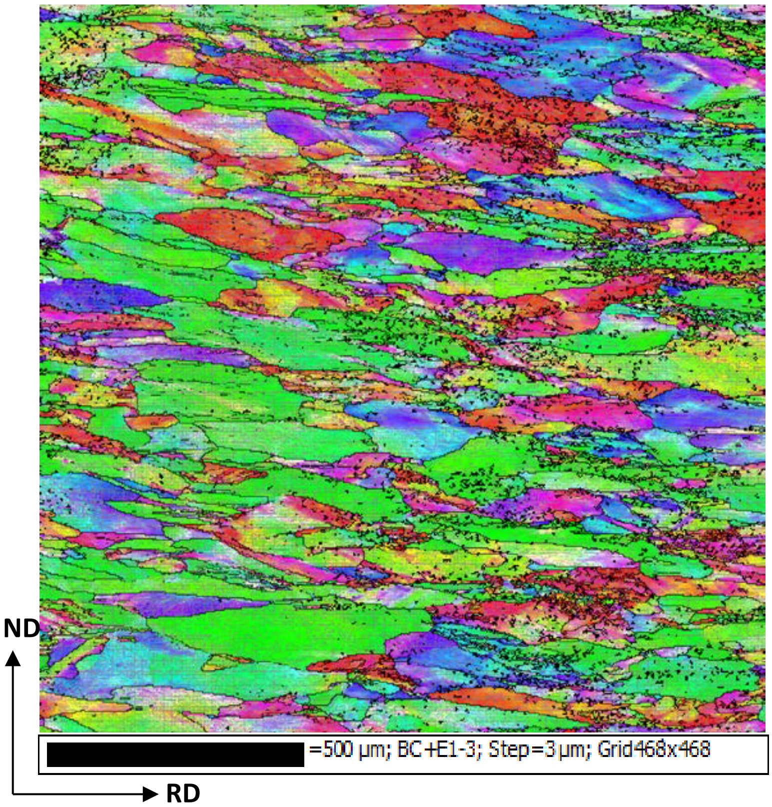

Fig. 39. Orientation maps obtained by EBSD for the as-received tungsten plate W90. The observed section corresponds to the rolling plane RD/ND, with RD being horizontal in both maps. IPF coloring of the rolling direction is used. The map was obtained with 3 µm step size, covering an area of and 1404x1404 µm^2. Black lines represent HABs (>15°) and grey lines LABs (2-15°). Non-indexed points are represented as black pixels.

The pole figures show that for both plates, and especially for the plate warm-rolled to the highest strain (W90), the most dominant texture component is {111} parallel to ND. For a better description of the texture, the Orientation Distribution Functions (ODFs) were calculated for both plates. The corresponding calculated sections at ϕ_2=45° are presented in Fig. 40a and Fig. 40b.

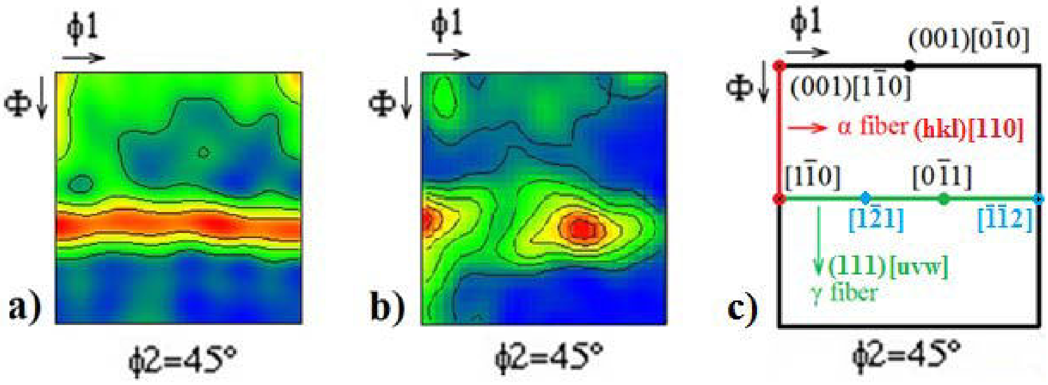

Fig. 40 ϕ_2=45° section of the orientation distribution function (ODF) calculated from the orientation data. a) Plate W67 showing a maximum density 3.7 times above random for the $\{111\}<1\bar{1}0>$component. b) Plate W90 showing a maximum density 6.4 times above random for the $\{111\}<1\bar{1}0>$component. c) Sketch of the

ϕ_2=45° section of orientation space, indicating the main components of a typical bcc rolling texture: the α fiber (red) and the γ fiber (green), as well as some of their components; the cube $\{001\} < 0\bar{1}0 >$ component, the rotated cube $\{001\} < 1\bar{1}0 >$ component, and the γ fiber components $\{111\} < 1\bar{1}0 >$ and $\{111\} < \bar{1}\bar{1}2 >$.

For both warm-rolled plates, the texture of the present material is a typical bcc rolling texture, with pronounced orientation densities along the so-called γ and α fibers, namely $\{111\} < uvw >$ and $\{hkl\} < 110 >$ respectively. Both plates present a more dominant γ fiber.

The plate warm-rolled to a moderate strain (W67) shows an almost complete α fiber and a complete and stronger γ fiber, with the γ fiber sharper than usually found in bcc rolling textures.

In contrast, for the plate warm-rolled to a higher strain (90% thickness reduction), the γ fiber presents a more usual appearance and also becomes more dominant. In fact, it is essentially only the $\{111\} < 1\bar{1}0 >$ component which is observed as a clear peak along the α fiber, a component evenly shared with the γ fiber. Moreover, the γ fiber is heterogeneous in that its orientation densities are shifted towards a $\{111\} < 1\bar{1}0 >$ dominating component. Apparently, the higher strain induces a stronger γ fiber texture with a dominating $\{111\} < 1\bar{1}0 >$ component.

Nevertheless, both plates show maximum orientation densities (3.7 and 6.4 for the plates W67 and W90 respectively) which are not very high, as it is typical for high temperature rolling of pure and low-alloyed bcc transition metals [48]. In contrast, cold-rolling of W has been shown to lead to stronger textures in which the rotated cube $\{001\} < 1\bar{1}0 >$ component dominates ([103], [48], [50]). For the present samples, only a rather weak peak with an orientation density 2 times above random is seen for this orientation (see Fig. 40a and Fig. 40b).

5.1.2 Subgrain structure

The abundance of low angle boundaries (LABs) with misorientations between 2° and 15° within the grains is characteristic for deformation structures with many deformation-induced dislocation boundaries. This abundance of LABs within the grains excludes the occurrence of dynamic recrystallization in the last rolling pass. Finding misorientation angles of more than 2° between almost all neighboring points, however, indicates that the spacing between dislocation boundaries in the deformation structure is smaller than the step size of 5 μm selected for gathering the orientation data. Hence, to better resolve the microstructure, a finer step size is required. Using a finer stepsize (i.e. 0.5 μm and 0.2 μm were found optimal for the plates W67 and W90 respectively), the subgrain structure could be revealed (see Fig. 41):

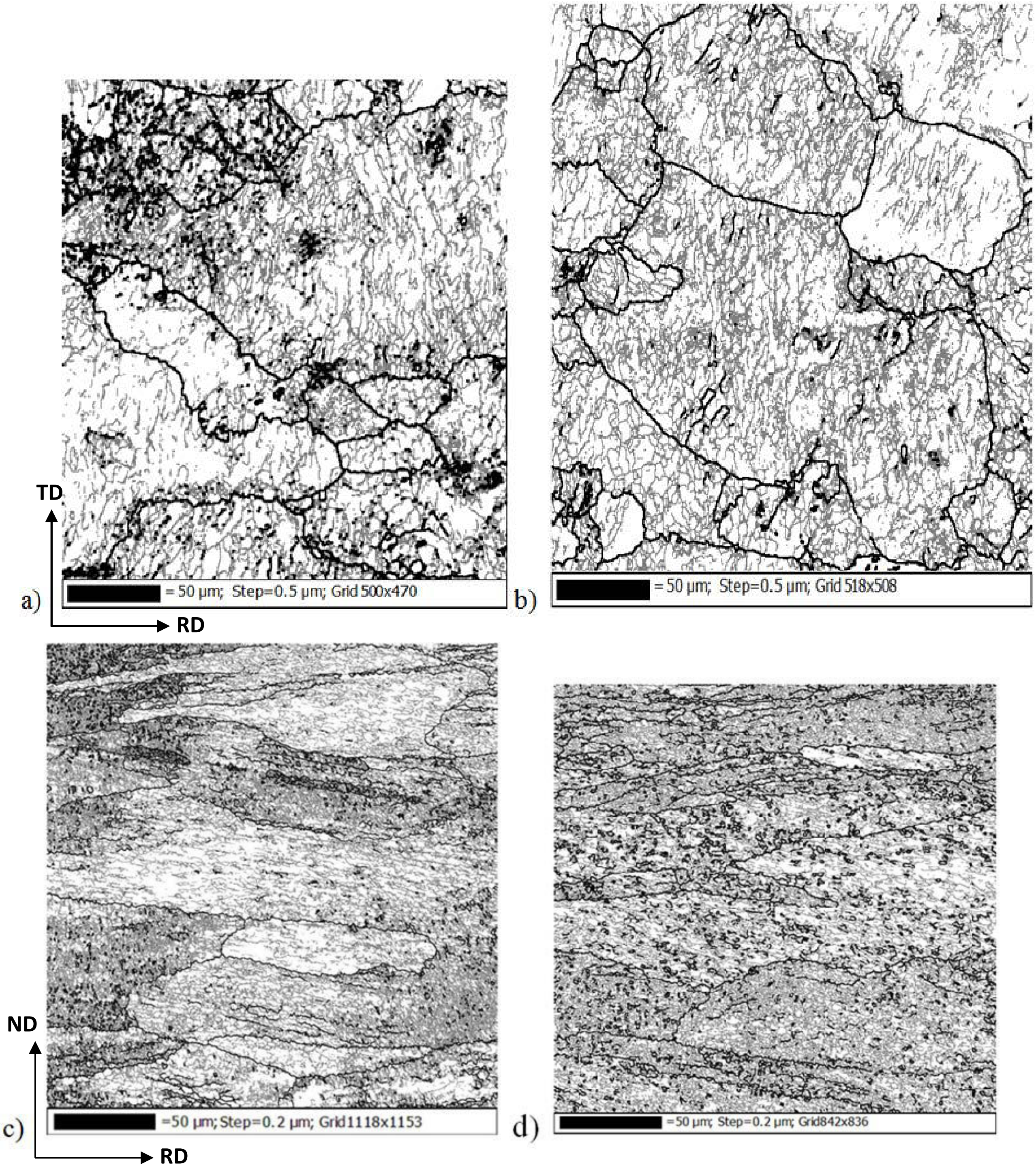

Fig. 41. Boundary maps obtained by EBSD. a), b): Maps corresponding to the plate W67 obtained with 0.5 µm stepsize and showing a LAB spacing of 2 µm. c), d): Maps corresponding to the plate W90 obtained with 0.2 µm stepsize and showing a LAB spacing of 0.67 µm. Grey lines represent LABs (2°-15°), whereas black lines represent HABs (>15°). The complete boundary map gathered for the plate W67 (a, b) (namely Fig. 42) covers a wider area; the smaller areas of this figure have been cropped from Fig. 42a, in order to visually compare the grain size and the LAB spacing at the same scale with the maps for the plate W90 (c, d).

Two grain boundary maps covering a wider area for the plate W67 (displayed on the same scale) and where the LABs are resolved are shown in Fig. 42.

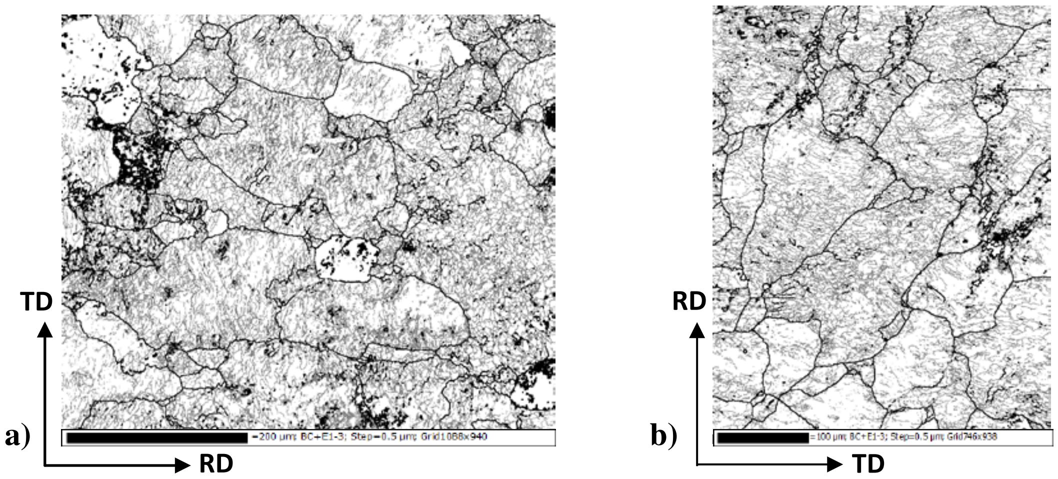

Fig. 42. Two boundary maps obtained by EBSD (a, b) on the RD/TD section for the plate W67. The maps were obtained with 0.5 µm stepsize and show a LAB spacing of 2 µm. The data summarized on Table 12 were obtained from these maps. The maps are displayed on the same scale for comparison purposes.

The specific surface density of LABs ($S_{V,LAB}$) and average misorientation angle for the LABs inside the deformed grains (namely $\theta_{av.}$) were measured from the orientation maps of Fig. 42a, b (Plate W67) and Fig. 41c, d (Plate W90). These parameters were measured for the individual grains of the previously presented boundary maps of both plates, and used to calculate stored energies (Δu) for the main texture components present in the as-received plates (see Fig. 40). The individual grains were defined as areas not exceeding a critical misorientation of 15°, using the grain detection tool of the software hkl Channel 5. Grains showing a maximum deviation ±15° from the ideal orientation were considered to belong to the same ideal texture component.

These data are summarized in Table 12 and Table 13 for the plates W67 and W90 respectively. The specific surface density for LABs ($S_{V,LAB}$), was calculated from the specific surface density for all boundaries (>2°, $S_{V,ALL}$) and the specific surface density for HABs (>15°, $S_{V,HAB}$), with the average chord lengths measured over both the horizontal and vertical direction in the boundary maps, according to (Eq. 5.2)

$$S_{v(LAB)} = S_{v(ALL)} - S_{v(HAB)} = \left(\frac{1}{\overline{\lambda}_{ALL,RD}} + \frac{1}{\overline{\lambda}_{ALL,TD}} \right) - \left(\frac{1}{\overline{\lambda}_{HAB,RD}} + \frac{1}{\overline{\lambda}_{HAB,TD}} \right) \qquad (5.2)$$

or $\overline{\lambda}_{HAB,ND}$ and $\overline{\lambda}_{ALL,ND}$ (instead of $\overline{\lambda}_{HAB,TD}$ and $\overline{\lambda}_{ALL,TD}$) in the case of the plate W90, where the transversal plane (RD/ND) was mapped. For clarity purposes, the mean chord lengths for LABs are also presented in Table 12 and Table 13. The parameters $\overline{\lambda}_{LAB,RD}$ and $\overline{\lambda}_{LAB,TD}$ (or $\overline{\lambda}_{LAB,ND}$ for the plate W90) presented in Table 12 and Table 13 are obtained according to Eq. 5.3, where *D* represents the corresponding direction RD, TD or ND:

$$\frac{1}{\bar{\lambda}_{LAB,D}} = \frac{1}{\bar{\lambda}_{ALL,D}} - \frac{1}{\bar{\lambda}_{HAB,D}} \tag{5.3}$$

The stored energies (Δu) were calculated from the data obtained from two orientation maps for the plate W67 (Fig. 42) and two orientation maps for the plate W90 (Fig. 41c, d), by application of Eq. 3.5 [21], previously presented chapter 3.

Table 12. Tungsten plate W67. The parameters $S_{V,LAB}$, $S_{V,HAB}$ and $\theta_{av.}$ are determined from two orientation maps (Fig. 42) obtained on the rolling plane (RD/TD). The main texture components of the deformed structure are listed in the table. The stored energy in LABs (Δu_{LAB}) and the total stored energy (Δu) are calculated according to Eq. 3.5. The mean chord lengths for LABs along RD and TD, namely $\bar{\lambda}_{LAB,RD}$ and $\bar{\lambda}_{LAB,TD}$, and the fraction of LABs inside the grains (f_{LAB}) are presented as well. The data for each texture component are averages from 5 grains mapped for each orientation.

Warm-rolled 67% Texture components	$S_{V,LAB}$ (μm^{-1})	$S_{V,HAB}$ (μm^{-1})	$\theta_{av.}$ (°)	Δu_{LAB} (kJ/m^3)	Δu (kJ/m^3)	$\bar{\lambda}_{LAB,RD}$ (μm)	$\bar{\lambda}_{LAB,TD}$ (μm)	f_{LAB}
Average all orientations	0.934	0.085	4.5	536.6	610.5	1.83	2.53	0.92
Cube $\{001\}<0\bar{1}0>$	0.890	0.096	4.6	517.5	600.9	2.11	2.40	0.90
Rotated cube $\{001\}<1\bar{1}0>$	0.894	0.057	4.6	519.8	569.3	2.14	2.36	0.94
All components γ fiber	0.956	0.052	4.5	549.2	594.4	1.88	2.36	0.95
γ fiber component $\{111\}<11\bar{2}>$	1.079	0.098	4.4	612.3	697.5	1.64	2.13	0.94
γ fiber component $\{111\}<1\bar{1}0>$	0.858	0.056	4.5	493.0	541.6	2.14	2.56	0.88

Table 13. Tungsten plate W90. The parameters $S_{V,LAB}$, $S_{V,HAB}$ and $\theta_{av.}$ are determined from two orientation maps (Fig 41c, Fig. 41d) obtained on the transversal plane (RD/ND). The main texture components of the deformed structure are listed in the table. The stored energy in LABs (Δu_{LAB}) and the total stored energy (Δu) are calculated according to Eq. 3.5. The mean chord lengths for LABs along RD and ND, namely $\lambda_{LAB,RD}$ and $\lambda_{LAB,ND}$, and the fraction of LABs inside the grains (f_{LAB}) are presented as well. The data for each texture component are averages from 5 grains mapped for each orientation.

Warm-rolled 90% Texture components	$S_{V,LAB}$ (μm^{-1})	$S_{V,HAB}$ (μm^{-1})	$\theta_{av.}$ (°)	Δu_{LAB} (kJ/m^3)	Δu (kJ/m^3)	$\overline{\lambda}_{LAB,RD}$ (μm)	$\overline{\lambda}_{LAB,ND}$ (μm)	f_{LAB}
Average all orientations	2.945	0.102	5.8	1929.6	2018.3	0.64	0.73	0.92
Cube $\{001\}<0\bar{1}0>$	2.880	0.114	5.9	1902.8	2001.8	0.64	0.75	0.92
Rotated cube $\{001\}<1\bar{1}0>$	2.920	0.139	5.7	1897.0	2017.8	0.63	0.76	0.91
All components γ fiber	2.786	0.133	5.9	1840.7	1956.2	0.68	0.76	0.91
γ fiber component $\{111\}<11\bar{2}>$	3.147	0.107	5.9	2079.2	2172.2	0.61	0.66	0.92
γ fiber component $\{111\}<1\bar{1}0>$	2.703	0.098	5.8	1771.1	1856.2	0.70	0.78	0.91

A considerably higher stored energy is obtained for the most highly-deformed plate (W90), mainly due to its considerably higher $S_{V,LAB}$ (i.e. lower LAB spacing). This is expected since higher strains introduce more stored energy in the material in the form of dislocations. Since the average misorientations ($\theta_{av.}$, Table 12) as well as the misorientation distributions (Fig. 43) are similar for all texture components, it can be deduced from Eq. 3.5 that the difference in stored energy between the different texture components and the different plates is mainly caused by a difference in the LAB spacing. This explains the good correspondence between the difference in specific surface density of LABs ($S_{v,LAB,W67} \approx 3S_{v,LAB,W90}$; e.g. see Fig. 41) and the stored energy ($\Delta u_{W90} \approx 3.3\Delta u_{W67}$) for both plates. Moreover, a clear difference in stored energy between the two main γ fiber texture components can also be observed for both plates. Apparently, the most dominant γ fiber component $\{111\}<1\bar{1}0>$ presents a considerably lower stored energy than the less dominant γ fiber component $\{111\}<11\bar{2}>$. The fraction of LABs (f_{LAB}) refers to the fraction of LABs inside the grains with respect to the present HABs in those grains (including both HABs surrounding the grains and HABs that might be present in the grain interiors). Both plates W67 and W90 show very similar values of

(f_{LAB}). Although the grain interiors of the plate W90 clearly show a higher fraction of LABs (as reflected by the shorter LAB spacing $\bar{\lambda}_{LAB}$), these grains also seem to present a higher fraction of internal HABs, leading to a shorter HAB spacing $\bar{\lambda}_{HAB}$ for the individual grains, due to the higher presence of HABs in the grain interiors of the plate W90. It is possible that the extra amount of LABs could be counterbalanced by the extra amount of HABs in the plate W90, making the fraction (f_{LAB}) similar for both plates.

The higher stored energy of the $\{111\}<11\bar{2}>$ component as compared to all other components (see Table 12 and Table 13) is in good agreement with [104] on hot-rolled molybdenum, which also finds the $\{111\}<11\bar{2}>$ γ component to have the higher stored energy. The texture of the as-rolled molybdenum of [104] consists of a predominant α fiber (with a dominant rotated-cube component) and a less dominant γ fiber (with dominant $\{111\}<11\bar{2}>$). In [104], it is observed that the γ fiber (with dominant $\{111\}<11\bar{2}>$ component) presents the highest stored energy among all other components. However, the dominant γ fiber component $\{111\}<11\bar{2}>$ of [104] is not compared to the component $\{111\}<1\bar{1}0>$ in [104]; the γ fiber is treated instead as a whole of all its components.

The misorientation distributions (a, b) and accumulated misorientation angle distributions (c, d) for both as-received plates for misorientation angles between 2-30° are presented in Fig. 43.

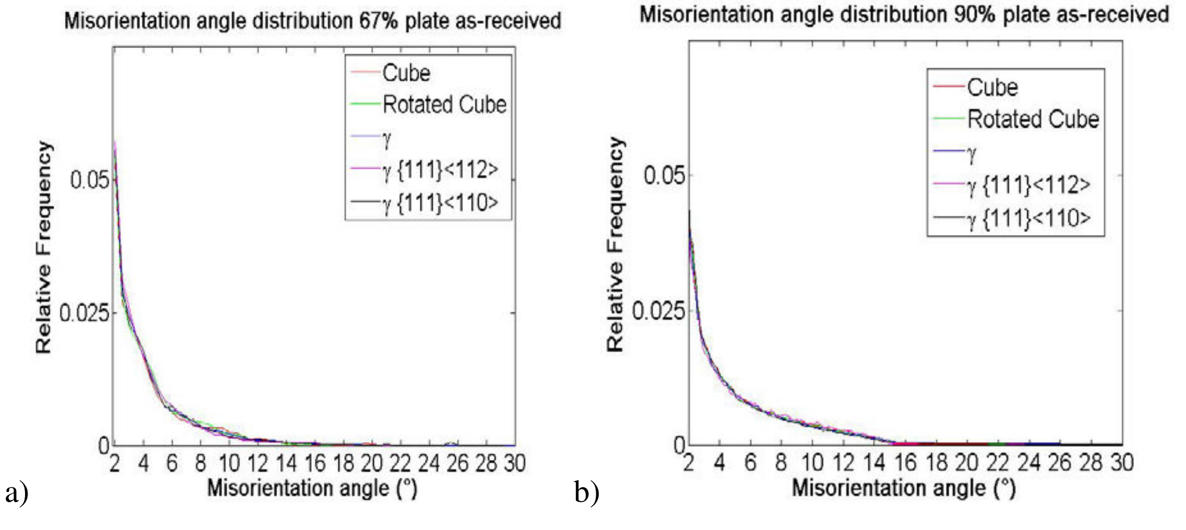

a) b)

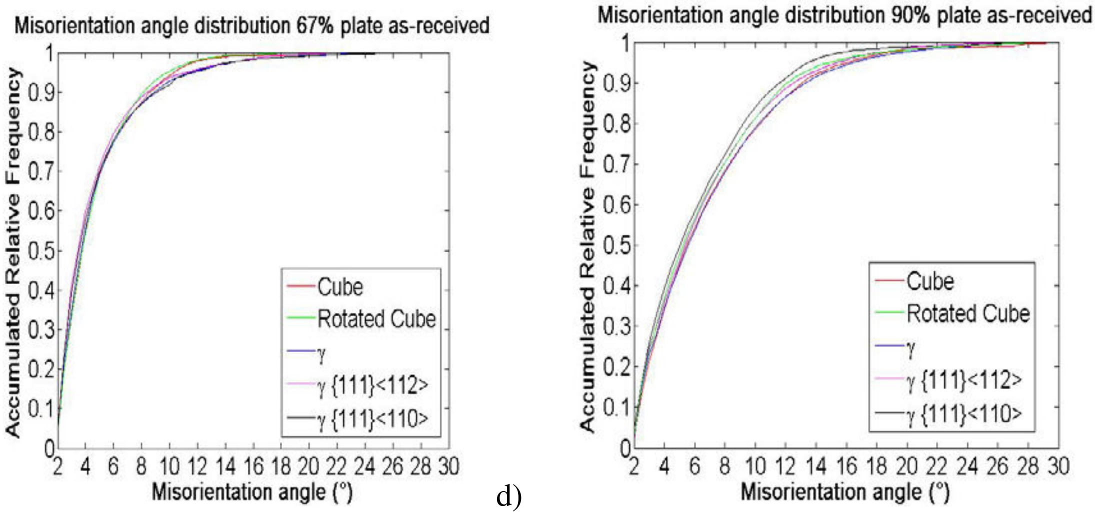

c) d)

Fig. 43. Misorientation angle distributions for the different texture components present in the as-received plates. a) Plate W67. b) Plate W90. c) Accumulated misorientation angle distribution corresponding to Fig. 43a (W67). d) Accumulated misorientation angle distribution corresponding to Fig. 43b (W90). The misorientation frequencies were obtained from HKL Channel 5, using a bin size of 0.1°.

The accumulated misorientation angle distributions (Fig. 43c, Fig. 43d) were plotted in order to highlight the small misorientation differences that might exist between the different components of the as-received texture. Slight differences are found in Fig. 43c and Fig. 43d between the different components. For example, in the case of Fig. 43d, the rotated cube component and the $\{111\} < 1\bar{1}0 >$ γ fiber component tend to show slightly lower misorientations than the others. This is in good agreement with Table 13, where the aforementioned components show lower average misorientation $\theta_{av.}$.

The misorientation data from 2-15° only were selected from Fig. 43c and Fig. 43d, and the plots of the misorientation angle distributions for LABs only (2-15°) shown in Fig. 44c, and Fig. 44d respectively. The idea is to check if it could be the HABs (15-30°) which cause the slight misorientation differences of Fig. 43c and Fig. 43d. The misorientation angle distribution where only LABs (2-15°) are selected (Fig. 44c and Fig. 44d) show a better overlap among all components as compared to Fig. 43d. Therefore, it seems that a difference in HABs partly causes the small misorientation differences between the different components of Fig. 43c and Fig. 43d, while the still remaining slight misorientation differences between 2-15° seem to be directly related to the average misorientation of LABs (θ_{av}) for each component (see Fig. 44c and Fig. 44d). A considerable homogeneity of the texture components in terms of the misorientation of the LABs is observed in Fig. 44c and Fig. 44d for both plates. Comparison of the accumulated misorientation angle distributions of Fig. 44c (W67) and Fig. 44d (W90) shows that there is a higher frequency for more highly-misoriented LABs for the plate W90, as compared to the plate W67. The increase of the average misorientation with increasing strain is expected.

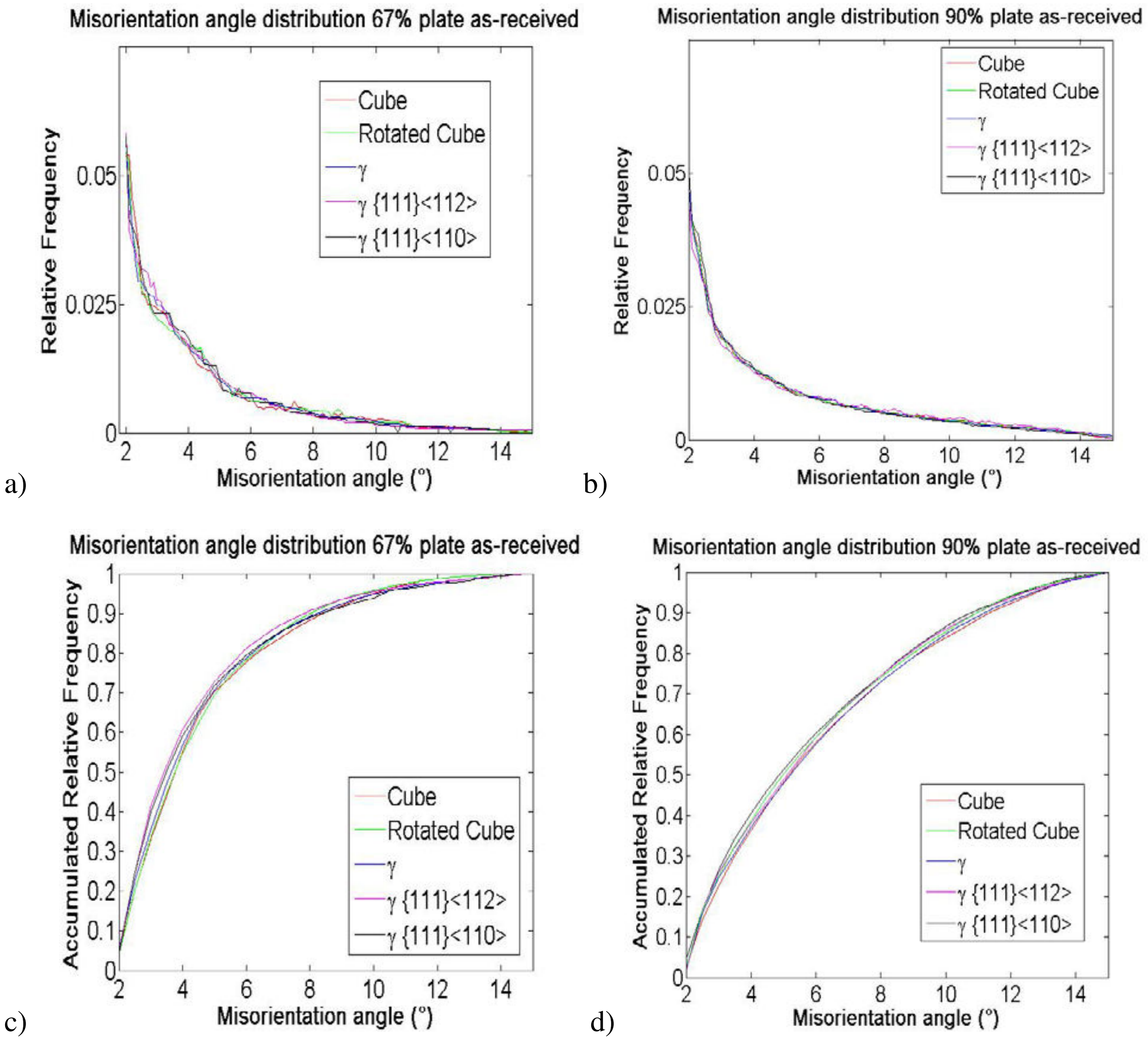

Fig. 44. Misorientation angle distribution between 2-15° for the different texture components present in the as-received plates. a) Plate W67. b) Plate W90. c) Accumulated misorientation distribution analogous to Fig. 44a. d) Accumulated misorientation distribution analogous to Fig. 44b. The misorientation frequencies were obtained from HKL Channel 5, using a bin size of 0.1°.

5.2 Recovery

For the study of recovery in terms of subgrain size coarsening during recovery, the subgrain size was measured during annealing of the plate W67 at 1250 °C for recovered grains of the main rolling texture component (i.e. γ fiber component $\{111\}<1\bar{1}0>$). The study of recovery is done on grains of orientation $\{111\}<1\bar{1}0>$ because this rolling component is the most abundant in the texture of the rolled tungsten plates. Three grains of this orientation were characterized for each annealing stage. The results, expressed as the evolution of the surface density of LABs ($S_{V,LAB}$) with annealing time, are shown in Fig. 45a. It is shown in Fig. 45b that the logarithmic time dependence (Eq. 4.2) also describes the evolution of subgrain size with annealing time. Examples of some orientation maps for grains of orientation $\{111\}<1\bar{1}0>$ within a spread of ±15°, at different recovery stages, are presented in Fig. 46 (seen in green, since IPF coloring along RD was used).

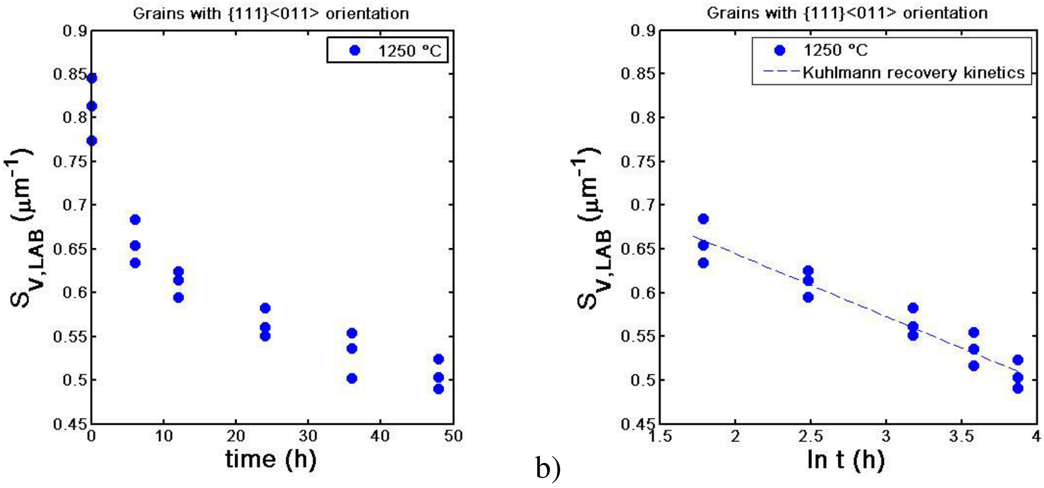

a) b)

Fig. 45. Recovery of the plate W67. a) Specific surface density of low angle boundaries $S_{V,LAB}$ obtained in grains of $\{111\}<1\bar{1}0>$ orientation (±15°) as a function of annealing time at 1250 °C. b) Semi-logarithmic plot of Fig. 45a where it is shown that a logarithmic recovery kinetics can successfully describe the evolution of subgrain size over annealing time at 1250 °C. Three grains with $\{111\}<1\bar{1}0>$ orientation were mapped for each annealing stage.

Additionally to the specific surface dentisy $S_{V,LAB}$, the average misorientation angle for the LABs between 2° and 15°, namely $\theta_{av.}$, was also determined. This allowed to calculate the evolution of the stored energy Δu during recovery at 1250 °C, according to Eq. 3.5. The data are summarized in Table 14.

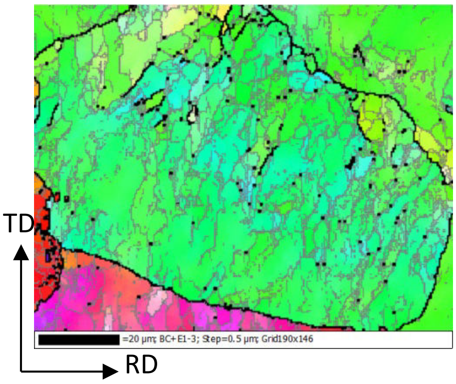
TD
RD
=20 µm; BC+E1-3; Step=0.5 µm; Grid190x146

(a)

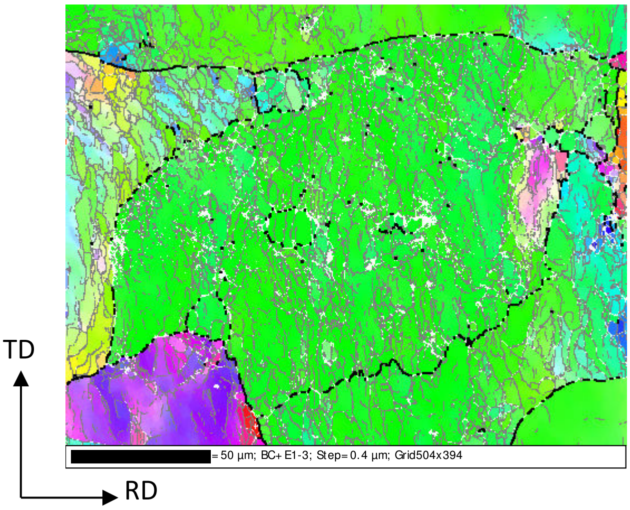
TD
RD
= 50 µm; BC+ E1-3; Step= 0.4 µm; Grid504x394

b)

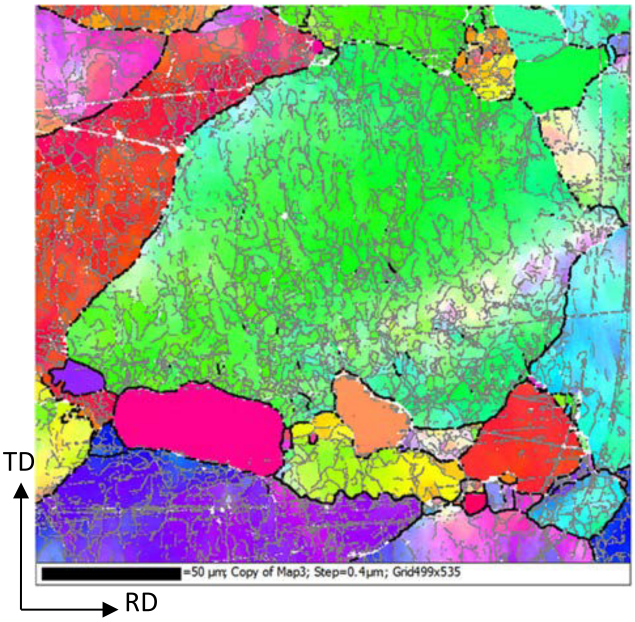
TD
RD
=50 µm; Copy of Map3; Step=0.4µm; Grid499x535

(c)

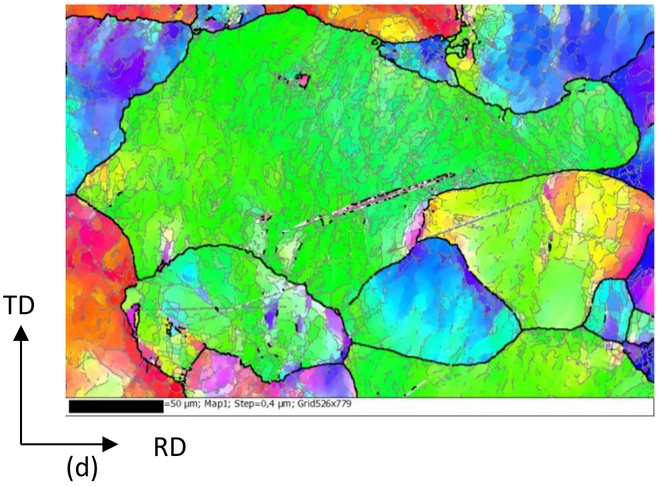
TD
RD
=50 µm; Map1; Step=0,4 µm; Grid526x779

(d)

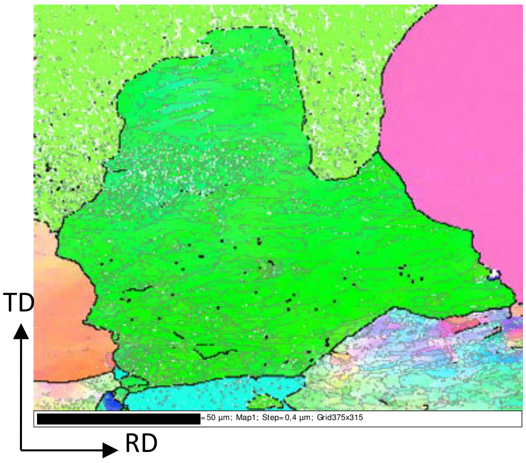
TD
RD
=50 µm; Map1; Step=0,4 µm; Grid375x315

(e)

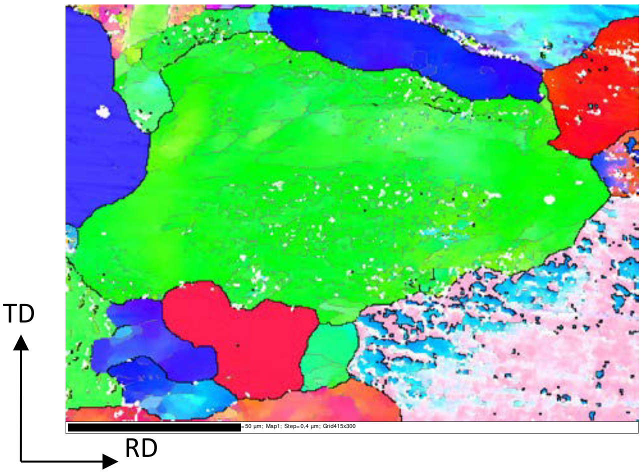
TD
RD
=50 µm; Map1; Step=0,4 µm; Grid415x300

f)

Fig. 46. Orientation maps obtained by EBSD with a step size of 0.4 μm for grains with orientations close to $\{111\}<1\bar{1}0>$ (±15°), for the plate W67. The rolling plane (RD/TD) is mapped in all cases, with the crystallographic direction along the rolling direction (horizontal) being colored. The mapped grains correspond to the as-received state (a), and recovered states after annealing at 1250 °C for different times (b) 6 h, c) 12 h, (d) 24 h, (e) 36 h, (f) 48 h.

Table 14: Evolution of different parameters during annealing of the tungsten plate W67. The evolution of the parameters $S_{V,LAB}$, $S_{V,HAB}$ and $\theta_{av.}$ during recovery is measured and averaged from three individual grains of $\{111\}<1\bar{1}0>$ orientation (±15°) for each annealing stage (see Fig. 45). The mapped grains were inspected on the rolling plane (RD/TD). The stored energy in LABs (Δu_{LAB}) and the total stored energy (Δu) are calculated according to Eq. 3.5. The mean chord lengths for LABs along RD and TD, namely $\lambda_{LAB,RD}$ and $\lambda_{LAB,TD}$, are also presented. $\bar{\theta}_{recov}$ represents the average misorientation predicted theoretically during recovery, as according to Eq. 5.5.

Warm-rolled 67% Texture comp. $\{111\}<1\bar{1}0>$	$S_{V,LAB}$ (μm^{-1})	$S_{V,HAB}$ (μm^{-1})	$\theta_{av.}$ (°)	Δu_{LAB} (kJ/m^3)	Δu (kJ/m^3)	$\lambda_{LAB,RD}$ (μm)	$\lambda_{LAB,TD}$ (μm)	$\bar{\theta}_{recov}$ $Eq.(5.5)$ (°)
As-received state	0.811	0.049	4.5	465.9	508.5	2.41	2.54	4.5
Annealed 6 h at 1250 °C	0.657	0.041	4.8	390.8	426.5	2.92	3.18	4.9
Annealed 12 h at 1250 °C	0.611	0.043	5	371.4	408.7	3.18	3.37	5
Annealed 24 h at 1250 °C	0.565	0.033	5.2	350.5	379.2	3.45	3.63	5.2
Annealed 36 h at 1250 °C	0.531	0.035	5.3	332.6	363.0	3.68	3.87	5.3
Annealed 48 h at 1250 °C	0.506	0.038	5.4	320.0	353.0	3.84	4.07	5.4

The evolution of the misorientation angle distribution for grains of $\{111\}<1\bar{1}0>$ orientation with annealing time at 1250 °C is also shown in Fig. 47.

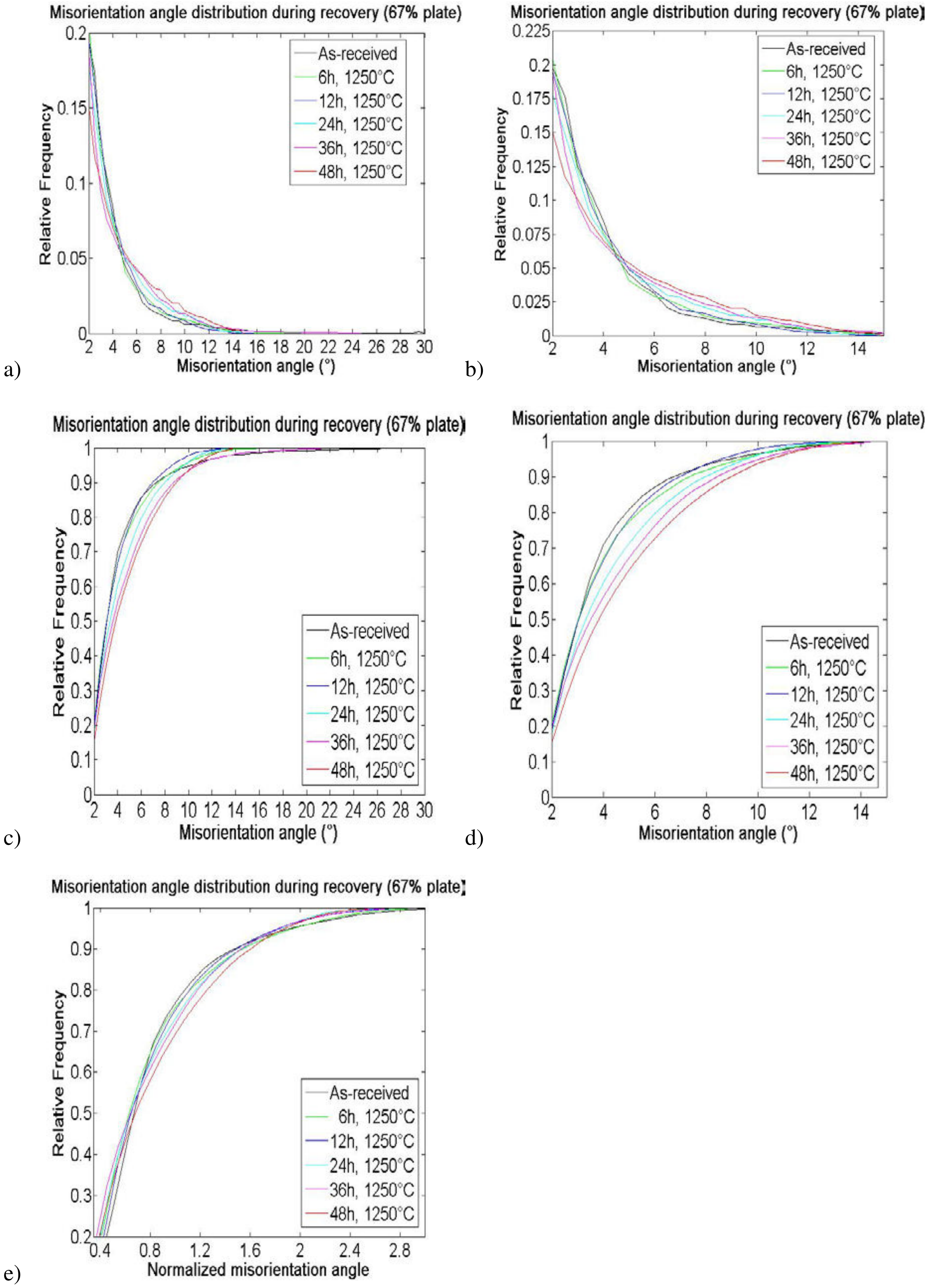
a) b) c) d) e)

Fig. 47. Misorientation angle distribution evolution during recovery of $\{111\}<1\bar{1}0>$orientation grains present in the tungsten plate W67. a) misorientation angle distribution from 2° to 30°. b) Misorientation

angle distribution from 2 to 15°, corresponding to LABs. c) Accumulated misorientation angle distribution calculated from Fig 47a. d) Accumulated misorientation angle distribution calculated from Fig 47b. e) Misorientation angle distribution from 2 to 15° normalized by the average misorientation angle of each annealing stage. Recovery was studied up to 48 h at 1250 °C. The misorientation frequencies were obtained from HKL Channel 5, using a bin size of 0.1°.

In Fig. 47, it can be seen how the misorientation distributions shift to higher misorientation angles as recovery proceeds during annealing (seen more clearly in the accumulated misorientation distribution for LABs only (2-15°) of Fig 47d). From Fig 47d, it can be seen that it is the misorientation of the LABs present in the grain interiors which tends to increase as recovery proceeds during annealing. This is in good agreement with the increase of the average misorientation angle for LABs (θ_{av}) during recovery reported in Table 14. In order to study whether the misorientation differences of Fig. 47 are entirely due to the increase of θ_{av} during recovery, or there is an additional effect contributing to the misorientation angle distribution differences, each misorientation angle distribution has been normalized by the average misorientation angle (θ_{av}) at each annealing condition (see Fig. 47e). This removes the shifting to higher misorientation angles, and allows direct comparison of the misorientation differences that might exist between the different annealing conditions. It can be seen in Fig 47e that the misorientation distributions at all annealing stages shows a better overlap than the non-normalized distribution of Fig. 47d, which indicates that the misorientation differences for the different recovery stages are partly due to the increase of the average misorientation angle $\overline{\theta}_{av}$ during recovery. However, some small differences are still appreciated between the normalized misorientation distributions, where it can be seen that the distribution of the LABs becomes broader as recovery proceeds.

The increase of the average misorientation angle of the LABs $(\theta_{av.})$ during recovery is displayed in Fig. 48, where $\theta_{av.}$ at each recovery stage (as averaged from 3 grains for each stage) is plotted versus the inverse of the surface density of LABs, namely $(1/S_{v(LAB)})$.

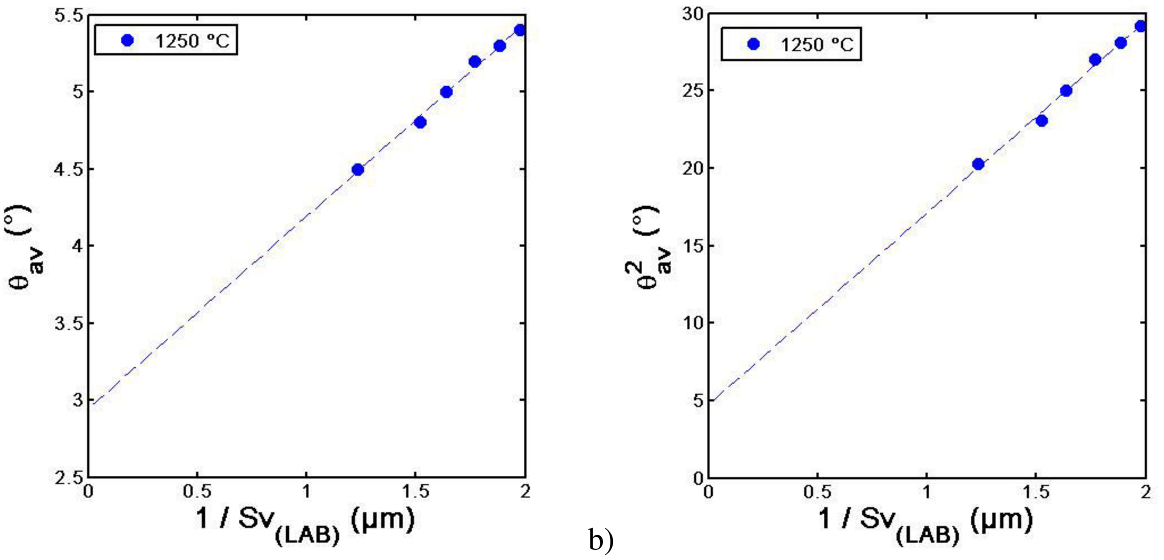

a) b)

Fig. 48. Misorientation distribution evolution during recovery at 1250 °C of $\{111\}<1\bar{1}0>$ orientation grains (±15°) present in the tungsten plate W67. Recovery was studied up to 48 h. The misorientation of the LABs present in the grain interiors tends to increase as recovery proceeds during annealing.

As can be seen from Fig. 48, for both the average misorientation angle $(\theta_{av.})$ and its square root $(\theta^2_{av.})$ a reasonably good linear fit to the average LAB spacing can be observed (Fig 48b).

The increase of average misorientation of the LABs with increasing subgrain size during recovery has already been modelled, for example, in Eq. 5.4 (from [105]), which can be re-written as:

$$\bar{\theta}_{recov} = \bar{\theta}_{deform} \sqrt{\frac{\lambda_{LAB(recov)}}{\lambda_{LAB(deform)}}} \qquad (5.4)$$

Or, formulated differently in Eq. 5.5,

$$\bar{\theta}_{recov} = \bar{\theta}_{deform} \left(\frac{\lambda_{LAB(recov)}}{\lambda_{LAB(deform)}} \right)^n \qquad (5.5)$$

where $\bar{\theta}_{recov}$ is the average misorientation of the LABs at each recovery stage, $\bar{\theta}_{deform}$ is the average misorientation of the LABs in the as-received state, $\lambda_{LAB(recov)}$ is the spacing between LABs at each recovery stage, $\lambda_{LAB(deform)}$ is the spacing between LABs in the as-received state, and the n exponent of Eq. 5.5 equals $n = 0.5$ in Eq. 5.4.

A slightly higher average misorientation $\bar{\theta}_{recov}$ than the measured $\theta_{av.}$ during recovery is predicted by Eq. 5.4. Fitting of the exponent n of Eq. 5.5 to the experimentally measured average misorientation $(\theta_{av.})$ led to an exponent n = 0.4 (slightly lower than the exponent n = 0.5 of reference [105]) which yielded a very good prediction of the experimental average misorientation

$(\theta_{av.})$ with the misorientation predicted by Eq. 5.5 $(\overline{\theta}_{recov})$, as shown in Table 14 by comparing the values $\theta_{av.}$ and $\overline{\theta}_{recov}$ of this table.

The value of the exponent *n* was obtained from the double logarithmic fit of the data of Fig. 48a, resulting into Fig. 49. The exponent *n* = 0.4 represents the slope of the linear fit of the plot of Fig. 49. The exponent *n* = 0.4 is closer to the exponent *n* = 0.5 which represents the quadratic fit. Therefore, it is concluded that a better fit can be obtained using the quadratic fit of Fig. 48b.

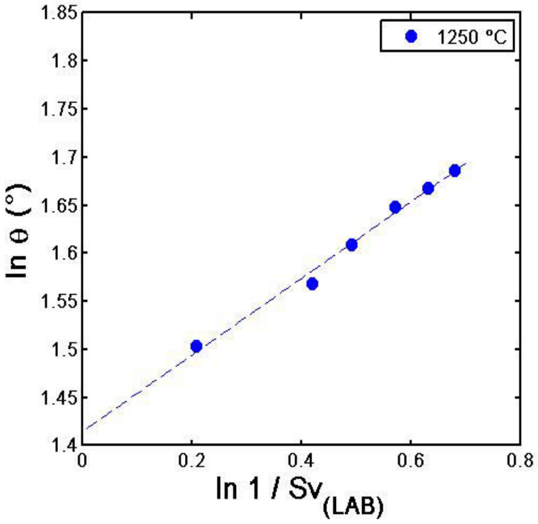

Fig. 49. Double logarithmic plot of the average misorientation angle $(\theta_{av.})$ and the average LAB spacing $(1/S_{v(LAB)})$ during recovery at 1250 °C of $\{111\}<1\overline{1}0>$ orientation grains (±15°) present in the tungsten plate W67. The data correspond to the data of Fig. 48a.

Only a slight modification of the exponential factor to $n = 0.4$ in Eq. 5.5 was required, as compared to $n = 0.5$ in Eq. 5.4 from [105]. Therefore, it was concluded that the misorientation angle increases linearly with subgrain coarsening during recovery, in a similar manner to that predicted in [105]. This finding is contrary to [40], where a slight decrease of the average misorientation $\theta_{av.}$ is found during the earlier stages of recovery in aluminum, until the average misorientation stabilizes at a constant value.

During recovery, the stored energy of the material decreases (see Table 14). This is achieved by rearrangement and annihilation of dislocations. As recovery proceeds, the subgrain size tends to increase ($S_{V,LAB}$ decreases), while the subgrain walls made up of dislocation arrays increase their misorientation ($\theta_{av.}$ increases), as can be seen from Fig. 47 and Table 14. As the misorientation of the LABs increases, so does the amount of dislocations per LAB. During this process, the stored energy per dislocation decreases as the LABs increase in misorientation (as seen in Fig. 47). Therefore, the subgrain coarsening during recovery and its corresponding increase of the LAB average misorientation ($\theta_{av.}$) induce a decrease of stored energy in the material. This is the driving force for subgrain growth.

It shall be noted that, at this stage, both the hardness evolution (subchapter 4.1.2) and the subgrain size evolution (current subchapter) during recovery have been characterized by logarithmic recovery kinetics over annealing time. For this reason, Fig. 50 attempts to relate the evolution of the microstructure (through the inverse of the intercept length between LABs, namely $S_{V,LAB}$) with the mechanical properties (through the decrease of Vickers hardness HV) during recovery. The linear relationship between the Vickers hardness and the subgrain size (Eq. 5.6) [106]:

$$HV = 3\sigma_y = HV_0 + 3K\mu b S_{v,LAB} \qquad (5.6)$$

is met in Fig. 50, where $\mu = 1.61 \cdot 10^5$ MPa or $\mu = 1.64 \cdot 10^4$ kgf/m^2 is the shear modulus of tungsten $b = 2.74 \cdot 10^{-4}$ µm is the Burgers vector for tungsten, and K is a proportionality constant. The good fit of the experimental data to Eq. 5.6 illustrates that the strength of the metal is inversely proportional to the subgrain size. The tungsten plate becomes softer as recovery occurs during annealing, due to the annihilation and rearrangement of dislocations induced by recovery, which results in the coarsening of the subgrain size. The linear fit of Eq. 5.6 allows the calculation of the value $K_W = 3.4$ for the proportionality constant of this tungsten material (plate W67) from the linear fit of Fig. 50. This value is comparable to that of the similar refractory metal molybdenum $K^*_{Mo} = 2.7$ [107], showcasing a similar relationship between changes in subgrain size and strength for both metals.

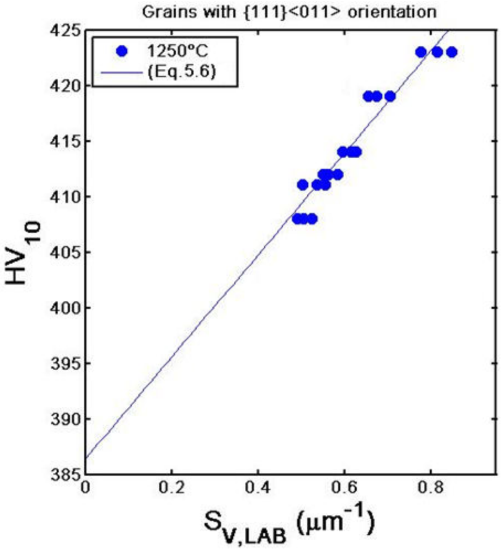

Fig. 50. Evolution of the specific surface density of LABs ($S_{V,LAB}$) and the Vickers hardness (HV_{10}) during recovery of grains with orientation $\{111\} < 1\bar{1}0 >$, for samples annealed at 1250 °C and up to 48 h. The plot shows that the experimental data fit a linear relationship between hardness and LAB surface density and hence an inverse proportionality between hardness and subgrain size (Eq. 5.6).

5.3 Recrystallization: EBSD characterization

In this chapter, orientation maps for both tungsten plates (W67 and W90) were analyzed using HKL Channel 5, which allowed to obtain recrystallization-related parameters at each annealing stage. The software DRG was used in order to identify the recrystallized grains and recrystallized fraction X_{EBSD}. Maps of recrystallized grains obtained using DRG software (where the recrystallized grains are shown in random colors) are placed next to each orientation map for comparison.

5.3.1 Moderately-rolled plate (W67)

Orientation maps at the different recrystallization stages were obtained for the plate W67 for three temperature series: namely after annealing at 1150 °C, 1200 °C and 1250 °C. The EBSD orientation data were mapped with a stepsize ranging from 3-20 µm. The smaller stepsizes were used for intercept length studies, while the bigger stepsizes were used for textural studies. The maps were taken on the rolling plane (RD/TD). The recrystallization-related parameters obtained from the EBSD orientation maps are compiled in Table 15, Table 16 and Table 17 for annealing of the plate W67 at 1150 °C, 1200 °C and 1250 °C respectively.

One EBSD orientation map at each annealing stage from 750 h to 2200 h at 1150 °C is presented from Fig. 51 to Fig. 57. Note that 750 h is the shortest available annealing time, just before the incubation time of 887 h as estimated by Vickers hardness in subchapter 4.1.3. In this map, only a few nuclei are observed.

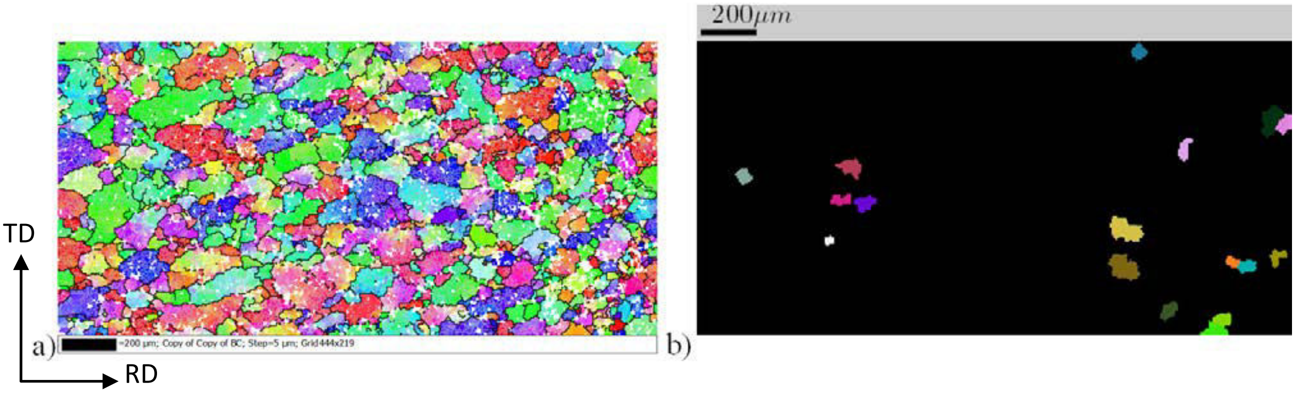

Fig. 51. a) Orientation map obtained on the RD/TD plane after annealing for 750 h at 1150 °C. The map was taken with 5 µm stepsize and is displayed with IPF coloring along RD, with RD horizontal. b) Detection of recrystallized grains using the software DRG, covering a recrystallized fraction $X_{EBSD} = 0.03$.

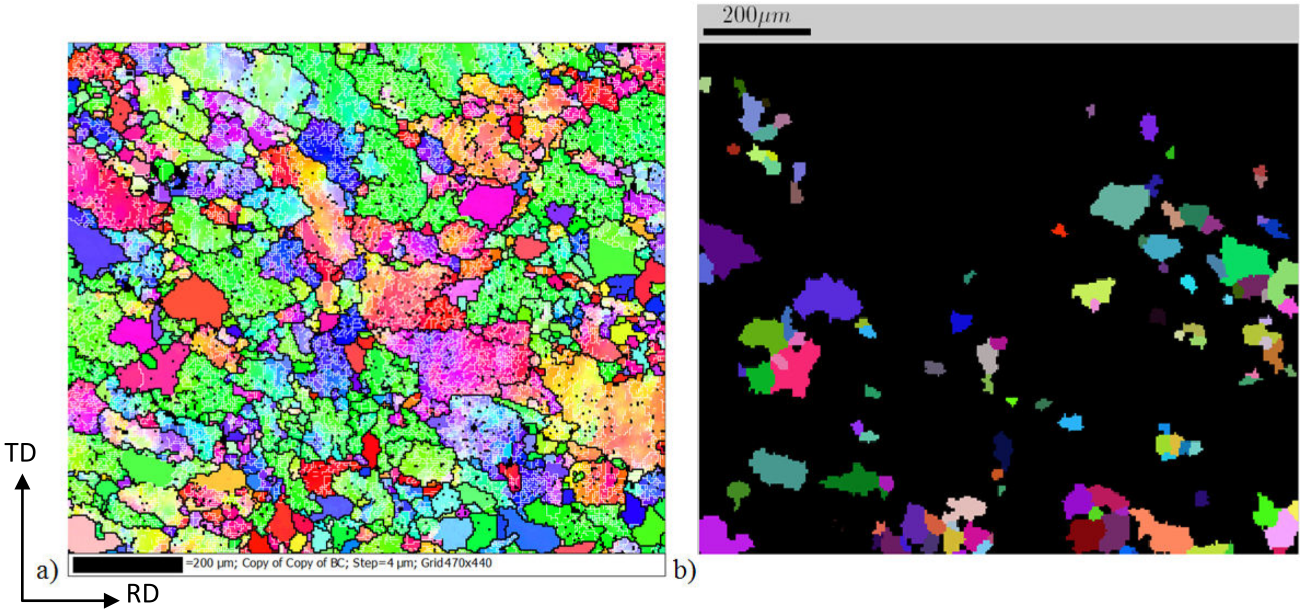

Fig. 52. a) Orientation map obtained on the RD/TD plane after annealing for 950 h at 1150 °C. The map was taken with 4 µm stepsize and is displayed with IPF coloring along RD, with RD horizontal. b) Detection of recrystallized grains using the software DRG, covering a recrystallized fraction $X_{EBSD} = 0.15$.

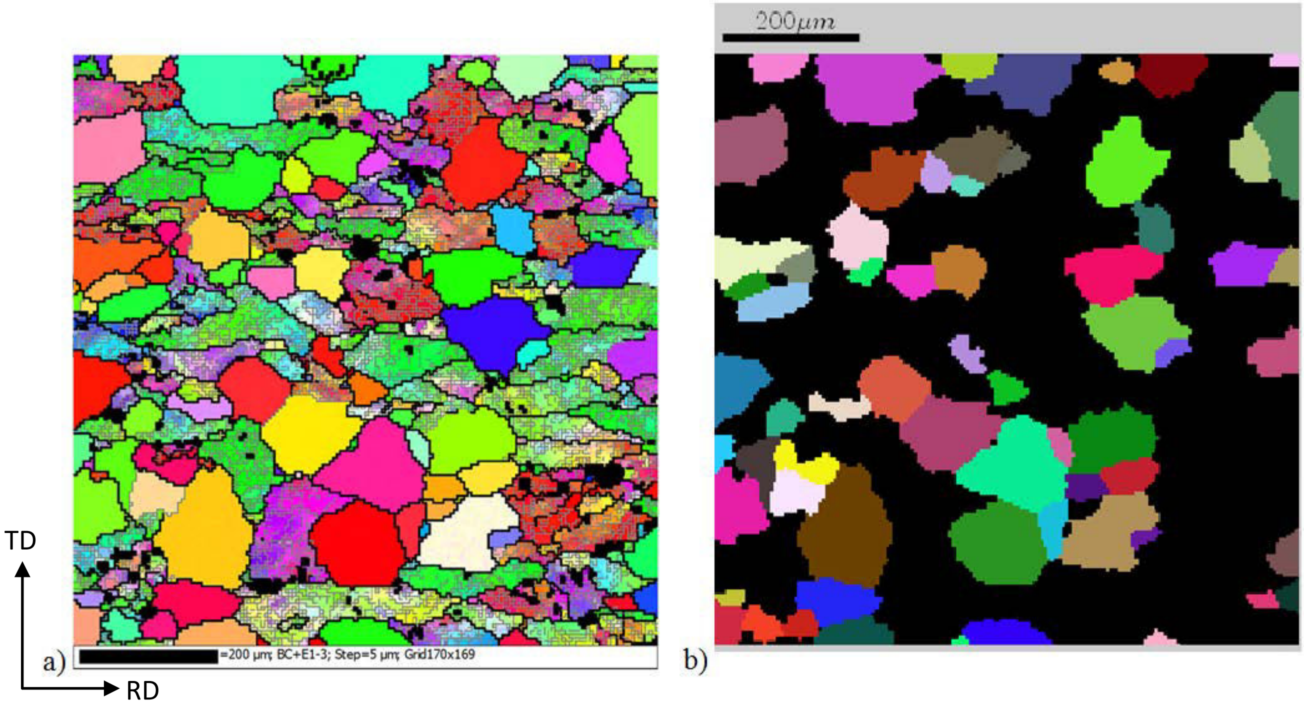

Fig. 53. a) Orientation map obtained on the RD/TD plane after annealing for 1213 h at 1150 °C. The map was taken with 5 µm stepsize and is displayed with IPF coloring along RD, with RD horizontal. b) Detection of recrystallized grains using the software DRG, covering a recrystallized fraction $X_{EBSD} = 0.41$.

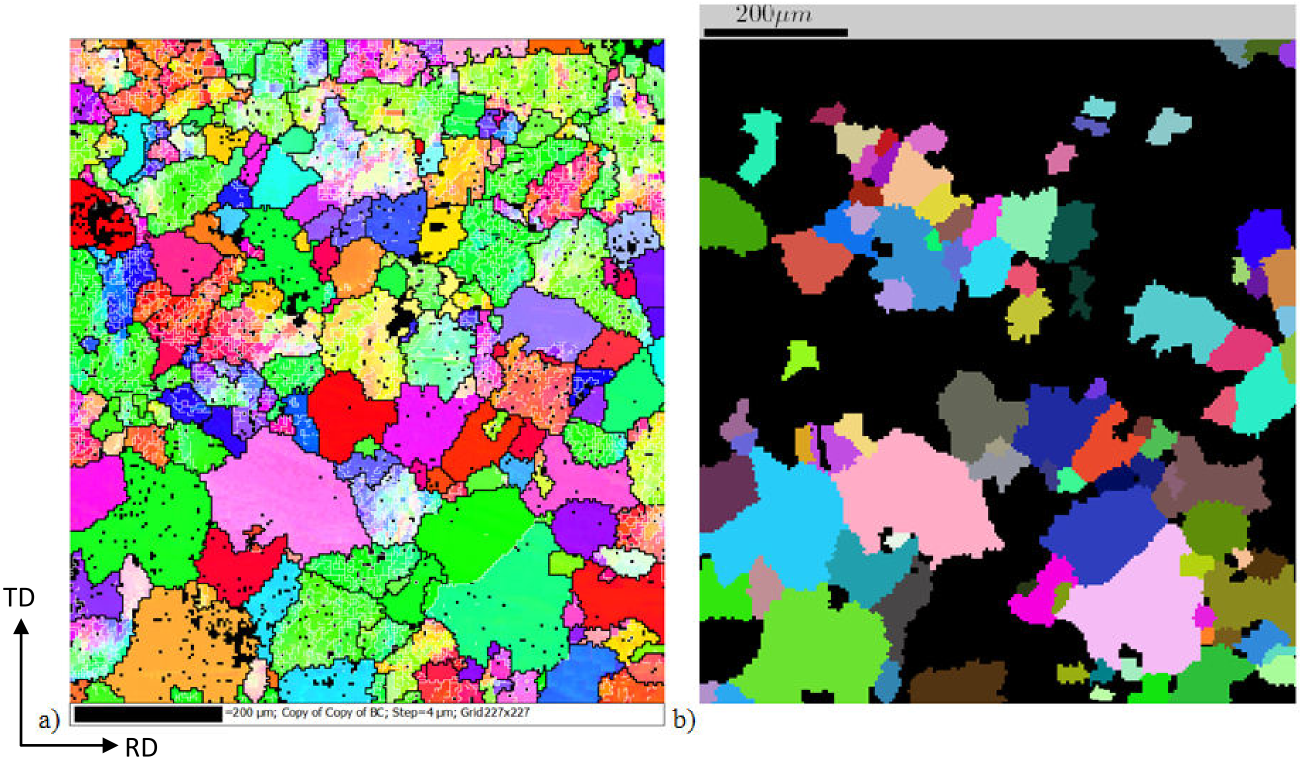

Fig. 54. a) Orientation map obtained on the RD/TD plane after annealing for 1373 h at 1150 °C. The map was taken with 4 µm stepsize and is displayed with IPF coloring along RD, with RD horizontal. b) Detection of recrystallized grains using the software DRG, covering a recrystallized fraction $X_{EBSD} = 0.44$.

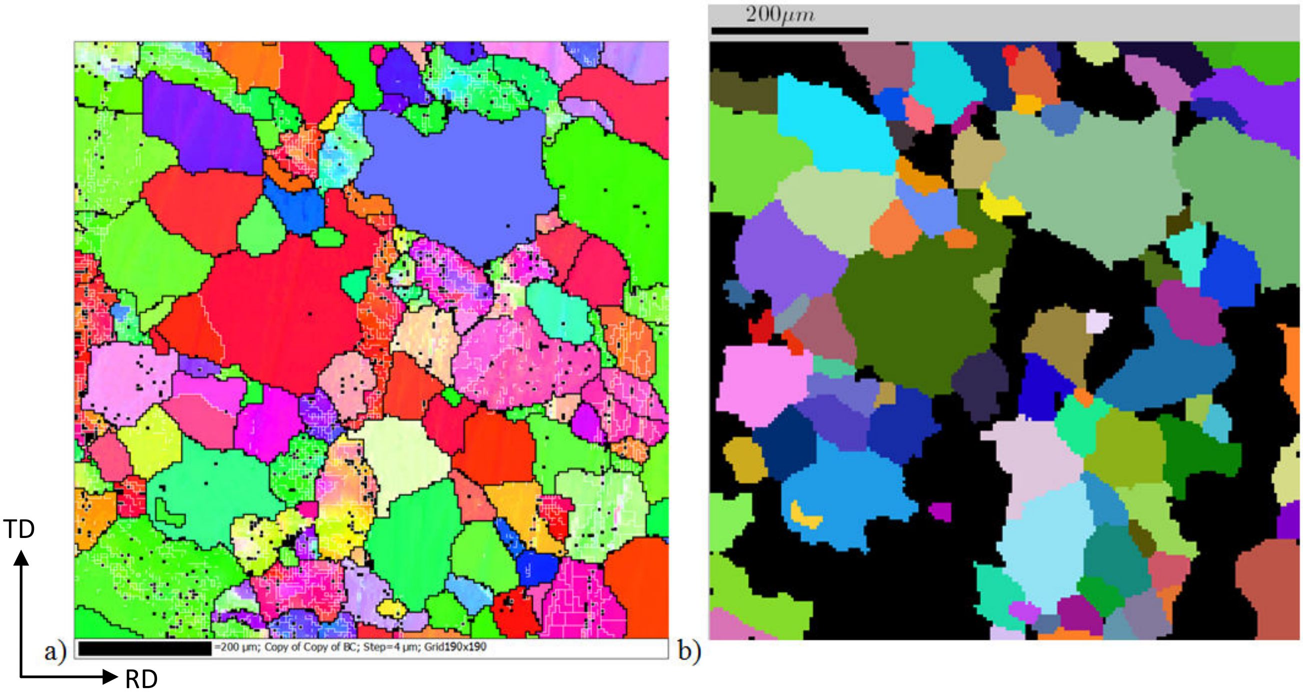

Fig. 55. a) Orientation map obtained on the RD/TD plane after annealing for 1582 h at 1150 °C. The map was taken with 4 µm stepsize and is displayed with IPF coloring along RD, with RD horizontal. b) Detection of recrystallized grains using the software DRG, covering a recrystallized fraction $X_{EBSD} = 0.69$.

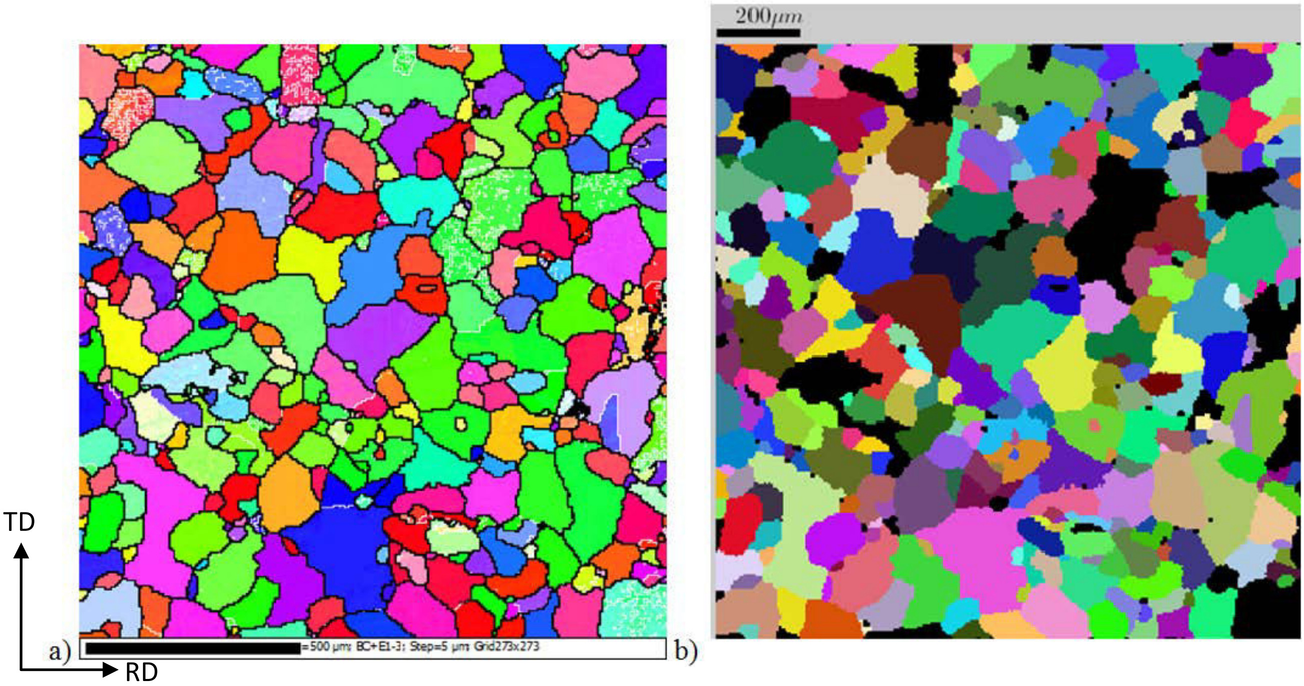

Fig. 56. a) Orientation map obtained on the RD/TD plane after annealing for 1900 h at 1150 °C. The map was taken with 5 µm stepsize and is displayed with IPF coloring along RD, with RD horizontal. b) Detection of recrystallized grains using the software DRG, covering a recrystallized fraction $X_{EBSD} = 0.86$.

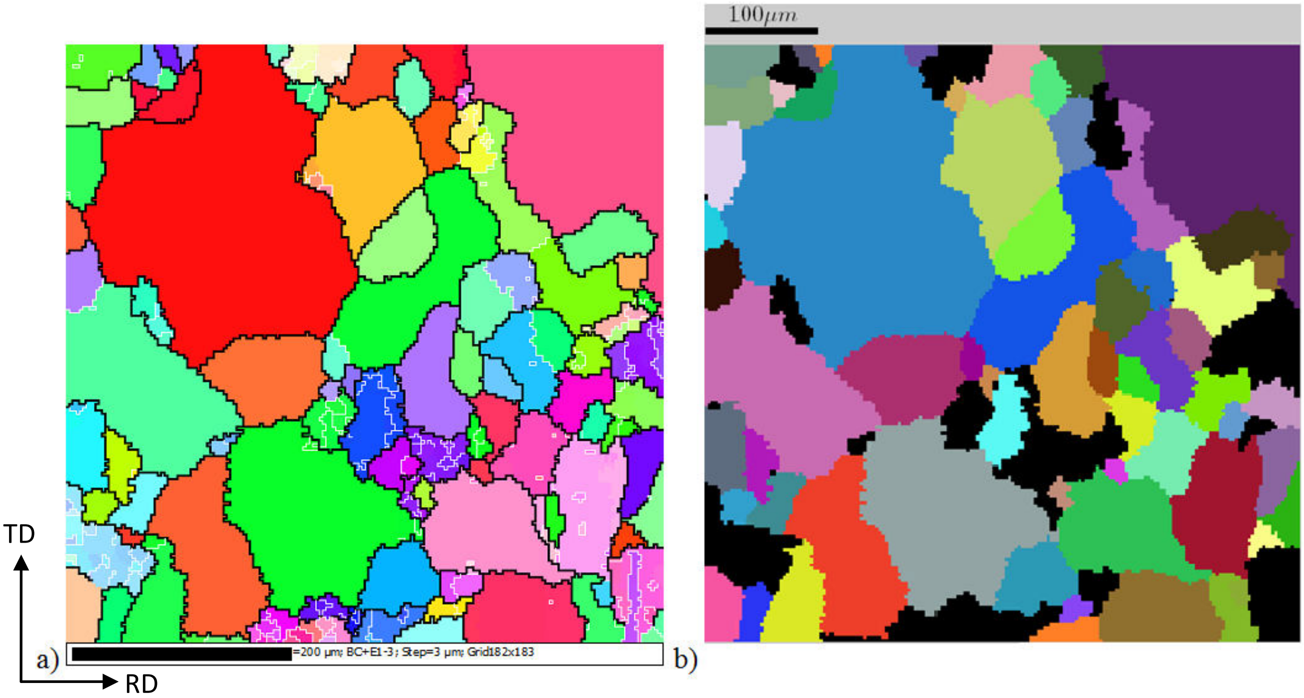

Fig. 57. a) Orientation map obtained on the RD/TD plane after annealing for 2200 h at 1150 °C. The map was taken with 3 µm stepsize and is displayed with IPF coloring along RD, with RD horizontal. b) Detection of recrystallized grains using the software DRG, covering a recrystallized fraction $X_{EBSD} = 0.90$. Note the higher magnification of this latter orientation map as compared to Fig. 56.

Table 15. Plate W67 in the as-received condition and after different annealing treatments at 1150 °C: mean chord length for all grains along the rolling $(\lambda_{HAB,RD})$ and transversal direction $(\lambda_{HAB,TD})$, specific surface density of high angle boundaries $(S_{v,HAB})$ in the RD/TD plane and recrystallized volume fractions X_{EBSD} and X_{HV} as obtained by EBSD and Vickers hardness measurements respectively. $S_{v,HAB}$ is calculated from the average chord lengths along both directions, namely $\overline{\lambda}_{LAB,RD}$ and $\overline{\lambda}_{LAB,TD}$

Annealing time at 1150 °C	$\overline{\lambda}_{HAB,RD}$ (µm)	$\overline{\lambda}_{HAB,TD}$ (µm)	$S_{V,HAB}$ (µm^{-1})	X_{EBSD}	X_{HV}
Warm-rolled W67	36	37	0.055	0	0
750 h	38	36	0.054	0.03	0
950 h	41	38	0.050	0.15	0.14
1213 h	49	46	0.042	0.41	0.37
1373 h	54	51	0.038	0.44	0.44
1582 h	66	59	0.032	0.69	0.61
1900 h	77	70	0.027	0.86	0.76
2200 h	81	74	0.026	0.90	0.85

One orientation map per annealing stage from 240 h to 600 h at 1200 °C is presented from Fig. 58 to Fig. 63. 240 h is the shortest annealing time for which orientation data were available after annealing at 1200 °C. Note that 240 h is very close to the incubation time of 232 h estimated with Vickers hardness in subchapter 4.1.3.

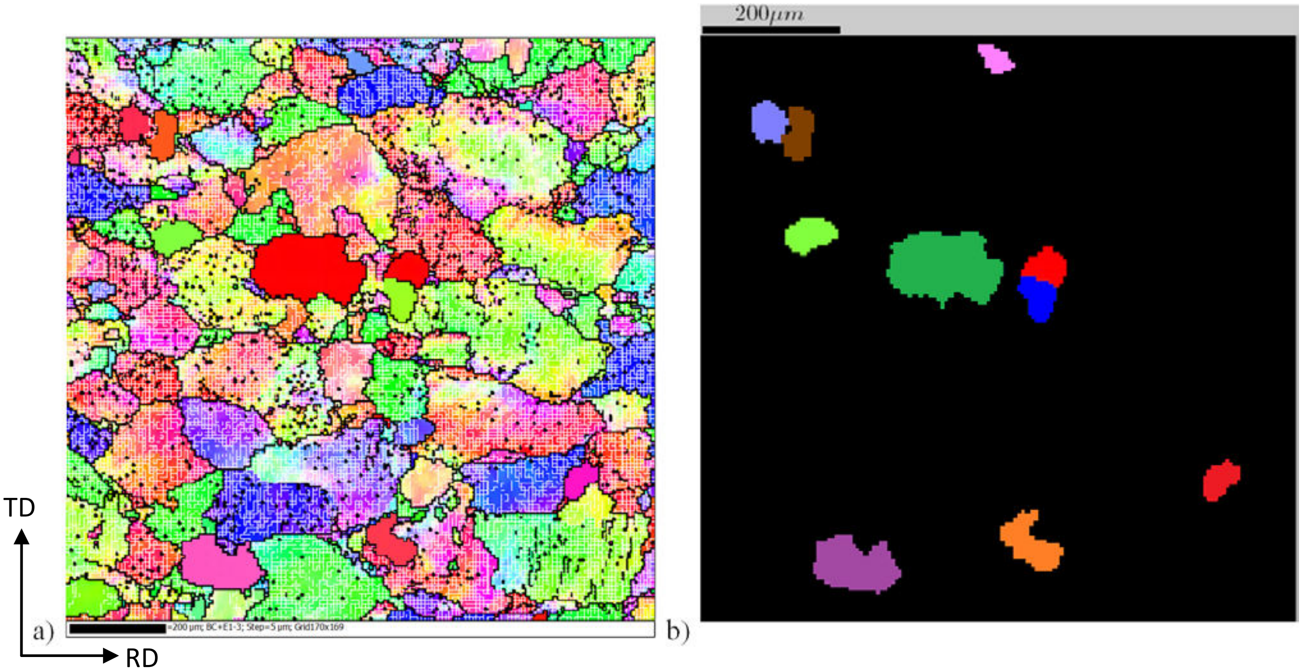

Fig. 58. a) Orientation map obtained on the RD/TD plane after annealing for 240 h at 1200 °C. The map was taken with 5 µm stepsize and is displayed with IPF coloring along RD, with RD horizontal. b) Detection of recrystallized grains using the software DRG, covering a recrystallized fraction $X_{EBSD} = 0.05$.

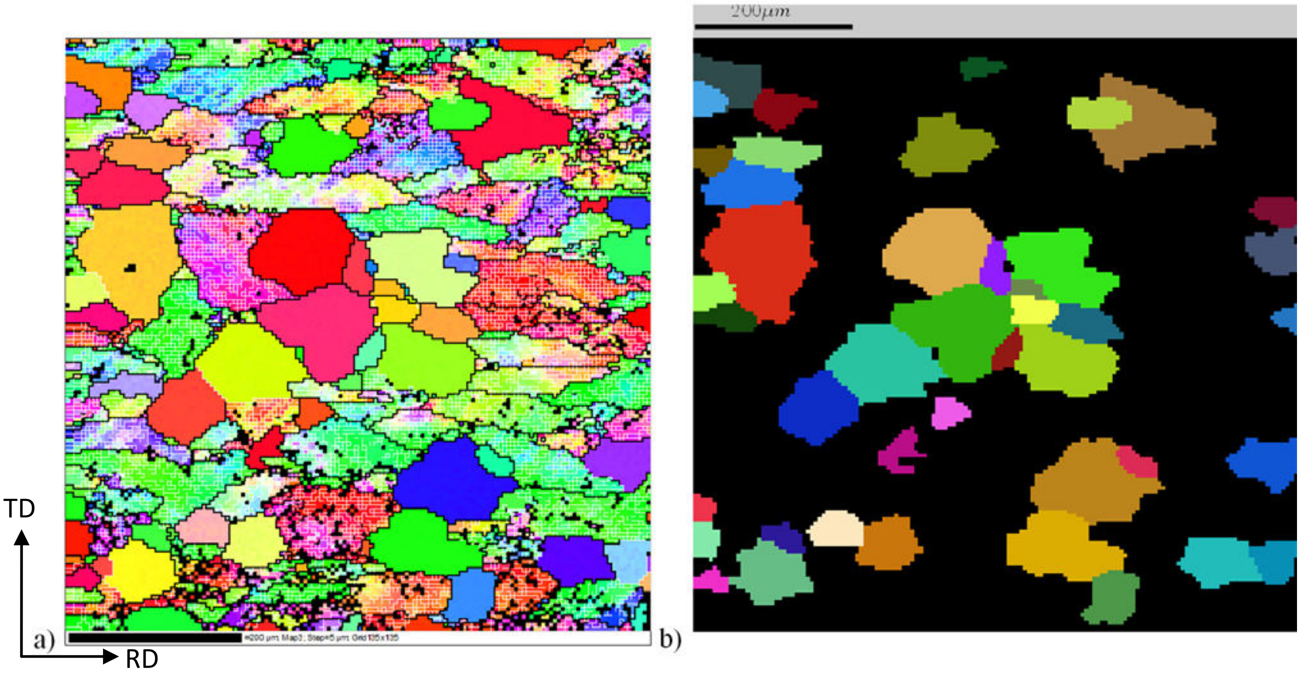

Fig. 59. a) Orientation map obtained on the RD/TD plane after annealing for 300 h at 1200 °C. The map was taken with 5 µm stepsize and is displayed with IPF coloring along RD, with RD horizontal. b) Detection of recrystallized grains using the software DRG, covering a recrystallized fraction $X_{EBSD} = 0.32$.

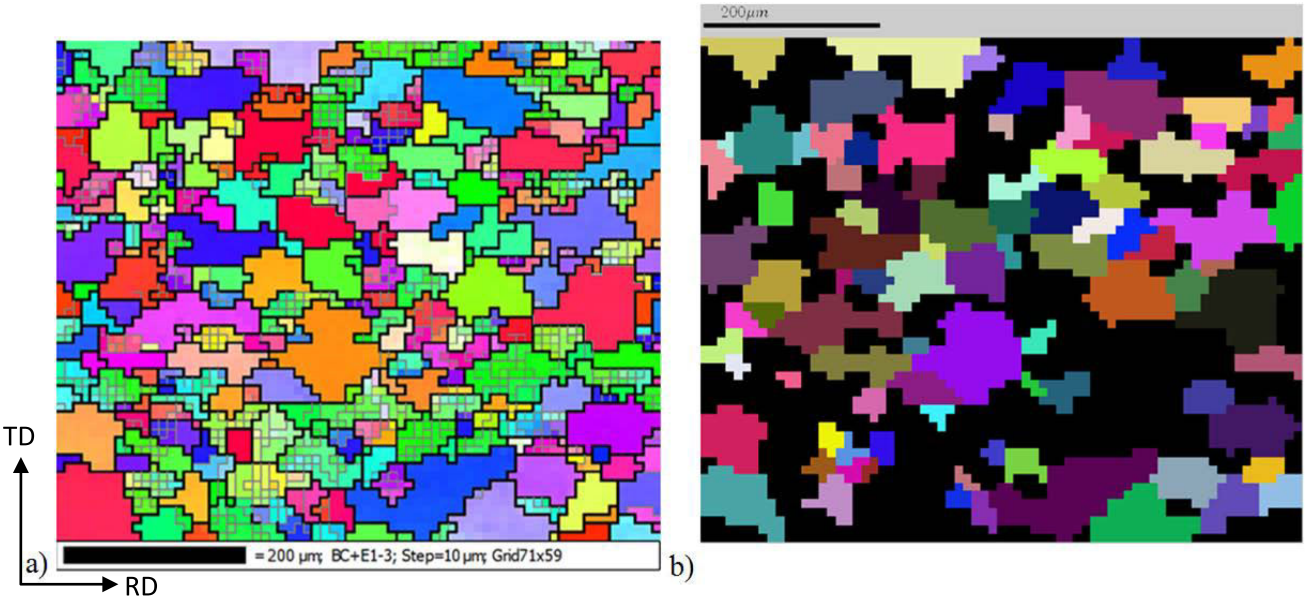

Fig. 60. a) Orientation map obtained on the RD/TD plane after annealing for 320 h at 1200 °C. The map was taken with 10 µm stepsize and is displayed with IPF coloring along RD, with RD horizontal. b) Detection of recrystallized grains using the software DRG, covering a recrystallized fraction $X_{EBSD} = 0.49$.

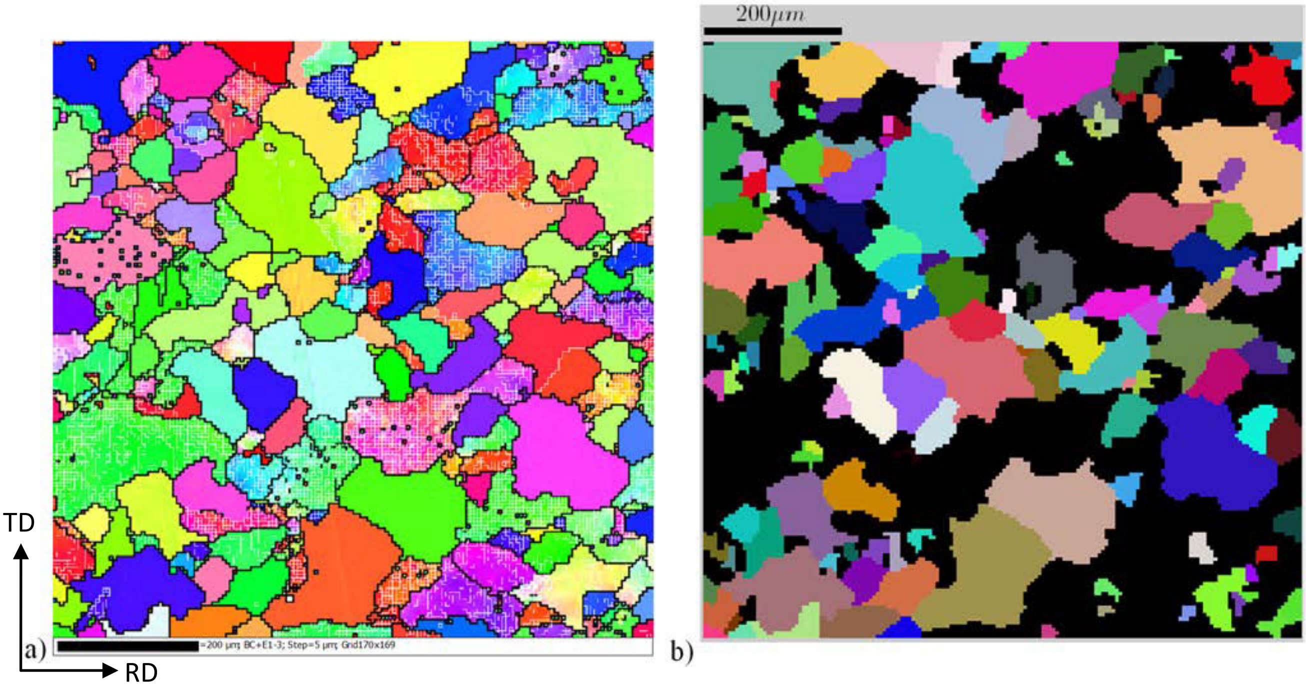

Fig. 61. a) Orientation map obtained on the RD/TD plane after annealing for 359 h at 1200 °C. The map was taken with 5 µm stepsize and is displayed with IPF coloring along RD, with RD horizontal. b) Detection of recrystallized grains using the software DRG, covering a recrystallized fraction $X_{EBSD} = 0.58$.

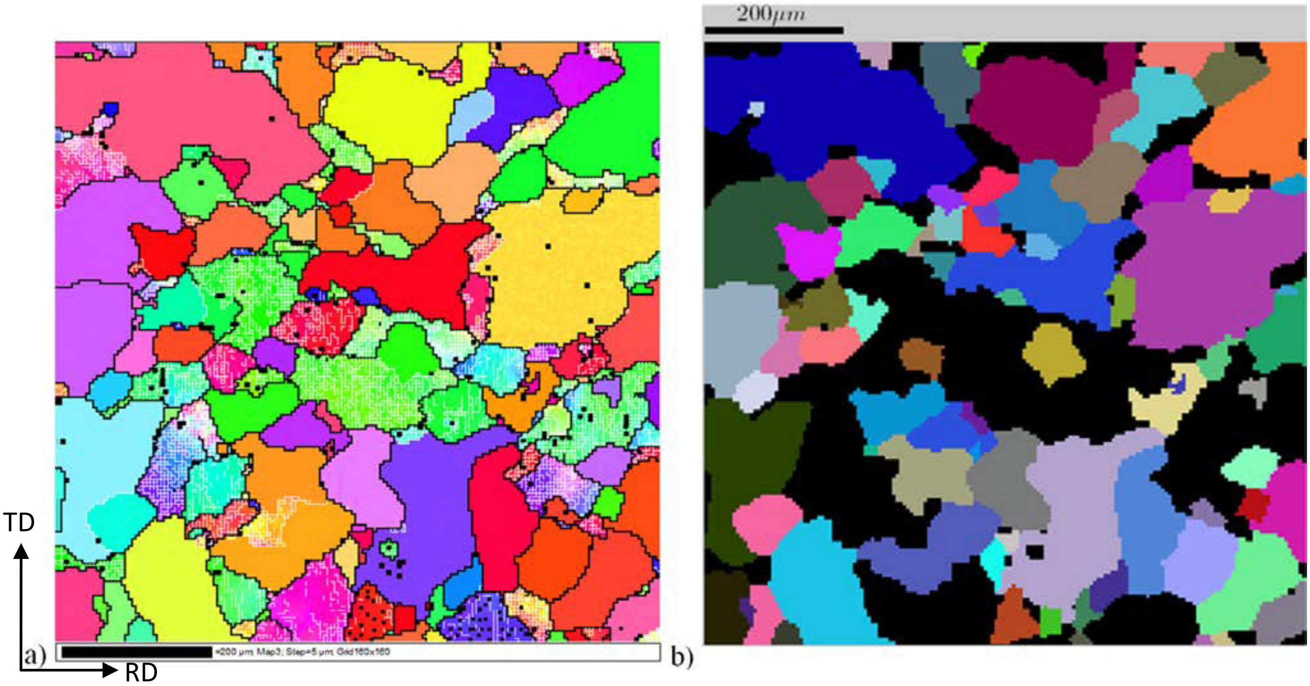

Fig. 62. a) Orientation map obtained on the RD/TD plane after annealing for 480 h at 1200 °C. The map was taken with 5 µm stepsize and is displayed with IPF coloring along RD, with RD horizontal. b) Detection of recrystallized grains using the software DRG, covering a recrystallized fraction $X_{EBSD} = 0.77$.

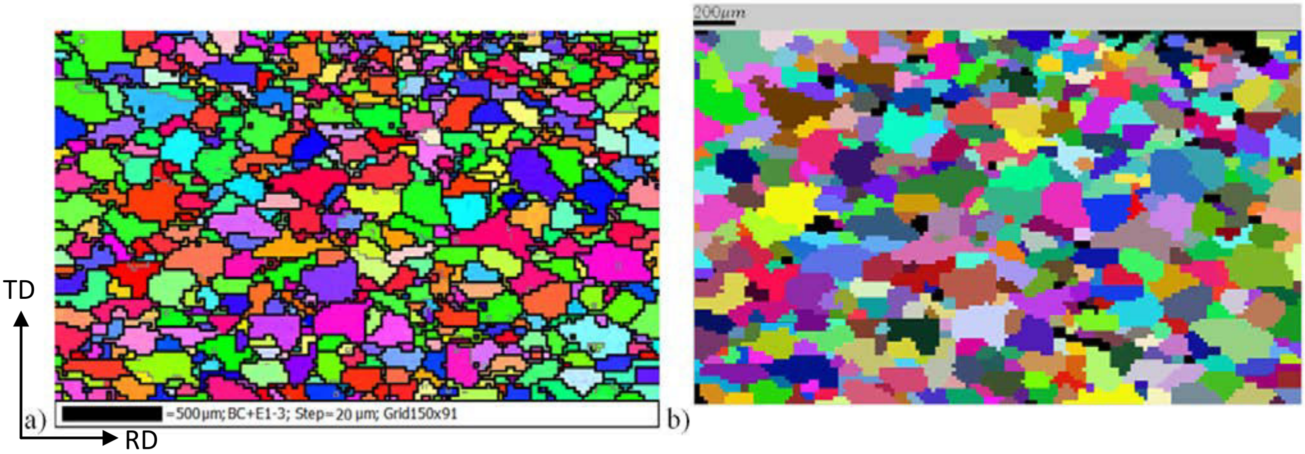

Fig. 63. a) Orientation map obtained on the RD/TD plane after annealing for 600 h at 1200 °C. The map was taken with 20 µm stepsize and is displayed with IPF coloring along RD, with RD horizontal. b) Detection of recrystallized grains using the software DRG, covering a recrystallized fraction $X_{EBSD} = 0.97$.

Table 16: Plate W67 in the as-received condition and after different annealing treatments at 1200 °C: mean chord length for all grains along rolling and transversal direction, specific surface density of high angle boundaries in the RD/TD plane and recrystallized volume fractions as obtained by EBSD and Vickers hardness measurements. $S_{v,HAB}$ is calculated from the average chord lengths along both directions, namely $\overline{\lambda}_{LAB,RD}$ and $\overline{\lambda}_{LAB,TD}$

Annealing time at 1200 °C	$\overline{\lambda}_{HAB,RD}$ (µm)	$\overline{\lambda}_{HAB,TD}$ (µm)	$S_{V,HAB}$ (μm^{-1})	X_{EBSD}	X_{HV}
Warm-rolled W67	36	37	0.055	0	0
240 h	37	35	0.055	0.05	0
300 h	45	36	0.050	0.32	0.39
320 h	48	43	0.044	0.49	0.47
359 h	53	45	0.041	0.58	0.59
480 h	75	69	0.028	0.77	0.87
600 h	105	94	0.021	0.97	0.99

One orientation map per annealing stage from 6 h to 110 h at 1250 °C is presented from Fig. 64 to Fig. 70. 24.5 h at 1250 °C was the estimated incubation time by Vickers hardness in subchapter 4.1.3.

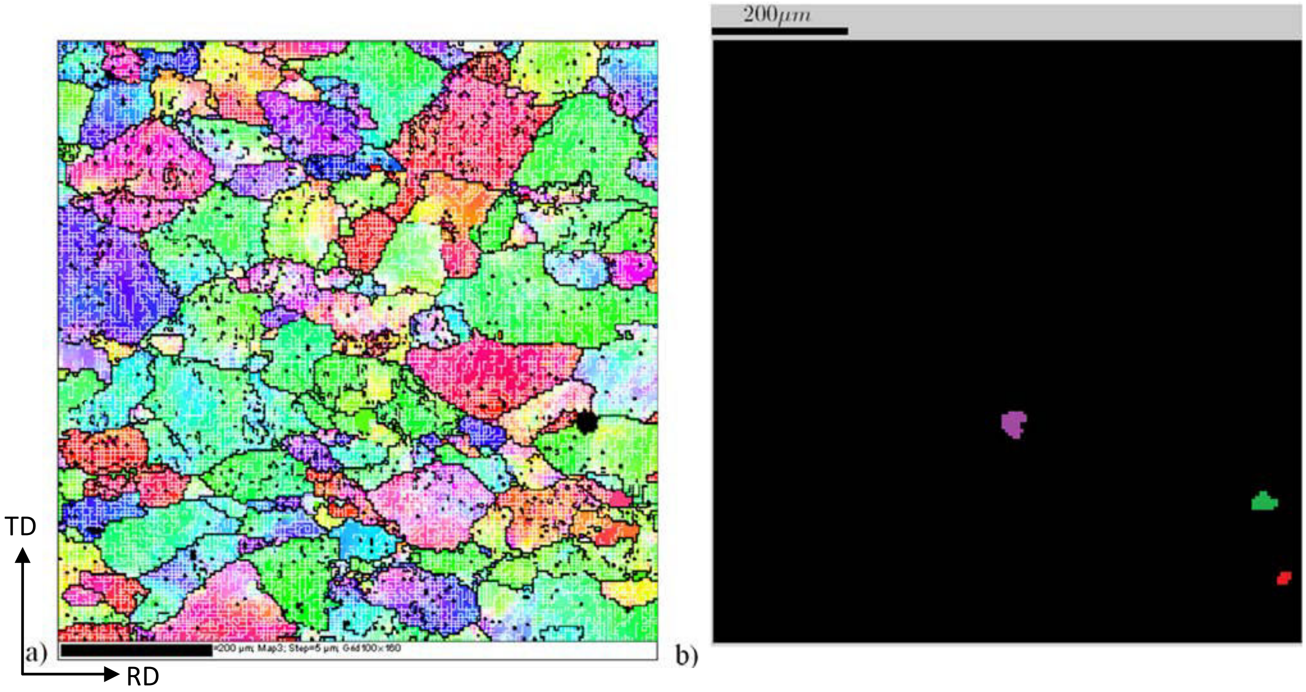

Fig. 64. a) Orientation map obtained on the RD/TD plane after annealing for 6 h at 1250 °C. The map was taken with 5 µm stepsize and is displayed with IPF coloring along RD, with RD horizontal. b) Detection of recrystallized grains using the software DRG, covering a recrystallized fraction $X_{EBSD} = 0.003$.

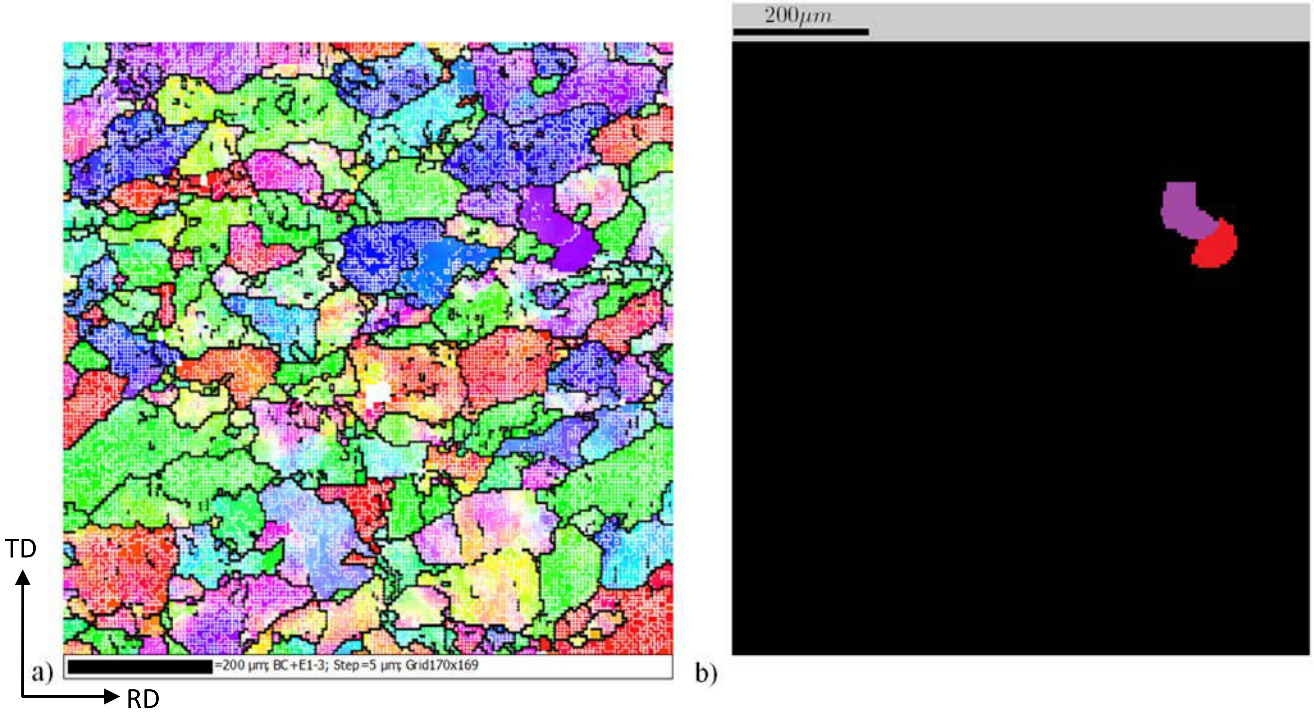

Fig. 65. a) Orientation map obtained on the RD/TD plane after annealing for 12 h at 1250 °C. The map was taken with 5 µm stepsize and is displayed with IPF coloring along RD, with RD horizontal. b) Detection of recrystallized grains using the software DRG, covering a recrystallized fraction $X_{EBSD} = 0.01$.

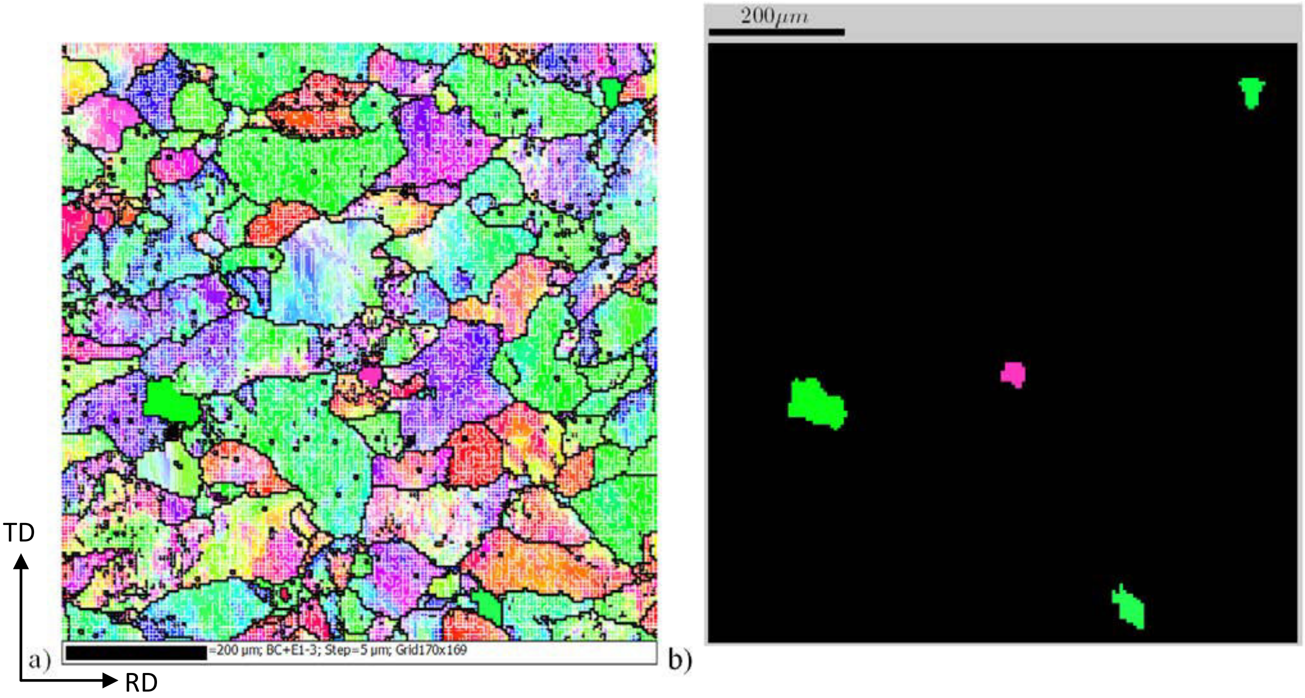

Fig. 66. a) Orientation map obtained on the RD/TD plane after annealing for 24 h at 1250 °C. The map was taken with 5 µm stepsize and is displayed with IPF coloring along RD, with RD horizontal. b) Detection of recrystallized grains using the software DRG, covering a recrystallized fraction $X_{EBSD} = 0.01$.

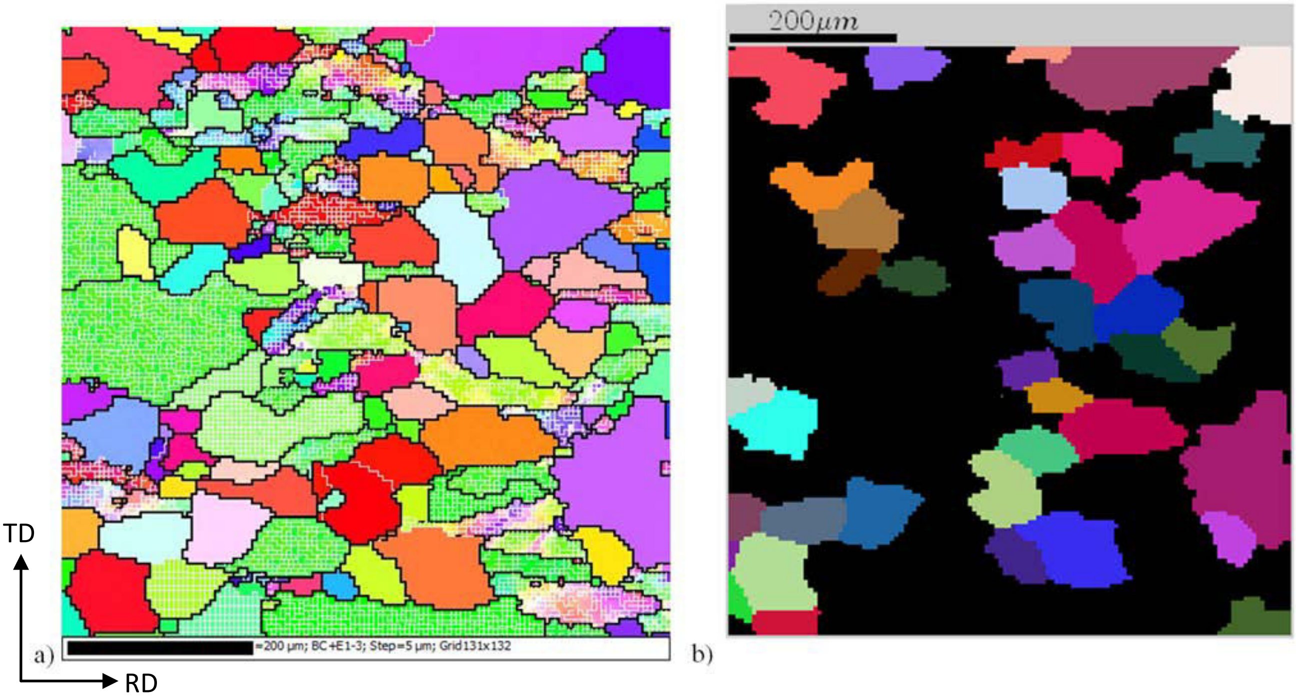

Fig. 67. a) Orientation map obtained on the RD/TD plane after annealing for 36 h at 1250 °C. The map was taken with 5 µm stepsize and is displayed with IPF coloring along RD, with RD horizontal. b) Detection of recrystallized grains using the software DRG, covering a recrystallized fraction $X_{EBSD} = 0.39$.

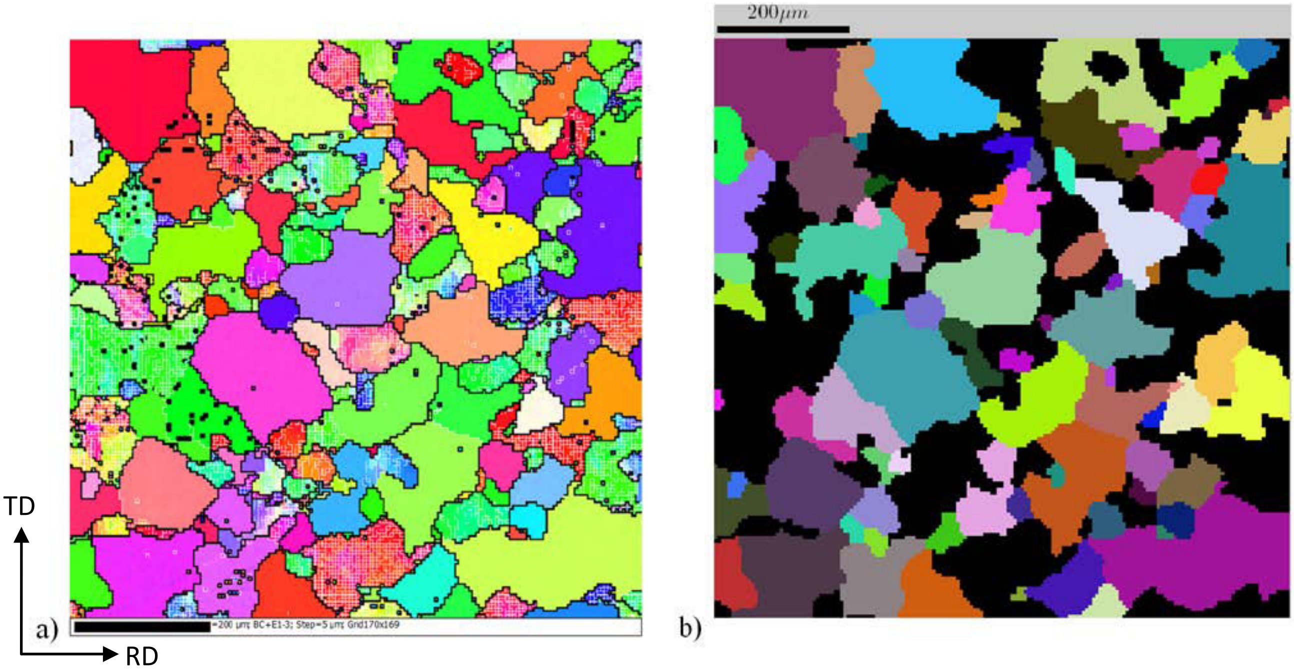

Fig. 68. a) Orientation map obtained on the RD/TD plane after annealing for 48 h at 1250 °C. The map was taken with 5 μm stepsize and is displayed with IPF coloring along RD, with RD horizontal. b) Detection of recrystallized grains using the software DRG, covering a recrystallized fraction $X_{EBSD} = 0.68$.

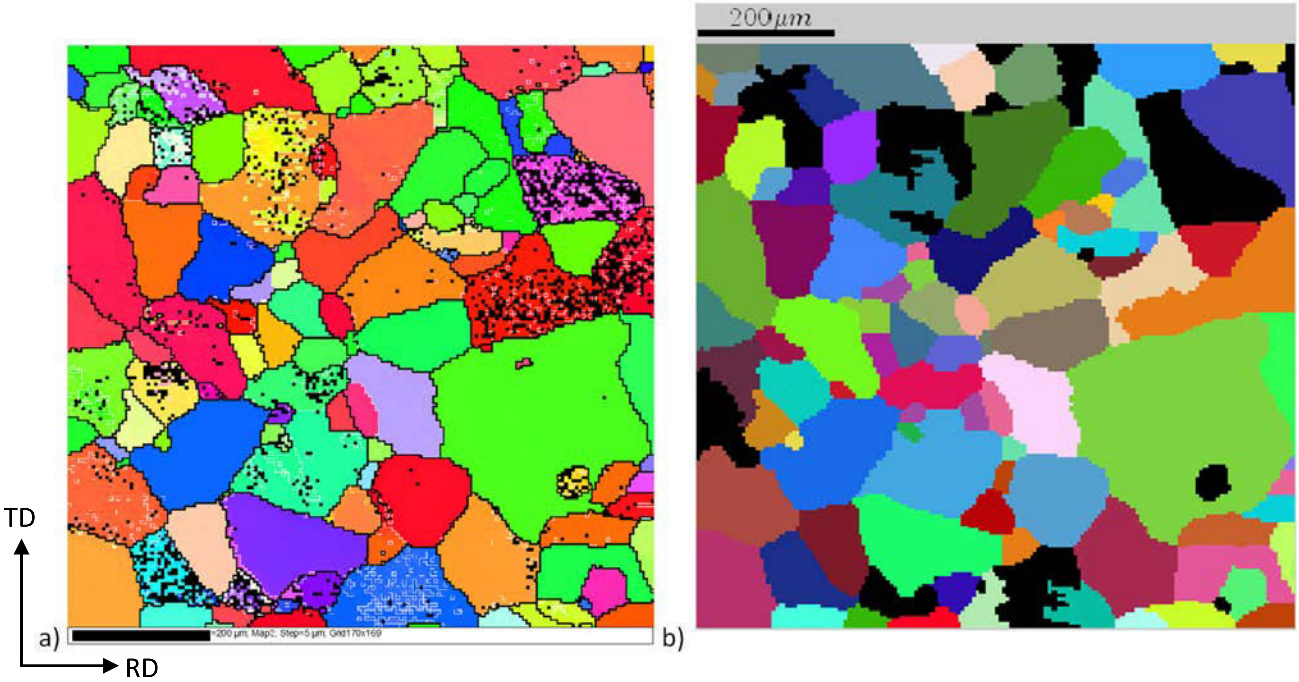

Fig. 69. a) Orientation map obtained on the RD/TD plane after annealing for 72 h at 1250 °C. The map was taken with 5 μm stepsize and is displayed with IPF coloring along RD, with RD horizontal. b) Detection of recrystallized grains using the software DRG, covering a recrystallized fraction $X_{EBSD} = 0.83$.

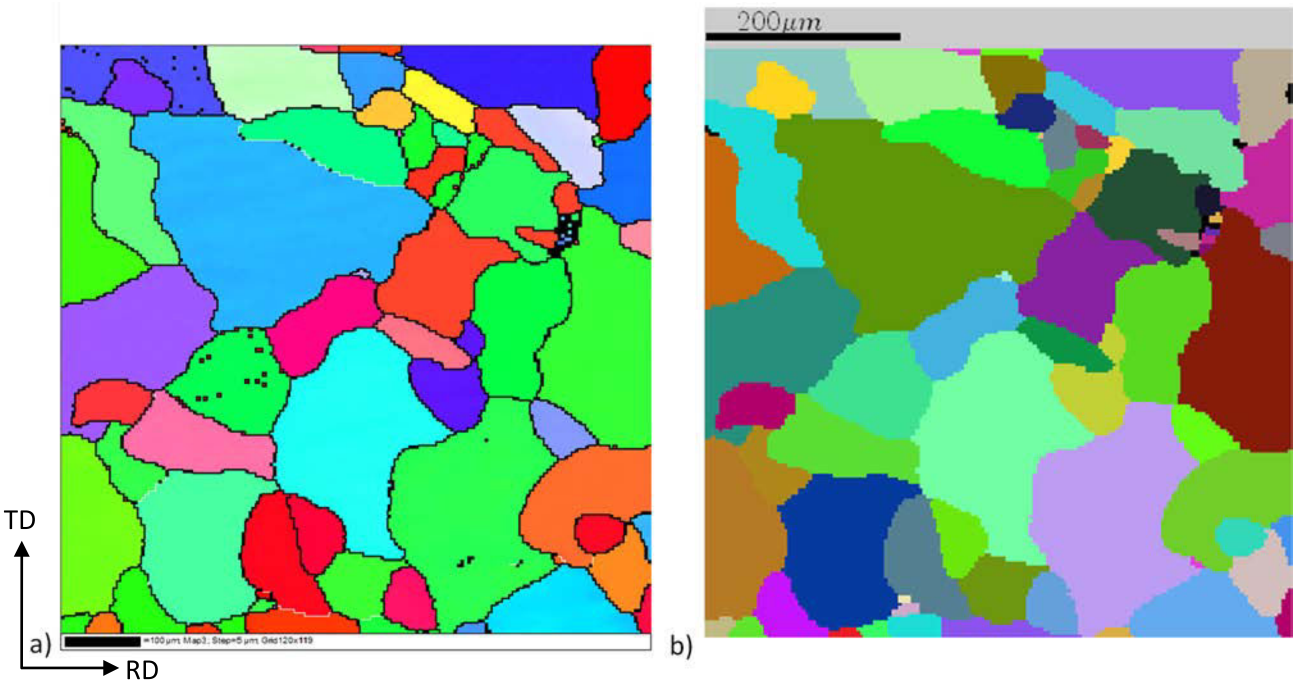

Fig. 70. a) Orientation map obtained on the RD/TD plane after annealing for 110 h at 1250 °C. The map was taken with 5 µm stepsize and is displayed with IPF coloring along RD, with RD horizontal. b) Detection of recrystallized grains using the software DRG, covering a recrystallized fraction $X_{EBSD} = 0.99$.

Table 17. Plate W67 in the as-received condition and after different annealing treatments at 1250 °C: mean chord length for all grains along rolling and transversal direction, specific surface density of high angle boundaries $(S_{v,HAB})$ in the RD/TD plane and recrystallized volume fractions as obtained by EBSD and Vickers hardness measurements. $S_{v,HAB}$ is calculated from the average chord lengths along both directions, namely $\overline{\lambda}_{LAB,RD}$ and $\overline{\lambda}_{LAB,TD}$.

Annealing time at 1250 °C	$\overline{\lambda}_{HAB,RD}$ (μm)	$\overline{\lambda}_{HAB,TD}$ (μm)	$S_{V,HAB}$ (μm^{-1})	X_{EBSD}	X_{HV}
Warm-rolled W67	36	37	0.055	0	0
6 h	36	33	0.058	0	0
12 h	34	32	0.060	0.01	0
24 h	37	39	0.052	0.01	0
36 h	36	32	0.059	0.39	0.39
48 h	50	48	0.041	0.68	0.61
72 h	68	62	0.031	0.83	0.87
110 h	87	81	0.024	0.99	0.99

As observed from the tables (Table 15, Table 16, Table 17) and the EBSD orientation maps (Fig. 51 to Fig. 70 obtained on the RD/TD section) during isothermal recrystallization annealing in the range 1150-1250 °C the nearly equiaxed warm-rolled grain structure of the plate W67 in the as-received state (36 μm x 37 μm) is replaced by new, also equiaxed, recrystallized grains which become larger than those in the as-received state (e.g up to 105 μm x 94 μm after annealing at 1200 °C for 600 h). It may be possible that, for annealing at 1250 °C, grain growth has already occurred, since after annealing at 72 h most grains have already impinged, yet an increase in recrystallized grain size is still observed after annealing at 110 h. Consequently, recrystallization at all temperatures leads to a reduction of specific surface density $S_{V,HAB}$ of high angle boundaries and an increase in grain size for the plate W67.

5.3.2 Highly-rolled plate (W90)

EBSD maps at the different recrystallization stages were obtained for the plate W90 after annealing at 1200 °C. The maps were obtained with a stepsize ranging from 3-15 µm. The smaller stepsizes were used for intercept length studies, while the bigger stepsizes were used for texture studies. The maps for the plate W90 were taken on the transversal plane (RD/ND), in contrast to the maps for the plate W67, which were taken on the rolling plane (RD/TD). The reason for this change is that, in this way, the surface on which the Vickers hardness measurements were made corresponds to the mapped EBSD section for each plate. This allows a better correlation between the hardness evolution and the microstructural evolution.

Additionally, each of the EBSD orientation maps was analyzed using the software DRG (see experimental details subchapter 3.1), from which the recrystallized fraction X_{EBSD} was obtained. The recrystallized grains map obtained using the software DRG is shown next to each orientation map for comparison. The recrystallization-related parameters obtained from the orientation maps are compiled in Table 18 for annealing of the plate W90 at 1200 °C.

One orientation map per annealing stage from 5.5 h to 25 h at 1200 °C is presented from Fig. 71 to Fig. 81. The sample annealed for 5.5 h corresponds to the shortest available annealing time, which is right before the incubation time of 7 h estimated by Vickers hardness in subchapter 4.2.3.

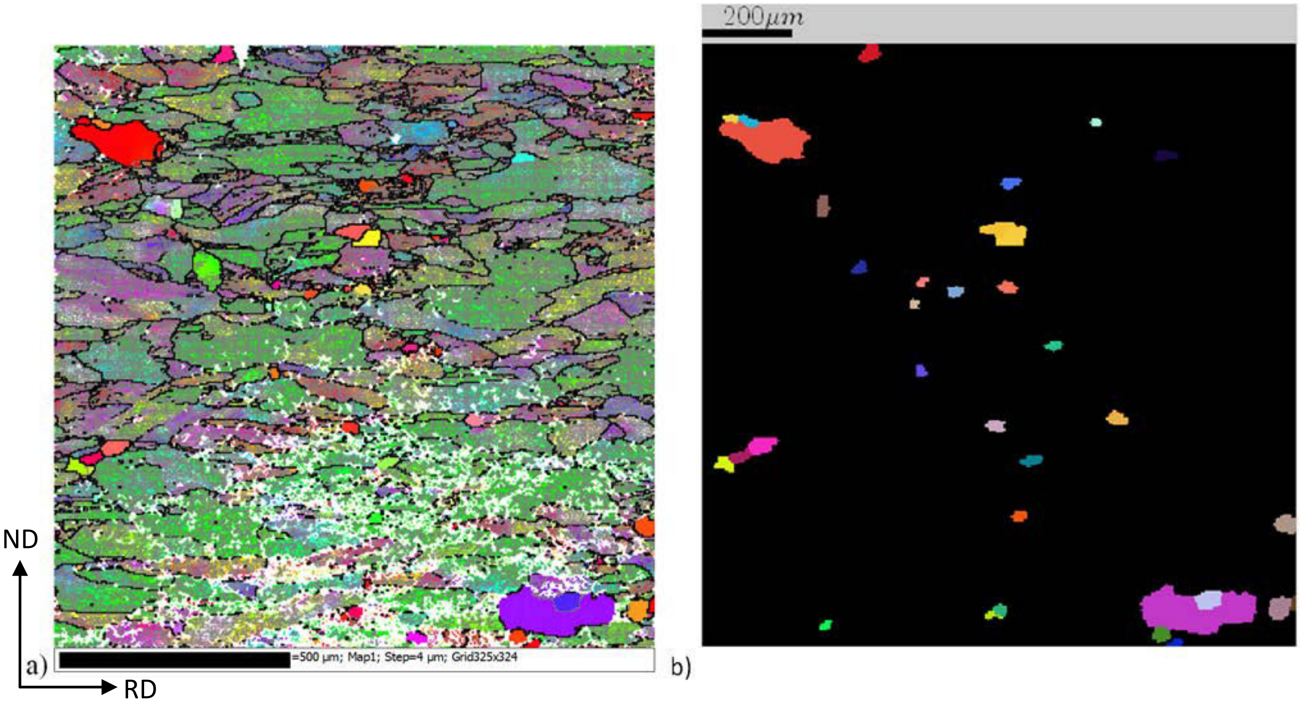

Fig. 71. a) Orientation map obtained on the RD/ND plane after annealing for 5.5 h at 1200 °C. The map was taken with 4 µm stepsize and is displayed with IPF coloring along RD, with RD horizontal. b) Detection of recrystallized grains using the software DRG, covering a recrystallized fraction $X_{EBSD} = 0.03$

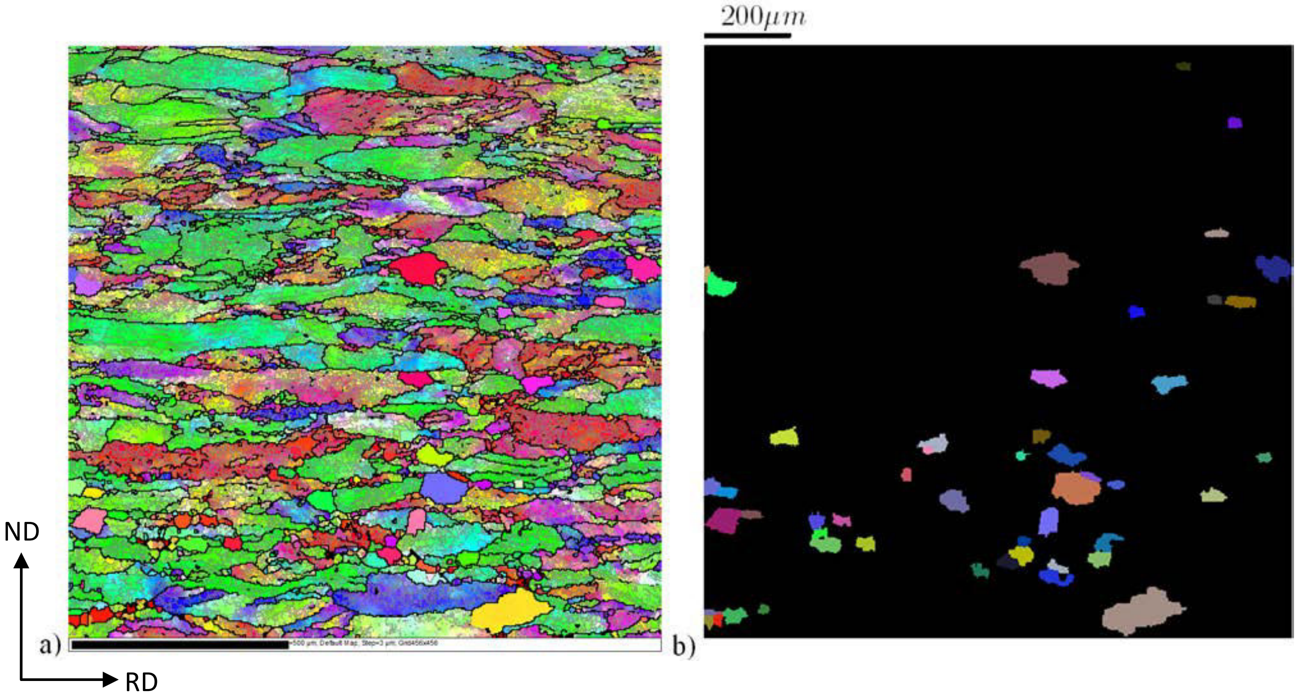

Fig. 72. a) Orientation map obtained on the RD/ND plane after annealing for 7 h at 1200 °C. The map was taken with 3 μm stepsize and is displayed with IPF coloring along RD, with RD horizontal. b) Detection of recrystallized grains using the software DRG, covering a recrystallized fraction $X_{EBSD} = 0.05$.

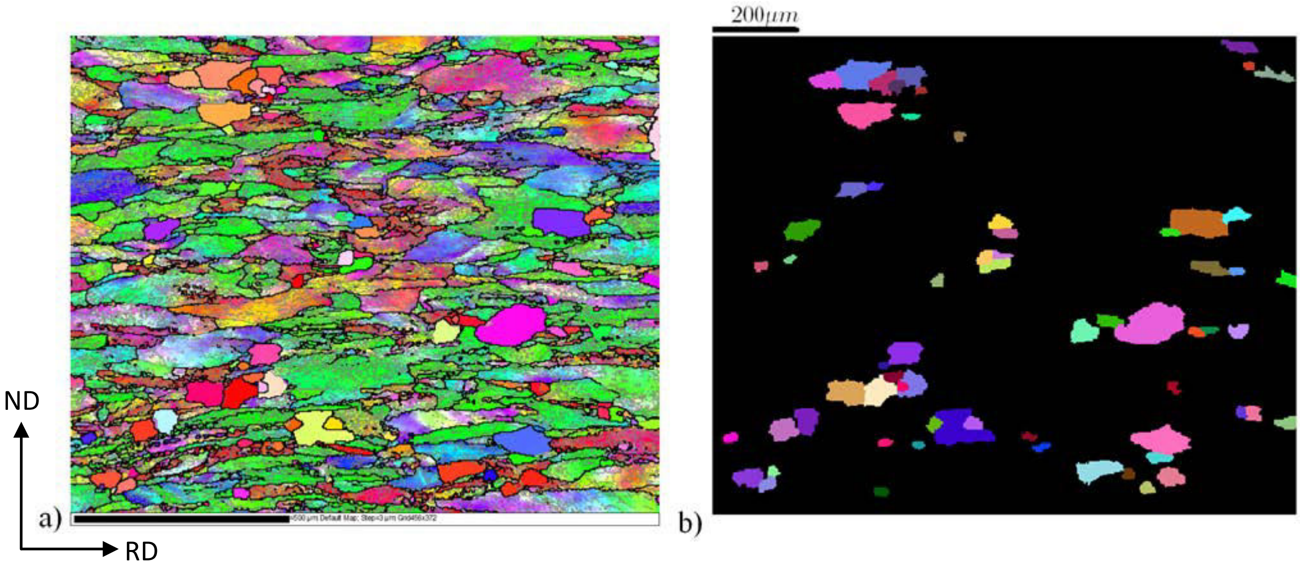

Fig. 73. a) Orientation map obtained on the RD/ND plane after annealing for 8 h at 1200 °C. The map was taken with 3 μm stepsize and is displayed with IPF coloring along RD, with RD horizontal. b) Detection of recrystallized grains using the software DRG, covering a recrystallized fraction $X_{EBSD} = 0.08$.

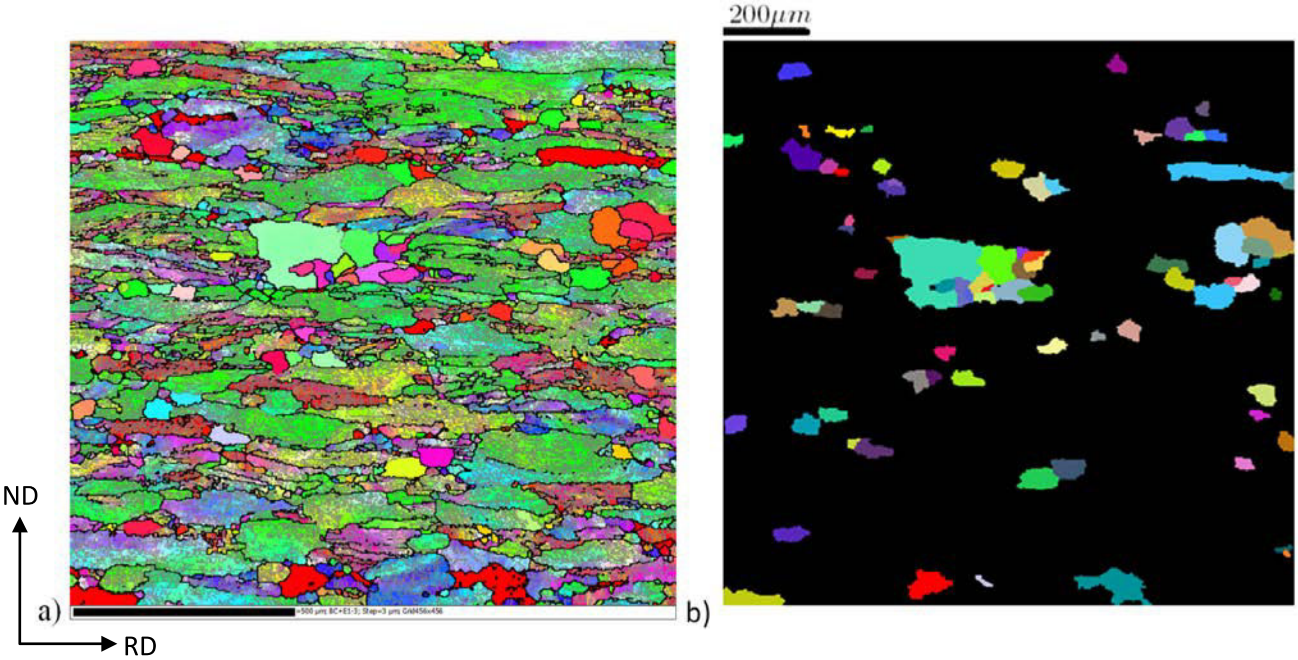

Fig. 74. a) Orientation map obtained on the RD/ND plane after annealing for 8.5 h at 1200 °C. The map was taken with 3 µm stepsize and is displayed with IPF coloring along RD, with RD horizontal. b) Detection of recrystallized grains using the software DRG, covering a recrystallized fraction $X_{EBSD} = 0.09$.

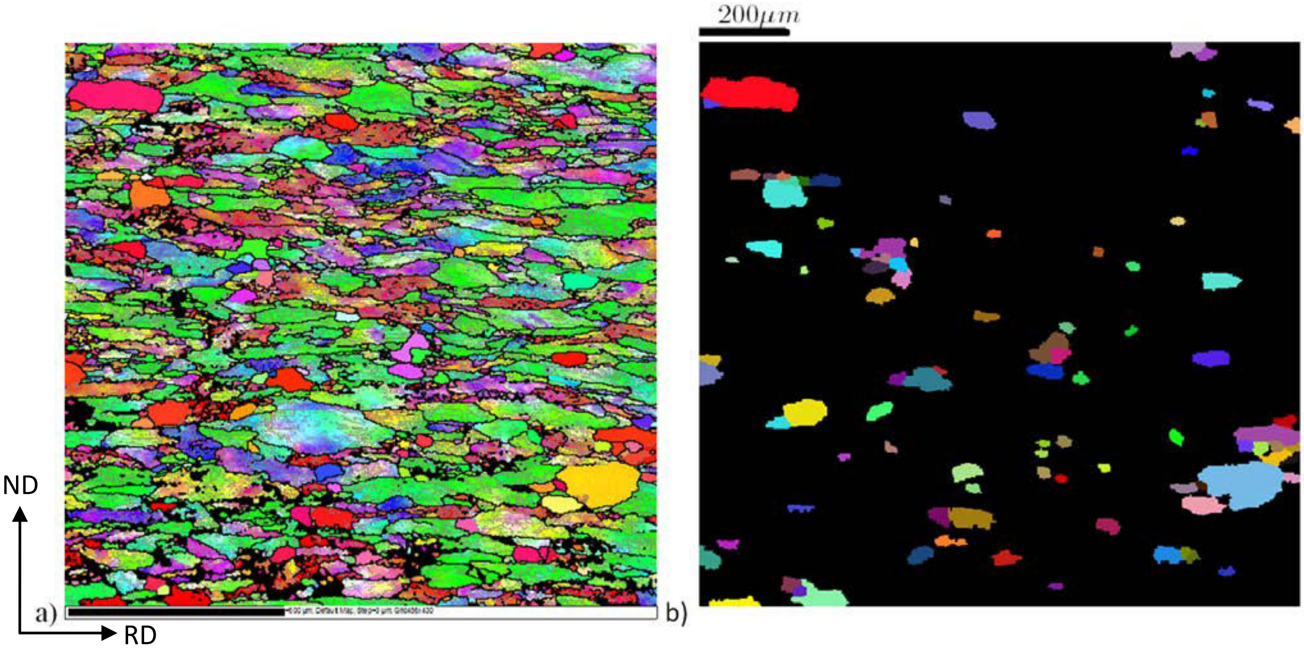

Fig. 75. a) Orientation map obtained on the RD/ND plane after annealing for 9 h at 1200 °C. The map was taken with 3 µm stepsize and is displayed with IPF coloring along RD, with RD horizontal. B) Detection of recrystallized grains using the software DRG, covering a recrystallized fraction $X_{EBSD} = 0.10$.

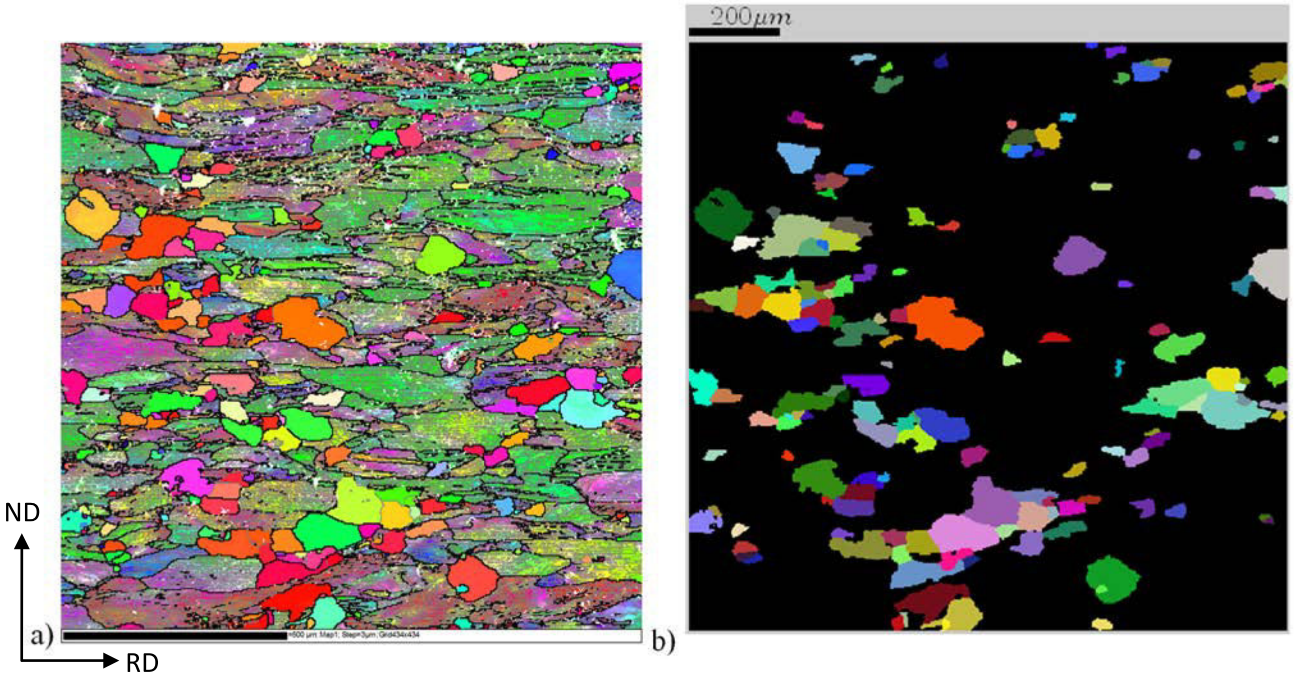

Fig. 76. a) Orientation map obtained on the RD/ND plane after annealing for 10 h at 1200 °C. The map was taken with 3 μm stepsize and is displayed with IPF coloring along RD, with RD horizontal. b) Detection of recrystallized grains using the software DRG, covering a recrystallized fraction $X_{EBSD} = 0.18$

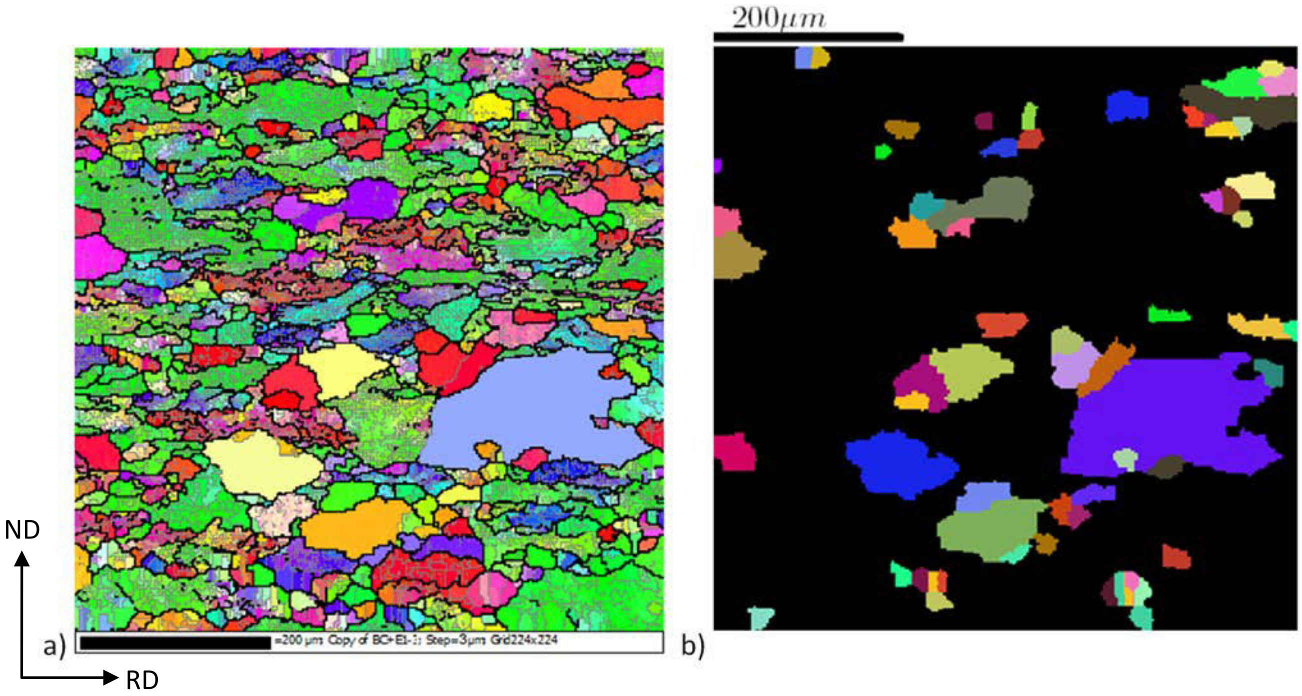

Fig. 77. a) Orientation map obtained on the RD/ND plane after annealing for 11 h at 1200 °C. The map was taken with 3 μm stepsize and is displayed with IPF coloring along RD, with RD horizontal. b) Detection of recrystallized grains using the software DRG, covering a recrystallized fraction $X_{EBSD} = 0.29$

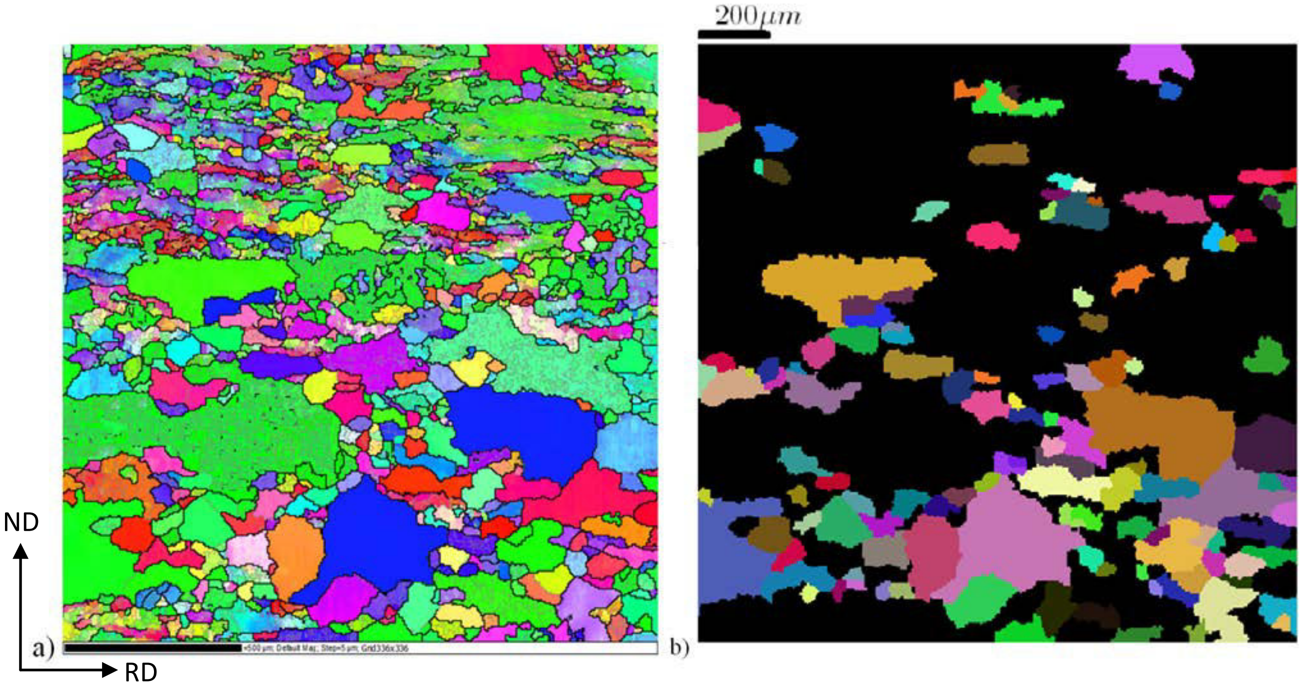

Fig. 78. a) Orientation map obtained on the RD/ND plane after annealing for 13 h at 1200 °C. The map was taken with 5 µm stepsize and is displayed with IPF coloring along RD, with RD horizontal. b) Detection of recrystallized grains using the software DRG, covering a recrystallized fraction $X_{EBSD} = 0.41$.

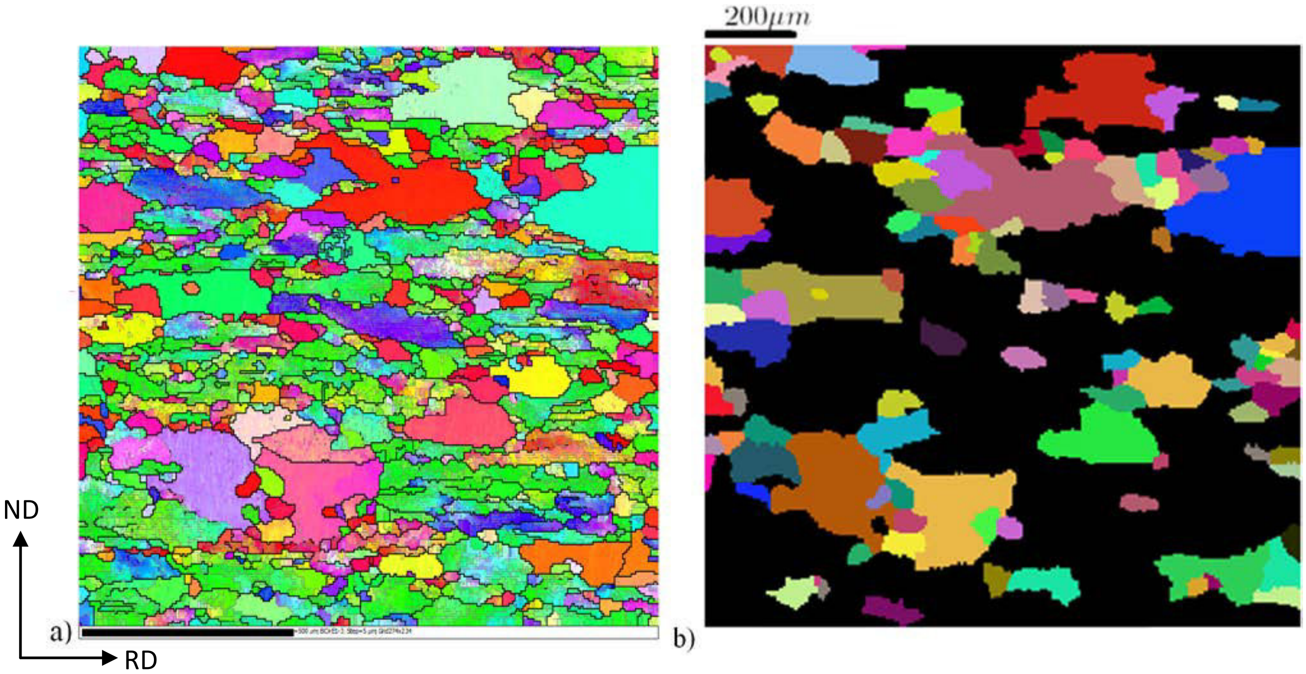

Fig. 79. a) Orientation map obtained on the RD/ND plane after annealing for 15 h at 1200 °C. The map was taken with 5 µm stepsize and is displayed with IPF coloring along RD, with RD horizontal. b) Detection of recrystallized grains using the software DRG, covering a recrystallized fraction $X_{EBSD} = 0.52$.

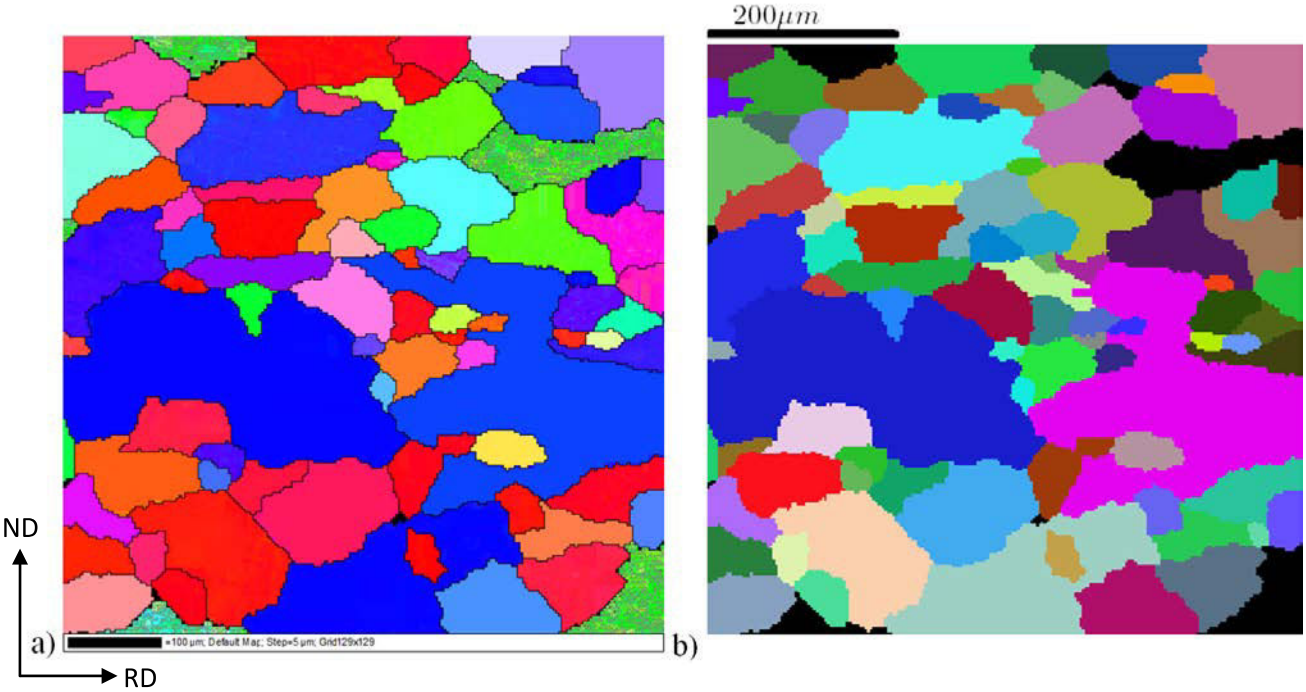

Fig. 80. a) Orientation map obtained on the RD/ND plane after annealing for 20 h at 1200 °C. The map was taken with 5 µm stepsize and is displayed with IPF coloring along RD, with RD horizontal. b) Detection of recrystallized grains using the software DRG, covering a recrystallized fraction $X_{EBSD} = 0.93$.

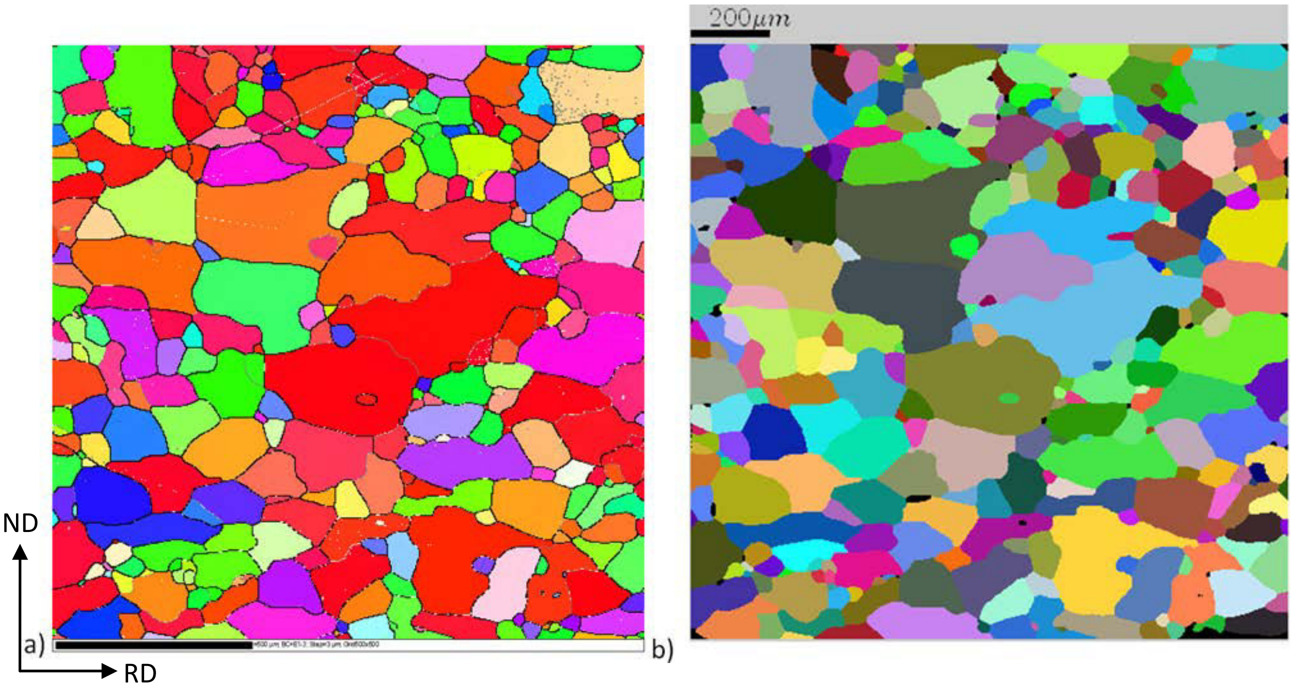

Fig. 81. a) Orientation map obtained on the RD/ND plane after annealing for 25 h at 1200 °C. The map was taken with 3 µm stepsize and is displayed with IPF coloring along RD, with RD horizontal. b) Detection of recrystallized grains using the software DRG, covering a recrystallized fraction $X_{EBSD} = 0.99$.

Table 18. Plate W90 in the as-received condition and after different annealing treatments at 1200 °C: mean chord length for all grains along rolling and transversal direction, specific surface density of high angle boundaries in the RD/ND plane and recrystallized volume fractions as obtained by EBSD and Vickers hardness measurements. $S_{v,HAB}$ is calculated from the average chord lengths along both directions, namely $\overline{\lambda}_{LAB,RD}$ and $\overline{\lambda}_{LAB,ND}$.

Annealing time at 1200 °C	$\overline{\lambda}_{HAB,RD}$ (μm)	$\overline{\lambda}_{HAB,ND}$ (μm)	$S_{V,HAB}$ (μm^{-1})	X_{EBSD}	X_{HV}
Warm-rolled W90	57	18	0.073	0	0
5.5 h	50	25	0.060	0.03	0
7 h	39	24	0.067	0.05	0.02
8 h	37	22	0.072	0.08	0.05
8.5 h	39	24	0.067	0.09	0.08
9 h	35	27	0.066	0.10	0.10
10 h	50	29	0.054	0.18	0.16
11 h	54	38	0.045	0.29	0.24
13 h	55	42	0.042	0.41	0.45
15 h	72	49	0.034	0.52	0.61
20 h	104	80	0.022	0.93	0.91
25 h	119	98	0.019	0.99	1

As observed from Table 18 and orientation maps (Fig. 71 to Fig. 81 obtained on the RD/TD section) during isothermal recrystallization at 1200 °C, the initial as-received elongated microstructure along RD (57 μm x 18 μm) is replaced by new recrystallizing grains that end up being larger than those of the as-received microstructure (e.g up to 119 μm x 98 μm after annealing at 1200 °C for 25 h). Consequently, recrystallization leads to a reduction of specific surface density $S_{V,HAB}$ of high angle boundaries and an increase in grain size for the plate W90. The aspect ratio in the RD/ND section decreases from an elongated microstructure along RD in the as-received state (with an aspect ratio 3.2) to a nearly-equiaxed microstructure (with an aspect ratio 1.2) after full-recrystallization. Notice that the aspect ratio of 1.3 previously obtained in subchapter 5.1.1 for the as-received plate W90 referred to another plane of observation (namely the rolling plane RD/TD) and is not comparable to the aspect ratio of 3.2 measured on the RD/ND section. Also notice that the orientation maps during recrystallization have been obtained on the rolling plane (RD/TD) for the plate W67 and on the transversal plane for the plate W90 (RD/ND). Therefore, the aspect ratios during recrystallization of both plates are not directly comparable given the different plane of observation.

5.3.3 Grain size evolution during recrystallization

Fig. 82 and Fig. 83 present the grain size distribution (for all grains present, indistinctively of whether they are recovered or recrystallized grains) for all annealing stages during recrystallization annealing for the plates W67 and W90 respectively. The grain areas have been obtained from orientation grain maps. The grains were identified using the grain detection tool on the software hkl channel 5, as those areas which did not surpass a critical misorientation of 15°. The mapped sections correspond to the rolling plane (RD/TD) for the plate W67 and the transversal plane (RD/ND) for the plate W90. The grain size distributions cover a broad range (for all annealing stages) as seen from the grain area distribution of Fig. 82a. and Fig 83a. Such wide grain size distributions are typical for hot-deformed samples ([108], [109]). These distributions tend to shift to the right (to larger grain areas) for the later recrystallization stages, because at these stages the new recrystallizing grains become bigger than the grains of the as-received material due to nuclei growth during recrystallization. Notice that the large last peak for the largest grain area of Fig. 82a and Fig. 83a (located at x=20000 μm^2) results from the fact that, unlike the other bins which include grains with sizes ±500 μm^2, the last bin includes all grains whose area is $A>20000$ μm^2. This peak just represents that there are still some grains larger than the end of the x axis, and shall not be compared to the other bins directly. A direct comparison becomes possible for Fig. 82c and Fig. 83c, where the area of each bin has been divided by the average grain area. This normalization distributes the data of the former large peak among all peaks with a minimum size. For example, for the plate W67 (Fig. 82a), the data for the fully-recrystallized sample become distributed among all bins with axis $A/A_0 \geq 2$ (since the average apparent grain area for the sample annealed for 110 h at 1250 °C is approximately 11500 μm^2). In other words, the data of the large peak of Fig. 82a and Fig. 83a become more evenly distributed among all peaks in Fig. 82c and Fig. 83c, and are directly comparable.

The increasing grain size during recrystallization results from the growth of recrystallizing grains. This effect can be more clearly seen in the accumulated grain size distributions of Fig. 82b and Fig. 83b for the plates W67 and W90 respectively. In fact, this effect is not observed in cold-rolled plates, where the recrystallized grains are typically smaller than the grains of the as-rolled material ([21], [110]). It is speculated that, because the current plates were warm-rolled, dynamic recovery might have reduced the stored energy of the potential nucleation sites, leading to lower nucleation as compared to cold-rolling, which might explain the bigger grain size of the recrystallized current warm-rolled plates. At the beginning of recrystallization for the plate W67 (after annealing for 6 h at 1250 °C) the maximum apparent grain area was 17500 μm^2 and the average apparent grain area was 3500 μm^2. The fully-recrystallized state (after annealing for 110 h at 1250 °C) shows a maximum apparent grain area of 93500 μm^2 and an average apparent grain area of 11500 μm^2. At the beginning of recrystallization for the plate W90 (after annealing for 7 h at 1200 °C) the maximum apparent grain area was 10500 μm^2 and the average apparent grain area was 1800 μm^2. The fully-recrystallized state (after annealing for 25 h at 1200 °) shows a maximum apparent grain area of 108000 μm^2 and an average apparent grain area of 12000 μm^2. The maximum apparent grain area represents the area of the biggest grain found for that sample, whereas the average apparent grain area represents the average size of all grains for that sample. Notice that, in Fig. 82b and Fig. 83b, except for the as-received samples and the fully-recrystallized samples, the mapped grains are a combination of both recovered and recrystallized grains.

From Fig. 82b and Fig. 83b, it can be seen that both the as-received material and the earlier stages of recrystallization show very similar grain size distributions, with a predominance for smaller grain sizes, for both plates W67 and W90. At higher recrystallization stages (after approximately $X_{EBSD} > 0.3$), a noticeable decrease of the fraction of the smaller grain sizes starts to occur, as well as an increase of the fractions of the bigger grain sizes for both plates W67 and W90. However, a difference can be appreciated between the plates W67 and W90 by comparing states of similar recrystallized fraction of both plates. As recrystallization proceeds, the fraction of smallest grain sizes seems to decrease more slowly for the plate W67 (see Fig. 82a), while a more abrupt decrease of the fraction of the smallest grain sizes and a shift of this peak to the right (to slightly bigger grain sizes) is observed in the plate W90 at similar recrystallized fractions (see Fig. 83b). In contrast, this peak never shifts during recrystallization for the plate W67, although it decreases in intensity. All in all, at similar recrystallized fractions for the plate W67 and W90, a higher fraction of nuclei of bigger sizes seems present for the plate W90. A plausible reason for this might be that the new recrystallizing nuclei impinge more upon one another in the plate W67 (as compared to the plate W90) limiting more their growth, while the nuclei of the plate W90 could be less impinged and allowed to grow further. This might explain the shift of the peak of the smallest grain sizes to the right as recrystallization proceeds (see Fig. 83b). In fact, as will be observed in chapter 5.5.1 on nucleation, a higher tendency for site-saturation of nuclei is observed for the plate W67 as compared to the plate W90, which is in good agreement with the former impingement argument. Finally, at the latest recrystallization stages and for both plates, most grains present bigger grain sizes as expected due to nuclei growth.

From Fig. 82a and Fig. 82b, it seems apparent that recrystallization leads to an increase of the average grain size. However, in order to better analyze the small differences that might exist between the different grain size distributions, and see if these differences can be accounted for entirely by the increase of grain size due to nuclei growth during recrystallization, the effect of the increasing grain size was deducted from the distribution. This normalization is done by dividing the grain distribution by the average grain size at each recrystallization stage in Fig. 82c and Fig. 82d for the plate W67 (and analogously in Fig. 83c and Fig. 83d for the plate W90). Close examination of Fig. 82c and Fig. 82d (for the plate W67) and Fig 83c and Fig 83d (for the plate W90) reveals (by the superposition of all recrystallization stages in the plate W67) that the shape of the normalized grain size distribution remains almost unaltered during recrystallization for the plate W67, while a shift to the right is still present during recrystallization for the plate W90 which is due to reasons different to nuclei growth. This additional effect could explain the fastest decrease of the fraction of the smallest grain sizes for the plate W90, as compared to the plate W67. All in all, this indicates that nuclei growth during recrystallization alone accounts for the shifting of the distribution to bigger grain sizes as recrystallization proceeds for the plate W67, while grain growth contributes only partially to this shift for the plate W90. It can also be deduced from Fig. 82c and Fig. 82d for the plate W67 that there seems to be a similar growth rate for all grain orientations and sizes during recrystallization of the plate W67; textural changes during recrystallization are expected to occur, yet the normalized size distributions perfectly fit together regardless of the texture of the material at each recrystallization stage. The same cannot be said for the plate W90. A more detailed study of growth during recrystallization will be done in subchapter 5.6.

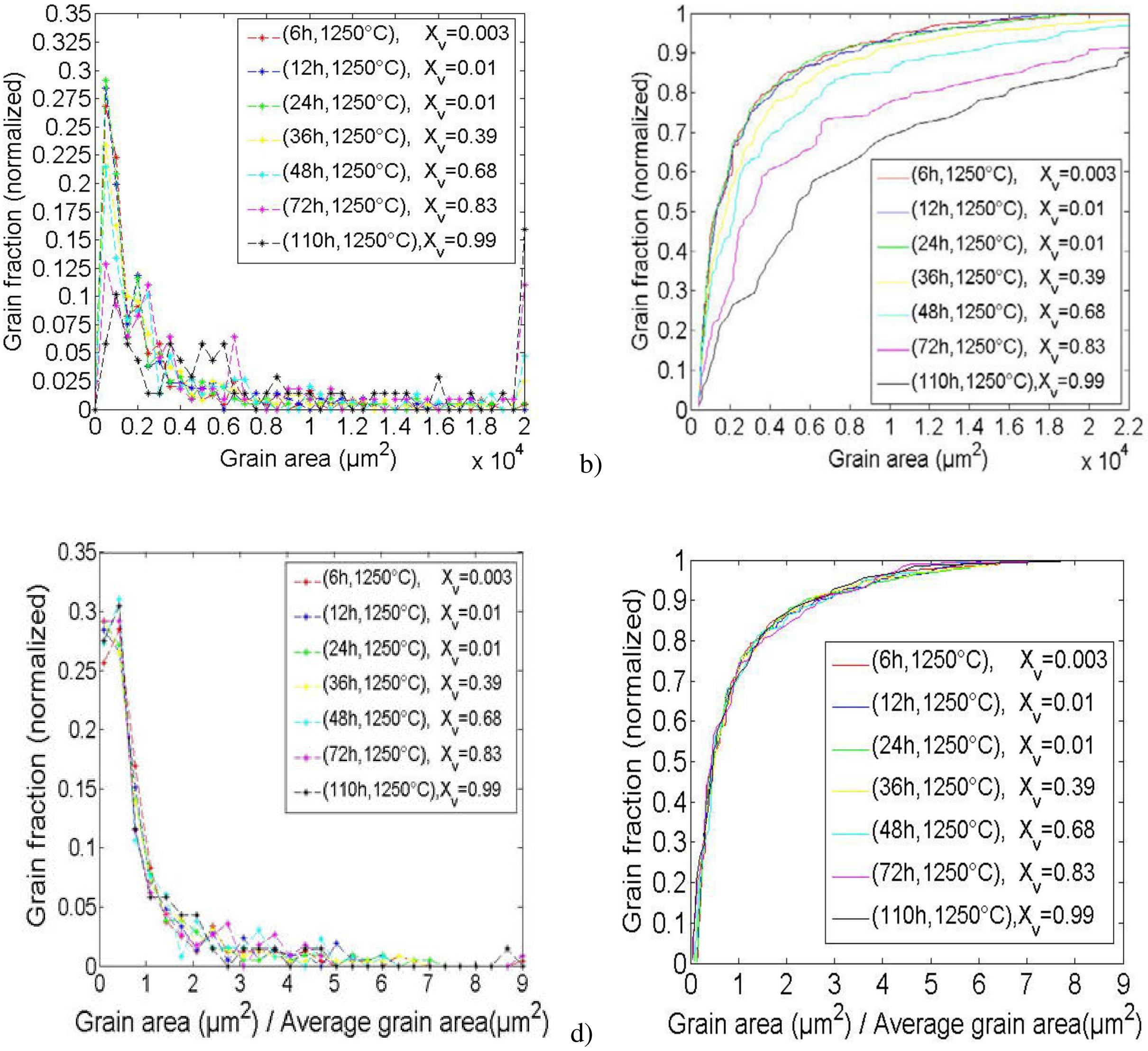

a) b) c) d)

Fig. 82. Grain size distribution evolution during recrystallization of the plate W67 after annealing at 1250 °C. a) Grain area distribution. b) Accumulated grain area distribution obtained from binned data in Fig. 82a. c) Grain area distribution normalized by the average grain area of each annealing stage. d) Accumulated misorientation distribution normalized by the average grain area; analogous to Fig. 82c. The grain areas presented here were measured using HKL Channel 5, including both recovered and recrystallized grains. A bin size of 600 µm^2 was used for the misorientation distributions of Fig. 82a and Fig. 82b.

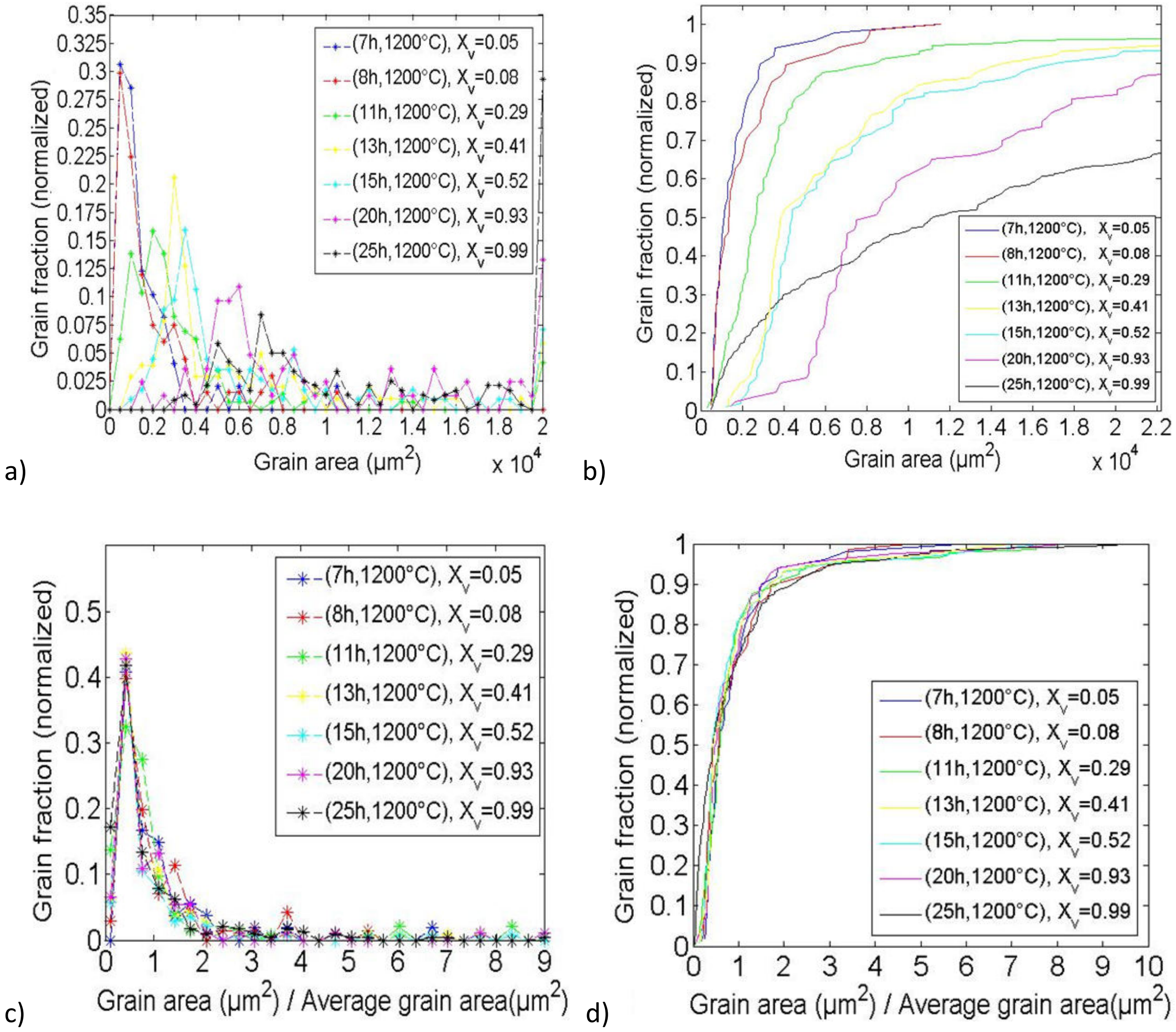

Fig. 83. Grain size distribution evolution during recrystallization of the plate W90 after annealing at 1200 °C. a) Grain area distribution. b) Accumulated grain area distribution obtained from binned data in Fig. 83a. c) Grain area distribution normalized by the average grain area of each annealing stage d) Accumulated misorientation distribution normalized by the average grain area; analogous to Fig. 83c. The grain areas presented here were measured using HKL Channel 5, including both recovered and recrystallized grains. A bin size of 600 µm^2 was used for the misorientation distributions of Fig. 83a and Fig. 83b.

5.4 Textural evolution during recrystallization

Upon annealing at all temperatures for times shorter than the incubation time for recrystallization, the texture of the plates during this recovery stage remains almost unaltered. This is expected because of no considerable nucleation of any new grains which may have a different texture. As an example, the texture of the plate annealed at 1150 °C for a time of 750 h (right before the incubation time of 887 h) is provided in Fig. 84a. Also, the texture of the plate W67 annealed at 1250 °C for a time of 24 h (right before the incubation time of 24.5 h) is shown in Fig. 85a. Both textures are perfectly comparable to the texture of the as-received plate W67 (Fig. 38a). The same is observed for the plate W90, where the texture of the plate W90 annealed for 7 h at 1200 °C (corresponding to the incubation time) of Fig. 88a is perfectly comparable to the as-received texture of the plate W90 (Fig. 38b). Once the incubation time for recrystallization has been reached, recrystallization sets in and changes in the texture start to occur.

5.4.1 Moderately-rolled plate (W67)

The textural evolution for the plate W67 during recrystallization annealing at 1150 °C and 1250 °C is shown in Fig. 84 and Fig. 85 respectively. These correspond to the lower and higher annealing temperatures for which orientation data has been gathered for the plate W67.

Upon recrystallization at all temperatures, new recrystallization texture components start to appear, with no real preference for any particular component, except for a weak component not too far in orientation from the cube component. This leads to a considerable randomization of the texture during recrystallization, as can be observed by the appearance of green shaded regions in the pole figures (of intensity close to 1) as recrystallization proceeds (see Fig. 84 and Fig. 85). This means that all orientations tend to be equally present as recrystallization proceeds or, in other words, the texture becomes increasingly random during recrystallization. As recrystallization proceeds, a very slight predominance of orientations not too far in orientation from the cube component can be observed in an otherwise almost-random recrystallized texture (see Fig. 84 and Fig. 85). For example, the recrystallized texture of this fully-recrystallized tungsten plate (W67) after annealing at 1150 °C consists of a random texture with higher intensities for components not too far from the ideal cube orientation (with intensity 3.5 times above random as seen near the centre of the {100} pole figure of Fig. 84d).

The recrystallization temperature may or may not affect the microstructural development, as has been observed for example in aluminum at different strains (e.g. [111], [112]). In the current study, the annealing temperature had no considerable effect on the textural evolution during recrystallization (compare Fig. 84 and Fig. 85).

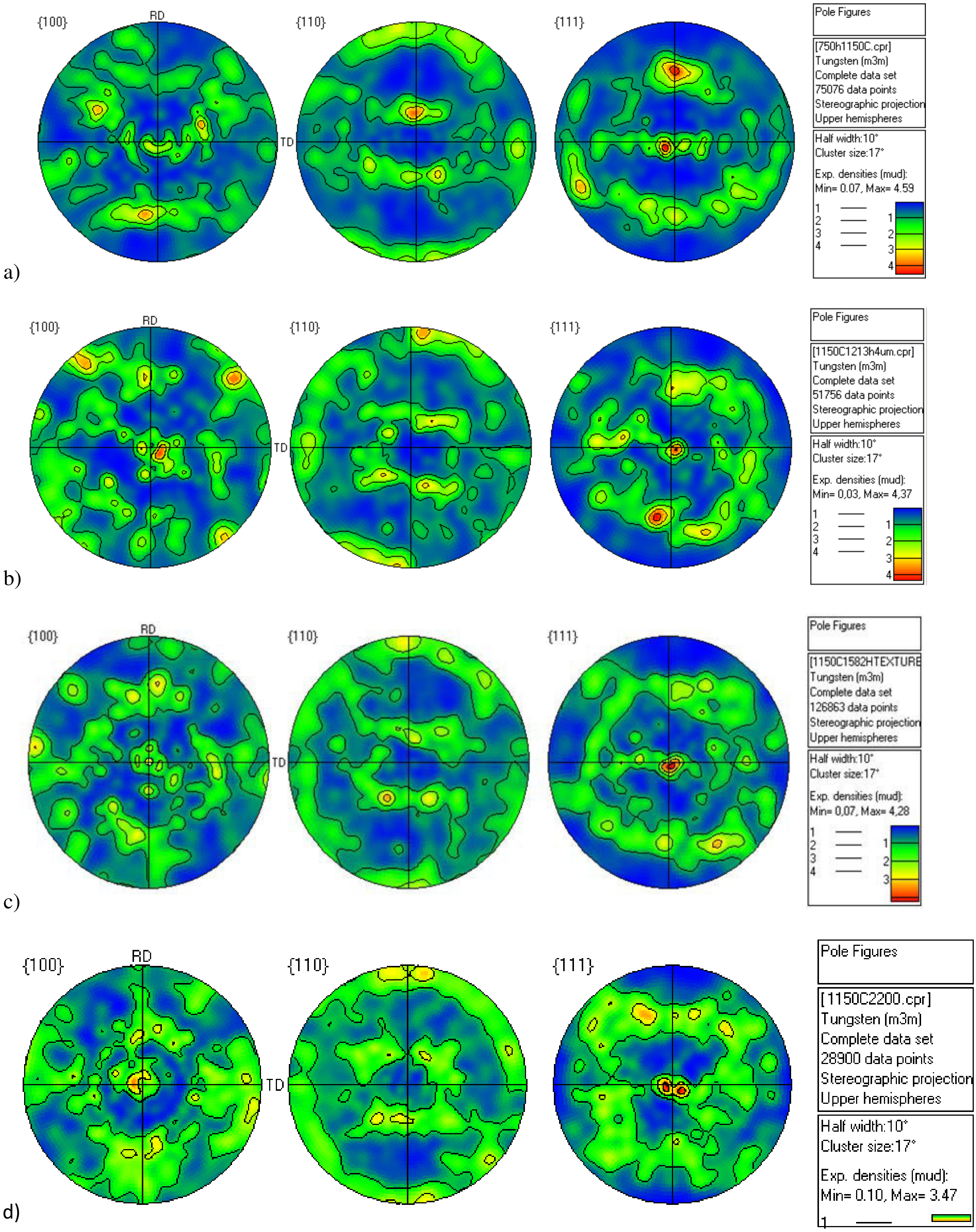

Fig. 84. {100}, {110} and {111} pole figures contoured using a Gaussian spread function with 10° half width and a cluster size of 17°, showing the texture of the plate W67 during recrystallization at 1150 °C. a)

Annealed for 750 h at 1150 °C, right before the incubation time for the start of recrystallization $(X_{EBSD} = 0.03)$. b) Annealed for 1213 h at 1150 °C to a state before half-recrystallization $(X_{EBSD} = 0.41)$. c) Annealed for 1582 h at 1150 °C to a state after half-recrystallization $(X_{EBSD} = 0.69)$. d) Annealed for 2200 h at 1150 °C to a state close to a fully-recrystallized state $(X_{EBSD} = 0.90)$.

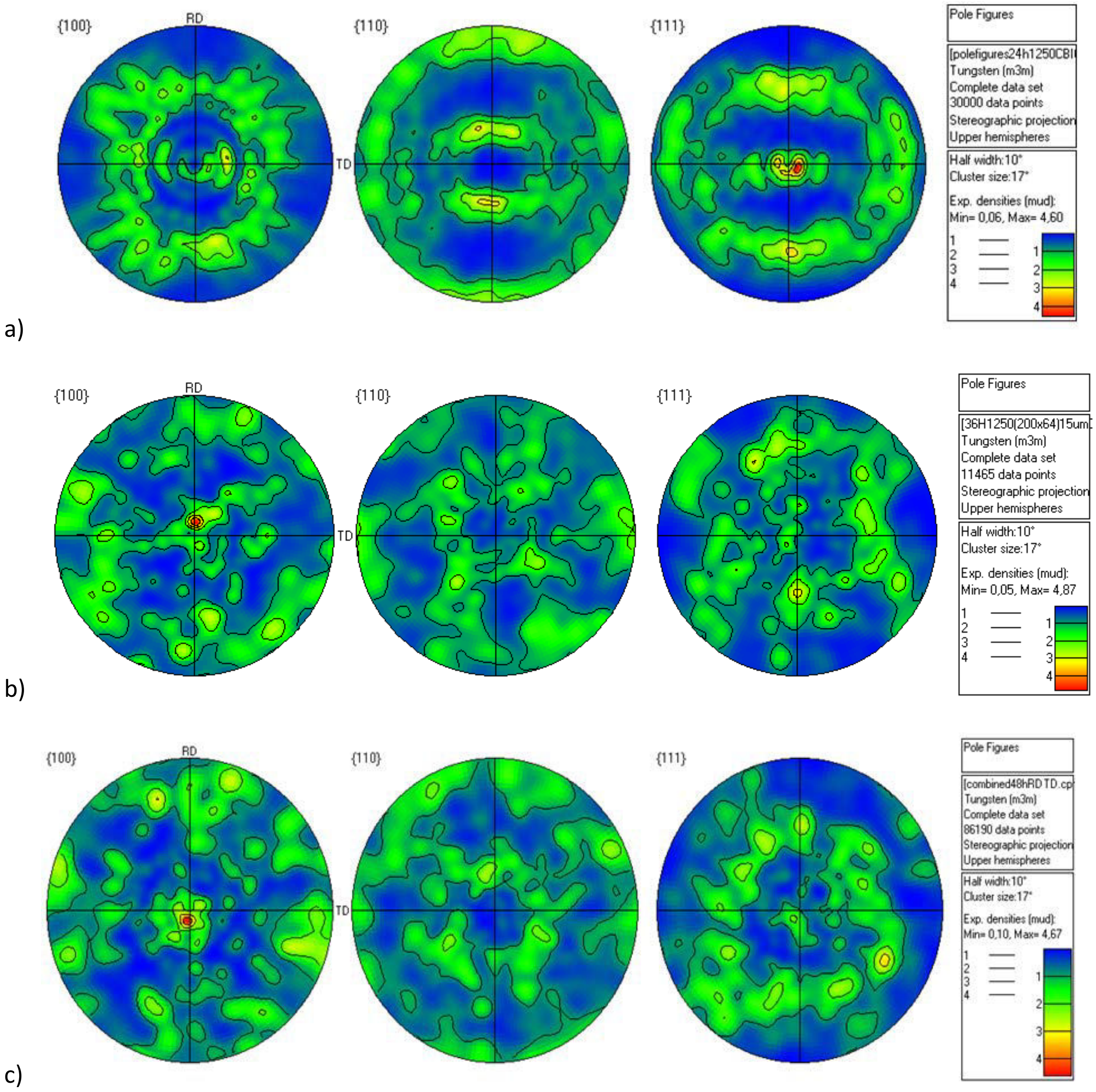

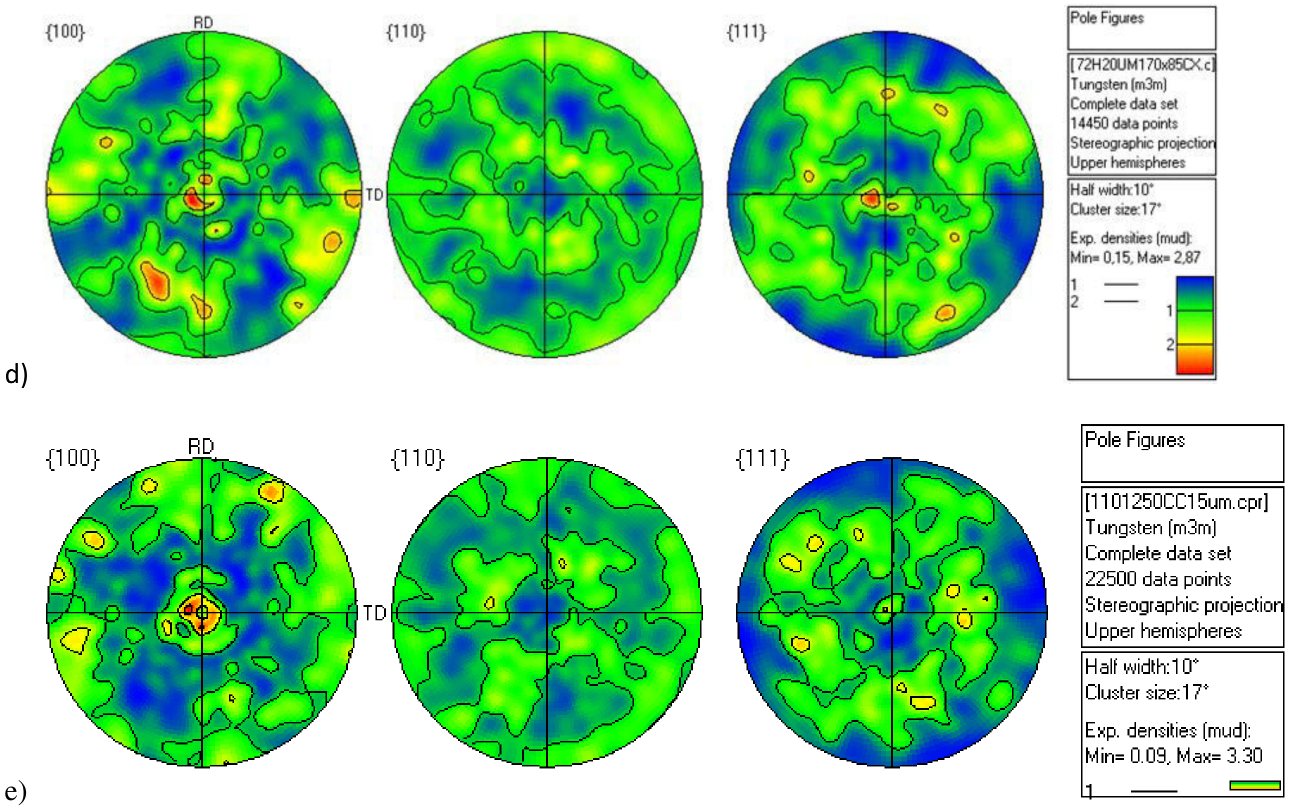

Fig. 85. {100}, {110} and {111} pole figures contoured using a Gaussian spread function with 10° half width and a cluster size of 17°, representing the texture of the plate W67 during recrystallization annealing at 1250 °C. a) Annealed for 24 h at 1250 °C, right before the incubation time for the start of recrystallization $(X_{EBSD} = 0.01)$. b) Annealed for 36 h at 1250 °C to a state before half-recrystallization $(X_{EBSD} = 0.39)$. c) Annealed for 48 h at 1250 °C to a state after half-recrystallization $(X_{EBSD} = 0.68)$. d) Annealed for 72 h at 1250 °C to a state close to full-recrystallization $(X_{EBSD} = 0.83)$. e) Annealed for 110 h at 1250 °C to a fully-recrystallized state $(X_{EBSD} = 0.99)$.

For a better description of the texture evolution during annealing, the Orientation Distribution Functions (ODFs) were calculated at the beginning of recrystallization, in the half-recrystallized state and in the fully-recrystallized state. The calculated ODF sections at $\phi_2 = 45°$ are presented in Fig. 86.

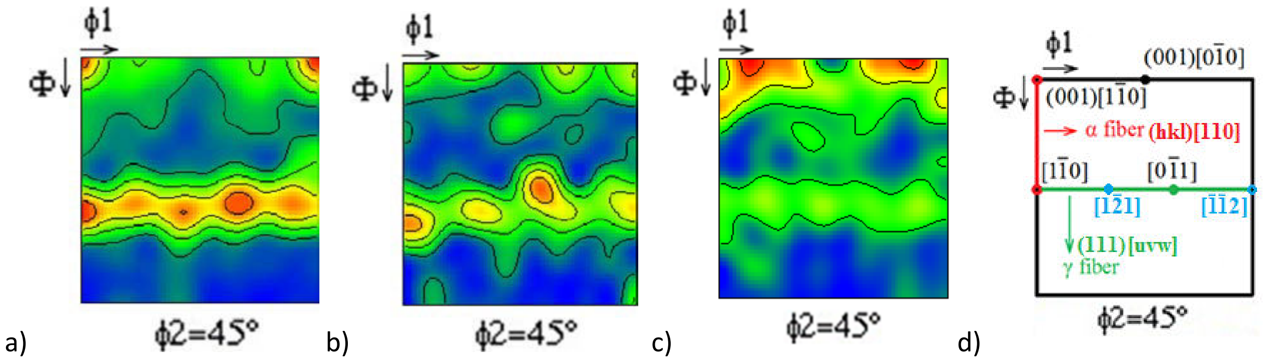

Fig. 86. ϕ_2=45° section of the orientation distribution function (ODF) calculated from the orientation data for the plate W67 annealed at 1250 °C. a) Annealed for 24 h at the beginning of recrystallization, showing a maximum density 4.3 times above random for the $\{111\}<1\bar{1}0>$ component. b) Annealed for 36 h to the half-recrystallized state, showing a maximum density 4.1 times above random for the $\{111\}<1\bar{1}0>$ component. c) Annealed for 110 h to the fully-recrystallized state, showing a maximum density 3.3 times above random for components approximately 30° off along ϕ_1 from the ideal cube component. d) Sketch of the ϕ_2=45° section of orientation space, indicating the main components of a typical bcc rolling texture: the α fiber (red) and the γ fiber (green), as well as some of their components; the cube component, the rotated cube $\{001\}<1\bar{1}0>$ component, and the γ fiber components $\{111\}<1\bar{1}0>$ and $\{111\}<\bar{1}\bar{1}2>$.

From Fig. 86, it can be observed that the texture of the plate W67 at the beginning of recrystallization (Fig. 86a) is mainly composed of two fibers: the dominating γ fiber ($\{111\}<uvw>$ or $\{111\}$ parallel to ND) and the α fiber ($\{hkl\}<110>$ or <110> parallel to RD). The γ fiber component $\{111\}<1\bar{1}0>$ is slightly stronger than the $\{111\}<11\bar{2}>$ γ fiber component. The α fiber mainly consists of the rotated cube component (with intensity 4.1). All in all, the texture is quite weak and very similar to the texture of the as-received W67 plate (compare to Fig. 40a).

The texture in the half-recrystallized state (Fig. 86b) shows a decrease of the intensity of the γ fiber and a slight increase of texture components closer in orientation to the cube component as compared to the rotated cube component. A reduction of the intensity of the rotated cube component $\{001\}<1\bar{1}0>$ is also observed. It seems that the recovered γ fiber and the rotated cube component, which mainly comprise the as-received texture, are being replaced by other textural components during recrystallization, with a very low preference for components closer to the ideal cube component. Careful inspection of Fig. 86b shows a slightly higher presence of the $\{111\}<1\bar{1}0>$ γ fiber component, as compared to the $\{111\}<11\bar{2}>$ γ fiber component. The lower presence of the $\{111\}<11\bar{2}>$ component could indicate preferential growth of the recrystallized components into this recovered γ fiber component. The higher stored energy of the deformed $\{111\}<112>$ component as compared to the $\{111\}<1\bar{1}0>$ component (see Table 12 and Table 13 in subchapter 5.1.2) could explain this selective consumption; the higher stored energy of this component could lead to faster growth of recrystallized components into the $\{111\}<112>$ recovered matrix, as compared to the other $\{111\}<1\bar{1}0>$ component of the γ fiber.

The texture of the fully-recrystallized sample from the plate W67 after annealing for 110 h at 1250 °C (Fig. 86c) is quite random, consisting of remaining γ-fiber and a weak predominant texture consisting of recrystallized components 30° off along ϕ_1 from the ideal cube component (with maximum intensity 3.2 times above random). Therefore, the recrystallization texture is a nearly-random texture showing slightly higher intensities for components closer in misorientation to the cube component than the initial rotated cube components of the as-received texture.

The misorientation distribution evolution during recrystallization of the plate W67 at 1150 °C and 1250 °C is shown in Fig. 87. At the earlier stages of recrystallization, a higher fraction of LABs is present. As recrystallization proceeds, the contribution of the HABs increases while that of LABs decreases. The reduction of LABs is expected because the recovered regions with an abundance of LABs become replaced by almost deformation-free recrystallized grains. At the later stages of recrystallization, this leads to a misorientation distribution which is more nicely described by the theoretical Mackenzie distribution [113], which corresponds to the misorientation angles between randomly oriented crystallites of cubic symmetry. In other words, the Mackenzie distribution represents the distribution corresponding to a random texture of the material. As an example, the misorientation distributions during recrystallization after annealing at 1150 °C and 1250 °C are presented in Fig. 87. Although the misorientation distributions at both temperatures resemble more closely the Mackenzie distribution at the later recrystallization stages (e.g. see Fig. 84 and Fig. 85), this cannot be directly related to a randomization of the texture during recrystallization because LABs still exist that present a misfit with the Mackenzie distribution that represents a random texture.

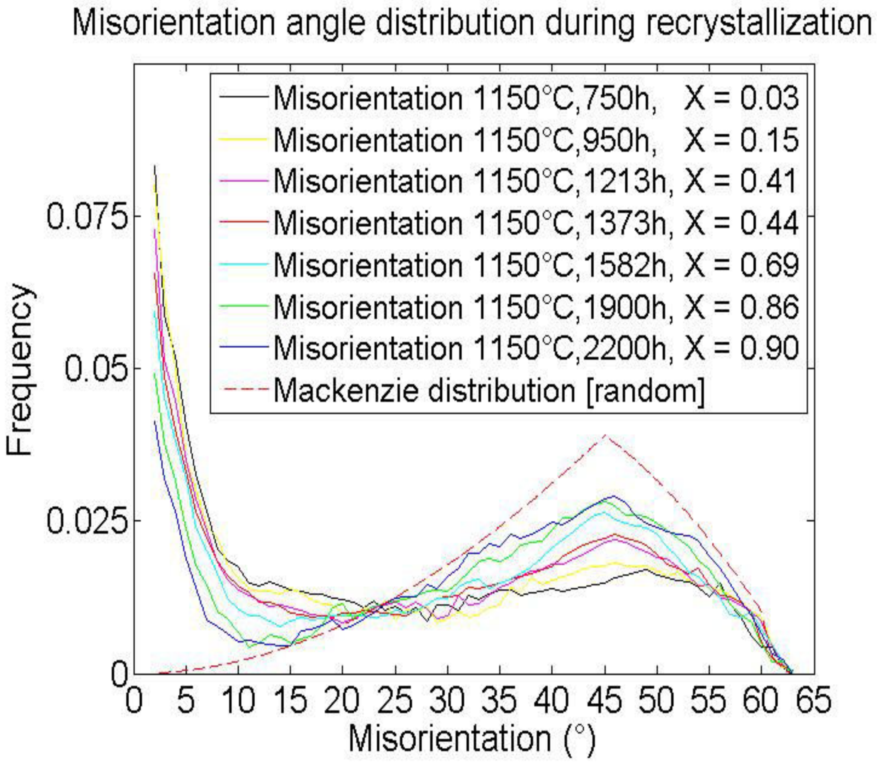

a)

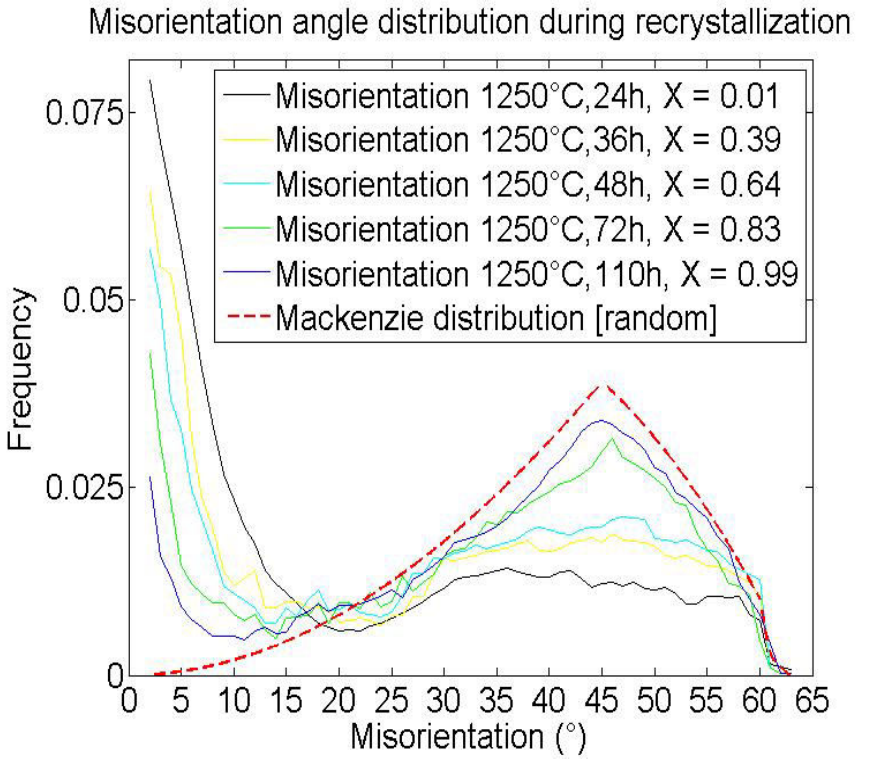

b)

Fig. 87. Misorientation angle distribution evolution for the plate W67 during recrystallization after annealing at: a) 1150 °C, b) 1250 °C. The misorientation frequencies were obtained from HKL Channel 5, The Mackenzie misorientation distribution (discontinuous red line) represents the misorientation distribution that would be expected in a material of random texture.

5.4.2 Highly-rolled plate (W90)

The textural evolution during recrystallization at 1200 °C is shown in Fig. 88. Recrystallization of the plate W90 at 1200 °C showed the appearance of a stronger cube component during recrystallization (see the textural evolution of Fig. 88), as compared to the recrystallized W67 plate. Analogously to the plate W67, the intensity of the dominant γ fiber has considerably decreased after recrystallization, although part of the γ fiber still remains after recrystallization. Whether the textural evolution is determined by oriented nucleation or oriented growth will be discussed later in subchapters 5.5 and 5.6

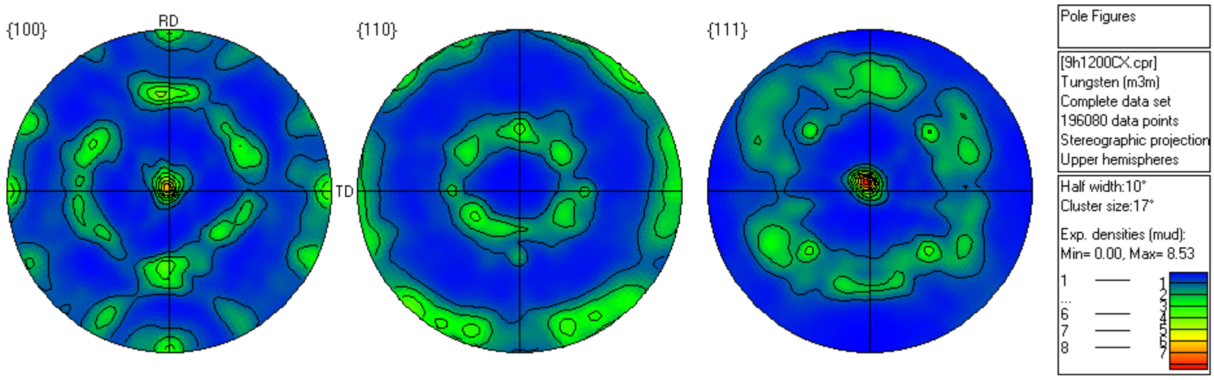

a)

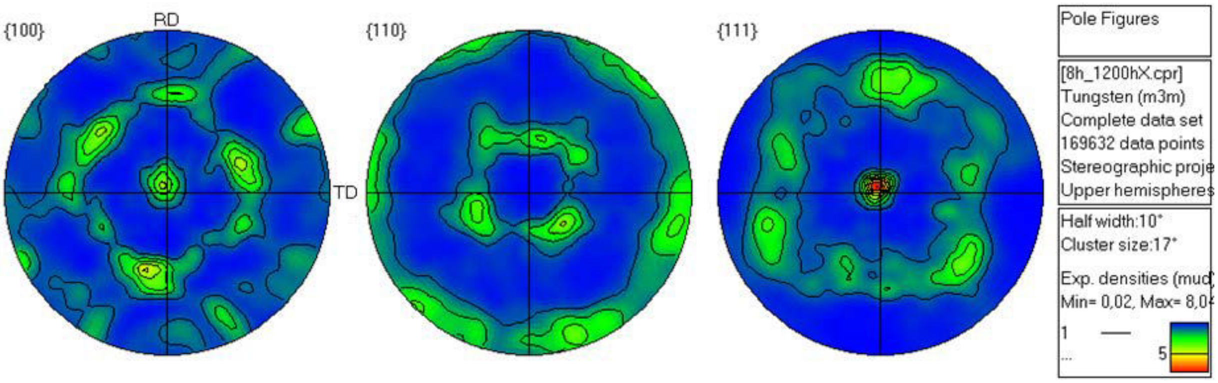

b)

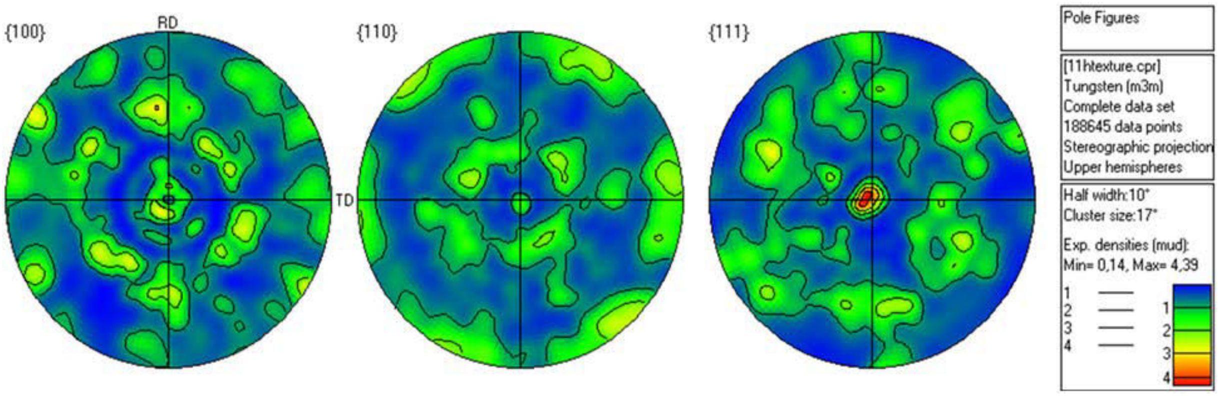

c)

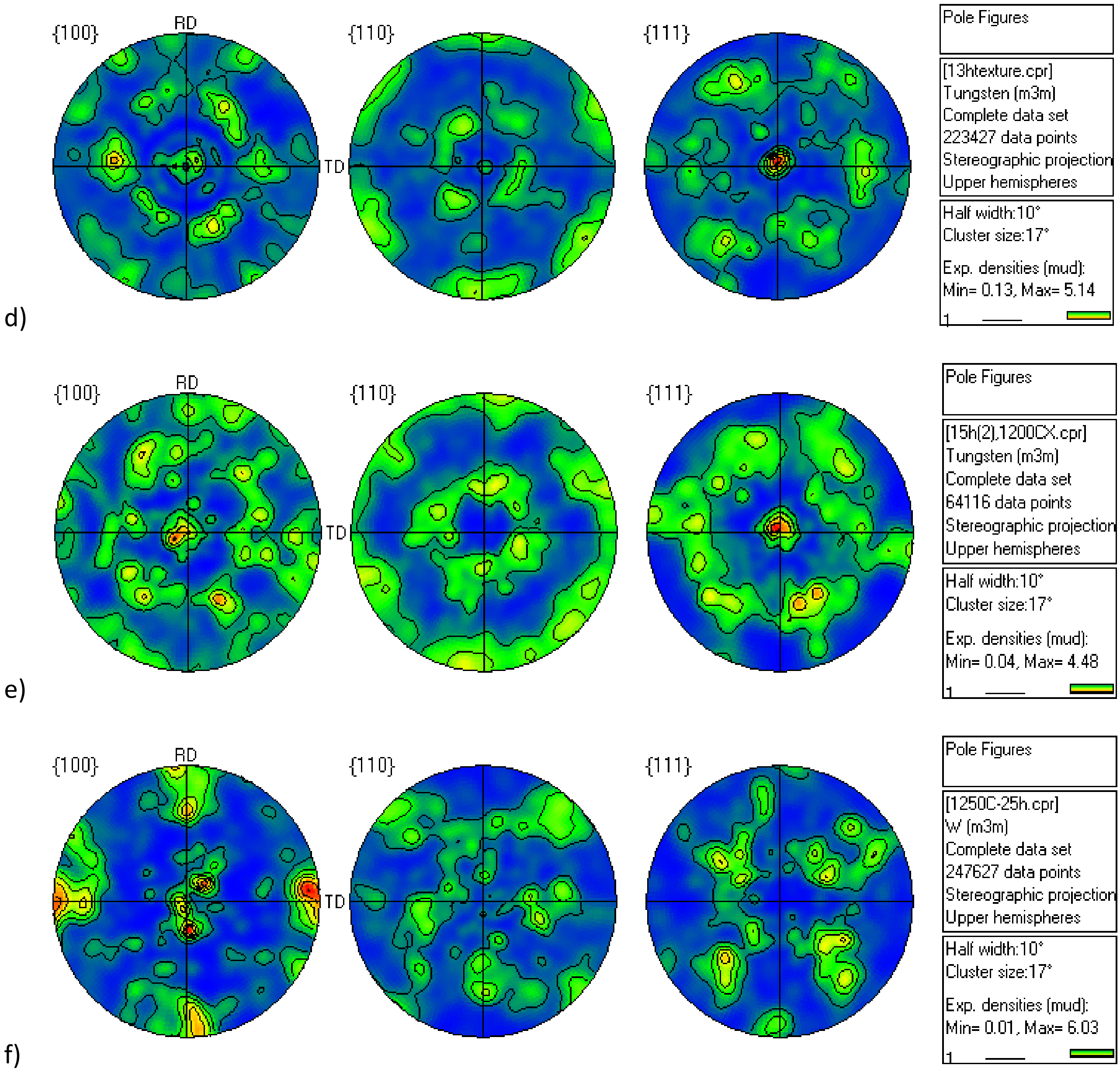

Fig. 88. {100}, {110} and {111} pole figures contoured using a Gaussian spread function with 10° half width and a cluster size of 17°, representing the texture of the plate W90 during recrystallization annealing at 1200 °C. a) Annealed for 7 h at 1200 °C, right at the incubation time for the start of recrystallization $(X_{EBSD} = 0.05)$.b) Annealed for 8 h at 1200 °C to an early recrystallization stage $(X_{EBSD} = 0.08)$. c) Annealed for 11 h at 1200 °C to a more advanced recrystallization stage before half-recrystallization $(X_{EBSD} = 0.29)$.d) Annealed for 13 h at 1200 °C to a state right before half-recrystallization $(X_{EBSD} = 0.41)$.e) Annealed for 15 h at 1200 °C to a state right after half-recrystallization $(X_{EBSD} = 0.52)$. f) Annealed for 25 h at 1200 °C to an almost fully-recrystallized state $(X_{EBSD} = 0.93)$.

For a better description of the textural evolution at 1200 °C, the Orientation Distribution Functions (ODFs) were calculated at the beginning of recrystallization, the half-recrystallized state and the fully-recrystallized state. The sections at $\phi_2 = 45°$ are presented in Fig. 89.

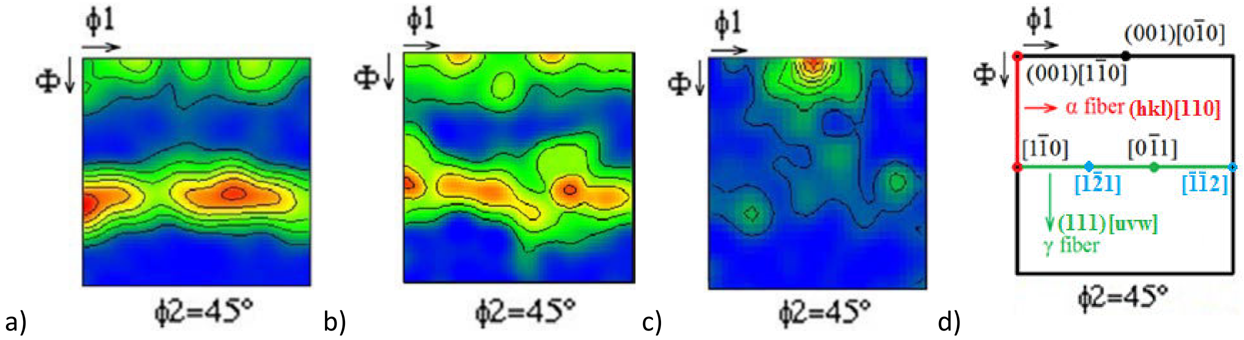

Fig. 89. ϕ_2=45° section of the orientation distribution function (ODF) calculated from the orientation data of the plate W90 annealed at 1200 °C. a) Annealed for 8 h at the beginning of recrystallization, showing a maximum density 6.6 times above random for the $\{111\}<1\bar{1}0>$ component. b) Annealed for 15 h to the half-recrystallized state, showing a maximum density 4.5 times above random for the $\{111\}<1\bar{1}0>$ component. c) Annealed for 25 h to the fully-recrystallized state, showing a maximum density 8.8 times above random for the cube component d) Sketch of the ϕ_2=45° section of orientation space, indicating the main components of a typical bcc rolling texture: the α fiber (red) and the γ fiber (green), as well as some of their components; the cube component, the rotated cube $\{001\}<1\bar{1}0>$ component, and the γ fiber components $\{111\}<1\bar{1}0>$ and $\{111\}<\bar{1}\bar{1}2>$.

From Fig. 89, it can be observed that the texture at the beginning of recrystallization (Fig. 89a) is mainly composed by the γ fiber. A considerably higher presence of the $\{111\}<1\bar{1}0>$ γ fiber component (red-shaded regions with an intensity 4.5 times above random) is observed as compared to the less dominant $\{111\}<11\bar{2}>$ γ fiber component. The rotated cube component $\{001\}<1\bar{1}0>$ seems to be the only component of the less dominant α fiber. Obviously, the texture at this stage is very similar to the as-received texture (compare to Fig. 40b). The slightly higher intensity of cube and near-cube components (green-shaded regions with intensity 2 and 3 times above random in Fig. 89a that were not observed in the as-received texture of the plate W90 in Fig. 40b) could indicate the nucleation of a few grains with near-cube texture right at the beginning of recrystallization.

The texture in the half-recrystallized state (Fig. 89b) shows a decrease of the intensity of the γ fiber and an increase of texture components closer to the cube component during recrystallization. Careful inspection of Fig. 89b shows a higher presence of the $\{111\}<1\bar{1}0>$ γ fiber component, as compared to the $\{111\}<11\bar{2}>$ γ fiber component. The higherer presence of the $\{111\}<1\bar{1}0>$ component could indicate higher stability of this recovered component, which is less consumed by the recrystallizing grains. The higher stored energy of the deformed $\{111\}<11\bar{2}>$ component as compared to the $\{111\}<1\bar{1}0>$ component (see Table 12 and Table 13 in subchapter 5.1.2) could explain the faster growth of recrystallized components into the $\{111\}<11\bar{2}>$ recovered matrix, and therefore its faster consumption.

The texture of the fully-recrystallized state from the plate W90 after annealing for 25 h at 1200 °C (Fig. 89c) consists of few remaining orientations along the γ-fiber and a marked yet not too strong cube component $\{001\}<0\bar{1}0>$. This marked cube component is observed in the fully-recrystallized state (red-shaded region with intensity 8.8 times above random). The simultaneous recrystallization of other weak texture components in a somewhat random fashion may be the reason of the not too strong fully-recrystallized near-cube texture.

In the misorientation distribution evolution during recrystallization of the plate W90 at 1200 °C (see Fig. 90), a higher presence of LABs is present at the later stages of recrystallization of the plate W90 and a worse fit with the Mackenzie distribution is observed as compared to the plate W67. The presence of a higher fraction of LABs (especially those below 5°) at the later recrystallization stages for the plate W90 (e.g. blue line of Fig. 90, corresponding to the fully-recrystallized state) is related to the sharper recrystallization texture developed for the plate W90.

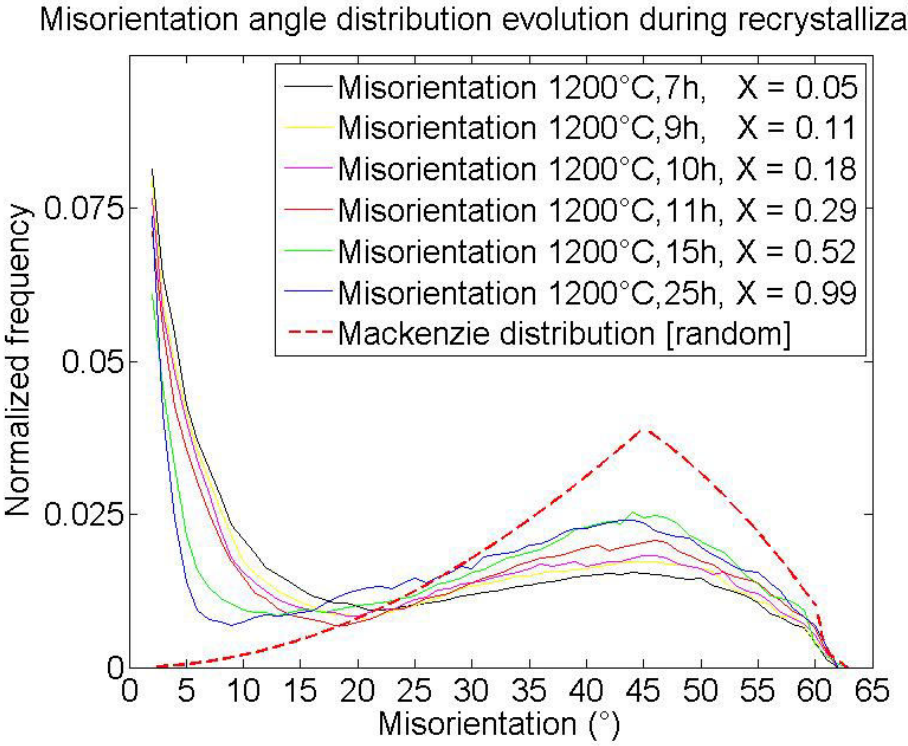

Fig. 90. Misorientation angle distribution evolution for the plate W90 during recrystallization at 1200 °C. The misorientation frequencies were obtained from HKL Channel 5. The Mackenzie misorientation distribution (discontinuous red line) represents the misorientation distribution that would be expected in a material of random texture.

Theories are available which successfully predict how the typical $\{001\}<1\bar{1}0>$ component seen in cold-rolled W transforms during recrystallization into a weak cube texture ([50], [114]). According to these models, the weakening of the texture is related to the elastic isotropy of tungsten, which allows the rotated cube $\{001\}<1\bar{1}0>$ components to transform into various recrystallization texture components by <110> rotations. In fact, as mentioned earlier, a very weak texture misoriented around 30° from the cube texture develops for the recrystallized plate W67 (see Fig. 84e), while a stronger yet still weak near-cube texture develops for the recrystallized plate W90 (see Fig. 88f respectively). It is speculated that these recrystallized components could arise from the as-received deformed cube components, being transformed by the aforementioned mechanism. It is also speculated, that the highest strain for the plate W90 could be related to the better alignment of the recrystallized cube component as compared to the plate W67 (where a weak component 30° off from the ideal cube appeared). The higher alignment of the recrystallized cube component with the ideal cube orientation with increasing rolling deformation has been previously observed in other metals (e.g. for copper in [115]).

However, these models ([50], [114]) cannot fully explain the development of the recrystallized texture of the plates W67 and W90 of this study. The reason is that the deformation texture of the present plates W67 and W90 (see Fig. 40a and Fig. 40b respectively) is different from the simple $\{001\}<1\bar{1}0>$ texture assumed in the model. Although some rotated cube components are present in the as-received plates, the texture of the present plates is mainly composed of the γ fiber. Therefore, in the following subchapters 5.5 and 5.6, orientation effects for both nucleation and growth of recrystallizing grains during recrystallization are studied, in order to understand the textural evolution during recrystallization microstructurally. In the next sections on nucleation (5.5) and growth (5.6), nucleation densities and growth rates (as well as orientation relationships) were studied in detail. The latter allowed to elucidate whether the recrystallized texture was due to oriented nucleation or oriented growth.

5.5 Nucleation

5.5.1 Nuclei density evolution during recrystallization

The number of nuclei in each orientation map was determined using the software DRG for the plates W67 and W90. The nuclei evolution during recrystallization was determined for the plate W67 at three temperatures (namely 1150 °C, 1200 °C and 1250 °C) and at 1200 °C for the plate W90. These correspond to the annealing temperatures for which complete series of EBSD data were available at a wide range of annealing stages.

Secondly, the number of nuclei was normalized by the area covered by each orientation map, thereby obtaining the density N_a, or number of nuclei per unit area μm^2. Furthermore, it must be noted that the orientation maps represent two-dimensional sections of the tungsten plates. Since the material is three-dimensional in nature, the chance of mapping a grain in a 2D section of the material must be also taken into account; there will always be a higher chance to map a bigger grain than a smaller grain in the 2D section. In fact, only nuclei which are a distance lower or equal to *R* away from the 2D section (either above or below the section, namely within a distance 2*R*) will be mapped in the 2D section. This is expressed by Eq. 5.7, which allows determination of the nuclei density per unit volume (N_v),

$$N_v = N_a / 2R \qquad (5.7)$$

where N_a is the number of nuclei per μm^2 and *R* is the average radius of the nuclei, as measured from the average chord lengths between HABs surrounding the nuclei, with Eq. 5.8 (from [111]):

$$R = \frac{3}{4}\bar{\lambda}_{HAB} = \frac{3}{4}\cdot\left(\frac{\lambda_{HAB,RD} + \lambda_{HAB,TD}}{2}\right) \qquad (5.8)$$

or $\lambda_{HAB,ND}$ (instead of $\lambda_{HAB,TD}$) in the case of the plate W90, where the transversal plane (RD/ND) was mapped. The choice of different 2D sections for the acquisition of the EBSD orientation data (RD/TD section for the plate W67, vs. RD/ND section for the plate W90) could affect the results only if there is a preference for the growth of the nuclei along either TD or ND, since the chance that nuclei are mapped is higher with increasing nuclei area. However, there does not seem to be any preferential nuclei growth along any direction, as reflected by the nearly-equiaxed aspect ratio of the recrystallizing grains determined from the orientation maps in subchapter 5.3.

The calculated nuclei area density (N_a) for the plate W67 after annealing at the temperatures 1150 °C, 1200 °C and 1250 °C is presented as a function of the annealing time *t* (h) and the recrystallized fraction *X* in Fig. 91 and Fig. 92 respectively. The nuclei volume density (N_v) is also plotted as a function of the annealing time *t* (h) and the recrystallized fraction *X* in Fig. 93 and Fig. 94 respectively.

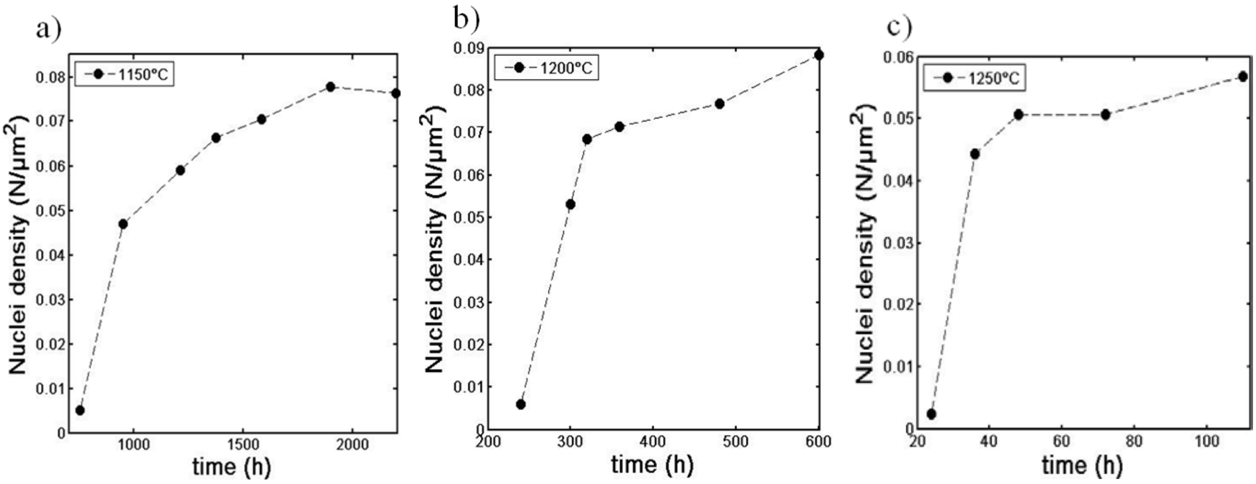

Fig. 91. Nuclei area density as a function of annealing time during recrystallization at: a) 1150 °C, b) 1200 °C , c) 1250 °C.

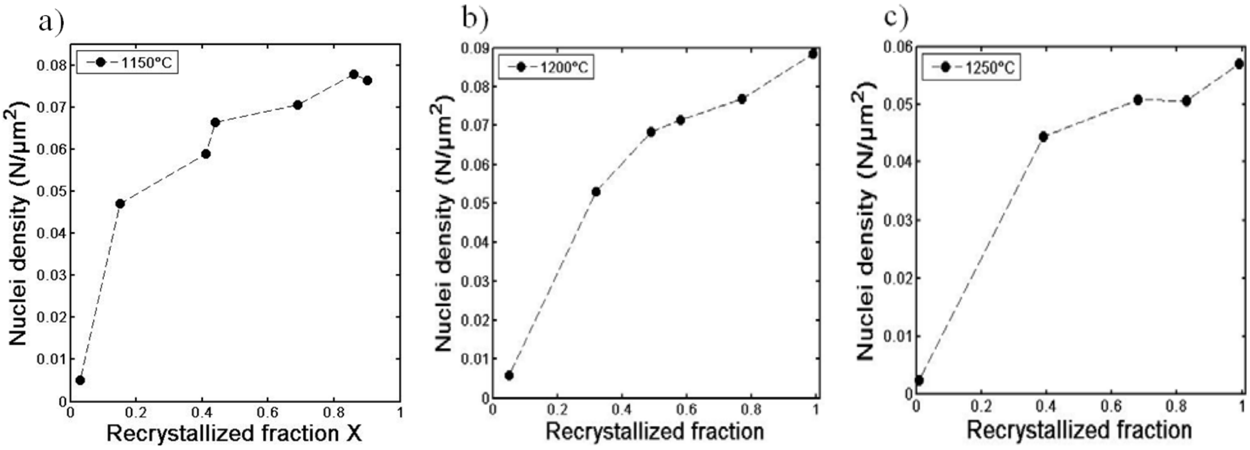

Fig. 92. Nuclei area density as a function of the recrystallized fraction at: a) 1150 °C, b) 1200 °C ,c) 1250 °C.

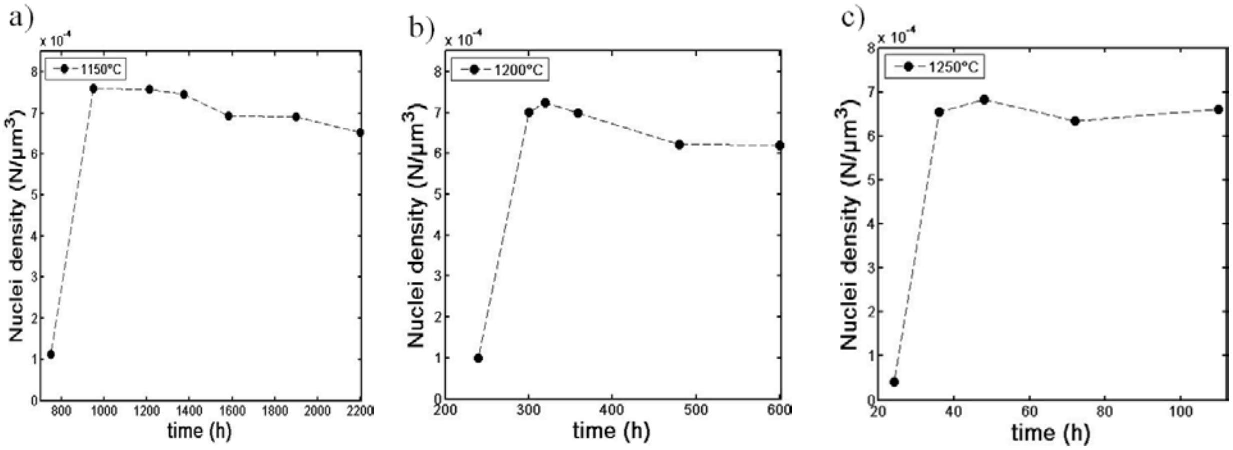

Fig. 93. Nuclei volume density as a function of annealing time during recrystallization at: a) 1150 °C , b) 1200 °C , c) 1250 °C.

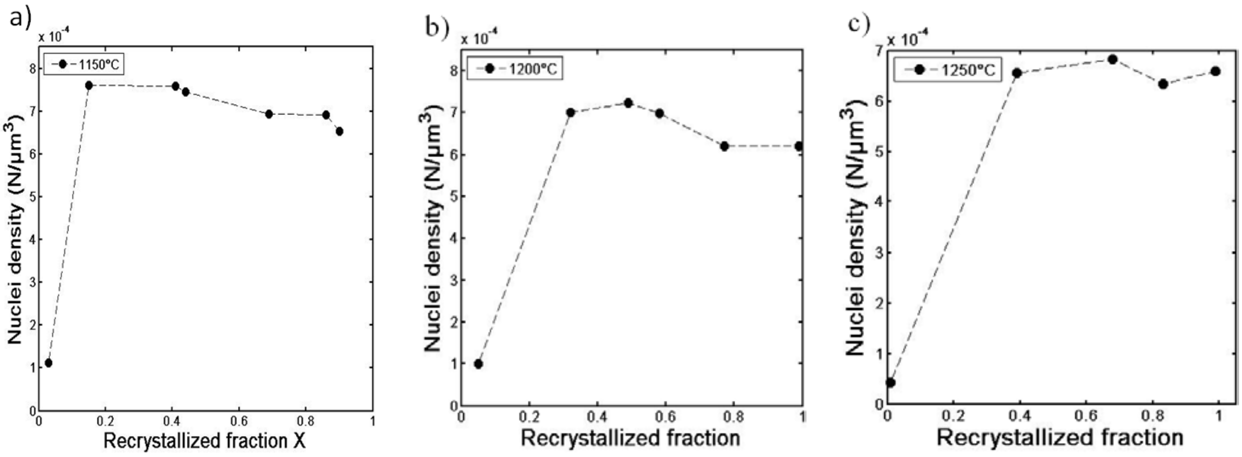

Fig. 94. Nuclei volume density as a function of the recrystallized fraction at: a) 1150 °C , b) 1200 °C , c) 1250 °C.

The calculated nuclei area density (N_a) and nuclei volume density (N_v) for the plate W90 after annealing at 1200 °C are presented as a function of the annealing time t (h) and the recrystallized fraction X in Fig. 95.

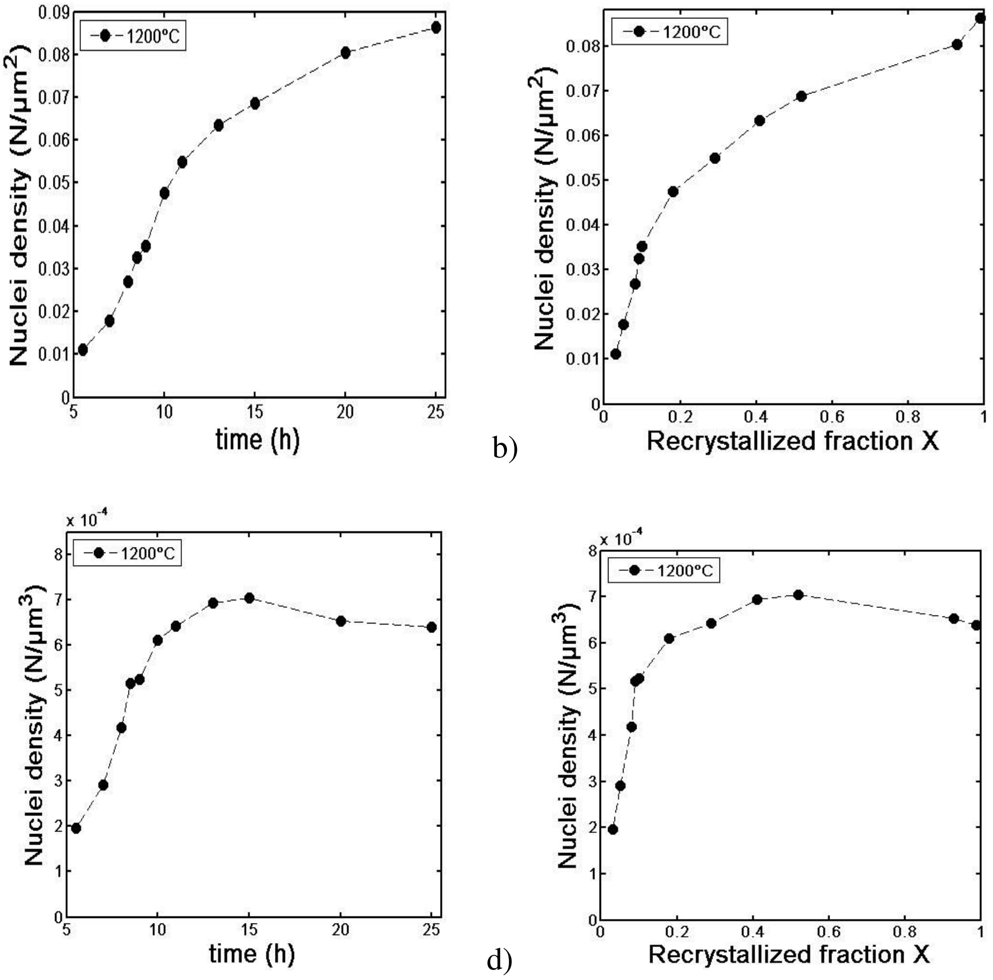

a) b) c) d)

Fig. 95. (a, b) Nuclei area density evolution during recrystallization at 1200°C ; a) as a function of annealing time, b) as a function of the recrystallized fraction. (c, d) nuclei volume density evolution during recrystallization at 1200°C; c) as a function of annealing time, d) as a function of the recrystallized fraction.

Comparison of the nuclei volume density evolution (N_v) between the plate W67 (see Fig. 94) and the plate W90 (see Fig. 95d) seems to indicate a tendency for site-saturation (i.e most nuclei form at early stages of recrystallization) for the plate W67, a tendency which is not as marked for the plate W90: in the case of the plate W67, from Fig. 94a, it can be seen that the maximum nuclei volume density during annealing of the plate W67 is already achieved at early stages of recrystallization for all annealing temperatures (e.g. after only 15% recrystallization, in the case of the sample annealed for 950 h at 1150 °C), indicating site-saturated nucleation. The slight decrease of the nuclei volume density after reaching the maximum volume density as recrystallization proceeds does not seem due to grain growth (namely due to the consumption of smaller recrystallized grains by bigger recrystallized grains), given that hardness and microstructural measurements did not show evidence for grain growth at 1150 °C . This seems to be a purely due to a statistical or stereological effect

In contrast, for the plate W90 annealed at 1200 °C (see Fig. 95d), the nuclei volume density (N_v) seems to keep increasing during annealing, until a state close to the half-recrystallized state is achieved (i.e. samples annealed for 13 h 15 h at 1200 °C, showing a recrystallized fraction of 0.41 and 0.52 respectively). At this point, it seems that most nuclei have already been formed, and as a consequence, the nuclei density seems to saturate up to full-recrystallization. Although it must be noted that the nucleation rate seems to drastically decrease after reaching a recrystallized fraction of 0.18 (i.e. for the sample annealed for 10 h at 1200 °C, see Fig. 95c and Fig. 95d), nuclei formation still occurs at a slower nucleation rate until the half-recrystallized state is reached. Therefore, it seems that the plate W67 shows a more site-saturation-like behavior, whereas nuclei are still forming in the plate W90 up to half-recrystallization. The nucleation behavior of the plate W90 could be explained as two nucleation regimes for which the nucleation rate seems approximately constant. First, up to a recrystallized fraction of 0.18, a faster and almost constant nucleation rate is observed. Secondly, after reaching a nuclei fraction of 0.18, the nucleation rate decreases considerably and seems to stay rather constant until reaching the half-recrystallized state. This is showcased by the almost linear relationship that exists for these 2 previously mentioned recrystallization regimes, as can be observed in the plot of the nuclei density vs. the recrystallized fraction of Fig. 95d. When the half-recrystallized state is reached, most nuclei seem to have already formed. It shall be noted that this nucleation behavior could also be due to a statistical or stereological effect.

This different nucleation behavior for the plates W67 (site-saturation) and W90 (constant nucleation rate) could be explained by the considerably smaller grain size of the as-received plate (with average chord lengths 36x37µm) as compared to the plate W90 (with average chord lengths 62x47µm). These chord lengths were both measured on the rolling plane along RD and TD.
A smaller initial grain size for the plate W67 entails a higher surface density of HABs which can act as potential nucleation sites. The presence of a higher surface density of HABs could lead to the presence of more potential nucleation sites (as compared to the plate W90 of lower surface density of HABs). This could lead to an effective site-saturation behavior in the plate W67; since the plate W67 has a higher surface density of HABs, the nuclei could form preferably at these HABs, and most nuclei could already have formed at earlier stages of nucleation.

The higher surface density of HABs for the plate W67 could also explain the similar nuclei densities that are found for the plates W67 and W90. In principle, the plate W90 would be expected to show higher nucleation density, since a higher stored energy was estimated for the as-received plate W90 (see Table 13), which increases the amount of potential nucleation sites available for nucleation. However, the extra surface density of HABs present in the plate W67 (due to its smaller grain size) might counteract the higher nucleation density expected for the most highly-deformed plate W90, which might explain the similar nucleation densities found for both plates W67 and W90.

Additionally, the different nucleation behavior of the plates W67 and W90 could also explain the lower Avrami exponent for the plate W67 ($n = 1.1$) observed in the JMAK recrystallization kinetics defined by hardness characterization in chapter 4, as compared to the higher Avrami exponent ($n = 2$) of the plate W90. Site-saturation behavior for the plate W67 and constant nucleation rate for the plate W90 might explain this difference in Avrami exponents. An Avrami exponent higher by 1 unit than that for site-saturation is expected for constant nucleation rates during recrystallization [21]. In fact, an Avrami exponent higher by 1 ($n = 2$) was found for the plate W90 as compared to the plate W67.

Regarding the spatial distribution of the nuclei of the earlier stages of recrystallization of the plate W67 (e.g nuclei from the samples annealed for 750 h and 950 h at 1150 °C of Fig. 51-52) and the plate W90 (i.e nuclei from the samples annealed for 7 h, 8 h and 8.5 h at 1200 °C of Fig. 39-41), it is observed that the nuclei develop relatively well spatially-distributed in the recovered matrix. Some weak clustering along RD is observed which is not surprising, taking into account the deformation-induced subdivision of the deformed grains that can be observed in Fig. 41a, b and Fig. 41c, d (subchapter 5.1.2) for the as-received plates W67 and W90 respectively.

5.5.2 Orientation of the nuclei

The orientations of the initial nuclei for the plates W67 and W90 were measured and presented as {111} pole figures in Fig. 96a and Fig. 96b respectively. This allows to study relationships between the orientation of the initial nuclei and the texture of the recrystallized material.

In Fig. 96a, the orientations of in total 134 nuclei observed in the plate W67 for the two samples annealed at 1150 °C for the shortest times showing recrystallization (i.e. 750 h and 950 h, corresponding to a recrystallized volume fraction of 0.03 and 0.15 respectively) are presented as a {111} pole figure. In Fig. 96b, the orientations of in total 184 nuclei observed in the plate W90 for the three samples annealed at 1200 °C for the shortest times showing recrystallization (i.e. 7 h, 8 h, and 8.5 h, corresponding to recrystallized volume fractions of 0.05, 0.08, and 0.09 respectively) are presented also as a {111} pole figure. Observation of Fig. 96 reveals a more random orientation distribution of the nuclei for the plate W67 (see Fig. 96a), as compared to the plate W90 which shows preference for nuclei of cube orientation (see Fig. 96b). This is in good agreement with the more random texture observed for the recrystallized plate W67 (see Fig. 86c), and the weak yet stronger cube texture observed for the recrystallized plate W90 (see Fig. 89c).

When the determined orientations are presented as calculated ODFs (see Fig. 97), it appears that the orientation distribution of the nuclei/grains at these early recrystallization stages resembles the texture of the fully-recrystallized plates (especially for the plate W90; e.g. compare Fig. 97a and Fig. 97b to Fig. 86c and Fig. 89c respectively, corresponding to the plates W67 and W90 respectively).

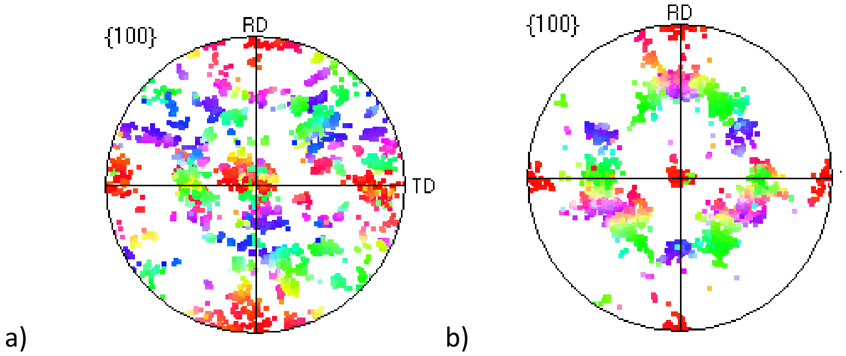

Fig. 96. {100} pole figures showing the orientation distribution of the nuclei at the early recrystallization stages for the plates, with IPF coloring along RD: a) W67 annealed at 1150 °C for 750 h and 950 h, b) W90 annealed at 1200 °C for 7 h, 8 h, 8.5 h.

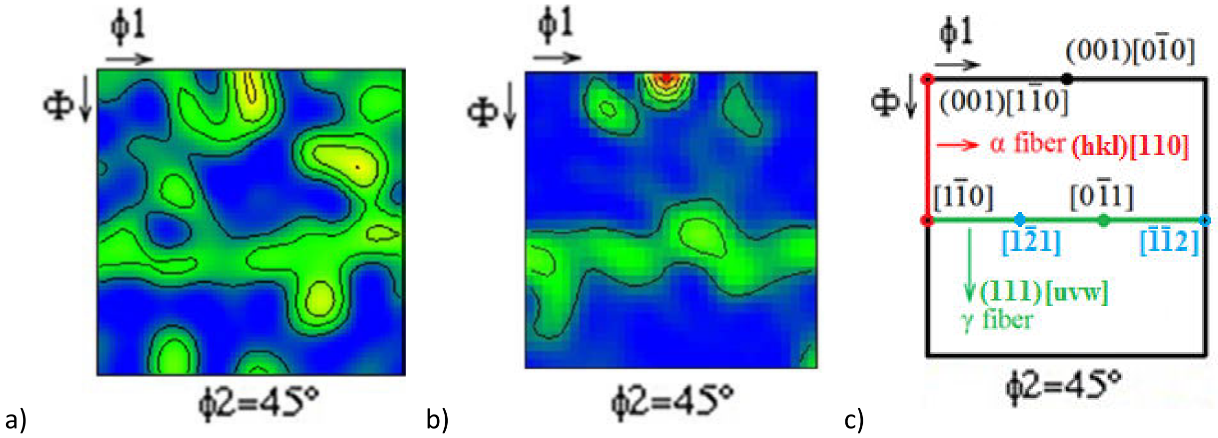

Fig. 97. ϕ_2=45° section of the orientation distribution function (ODF) calculated from the orientation data of the nuclei corresponding to the earlier recrystallization stages represented in Fig. 96 for the plates a) W67 annealed at 1150 °C for 750 h and 950 h, b) W90 annealed at 1200 °C for 7 h, 8 h, 8.5 h, c) Sketch of the ϕ_2=45° section of orientation space, indicating the main components of a typical bcc rolling texture: the α fiber (red) and the γ fiber (green), as well as some of their components; the cube component, the rotated cube $\{001\}<1\bar{1}0>$ component, and the γ fiber components $\{111\}<1\bar{1}0>$ and $\{111\}<\bar{1}\bar{1}2>$.

It therefore seems that the final recrystallized texture is largely determined by nucleation; slight oriented nucleation leads to the weak recrystallized cube texture of the plate W67, while more pronounced oriented nucleation of cube oriented nuclei seems responsible for the stronger near-cube texture of the plate W90.

Oriented nucleation is in fact given as a main reason for the development of a recrystallized cube texture in a review on the reasons for the formation of recrystallized cube texture in several fcc metals [116]. Nevertheless, one can only speculate that the higher strain applied during rolling of the plate W90 (as compared to the plate W67) might have led to the introduction of deformation structures that act as favorable nucleation sites for nucleation of cube nuclei. Evidence of higher strains leading to the formation of a stronger recrystallized cube texture is also found in literature on copper (e.g. [115])

5.5.3 Nucleation orientation relationships

The orientation relationship between the nuclei and the recovered matrix was studied statistically at an early recrystallization stage for the plate W90, namely after annealing at 1250 °C for just 1 h (Fig. 98). This sample was selected because it showed an unsually high amount of nuclei at a very early recrystallization stage, which allows for a representative statistical study of nucleation orientation relationships. However, it shall be noted that the nucleation behavior at 1250 °C was very different to that observed at 1200 °C. In fact, the series annealed at 1250 °C for the plate W90 was discarded from this study, since it presented a heterogeneous recrystallization behavior as observed with EBSD, which could not be related to the Vickers hardness measurements.

The misorientation between each nucleus and the neighbouring recovered matrix was measured both along RD and ND using the software HKL channel 5 for all non-impinged directions of the nuclei. This allowed obtaining the angle/axis pair that defined each misorientation, from which the orientation relationships could be studied. The nuclei were classified as three different types of nuclei; nuclei located at grain boundaries or triple junctions (in the following called "B" nuclei), nuclei located inside the recovered grains away from the grain boundaries (in the following called "M" nuclei), and nuclei belonging to nuclei clusters of more than 5 nuclei (in the following called "C" nuclei). The nuclei orientation relationship with the recovered matrix was measured for a total of 174 nuclei, both along RD and ND. An inspection of Fig. 98 revealed that 51% of the nuclei were of "B" type, 13% of the nuclei were of "M" type, and 36% of the nuclei were of "C" type. The highest presence of nuclei originating at grain boundaries or triple junctions is easily explained by the presence of original HABs and higher misorientation gradients at these sites, which become potential nucleation sites. This also explains the lowest presence of nuclei originating in the interior of the recovered matrix ("M"), given the difficulty for nucleation at sites that lack original HABs. In fact, the nuclei of type ("M") could have originally nucleated at a HAB even if they seem to be at the grain interiors (e.g. the original grain boundary may be on the third unseen dimension of the 2D section). The nuclei clusters ("C") seem to have started at grain boundaries. This would explain the slight clustering of the nuclei along RD (direction along which the grain boundaries extend), as compared to ND. In fact, 57% of the total impinged area of the nuclei of "C" type is impinged along RD, while the remaining 43% is impinged along ND.

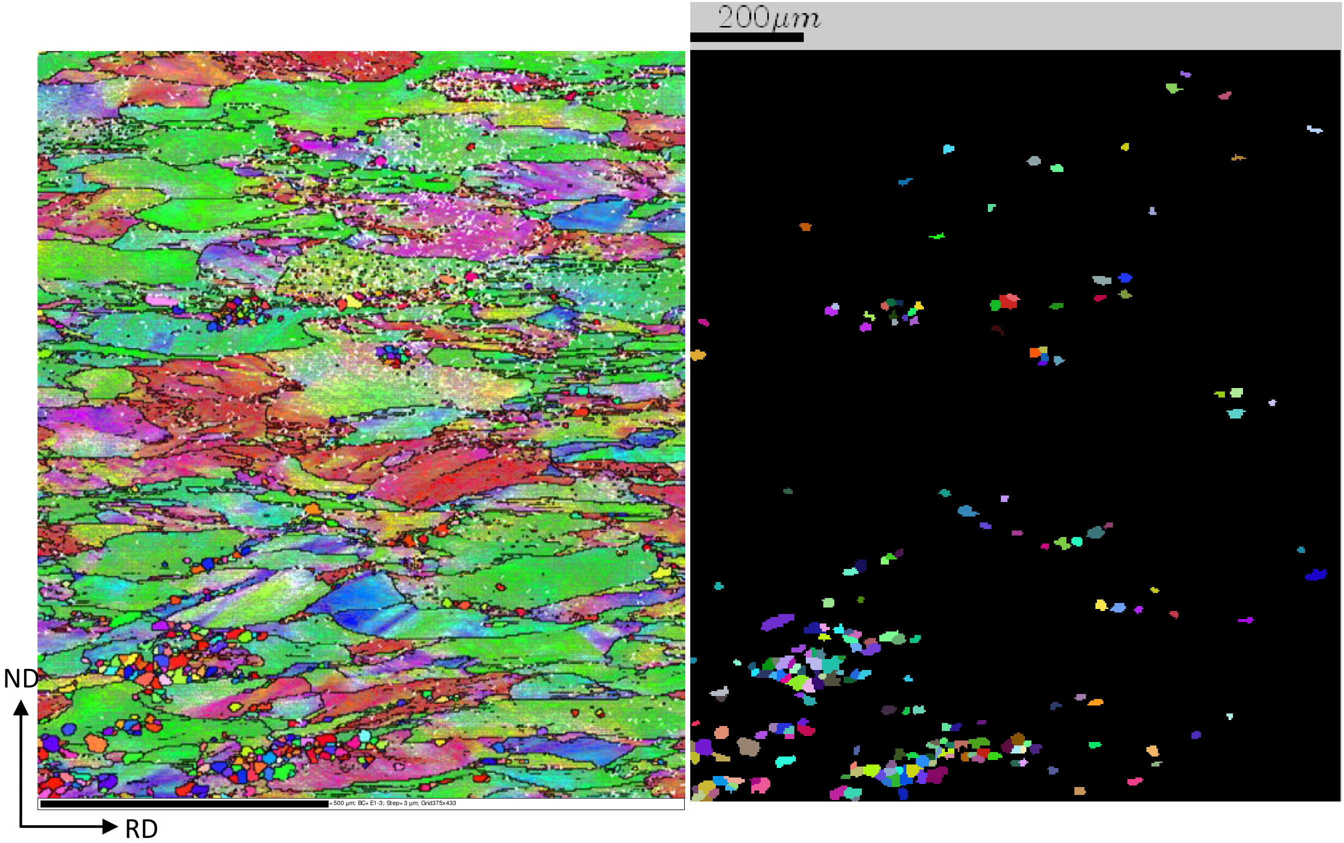

Fig. 98. a) Orientation map corresponding to the RD/ND section of the plate W90 after annealing for 1250 °C for 1 h to a very early recrystallization stage $(X = 0.04)$. b) nuclei map where the recrystallized nuclei can be clearly seen. Notice that many nuclei are present in this EBSD orientation map (namely 213 nuclei), which allows to study statistically the orientation relationship between the nuclei and the surrounding recovered matrix along both RD and ND.

The rotation axis was calculated from the original Euler angles $\varphi_1, \Phi, \varphi_2$ that define the orientation of each nucleus and its surrounding recovered matrix. For this, the Euler angles $\varphi_1, \Phi, \varphi_2$ were converted into the orientation matrix g (Eq. 5.9):

$$g = \begin{pmatrix} g_{11} & g_{12} & g_{13} \\ g_{21} & g_{22} & g_{23} \\ g_{31} & g_{32} & g_{33} \end{pmatrix} \left\{ \begin{array}{l} g_{11} = \cos\varphi_1 \cos\varphi_2 - \sin\varphi_1 \sin\varphi_2 \cos\phi \\ g_{12} = \sin\varphi_1 \cos\varphi_2 + \cos\varphi_1 \sin\varphi_2 \cos\phi \\ g_{13} = \sin\varphi_2 \sin\phi \\ g_{21} = -\cos\varphi_1 \sin\varphi_2 - \sin\varphi_1 \cos\varphi_2 \cos\phi \\ g_{22} = -\sin\varphi_1 \sin\varphi_2 + \cos\varphi_1 \cos\varphi_2 \cos\phi \\ g_{23} = \cos\varphi_2 \sin\phi \\ g_{31} = \sin\varphi_1 \sin\phi \\ g_{32} = -\cos\varphi_1 \sin\phi \\ g_{33} = \cos\phi \end{array} \right. \qquad (5.9)$$

The orientation matrix for the nucleus (g_n) and the recovered matrix (g_m) were calculated from the 3 corresponding Euler angles $\varphi_1, \Phi, \varphi_2$ of the nucleus or the recovered matrix respectively. The misorientation matrix g_r, which defines the misorientation between a nucleus and the surrounding recovered matrix, is calculated as $g_r = g_m \cdot g_n^{-1}$. The misorientation matrix g_r was further converted into the misorientation angle/rotation axis pair that defines the orientation relationship between the nucleus and the recovered matrix (Eq. 5.10), where the misorientation angle θ is in degrees.

$$\begin{aligned}\cos\theta &= \frac{(g_{11}+g_{22}+g_{33}-1)}{2}\\ r_1 &= \frac{(g_{23}-g_{32})}{(2\sin\theta)}\\ r_2 &= \frac{(g_{31}-g_{13})}{(2\sin\theta)}\\ r_3 &= \frac{(g_{12}-g_{21})}{(2\sin\theta)}\end{aligned} \tag{5.10}$$

This allowed to obtain the misorientation axis (in terms of its normalized indices r_1, r_2, r_3) as well as the misorientation angle between each nucleus and its surrounding matrix. The absolute value of such normalized indices was ordered in ascending order as $r_1 < r_2 < r_3$, and used to display in an inverse pole figure (Fig. 99) such misorientations by definition of its x, y axis via Eq. 5.11:

$$x = \frac{2r_1}{(1+r_3)}; \quad y = \frac{2r_2}{(1+r_3)} \tag{5.11}$$

The inverse pole figure (Fig. 99) shows the misorientation axes between all types of nuclei and their surrounding deformed matrix, measured along both RD and ND and for all misorientation angles (a). In order to observe the dependence of the rotation axes on the misorientation angle, all the calculated rotation axes were subdivided into 3 Inverse Pole Figures (b, c, d) covering three ranges of misorientation angles for a better interpretation. All in all, the distribution of rotation axes seems quite random. Comparison with the theoretical distribution of rotation axes of [117], which corresponds to the distribution for randomly distributed cubic crystals, yields a good match especially for Fig. 99d, with the slight maximum at [332] (along [101]-[111]). Therefore, it is concluded that the orientation relationship between the nuclei and the surrounding deformed matrix is random. The fact that all different types of nuclei (colored markers of Fig. 99) are similarly distributed in the inverse pole figures indicates that there is no dependence on the type of nuclei. The same distribution is observed when plotting only the individual measurement directions along either RD or ND (not shown here), indicating also an independence on the measurement direction RD and ND. In other words, there is no particular rotation axis that defines the orientation relationships between the nuclei and the recovered matrix.

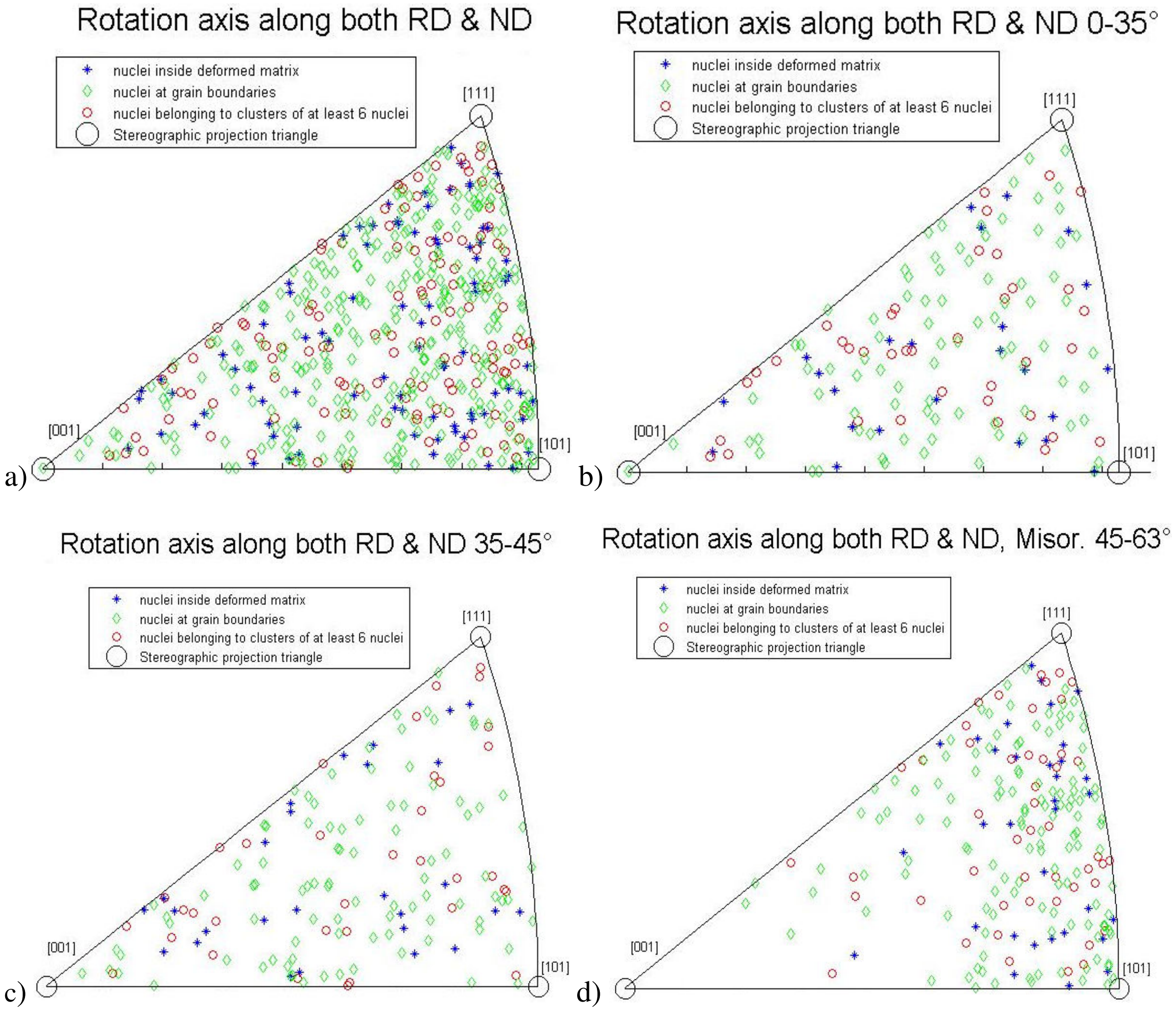

Fig. 99. Inverse pole figure corresponding to the misorientations between each nucleus and the surrounding deformed matrix for 174 nuclei of 3 different types, namely "M", "B" and "C" measured along both the RD and ND directions. a) for all misorientations, b) For misorientations between 0-35°, c) for misorientations between 35-45°, d) for misorientations between 45-63°.

Additionally, the misorientation angle θ calculated from the orientation relationship was also plotted for all types of nuclei and along both directions RD and ND as relative frequencies, in order to observe if there is a preference for certain misorientation angles θ (see Fig. 100). As can be observed from the normalized misorientation angle distribution of Fig. 100, misorientation angles close to 45° between the nuclei and the recovered matrix seem to be slightly favored for all 3 types of nuclei and along both directions RD and ND. The misorientation angle distributions closely resemble the Mackenzie distribution for randomly-oriented cubic crystals, showcasing the random orientation relationship between the nuclei and the surrounding deformed matrix.

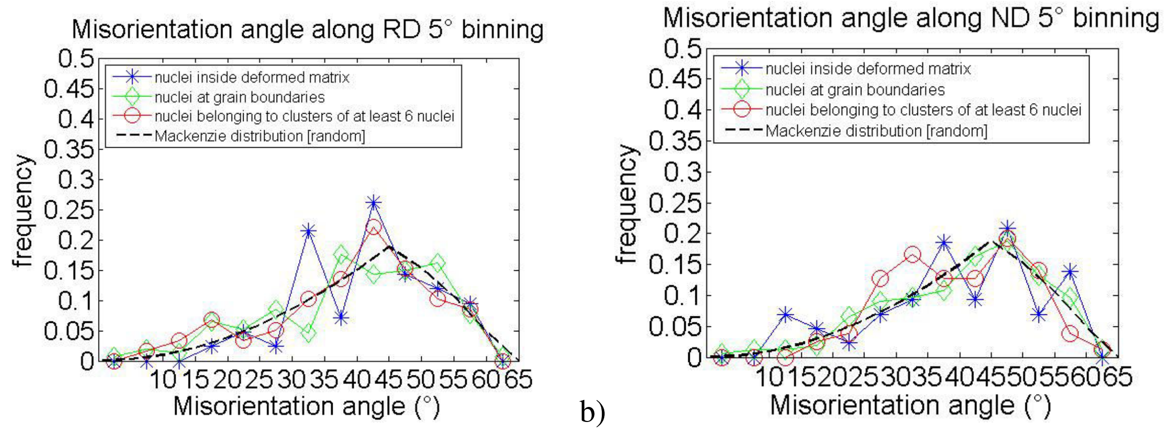

a) b)

Fig. 100. Normalized distribution of misorientation angles between the nuclei and the recovered matrix for all 3 types of nuclei, namely "M", "B" and "C". a) measured along RD, b) measured along ND. 5° binning was used to plot the data.

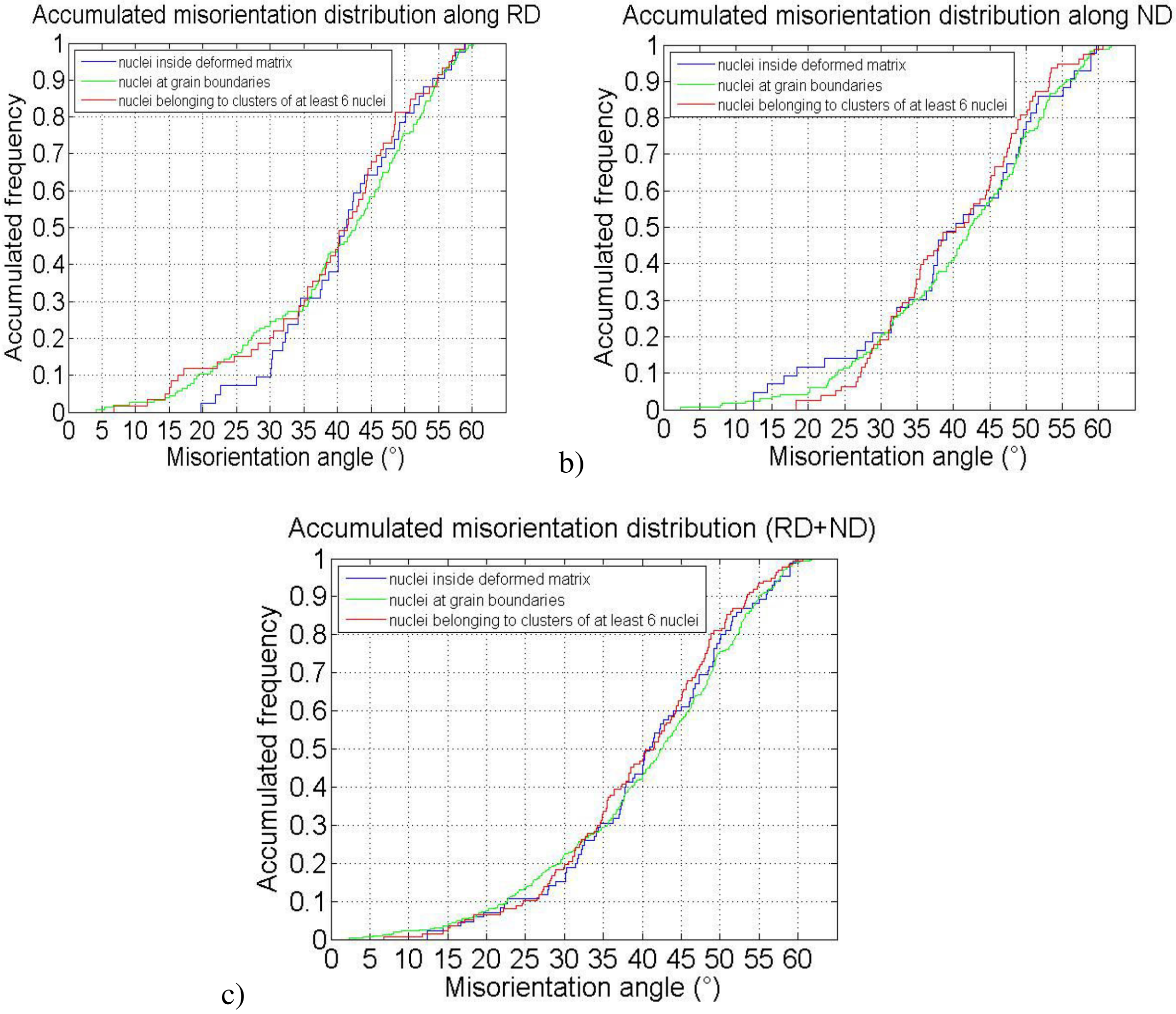

a) b)

c)

Fig. 101. Accumulated frequency distribution of misorientation angles θ between the nuclei and the deformed matrix for all 3 types of nuclei, namely "M", "B" and "C". a) measured along RD, b) measured along ND, c) Both RD and ND combined.

The accumulated misorientation distributions of Fig. 101) are constructed from the misorientation data of Fig. 100, and present the advantage of discarding the artifacts introduced by binning in Fig. 100 (since no binning is required for this type plot). From Fig. 101, it can also be seen that the misorientation distributions are similar for all types of nuclei and along both directions RD and ND, with a higher tendency for angles close to 45° (observed from the higher slopes of the distributions around 45°).

The texture of these initial nuclei is presented in Fig. 102. Their texture mainly consists of components with (100) parallel to ND (see Fig. 102b), among which some cube texture components are present. Some remaining γ fiber components are also present. All in all, there is no particular misorientation relationship between the formation of these nuclei and the surrounding recovered matrix.

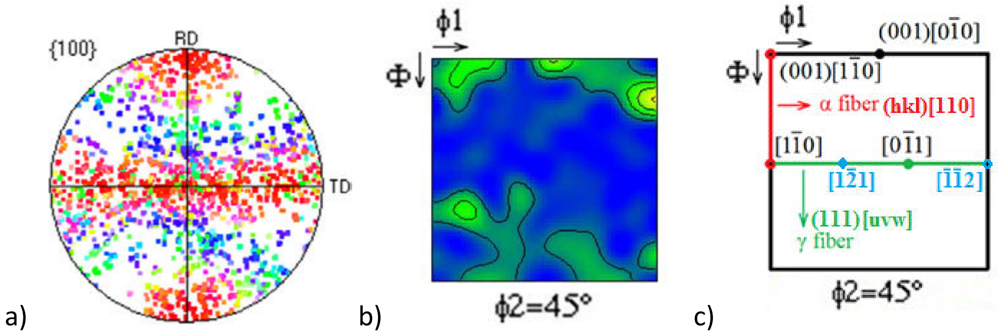

Fig. 102. a) {100} pole figure showing the orientation of the initial nuclei of the sample found after annealing for 1 h at 1250 °C in Fig. 98, with IPF coloring along RD. b) ϕ_2=45° section of the orientation distribution function (ODF) calculated from the orientation data of the nuclei of Fig. 98. c) Sketch of the ϕ_2=45° section of orientation space, indicating the main components of a typical bcc rolling texture: the α fiber (red) and the γ fiber (green), as well as some of their components; the cube $\{001\}<0\bar{1}0>$component, the rotated cube $\{001\}<1\bar{1}0>$ component, and the γ fiber components $\{111\}<1\bar{1}0>$and$\{111\}<\bar{1}\bar{1}2>$.

5.6 Growth

5.6.1 Evolution of texture components during growth

From the evolution of the different texture components during recrystallization, one can assess if the textural evolution during recrystallization is influenced by preferential growth of certain components during recrystallization, and if there is some preference for the consumption of certain deformation texture components by the recrystallizing grains. For this purpose, the volume fraction of each recrystallization and deformation texture component was measured at each stage of recrystallization, during annealing at 1200 °C for both plates W67 and W90. The volume fraction was determined with the software HKL channel 5, and grains with a maximum deviation of ±15° from each ideal orientation were included as being part of that texture component. The results are presented in Fig. 103 and Fig. 104 for the plates W67 and W90 respectively. The miller indices of each ideal orientation are presented in the graph legends.

The total volume fractions of the most relevant deformation and recrystallization texture components are shown in Fig. 103a and Fig. 103b for the plate W67, and in Fig. 104a and Fig. 104b for the plate W90. The recovered matrix without recrystallized grains is also studied separately. The volume fraction of each recovered deformation texture component as a fraction of the total recovered volume is shown in Fig. 103c and Fig. 103d for the plate W67 and in Fig. 104c and Fig. 104d for the plate W90.

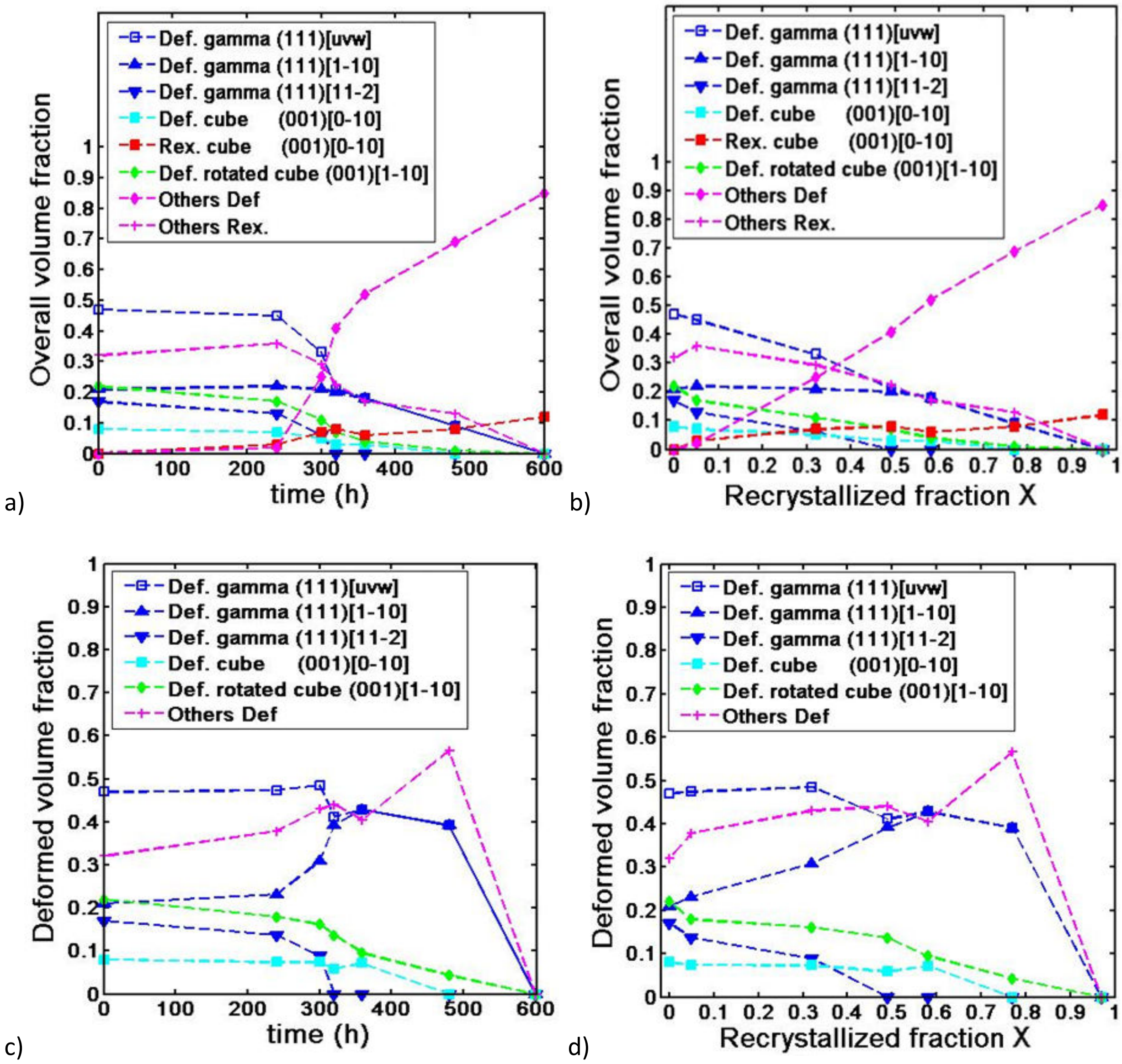

Fig. 103. Evolution of the different texture components (both deformation and recrystallization texture) during recrystallization of the plate W67 at 1200 °C. Evolution of the volume fraction of each component: a) with annealing time; b) with increasing recrystallized fraction during annealing.

Evolution of the volume fraction of the different deformation texture components with respect to the total recovered volume: c) as a function of annealing time; d) as a function of the total recrystallized fraction. Each orientation component is defined with a maximum deviation of ± 15° from the ideal orientation. The miller indices represent each ideal orientation. The terms “Def.” and “Rex.” represent deformation and recrystallization texture components respectively.

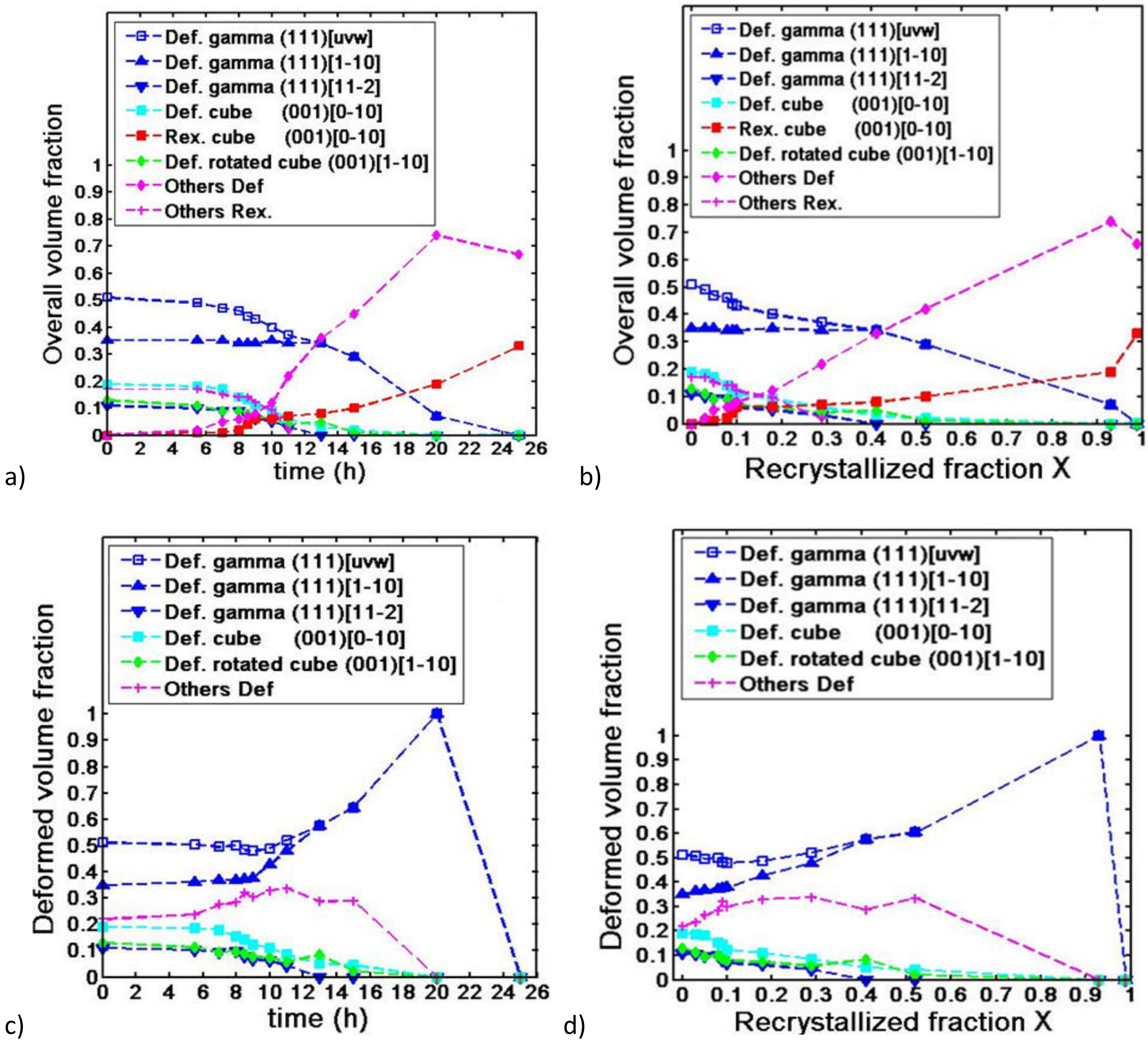

Fig. 104. Evolution of the different texture components (both deformation and recrystallization texture) during recrystallization of the plate W90 at 1200 °C. Evolution of the volume fraction of each component: a) with annealing time; b) with increasing recrystallized fraction during annealing.

Evolution of the volume fraction of the different deformation texture components with respect to the total recovered volume: c) as a function of annealing time; d) as a function of the total recrystallized fraction. Each orientation component is defined with a maximum deviation of ± 15° from the ideal orientation. The miller indices represent each ideal orientation. The terms “Def.” and “Rex.” represent deformation and recrystallization texture components respectively.

Regarding the evolution of the recrystallization texture components during recrystallization, it was only the recrystallized cube component $\{001\}<0\bar{1}0>$ which showed certain predominance in volume fraction with respect to other orientation components, which is why the other recrystallization components were denoted simply as "other". From Fig. 103, it can be seen that only a low fraction of the cube component is present at the later recrystallization stages, while the "other" recrystallized components are more dominating (which indicates no predominance for any other component different than cube). The predominance of the recrystallized cube component is higher for the plate W90, as compared to the plate W67.

During recrystallization, the different deformation texture components seem to have similar consumption rates. This tendency is observed for both plates W67 and W90 in Fig. 103d and Fig. 104d respectively, where the volume fraction of most of the different recovered or non-recrystallized components of the deformation texture seem to decrease similarly during recrystallization. A slower consumption rate is observed however for the more stable γ fiber component $\{111\}<1\bar{1}0>$ as compared to all other components, even as compared to the other γ fiber component $\{111\}<11\bar{2}>$, for both plates W67 and W90. This difference in stability between the two dominating γ fiber components was previously related to the lower stored energy present in the $\{111\}<1\bar{1}0>$ component. The higher stability of the γ fiber component $\{111\}<1\bar{1}0>$ (as compared to the γ fiber component $\{111\}<11\bar{2}>$) is also apparent from the ODFs for only the recovered matrix of the plates W67 and W90 in a partially-recrystallized state. As observed in Fig. 105, the γ fiber component $\{111\}<1\bar{1}0>$ is considerably more present in the recovered matrix than the γ fiber component $\{111\}<11\bar{2}>$, indicating that the former component must be more stable and less consumed during recrystallization.

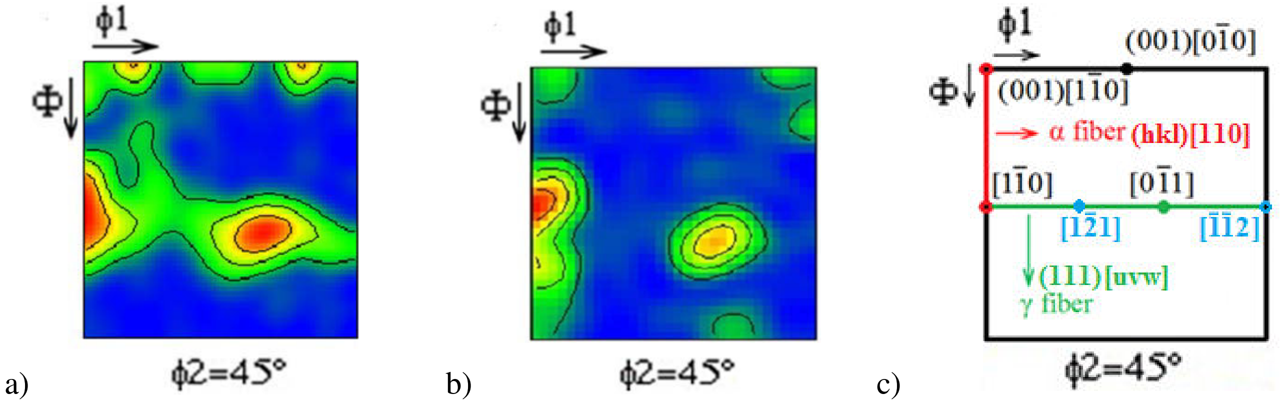

Fig. 105. φ_2=45° section of the ODF calculated from the non-recrystallized (or recovered) part of the microstructure of: a) partially recrystallized (X= 0.32) sample annealed for 300 h at 1200 °C from the plate W67. b) partially recrystallized (X=0.41) sample annealed for 13 h at 1200 °C from the plate W90. Contour lines indicate the orientation density in multiples of a random distribution from 1 to 4. The most dominant orientations (red-shaded regions in Fig. 105a and Fig. 105b) show an intensity 3.7 and 4.9 times above random respectively. The strongest texture component of the recovered matrix in the partly recrystallized

state (in the plates W67 and W90) is the γ fiber component $\{111\}<1\bar{1}0>$. c) Sketch of the ϕ_2=45° section of orientation space, indicating the main components of a typical bcc rolling texture: the α fiber (red) and the γ fiber (green), as well as some of their components; the cube component, the rotated cube $\{001\}<1\bar{1}0>$ component, and the γ fiber components $\{111\}<1\bar{1}0>$ and $\{111\}<\bar{1}\bar{1}2>$.

As mentioned earlier, the appearance of a nearly-random texture after recrystallization can be described by available theories ([50], [114]) from the presence of a $\{001\}<1\bar{1}0>$ component seen in cold-rolled W, which transforms during recrystallization into various recrystallization components by <110> rotations, leading to a nearly-random texture. Although the rotated cube is not the dominant component for any of the as-received plates (where the γ fiber {111}<hkl> dominates), comparison of the textures of the as-received plates W67 and W90 (Fig. 86a and Fig. 89a respectively) reveals in fact a stronger intensity for the rotated cube component $\{001\}<1\bar{1}0>$ in the as-received plate W67 (as compared to the plate W90). Comparison of Fig. 103 and Fig. 104 also reveals the higher presence of this rotated cube component in the recovered plate W67. It could be therefore the consumption of this rotated cube component by the recrystallizing grains which leads to the randomization of the texture in tungsten (as rationalized in [50]) and contributes to the more random recrystallization texture of the plate W67 as compared to the plate W90.

In contrast, recrystallization of the plate W90 (warm-rolled to 90% thickness reduction) leads to a weak recrystallized texture with a stronger recrystallized cube component. The formation of non-random recrystallized textures in tungsten has been observed in highly strained rolled tungsten (after 96% thickness reduction in [103]). In [103], a rotated cube $\{001\}<1\bar{1}0>$ deformation texture leads to a {001}<320> recrystallization texture. However, it must be noted that the plate W90 mainly consists of γ fiber texture components with a dominating component $\{111\}<1\bar{1}0>$ and only a minor rotated cube component; a comparison between these deformation textures is therefore not possible. In the current study, consumption of $\{111\}<11\bar{2}>$ components is the dominating texture evolution mechanism for both plates and leads to a nearly-random texture for both plates. The rotated cube component is more present in the as-received plate W67 which develops weaker cube recrystallization components.

It seems therefore clear that neither the consumption of this γ fiber component $\{111\}<11\bar{2}>$ nor the consumption of the rotated cube component $\{001\}<1\bar{1}0>$ (which should lead to a random texture) can account for the recrystallization cube texture of the plate W90. It is suggested here that the final cube recrystallization texture is not considerably affected by the orientation of the recovered matrix that is consumed during recrystallization. Oriented nucleation of cube nuclei is suggested to be responsible for the near-cube recrystallization texture of the plate W90, rather than oriented growth. In fact, it was observed in subchapter 5.5.2 that the initial nuclei for the plate W90 presented mostly a cube texture. Moreover, the orientation of the nuclei does not seem to depend on the orientation of the surrounding recovered matrix into which they originate, as was demonstrated by the random nuclei-recovered matrix misorientation relationships in subchapter 5.5.3.

5.6.2 Evolution of recrystallized grain size during growth

During recrystallization, the nuclei grow into the recovered matrix by migration of the nuclei boundaries, while no migration is expected where nuclei boundaries impinge upon each other. Average growth rates are often estimated by measuring the average size of the nuclei/recrystallized grains for samples annealed at different times. For this reason, the chord lengths between HABs for the nuclei present at the different stages of recrystallization were measured both along RD and TD (or ND) in the orientation maps. Nuclei growth during recrystallization was tracked during annealing at two different temperatures for the plate W67; namely 1150 °C and 1200 °C. Moreover, nuclei growth was also tracked for the plate W90 during recrystallization annealing at 1200 °C. The results are presented as the chord length increase along RD and TD directions in the case of the plate W67 (see Fig. 106), and the increase along the RD and ND directions in the case of the plate W90 (see Fig. 107).

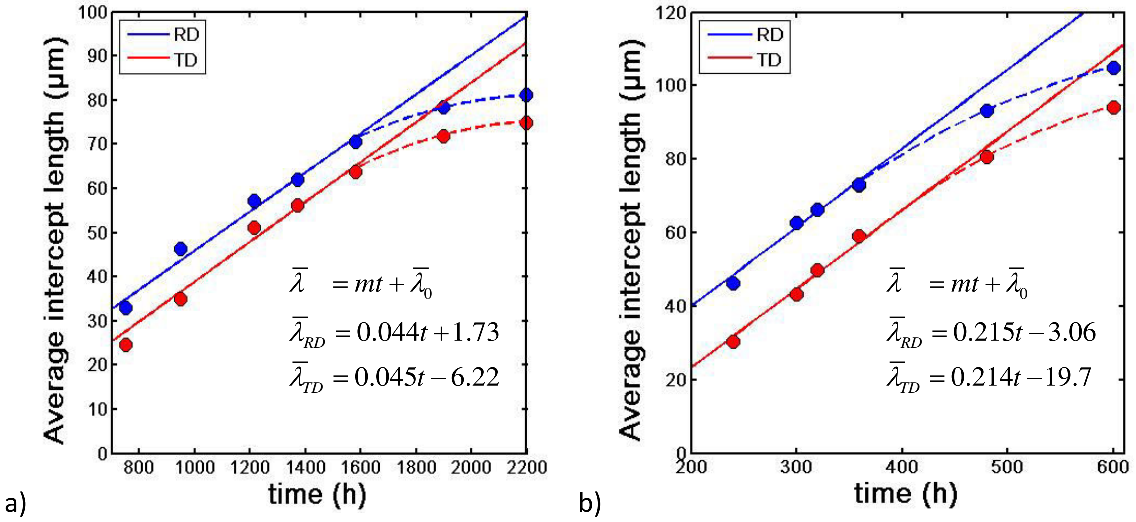

Fig. 106. a) Average size of the nuclei/recrystallizing grains measured as average intercept lengths along RD (blue) and TD (red) after annealing of the plate W67 at a) 1150 °C, and b) 1200 °C. The development of the average size fits a linear relationship with time, except for the two longest annealing times (480 h and 600 h in Fig. 106a, and 1900 h and 2200 h in Fig. 106b), where grain impingement limits the growth of the nuclei considerably.

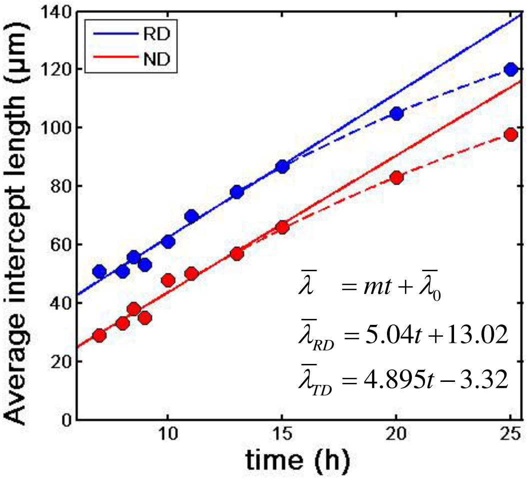

Fig. 107. Average size of the nuclei/recrystallizing grains measured as average intercept lengths along RD (blue) and ND (red) after annealing of the plate W90 at 1200 °C. The development of the average size fits a linear relationship with time, except for the two longest annealing times of 20 h and 25 h, where grain impingement limits the growth of the nuclei considerably.

In Fig. 106, it can be seen that the chord lengths of the recrystallized grains in W67 along both RD and TD directions increase linearly with annealing time up to 359 h and 1582 h for annealing at 1200 °C and 1150 °C respectively (corresponding to a recrystallized fraction of 58% and 69% respectively). In Fig. 107, the chord lengths of the recrystallized grains in W90 along both RD and ND directions increase linearly with annealing time up to 15 h, corresponding to a recrystallized fraction of 52%. In other words, a linear increase of the average intercept length is found with time while the boundaries are free to migrate. Once the moving boundaries impinge upon one another, the increase in chord length with time decreases, as expected from impingement between the recrystallizing grains. From these figures, it is concluded that grain impingement becomes significant after approximately half-recrystallization for both plates W67 and W90.

A first approach to quantify nuclei growth during recrystallization can be done from the slope of the linear fit of the evolution of the chord lengths of the recrystallized grains of Fig. 106 and Fig. 107, for the plates W67 and W90 respectively. Fig. 106 shows an increase in average intercept length during the early stages of recrystallization of the plate W67 of approximately 0.045 μm/h and 0.215 μm/h during annealing at 1150 °C and 1200 °C respectively, being very similar along RD and TD. The nuclei have a larger size by 10-20 μm along RD during recrystallization (compared to TD), which is reduced to approximately 10 μm at the later stages of recrystallization where the recrystallizing grains impinge upon one another. In fact, an almost-equiaxed aspect ratio of approximately 1.1 is observed for the nuclei at annealing stages close to the fully-recrystallized state. This is observed for both annealing temperatures of 1150 °C and 1200 °C in Fig. 106. Therefore, it seems that the aspect ratio of the nuclei of the W67 plate becomes more equiaxed as recrystallization proceeds.

Comparison of both annealing temperatures (1150 °C and 1200 °C) for the plate W67 shows an increase of average intercept length of the recrystallizing grains 4.8 times faster for annealing at

1200 °C, as compared to annealing at 1150 °C. The faster nuclei growth is expected given the higher annealing temperature. One can estimate the average growth rates at 1150 °C (v_{1150}) and 1200 °C (v_{1200}), as well as their ratio, from an Arrhenius relationship, with the activation energy for nucleation and growth determined from the Vickers hardness measurements of the plate W67 ($E_b = 599.5 kJ/mol$) according to Eq. 5.12.

$$\frac{v_{1200}}{v_{1150}} = \frac{v_0 \exp\left(-E_b / RT_{1200}\right)}{v_0 \exp\left(-E_b / RT_{1150}\right)} = 5.6 \qquad (5.12)$$

Eq. 5.12 predicts a ratio of 5.6 which is in good agreement with the ratio of 4.8 obtained from the measurement of the chord lengths. However, this agreement seems purely coincidental, since application of the more realistic Cahn Hagel method leads to a lower ratio of 3.9 (see Table 20).

Fig. 107 shows an increase in average intercept length during the early stages of recrystallization of the plate W90 with approximately 5 µm/h, being similar along RD and ND. A size advantage of 20 µm of the chord length along RD is observed (as compared to ND). An almost equiaxed aspect ratio of 1.2 in the fully-recrystallized state is observed, where the grains become increasingly equiaxed as recrystallization proceeds.

Comparison of the average growth rates at 1200 °C for the plates W67 and W90 yields a considerably faster average growth rate (23 times faster) for the highly strained plate W90. This big difference in average growth rates is expected because of the higher deformation. The much higher deformation of the plate W90 provides the deformed matrix with a considerably higher stored energy (compare Table 12 to Table 13 for the plates W67 and W90 respectively), which is the driving force for the growth of the nuclei into the recovered matrix during recrystallization. The considerably faster growth rate observed for the plate W90 could be entirely due to its faster recrystallization kinetics (as compared to W67), although it could also be affected by the lower activation energy for growth in W90 (as compared to W67). As was presented in Chapter 4, much lower activation energies close to the activation energy for grain boundary diffusion were observed for the plate W90. This argument applies only for annealing temperatures below 1480 °C, since extrapolation of the Arrhenius plots of the recrystallization kinetics of both plates to higher temperatures shows that the slopes of the activation energies for half-recrystallization would crossover (see Fig. 111b). Above 1480 °C, recrystallization kinetics would become theoretically faster for the plate W67 instead.

Assuming that (almost) spherical grains grow freely without impingement restrictions and no new nuclei appear, the average intercept length increase rate can be converted to a boundary migration rate/growth rate by dividing with a stereological factor 4/3 [111]. This allows for a stereological conversion of the two-dimensional data obtained on a section with EBSD into a three-dimensional interpretation. In this manner, the present data suggest a growth rate of about 0.034 µm/h and 0.160 µm/h for the early stage of recrystallization of the plate W67 during annealing at 1150 °C and 1200

°C respectively. A growth rate of about 3.8 µm/h is calculated for the early stage of recrystallization of the plate W90 during annealing at 1200 °C.

A much more precise (but also more labor-intense) method to determine growth rates during recrystallization has been proposed by Cahn and Hagel ([118], [119]). The Cahn Hagel method takes the impingement between recrystallized grains properly into account by considering the density S_v of the boundary area between nuclei and the recovered matrix. The surface density S_v was obtained in this work from the EBSD data using the software DRG. The advantage of the Cahn-Hagel method is that it realistically assumes that impinged boundaries cannot migrate. Another advantage is that it only needs a good description of the evolution of the recrystallized fraction over time (dX / dt), so that more complex parameters such as nucleation sites and rates need not be taken into account. Although the original Cahn-Hagel model is based on the calculation of the transformation rate of the pearlite phase during austenitic decomposition in steel, the model is equally applicable to recrystallization of pure metals like tungsten. The average growth rate (G) at each recrystallization stage can be calculated using the Cahn Hagel method via the expression (Eq. 5.13),

$$G = \frac{dX / dt}{S_v} \qquad (5.13)$$

where X is the volume fraction of recrystallized material, t is the annealing time and S_v is the density of total interfacial area between recrystallized and recovered material (or non-impinged nuclei boundary area).

It shall be noted that the description of the recrystallized fraction X over annealing time t is already available from JMAK recrystallization kinetics, which were defined using Vickers hardness data in chapter 4 for both plates W67 and W90 at all annealing temperatures. Therefore, the derivative (dX / dt) at each annealing stage can be easily calculated from JMAK recrystallization kinetics accounting for an incubation time t_{inc},

$$X = 1 - \exp\left(-b^n \left(t - t_{inc}\right)^n\right) \qquad (4.4)$$

$$dX / dt = -\exp\left(-b^n \left(t - t_{inc}\right)^n\right) \cdot d\{-b^n \left(t - t_{inc}\right)^n\} / dt$$

$$dX / dt = -\exp\left(-b^n \left(t - t_{inc}\right)^n\right) \cdot b^n n \left(t - t_{inc}\right)^{n-1} \qquad (5.14)$$

where the coefficient b, the Avrami exponent n, and the incubation time t_{inc} were calculated before by fitting hardness data to JMAK kinetics with an incubation time t_{inc} in chapter 4, for each plate and annealing temperature.

This allows to calculate an average growth rate $<G>$, by averaging the growth rates at each recrystallization stage. As a clarifying example, Table 19 lists all the relevant parameters as well as the calculated growth rate at each condition during annealing at 1200 °C from the plate W90, leading to an average growth rate $<G> = 4.6\ \mu\mathrm{m}/\mathrm{h}$

Table 19. Table with the relevant data for the calculation of the average Cahn Hagel growth rate of the recrystallizing grains during annealing of the plate W90 at 1200 °C; t (h) is the annealing time at 1200 °C, X_{EBSD} and S_v are the recrystallized fraction and the density of boundaries between nuclei and recovered matrix respectively (as measured using the software DRG), *dX/dt* is the derivative of the recrystallized fraction with annealing time as calculated from JMAK recrystallization kinetics in Eq. 5.14, and G is the growth rate for each annealing stage as calculated from Eq. 5.13. The average growth rate $<G> = 4.6\ \mu\mathrm{m}/\mathrm{h}$ is therefore the average of all the growth rates shown in the table.

Plate W90. Annealing time at 1200°C t (h)	X_{EBSD}	S_v (1/µm)	dX / dt	G (µm/s)	G (µm/h)
7	0.05	0.00387	0	0	0
8	0.08	0.00605	$5.63 \cdot 10^{-06}$	0.00093	3.35
8.5	0.09	0.00693	$8.34 \cdot 10^{-06}$	0.00120	4.32
9	0.1	0.00933	$1.09 \cdot 10^{-05}$	0.00117	4.21
10	0.18	0.01250	$1.56 \cdot 10^{-05}$	0.00125	4.49
11	0.29	0.01501	$1.93 \cdot 10^{-05}$	0.00129	4.64
13	0.41	0.01578	$2.36 \cdot 10^{-05}$	0.00150	5.38
15	0.52	0.01484	$2.36 \cdot 10^{-05}$	0.00159	5.72
20	0.93	0.00492	$1.31 \cdot 10^{-05}$	0.00147	5.29
25	0.99	0.00300	$3.71 \cdot 10^{-06}$	0.00124	4.46

The calculated average growth rates $<G>$ using all three different methods are summarized in Table 20.

Table 20. Summary of the different average growth rates $< G >$ calculated for the different annealing conditions using different calculation methods. First, the growth rates were studied from the evolution of the average intercept lengths of the recrystallized grains (simple linear intercept method). Secondly, the former average growth rates were divided by the stereological factor 4/3. Finally, growth rates were calculated using the Cahn Hagel method [118].

Calculation method / **Annealing condition**	2D linear intercepts	3D conversion factor 4/3	Cahn Hagel
Plate W67 annealed at 1150 °C	0.045 µm/h	0.034 µm/h	0.055 µm/h
Plate W67 annealed at 1200 °C	0.215 µm/h	0.16 µm/h	0.217 µm/h
Plate W90 annealed at 1200 °C	5 µm/h	3.8 µm/h	4.6 µm/h

The values calculated using the Cahn-Hagel method (for both plates W67 and W90) are slightly larger than those determined by dividing the growth rates calculated using the linear intercept method by the stereological factor 4/3. This is expected because even at the early stages of recrystallization (e.g. Fig. 51 for the plate W67 ; Fig. 73 for the plate W90), some nuclei already impinge upon each other, so not all boundaries are free to migrate and the growth of the nuclei must be achieved by a larger growth rate of the movable boundaries.

The evolution of the interfacial area between the nuclei and the recovered matrix (S_v) is presented as a function of the total recrystallized fraction (X) for all annealing stages of all 3 annealing conditions of Table 20 (see Fig. 108). As can be observed in Fig. 108, the interfacial area S_v at all 3 annealing conditions increases as recrystallization proceeds until a maximum is reached close to the half-recrystallized state. This is attributed to nucleation of new nuclei and growth of the existing nuclei, since both phenomena increase the contact area between the recovered matrix and the nuclei. After half-recrystallization, a decrease of the interfacial S_v is observed which is attributed to the impingement of the nuclei boundaries with other nuclei. This impingement renders the nuclei boundaries immobile and hinders further growth.

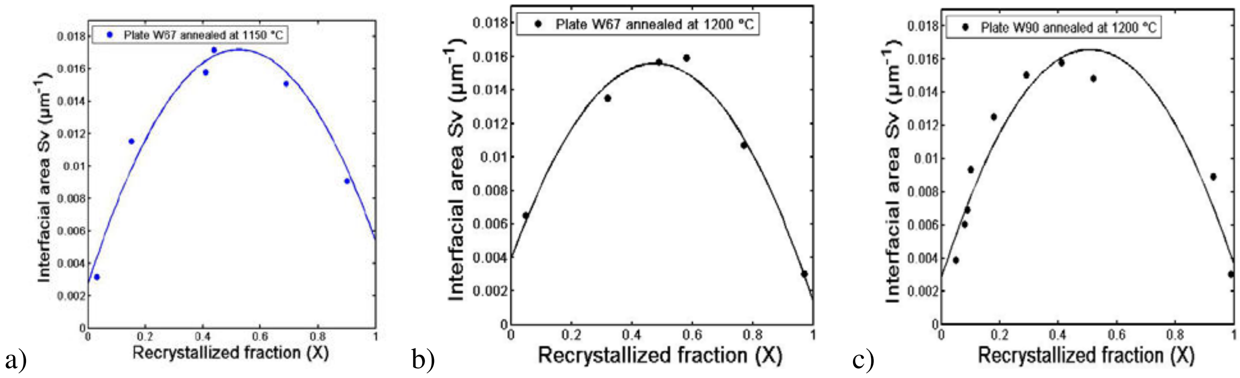

Fig. 108. Evolution of the interfacial area between the nuclei and the recovered matrix (S_v) as a function of the recrystallized volume fractions as determined by EBSD (X) for different annealing conditions: a) Plate W67 annealed at 1150 °C, (b) Plate W67 annealed at 1200 °C, (c) Plate W90 annealed at 1200 °C. The data have been fitted to a 2nd degree polynomial (solid lines).

5.7 Correlations between hardness and microstructural evolution

The recrystallized volume fractions X_{EBSD} of the recrystallized grains obtained from EBSD orientation maps were estimated using the in-house DRG software for the different annealing conditions and compared to the recrystallized volume fractions X_{HV} estimated from the Vickers hardness measurements (chapter 4). The data from the plate W67 is compared for all three annealing temperatures at which EBSD orientation maps were available; namely 1150 °C, 1200 °C and 1250 °C (Fig. 109).

Analogously, the data from the plate W90 are compared at the available annealing temperature of 1200 °C (Fig. 110). As indicated by the line $X_{EBSD} = X_{HV}$ of Fig. 109 (and also Fig. 110), both values match rather closely for all annealing temperatures and for both plates W67 and W90. This confirms not only the validity of the composite approach for calculating the hardness of partially recrystallized samples (Eq. 3.2), but also the method of identifying recrystallized regions by EBSD.

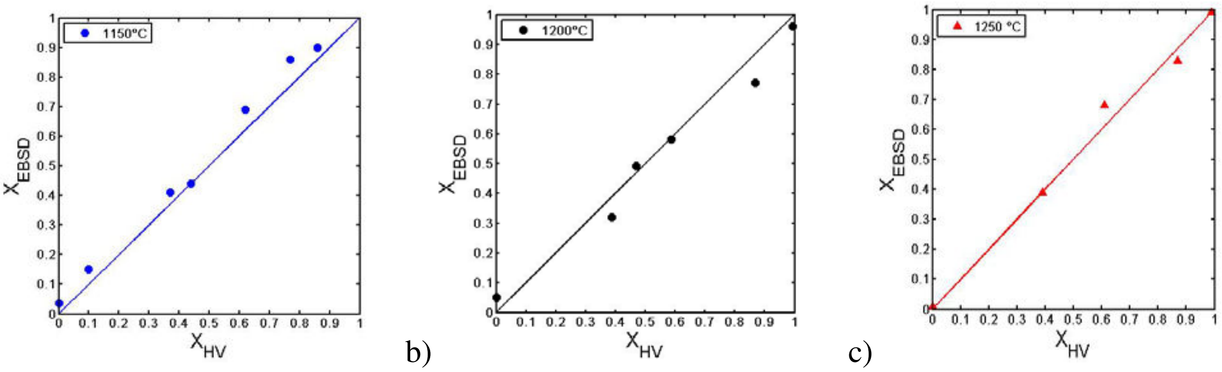

a) b) c)

Fig. 109. Recrystallized volume fractions as determined by EBSD and estimated from Vickers hardness measurements on warm-rolled tungsten W67 after annealing at 1150 °C (a), 1200 °C (b) and 1250 °C (c). The lines represent the ideal correlation $X_{EBSD} = X_{HV}$.

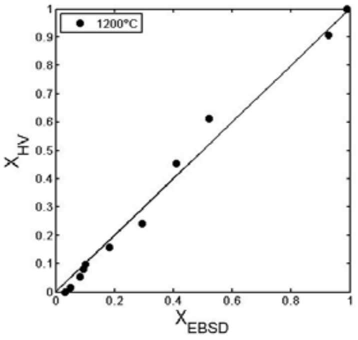

Fig. 110. Recrystallized volume fractions as determined by EBSD and estimated from Vickers hardness measurements on warm-rolled tungsten W90 after annealing at 1200 °C. The line is represents the ideal correlation $X_{EBSD} = X_{HV}$.

5.8 Summary of Chapter 5

The microstructure of two warm-rolled plates to 67% and 90% thickness reduction (W67 and W90 respectively) was characterized. Both plates present a relatively coarse initial microstructure. The plates W67 and W90 present a more equiaxed microstructure (or lower aspect ratio) than would be theoretically expected from the rolling reduction. Dynamic recrystallization is given as a possible cause for the difference between the theoretically expected and the experimental aspect ratio. The stored energy of the different texture components of the plates W67 and W90 was also studied from LAB spacing measurements. It was found that the average misorientation of the LABs was similar for all texture components within the same plate. A lower stored energy for the γ fiber component $\{111\}<1\bar{1}0>$ and a higher stored energy for the γ fiber component $\{111\}<11\bar{2}>$ was found for both plates, as calculated from the difference in the LAB spacing. A considerably higher stored energy as well as a higher misorientation for the LABs was found for the plate W90, expected given its higher deformation as compared to W67.

The recovery behavior was studied microstructurally during isothermal annealing at 1250 °C of the plate W67 and for grains of the most abundant orientation $\{111\}<1\bar{1}0>$. The logarithmic relationship elucidated by Kuhlmann is also met as an increase of the subgrain size or decrease of the specific surface of LABs (S_v), in good agreement with the mechanical characterization of Chapter 4. In fact, a linear relationship was obviously found between the decrease in hardness of the material and the subgrain size coarsening during recovery annealing. A linear increase of the misorientation angle of the LABs with subgrain coarsening during recovery was observed, showing that the average misorientation of the LABs increases as recovery proceeds. This behavior could be reasonably well defined by Eq. 5.5.

The long-term recrystallization kinetics of the plates W67 and W90 warm-rolled to different reductions were fully-characterized microstructurally via EBSD. It was found that the initial coarse deformed microstructures become replaced by a coarser and equiaxed recrystallized microstructure for both plates. As previously observed in the mechanical characterization of Chapter 4, the plate W90 shows much faster recrystallization kinetics than the plate W67, indicating that the rolling strain has a tremendous effect in accelerating recrystallization kinetics. A very good fit was found between the recrystallized fractions calculated with EBSD and those calculated mechanically in Chapter 4 (see section 5.7). This confirms the validity of the method to detect recrystallized regions with EBSD as well as the validity of the composite approach that considers the material to consist of both recovered and recrystallized regions.

The as-received textures of the plates were found to be typical rolling textures of bcc metals. The recrystallization texture for the plate W67 was almost random. A clear preference for the recrystallization of cube components was found for the most highly strained plate W90. It is suggested that the initial higher strain promotes the nucleation of cube components. Therefore, oriented nucleation was found as the cause for the development of cube components in the recrystallized textures.

Regarding nucleation density evolution during recrystallization, a tendency for site-saturation was found for the plate W67, while a tendency for a constant nucleation rate was found for the plate W90 microstructurally. This difference was explained in terms of the smaller grain size or higher density of original grain boundaries of the plate W67, since grain boundaries act as potential nucleation sites. The change of nucleation regime allowed to microstructurally justify that the plate W67 showed an Avrami exponent (*n*=1.1) 1 unit lower than the Avrami exponent for the plate W90 (*n*=2). In fact, a constant nucleation rate is expected to show an Avrami exponent higher by 1 unit as compared to site-saturation.

Regarding nuclei growth during recrystallization, it was found that the deformed γ fiber component $\{111\}<1\bar{1}0>$ was more stable (or less consumed by the growing recrystallized nuclei) during recrystallization for both plates. The higher stability of this specific texture component was not previously reported in literature, and is related in this work to the much lower stored energy content of the $\{111\}<1\bar{1}0>$ component as compared to other main deformed texture components. The size of the recrystallizing nuclei increased linearly with annealing time for both plates, until the migrating grain boundaries of the recrystallizing nuclei impinged on other nuclei.

Recrystallized grain sizes were calculated using the simple linear intercept method and also using the more elaborate Cahn-Hagel method, which accounts for a 3D interpretation of the data as well as for grain boundary impingement during recrystallization. As expected, it was observed that growth rates were faster for higher initial strain and higher annealing temperatures.

CHAPTER 6

Discussion

6.1 Recovery

The use of logarithmic recovery kinetics (expression of Eq. 4.2 in chapter 4), successfully described the decrease in hardness during the early stage of annealing. The coefficients $C/T = 3.1 \cdot 10^{-3}\ (1 \pm 8\%)\ \text{kgf K}^{-1}\text{mm}^{-2}$ and $C/T = 4.2 \cdot 10^{-3}\ (1 \pm 4\%)\ \text{kgf K}^{-1}\text{mm}^{-2}$ were obtained from the hardness characterization of the plates W67 and W90 respectively, which are related to the speed of the recovery kinetics. Comparison of both coefficients reveals faster recovery kinetics for the most highly-deformed plate (W90). This is expected since a higher deformation will induce a higher stored energy in the form of dislocations, which is the driving force for recovery.

It is also speculated that an additional reason for the faster recovery kinetics of the plate W90 could be a change in diffusion mechanism. In reference [102], recovery was tracked in aluminum polycrystals by measuring with electron microscopy the reduction of Trapped Lattice Dislocations near grain boundaries, during annealing before the start of recrystallization. Fig.4 of reference [102] shows a plot of the parameter C vs T, from which the average relationship C/T can be calculated. The approximate values $C/T = 2.8 \cdot 10^{-4}\text{kgf K}^{-1}\text{mm}^{-2}$ and $C/T = 4 \cdot 10^{-4}\text{kgf K}^{-1}\text{mm}^{-2}$ were deduced for recovery of aluminum polycrystals of low and high self-diffusivity respectively, in the temperature range 293-403K [102]. Both tungsten and aluminum are metals of high stacking fault energy in which cross-slip is easy and significant recovery occurs. Therefore, the speed of the recovery kinetics seems to be related to the low/high self-diffusivity in the same way for both the tungsten plates of this work and the aluminum polycrystals of reference [102].

The coefficient C/T has a physical interpretation in terms of dislocation mobility: it is inversely proportional to how far a dislocation can travel (i.e. activation volume V) before being trapped by another obstacle in the material (e.g. another dislocation), as expressed by Eq. 2.4 [31]. Therefore, the lower coefficient C/T for the plate W67 indicates that in this material dislocations can move along a wider area because of the lower dislocation density (as compared to the plate W90). Dislocations act as obstacles for dislocation motion.

Eq. 2.4 also allows the calculation of the activation volume of both plates ($V_{67} = 1.36 \cdot 10^{-27}$ m^3 ; $V_{90} = 1 \cdot 10^{-27}$ m^3) from the Boltzman constant (k = $1.38 \cdot 10^{-23}$ Nm/K) and the coefficients C/T for each plate W67 and W90 ($C/T = 30400\ (1 \pm 8\%)\ \text{N m}^{-2}\text{K}^{-1}$, and $C/T = 41200\ (1 \pm 4\%)\ \text{N m}^{-2}\text{K}^{-1}$ respectively). This activation volume can be more conveniently represented at the atomic scale, in terms of the Burgers vector ($b = 2.74 \cdot 10^{-10}\,\text{m}$), which represents the closest distance between atoms in the tungsten bcc crystal lattice. An activation volume $66b^3$ and $49b^3$ (times the cubic Burgers vector) was found for the plates W67 and W90 respectively.

The validity of logarithmic recovery kinetics was additionally proved microstructurally, where the increase of subgrain size during recovery for grains of orientation $\{111\}<1\bar{1}0>$ (± 15°) from the plate W67 also followed the logarithmic kinetics of Eq. 4.2 with annealing time (see Fig. 45b). Subgrain sizes found in literature on rolled tungsten before recovery annealing are comparable to the subgrain sizes of 2 μm and 0.67 μm of the as-received plates W67 and W90 respectively: moderately hot-rolled tungsten with 1.5 μm as the most probable cell size [28], warm-rolled tungsten to 75% thickness reduction with subgrain size 1.5-2 μm [27], warm-rolled to 4 rolling passes potassium doped tungsten with subgrain size 1-2 μm [19]. However, measured values of subgrain size evolution during recovery annealing in tungsten were not found in literature. Other literature studies (e.g. [34], [35]) showed that the decrease of electrical resistivity during recovery in tungsten also followed logarithmic recovery kinetics. The current work additionally shows that logarithmic recovery kinetics are also followed in tungsten as a decrease in hardness and an increase of the subgrain size during recovery.

6.2 Recrystallization

Temperatures of 1395°C and 1345°C are required to achieve the half-recrystallized state after 1 h annealing for the tungsten plates of this study (W67 and W90 respectively). The recrystallization temperature is a parameter that allows an easy overview and comparison of recrystallization kinetics. A few recrystallization temperatures similar to those observed in the current study were found in literature (i.e. [11], [27], [120], [121], [46]) and described in more detail below:

Mathaudhu et al. [11] studied the recrystallization behavior of PM hot-deformed (extruded) tungsten as a function of the applied strain and working temperature at 1000 °C and 1200°C. Specimens were annealed in the temperature range 400-1600°C for 1 h and the recrystallization process tracked via Vickers hardness indentation and SEM. The obtained recrystallization temperature was 1400 °C (comparable to that of the plate W67) and found to be independent of strain (number of extrusions) and working temperature. In contrast to these findings, it is well known that the recrystallization temperature decreases with increasing strain or rolling reduction [21].

Yuan et al. [27] report a recrystallization temperature of 1330 °C after 1 h annealing (comparable to that of the plate W67) for a high-purity tungsten plate warm-rolled at 1200 °C and manufactured by the same company AT&M. The fact that in [27] the furnace was heated with the samples inside at a very slow heating rate (2 K/min), and the samples cooled down inside the furnace, can account for the fact that this 75% plate shows slightly lower recrystallization temperature.

Stepper [120] studied recrystallization of powder metallurgy heavily-drawn undoped tungsten wires. The exact amount of deformation and impurity content are not mentioned. The wires were first irradiated with α particles and then isochronally annealed for 45 min. at 1400°C, 1600°C and 2200°C. The unirradiated portion had already recrystallized after 45min. annealing at 1400 °C. This temperature is comparable to the recrystallization temperatures after 45min. for both plates of the current study; namely 1405 °C and 1365 °C for the plates W67 and W90 respectively.

Lavrenko et al. [59] report a recrystallization temperature of 1350 °C after 2 hours annealing for powder metallurgy high purity tungsten deformed via compression to 40% height reduction. The plate W67 shows a perfectly comparable recrystallization temperature of 1365 °C after 2 hours annealing. It seems logical that tungsten similarly-deformed (moderately in both cases) shows similar recrystallization temperature.

Xiao-Xin et al. [64] provide a temperature of 1400 °C for half-hardness loss of a rolled (to 45% thickness reduction) pure tungsten plate after 2 h annealing. The plate W67 requires annealing at 1370 °C for 2 h to reach half-hardness loss. These two temperatures are comparable, and the fact that this temperature is 35 K lower for the currently studied plate could be explained by its higher reduction or higher stored energy.

However, most literature studies on tungsten provide different recrystallization temperatures (e.g. [14], [55], [122], [123] …). As an example, the previously mentioned studies provide less comparable recrystallization temperatures of 1300 °C [14], 1200 °C [55], 1250 °C and 1190 °C (for 67% and 90% thickness reduction respectively [122]) and 1550-1600 °C [123] after 1h annealing. The main reason for these different values is that recrystallization kinetics are not easily comparable due to different starting sintered tungsten conditions, working conditions and purity. Unfortunately, these conditions are rarely reported in literature.

Comparison of the parameters $t_{\Delta HV/2}$, $t_{X=0.5}$, t_{inc} and b for the plates W67 and W90 (obtained in Chapter 4 on hardness characterization) shows considerably faster recrystallization kinetics for the plate W90, as observed by the higher values of these parameters for the plate W90 (as compared to W67; see Fig. 111).

In fact, a much faster increase of the recrystallized fraction X_{HV} (estimated from Vickers hardness measurements) is observed at all temperatures for the plate W90, as compared to the plate W67 (compare Fig. 33 and Fig. 27). The same trend is observed microstructurally, as can be observed from the good fit of the recrystallized fraction estimated with Vickers hardness (X_{HV}) and microstructurally via EBSD (X_{EBSD}) shown in Fig. 109 and Fig. 110 for the plates W67 and W90 respectively. The physical explanation for this faster recrystallization kinetics for the plate W90 (as compared to the plate W67) is the higher stored energy of the as-received deformed matrix of the plate W90 (ΔU_{90} = 2018 kJ/m^3) as compared to the plate W67 (ΔU_{67} = 611 kJ/m^3), as it corresponds to higher deformations.

6.2.1 Nucleation

The fitted JMAK recrystallization kinetics show Avrami exponents n with only minor deviations from a common average value of 1.1 for the plate W67 and 2 for the plate W90. The lower exponent n obtained for the plate W67 (as compared to that of the plate W90) was explained by microstructural considerations in subchapter 5.5.1 during nucleation: site-saturated nucleation is observed for the plate W67, whereas a constant nucleation rate regime is found for the plate W90. Indeed, constant nucleation for the plate W90 is expected to lead to an Avrami exponent n higher by 1 unit as compared to site-saturation occurring in the plate W67 [21]. Nucleation occurs mostly at favorable nucleation sites (i.e. grain boundaries and triple junctions), as was observed in Fig. 98 of subchapter 5.5.3 for an early recrystallization stage.

Assuming nucleation at grain boundaries, which are potential nucleation sites, a reason for site-saturation occurring for the plate W67 could be its higher grain boundary area, given the smaller grain size of the plate W67 as compared to the plate W90. HABs are sites of localized high stored energy and misorientation gradients, and therefore HABs and especially triple junctions (sites where 3 HABs meet) are preferable nucleation sites; much more than the local misorientation gradients found at grain interiors (e.g. at less favourable nucleation sites like subgrains and other highly misoriented regions like transition bands and shear bands [39]). The higher presence of HABs for the plate W67 can be observed in subchapter 5.1.1 for the as-received microstructure of both plates observed in the rolling plane (Fig. 37). From Fig. 37, the values for the specific surface density of High Angle Boundaries were calculated as $S_{V,HAB} = 0.055$ µm^{-1} and $S_{V,HAB} = 0.037$µm^{-1} for the plates W67 and W90 respectively (see Table 11). The plate W67, with a higher surface density of HABs, will present more potential nucleation sites which require a lower thermal activation energy for nucleation. Therefore, nucleation at earlier stages of recrystallization is more likely for the plate W67 as compared to the plate W90. This is in good agreement with the site-saturation behavior found for the plate W67.

6.2.2 Growth

Regarding growth, the stored energy of the recovered matrices is the driving force for growth, and grains are expected to grow faster through recovered matrices of higher average stored energy. The average growth rate was found microstructurally to be 23 times faster for the plate W90 as compared to the plate W67 (for annealing at 1200 °C and calculated via the linear intercept method; see Table 19). Growth could also be studied from hardness measurements indirectly, from the Avrami coefficient b which represents the speed of recrystallization kinetics (which includes both nucleation and growth) without the dependence of the Avrami exponent n. Higher values for the coefficient b^{-1} were found for the plate W90 as compared to the plate W67 (compare Fig. 36 to Fig. 30). The values of b^{-1} for the plate W67 are close to the other parameters $t_{\Delta HV/2}$, $t_{X=0.5}$, t_{inc} (see Fig. 30). However, for the plate W90 the values of b^{-1} are considerably higher than the other parameters $t_{\Delta HV/2}$, $t_{X=0.5}$, t_{inc} (see Fig. 36). It was suggested that this difference in the exponent b^{-1} was due to the faster growth rate of the plate W90. The faster growth rate for the plate W90 is discussed in terms of its higher stored energy due to the higher deformation. Therefore, it is concluded that the coefficient *b* showed considerably faster growth kinetics for the plate W90 as compared to the plate W67 (see Fig. 111c). No considerable orientation growth preference was found microstructurally for any texture component. In fact, the predominance of the recrystallized cube orientation (especially for the plate W90) could be explained by oriented nucleation alone. For this reason, growth rates were treated as an average for all orientations.

6.3 Activation energies

As estimated from Vickers hardness measurements, the activation energy 352 kJ/mol for half recrystallization of the plate W90 is significantly lower than the value 579 kJ/mol obtained for half recrystallization of the plate W67 (see Fig. 111).

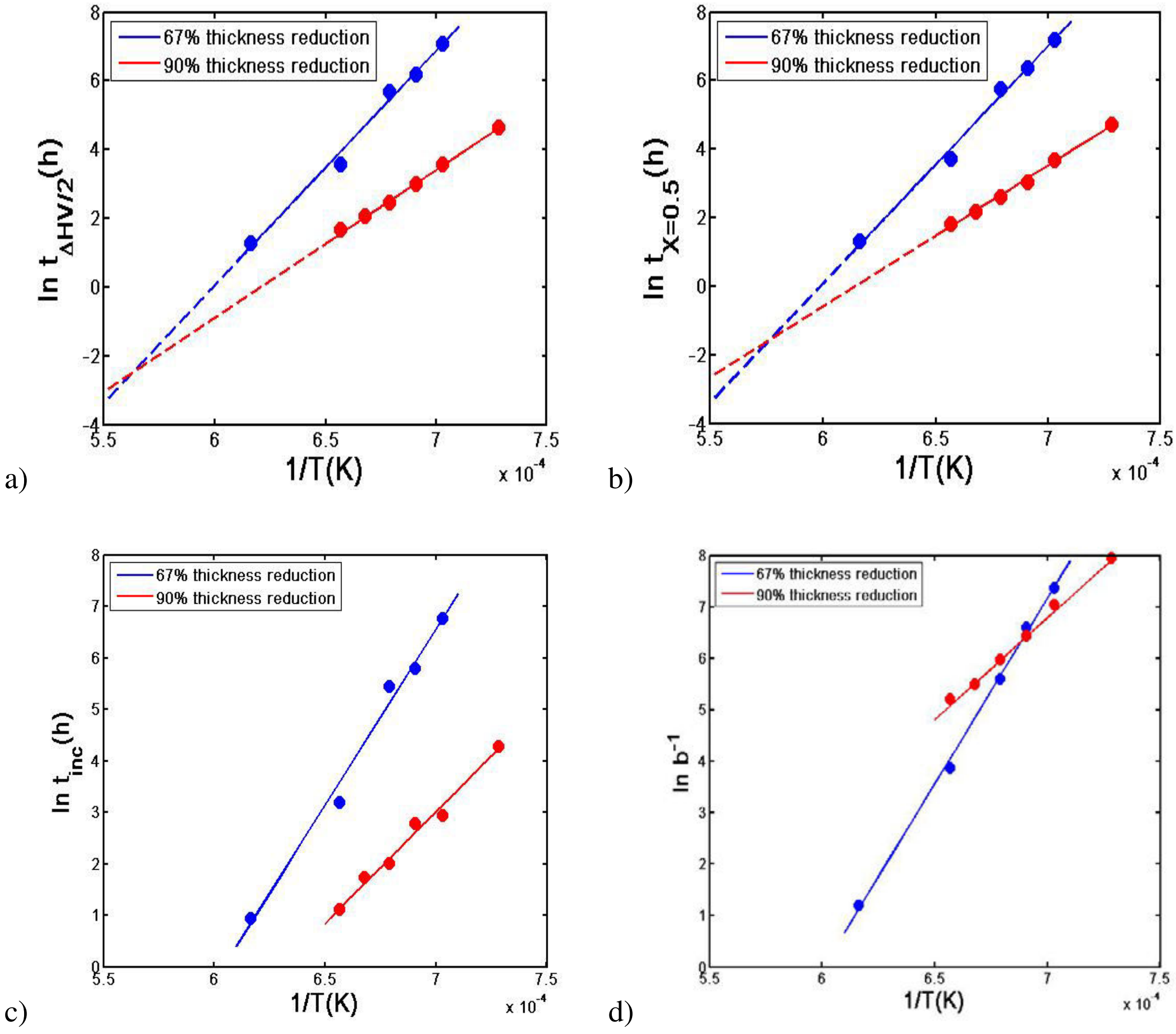

a) b) c) d)

Fig. 111. Arrhenius plot in dependence on the annealing temperature for both plates W67 and W90 of: a) time to reach half-hardness, b) time to reach half-recrystallization (as calculated using JMAK recrystallization kinetics), c) incubation time, d) parameter b^{-1}.

The times to reach half-hardness and half-recrystallization are very similar, and show faster recrystallization kinetics for the plate W90 due to its higher deformation (as compared to W67). From the slopes of the linear fits, the activation energies for half-hardness loss were calculated as ($E_{67\Delta HV/2} = 568$ kJ/mol) and ($E_{90\Delta HV/2} = 357$ kJ/mol) for the plates W67 and W90 respectively. The activation energies for half hardness loss were very similar to those for half-recrystallization: namely ($E_{67X=0.5} = 579$ kJ/mol) and ($E_{90X=0.5} = 352$ kJ/mol) respectively.

The activation energy for nucleation in the plate W90 ($E_{90t_{inc}} = 369$ kJ/mol) is considerably lower than that of the plate W67 ($E_{67t_{inc}} = 568$ kJ/mol). The shorter incubation times and lower activation energy for the plate W90 (as compared to W67; see Fig.110b) can be explained by the higher stored energy and higher orientation gradients present in the plate W90, which lead to the presence of potential nucleation sites which require a lower activation energy for nucleation (as compared to W67).

The parameter b^{-1} represents recrystallization kinetics in terms of nucleation and growth. The activation energy for nucleation and growth in the plate W90 ($E_{90b} = 328$ kJ/mol) is considerably lower than that of the plate W67 ($E_{67b} = 599.5$ kJ/mol). The higher difference between these two activation energies (as compared to the difference between the activation energies for nucleation of the last paragraph) is speculated to be due to the contribution of growth.

All these activation energies are within the range of the activation energy for grain boundary diffusion in tungsten $E_{GbD.vol} = 377-460 \text{ kJ/mol}$ for the plate W90 and the activation energy for bulk diffusion in tungsten $E_{SD.vol} = 586-628 \text{ kJ/mol}$ for the plate W67 [15]. Apparently, there is a change in atomic jump mechanism (a local effect at the HABs of the recrystallizing nuclei) from one with activation energy close to that of bulk diffusion to one with activation energy close to that of grain boundary diffusion. It is speculated by the author that another possibility is that the diffusion mechanism itself could change: bulk diffusion could dominate during recrystallization of the plate W67, while grain boundary diffusion (with a lower activation energy) could dominate during recrystallization of the plate W90. An important factor contributing to the faster recrystallization kinetics of the plate W90 could be the change to a grain boundary diffusion mechanism during recrystallization for the plate W90. However, there is no experimental evidence to prove a change in diffusion mechanism.

One reason for the change from the high activation energy of bulk diffusion to the lower activation energy of grain boundary diffusion for the highly-deformed material might be the presence of an abundance of LABs for the plate W90. As can be seen from the EBSD grain boundary map of Fig. 41, the spacing between low angle boundaries in the as-rolled plate W90 is only 0.67 µm, whereas in the as-rolled plate W67 LABs are still 2.0 µm apart. It is suggested that the presence of a higher fraction of LABs and a lower spacing between LABs for the plate W90 could aid the motion of tungsten atoms through the HAB interfaces between the recrystallizing nuclei and the recovered matrix that is required during recrystallization, therefore requiring a lower activation energy for tungsten diffusion during recrystallization. The decrease of the activation energy of recrystallization with increasing deformation could be the reason why the high purity (99.99%) W wires of 50 µm and 250 µm diameter of [53] present activation energies of 280 kJ/mol and 544 kJ/mol respectively. Notice that the wires with lower and higher diameter (possibly worked to a higher and lower strain respectively) show recrystallization activation energies which are comparable to grain boundary diffusion and bulk diffusion respectively, and in good agreement with the findings of this work. However, [53] does not specify if the lower diameter is due to a higher deformation strain, nor whether the starting material and processing conditions of both wires were the same. In fact, the activation energies of [53] are simply reported and never related to the deformation strain of the starting wires.

With the obtained values for the activation energies for the plate W67, the long-term annealing kinetics observed at temperatures of 1150 °C can be extrapolated to even lower temperatures. In this case, the Arrhenius fit of Fig. 30 was extrapolated to lower temperatures. Such an attempt allows prediction of characteristic time spans at various temperatures. Both the maximum operation temperature at which these plasma facing components would show a lifespan of at least 2 years, as well as the lifespan at a feasible operation temperature of 800 °C, have been extrapolated. For the plate W67, at 1075 °C and 800 °C (possible temperatures at the divertor in a fusion reactor [124]) half recrystallization would be achieved after 2.3 (1± 40%) years and not before 1 million years respectively, providing a sufficient lifespan for a potential application of this tungsten plate material in fusion reactors. Analogously, the annealing kinetics for the plate W90 were also extrapolated to lower temperatures using the activation energy obtained from the Arrhenius fit of Fig. 36. Accordingly, at 900 °C and 800 °C (expected normal operation temperatures at the divertor in fusion reactors [124]) half recrystallization for the plate W90 would not be achieved before 2.4 (1± 24%) years or 71 (1± 35%) years, respectively.

This means that the expected life time of 2 years for tungsten divertors can be guaranteed at operation temperatures of 1075 °C and 900 °C for the plates W67 and W90 respectively. It is concluded that the moderately warm-rolled plate W67 shows sufficient thermal stability for application as plasma facing component material, while the plate W90 shows a much worse thermal stability. Therefore, tungsten parts shall not be deformed to high strains for application in PFCs, as high rolling reductions considerably degrade the thermal stability of these tungsten parts.

CHAPTER 7
Conclusions and outlook

The goal of this study was to characterize the thermal stability of two plates warm-rolled to moderate (W67) and high (W90) strains at reasonably low temperatures which allowed estimating the behavior at possible operation temperatures of tungsten plasma facing components in fusion reactors. The chosen annealing temperature ranges were 1150-1350 °C and 1100-1250 °C for the plates W67 and W90 respectively, since long-term annealing kinetics could be characterized at these temperature ranges. The recovery and recrystallization kinetics were fully characterized both mechanically (via Vickers hardness) as well as microstructurally (via EBSD) for a wide range of annealing times. The hardness characterization also allowed determination of activation energies for recrystallization, which in turn allowed to extrapolate lifespans of these tungsten plasma facing components at expected lower operation temperatures in fusion reactors. The microstructural study done by EBSD allowed to characterize in more detail nucleation and growth during recrystallization. The conclusions of this work are presented below.

Recovery and recrystallization of both plates W67 and W90 were characterized from the reduction in hardness, where two characteristic annealing stages are identified. Further analysis of the kinetics in terms of classical models showed that the hardness loss during recovery can be nicely fit by the logarithmic time dependence rationalized by Kuhlmann. Faster recovery kinetics were observed for the plate W90, given its higher deformation. A proper description of the recrystallization behavior was obtained by using Johnson-Mehl-Avrami-Kolmogorov kinetics with an incubation time for the beginning of recrystallization. Faster recrystallization kinetics were also found for the plate W90, due to its higher deformation. This work provides a complete characterization of recovery and recrystallization kinetics at low temperatures and for long annealing times, similar to the conditions that tungsten components will find under fusion reactor conditions, very important to quantify the degradation of tungsten components during operation in future fusion reactors. No such long-term characterization at reasonably low temperatures is available in literature. The more complete characterization of this work allows a more accurate calculation of recrystallization activation energies as well as the extrapolation of lifespans of tungsten plasma facing components at normal operation temperatures.

The obtained activation energies were comparable to the activation energy of self-diffusion in tungsten for the plate W67 and to the activation energy of grain boundary diffusion in tungsten for the plate W90. Apparently, a different jump mechanism (with a different activation energy) occurs at the nuclei-recovered matrix interfaces during recrystallization for each plate. The reason for that change in jump mechanism could be related to the considerably higher content of low angle boundaries in the grain interiors of the plate W90, as compared to the plate W67. It is suggested that these LABs could aid the motion of tungsten atoms at the interfaces of the recrystallizing nuclei with the recovered matrix being consumed. Additionally, it is speculated in this work that the diffusion mechanism during recrystallization could also be different for the two plates. The diffusion mechanism could have changed from bulk diffusion for the plate W67 to grain boundary diffusion for the plate W90. However, no diffusivity measurements were done in this work to confirm the change in diffusion mechanism.

The activation energies allowed to calculate and compare the thermal stability of the plates W67 and W90. A much longer lifetime was obtained at 800 °C for the plate W67 (at least 1 million years) as compared to the plate W90 (71 years). This clearly demonstrates the accelerating effect that the higher stored energy and possible change of dominating diffusion mechanism have on the recrystallization kinetics of this highly-deformed plate (W90), and therefore on the degradation of the material. As a conclusion, the plate warm-rolled to a moderate strain (W67) shows a much better thermal stability, which seems to indicate that high strains have a detrimental effect on the thermal stability of tungsten, and shall be avoided. This extremely important sensitivity of the thermal stability on the prior degree of deformation has not been reported in literature. However, it must be said that the study of this thesis accounted for thermal stability alone, and the degrading effects caused by radiation were not considered.

Microstructurally, the good description of recovery provided by the logarithmic relationship of Kuhlmann was verified for the plate W67 from the increase of subgrain size with annealing time. Moreover, a good microstructural correspondence was found for the recrystallization kinetics elucidated with hardness measurements for both plates. It was found that the initial coarse and elongated deformed microstructure becomes replaced by a coarser and equiaxed recrystallized microstructure for both plates. The as-received textures of the plates were found to be typical rolling textures of bcc metals. The recrystallization textures were almost random for both plates, although a slight preference for the recrystallization of cube components was found, especially for the most highly strained plate W90. It is suggested that the initial higher strain promotes the nucleation of cube components, although the resulting recrystallized textures for both plates are weak. Therefore, oriented nucleation was found as the cause for the development of a slight preference of a cube texture in the almost-random recrystallized textures of the plates W67 and W90. There was no particular misorientation relationship between the recrystallized cube nuclei and the surrounding recovered matrix.

Regarding nucleation, a tendency for site-saturation was found for the plate W67, while a tendency for a constant nucleation rate was found for the plate W90 microstructurally. This difference was explained in terms of the smaller grain size or higher density of original grain boundaries of the plate W67, since grain boundaries act as potential nucleation sites. The change of nucleation regime allowed to microstructurally justify that the plate W67 showed an Avrami exponent $(n = 1.1)$ 1 unit lower than the Avrami exponent for the plate W90 $(n = 2)$. In fact, a constant nucleation rate is expected to show an Avrami exponent higher by 1 unit as compared to site-saturation [21].

Regarding nuclei growth during recrystallization, it was found that the deformed γ fiber component $\{111\} < 1\bar{1}0 >$ was more stable (or less consumed by the growing recrystallized nuclei) during recrystallization for both plates. The higher stability of this specific texture component was not previously reported in literature, and is related in this work to the much lower stored energy content of the $\{111\} < 1\bar{1}0 >$ component as compared to other main deformed texture components. No growth preference of any particular recrystallized texture component was observed. The size of the recrystallizing nuclei increased linearly with annealing time for both plates, until the migrating grain boundaries of the recrystallizing nuclei impinged on other nuclei. As expected, it was observed that growth rates were faster for higher initial strain and higher annealing temperatures.

For future work, it is suggested that the possible change of diffusion mechanism for the two plates should be confirmed by diffusivity measurements (e.g. diffusion of radioactive isotopes in the tungsten material). Additionally, it is proposed that a study of the influence of radiation on the degradation of these tungsten plates is made.

References

[1] M. Rieth et al., “Recent progress in research on tungsten materials for nuclear fusion applications”, Journal of Nuclear Materials 423 (2013) 482-500.

[2] G. Pintsuk, A. Prokhodtseva, ”Thermal shock characterization of tungsten deformed in two orthogonal directions”, Journal of Nuclear Materials, 417 (2011) 481-486.

[3] D. Serret, M. Richou, “Mechanical characterization of W-armoured plasma-facing components after thermal fatigue”, Physica. Scripta T145 (2011) 014077 (5pp.).

[4] M. Rieth, A.Hoffmann, “Influence of microstructure and notch fabrication on impact bending properties of tungsten materials”, International Journal of refractory Metals and Hard Materials, 28 (2010) 679-686.

[5] M. Rubel, ”Structure Materials in Fusion Reactors: Issues Related to Tritium, Radioactivity and Radiation-Induced Effects”, Transactions of Fusion Science and Technology, 53 (2008) 459-467.

[6] M. Ulrickson, G. Vieider, M. Akiba, I, Mazul, V. Barabash, “Selection, development and characterisation of plasma facing materials for ITER” Journal of Nuclear Materials, 233-237 (1996) 718-723.

[7] M.I. Guseva, A.L. Suvorov, S.N. Korshunov, N.E. Lazarev, “Sputtering of beryllium, tungsten, tungsten oxide and mixed W-C layers by deuterium ions in the near-threshold energy range”, Journal of Nuclear Materials, 266 (1999) 222-227.

[8] A. Hoffmann, J. Reiser, M. Rieth, B. Dafferner, ”Tungsten foil laminate for structural divertor applications - Basics and outlook”, Journal of Nuclear Materials 423 (2012) 1-8.

[9] J.A. Dicarlo, J.T. Stanley, ”Energy dependence of electron-induced radiation damage in tungsten”, Radiation Effects 10 (1971) 259-272.

[10] Z. Zhang-jian, S. Shu-xiang, “High heat flux testing of tungsten plasma facing materials”, Journal of Nuclear Materials, 367-370 (2007) 1468-1471.

[11] S.N. Mathaudhu, A.J. deRosset, K.T. Hartwig, L.J. Kecskes, “Microstructures and recrystallization behavior of severely hot-deformed tungsten”, Materials Science and Engineering A 503 (2009) 28-31.

[12] A.V. Babak, E.I. Uskov, “High-Temperature Embrittlement of Tungsten”, Strength of Materials 15 (1983) 667-672.

[13] A. Hoffmann, D. Armstrong, M. Rieth, B. Dafferner, S. Heger, M.D. Hoffmann, U. Jäntsch, J. Reiser, M. Rohde, T. Scherer, V. Widak, H. Zimmermann, E. Materna-Morris, C. Kübel, “Tungsten as a structural divertor material”, Adv. Sci. Technol. 73 (2010) 11.

[14] K. Farrell, C. Schaffhauser, J. O. Stiegler, "Recrystallization, Grain Growth and the Ductile-Brittle Transition in Tungsten Sheet", Journal of less-common metals, 13 (1967) 141-155.

[15] E. Lassner, W.-D. Schubert, "Tungsten; Properties, Chemistry, Technology of the element, alloys and chemical compounds", Springer – Verlag (1999), 417 p., New York US.

[16] Patent publication number: CN103173670 A; Inventors: 周张健, 谈军, 丁庆明; Patent title: Preparation-method for in-situ synthesis of carbide enhanced tungsten-based composite material; Publication date: 9th April 2013.

[17] Tan Jun, Zhou Zhang-jian, Zhu Xiao-peng, Guo Shuang-quan, Qu Dan-dan, Lei Ming kai, Ge Chang-chun, "Evaluation of ultra-fine grained tungsten under transient high heat flux by high-intensity pulsed ion beam", Trans. Nonferrous Met. Soc. China 22 (2012) 1081-1085.

[18] I. Jenkins, J.V. Wood, "Powder metallurgy: An overview", Cambridge: Woodhead Publishing (1991) 396 p.

[19] C.L. Briant, F. Zaverl, E.L. Hall, "Warm rolling of sintered tungsten ingots" Materials Science and Technology 7 (1991) 923-936.

[20] A.V.Babak, "Effect of recrystallization on the fracture toughness of tungsten, Poroshkovaya Metallurgiya, 244 (1982) 87-90.

[21] F.J. Humphreys, M.Hatherly, "Recrystallization and Related Annealing Phenomena", Pergamon (1995) 497 p., Elsevier Science Ltd. UK.

[22] A. Godfrey, W.Q. Cao, N. Hansen, Q. Liu, "Stored energy, microstructure and flow stress of deformed metals", Metallurgical and Materials Transactions A, 36A (2005) 2371-2378.

[23] J.G. Sevillano, P. Vanhoutte, E. Aernoudt, "Large strain work-hardening and textures", Progress in Materials Science 25(1980) 69-412.

[24] J.S. Hirschhorn, "Stacking faults in the refractory metals and alloys – a review", J. Less-Common Metals, 5 (1963) 493 – 509.

[25] M. Hatherley, W.B. Hutchinson, "An Introduction to Textures in Metals", The Institution of Metallurgists (London), Monograph No 5, 1979.

[26] R.J. Amodeo, N.M. Ghoniem, "A review of experimental observations and theoretical models of dislocation cells and subgrains", Res Mechanica 23 (1988) 137-160.

[27] G. Tang, G.-N. Luo, Y. Yuan, W. Liu, B. Fu, and H. Xu, "The effects of electropulsing on the recrystallization behavior of rolled pure Tungsten", J.Mater.Res., 27 (2012) 2630-2638.

[28] E. É. Zasimchuk, V.I., Isaichev, “ Structural instability during rolling of tungsten in terms of nonlinear thermodynamics”, Soviet Physics Journal, 34 (1991) 217-224.

[29] L. Ekbom, T. Antonsson, “Tungsten heavy alloy: deformation texture and recrystallization of tungsten particles”, International Journal of Refractory Merals and Hard Materials, 20 (2002) 6375-6379.

[30] K. Chen-Ming, L. Chih-Sheng, “Static recovery activation energy of pure copper at room temperature”, Scripta Materialia 57 (2007) 667-670.

[31] D. Kuhlmann, G.Masing, J. Raffelsieper, “Zur Theorie der Erholung”, Zeitschrift für Metallkunde, 40 (1949) 241-246.

[32] J.R. Cahoon, W.H. Broughton, and A.R. Kutzak, The Determination of Yield Strength from Hardness Measurements, Metall. Trans. 2 (1971) 1979–1983.

[33] J.R. Cahoon, An Improved Equation Relating Hardness to Ultimate Strength, Metall. Trans., 3 (1972) 3040.

[34] E. Kovacs-Csetenyi, “Electrical resistivity change in cold-worked tungsten wires during recovery and recrystallization”, Acta Physica Academiae Scientiarum Hungaricae, 18 (1964) 11-18.

[35] A. Szokefalvinagy, G. Radnoczi, I. Gaal, “Stage-IV recovery in deformed tungsten”, Materials Science and Engineering, 93 (1987) 39-43.

[36] R.C. Koo, ”Recovery in cold-worked tungsten”, J. Less-Common Metals, 3 (1961) 412-428.

[37] William D. Callister, David G. Rethwisch, “Fundamentals of Materials Science and Engineering: 9th Edition (2013), John Wiley & Sons, Inc.

[38] R.D. Doherty. “Recrystallization and texture” Prog. Mater. Sci., 42 (1997), 39-58.

[39] R.D. Doherty, D.A. Hughes, F.J. Humphreys, J.J. Jonas, D. Juul Jensen, M.E. Kassner, W.E. King, T.R. McNelley, H.J. McQueen and A.D. Rollet, “Current issues in recrystallization: a review” Mater. Sci. Eng., A238 (1997), 219-274.

[40] A.O. Humphreys, F.J. Humphreys. in Proc. 4th Int. Conf. on Aluminum, Atlanta, 1 (1994) 211.

[41] R.A. Vandermeer, D. Juul Jensen. “The migration of High Angle Grain Boundaries during Recrystallization”, Interface Science 6 (1998) 95-104.

[42] Eric J. Mittemeijer, “Fundamentals of Materials Science: The microstructure- Property Relationship using Metals as Model Systems”, Springer-Verlag (2010), Berlin Heidelberg.

[43] Joseph R. Michael, ”Focused ion beam induced microstructural alterations: texture development, grain growth and intermetallic formation”, Microsc. Microanal. 17 (2011) 386–397.

[44] H. Kurishita, S. Matsuo, H. Arakawa, H. Okano, H. Watanabe, N. Yoshida, T. Sakamoto, S. Kobayashi, K. Nakai, M. Hatakeyama, T. Shikama, Y. Ueda, T. Takida, M. Kato, A. Ikegaya, Y. Torikai, and Y. Hatano, “Current status of nanostructured tungsten-based materials development”. Phys. Scr., T159 (2014) 1-7.

[45] H.Y. Xu, Y.B. Zhang, Y. Yuan, B.Q. Fu, A. Godfrey, G. De Temmerman, W. Liu, and X. Huang, “Observations of orientation dependence of surface morphology in tungsten implanted by low energy and high flux D plasma”. J. Nucl. Mater. 443 (2013) 452-457.

[46] Z. Xiao-Xin, Y. Qing-Zhi, Y. Chun-Tian; W. Tong-Nian; X. Min, G. Chang-Chun, “Recrystallization temperature of tungsten with different deformation degrees”, Rare Metals (2014).

[47] C.M. Parish, H. Hijazi, H.M. Meyer, F.W. Meyer, “Effect of tungsten crystallographic orientation on He-ion-induced surface morphology changes”, Acta Materialia 62 (2014) 173–181.

[48] D. Raabe, K. Lücke, “Rolling and annealing textures of bcc metals” Mater. Sci. Forum, 280 (1994) 597-610.

[49] Hsun Hu, “Texture of Metals”, Texture, 1 (1974) 233-258.

[50] Y.B. Park, D.N. Lee, G. Gottstein, “The evolution of recrystallization textures in body centered cubic metals”, Acta Mater. 46 (1998) 3371-3379.

[51] K., Okuda, K., Seto, “Recrystallization behavior of IF steel sheets immediately after hot-rolling in ferrite region”, ISIJ International, 53 (2013) 152-159.

[52] Gerardo Bruna, “Effects of hot and warm rolling on microstructure, texture and properties of low carbon steel”, REM-Revista Escola De Minas, 64 (2011) 57-62.

[53] L.N. Aleksandrov, S.N. Mordyuk, “Kinetics of Recrystallization in Tungsten”, Fizika Metallov I Metallovedenie, 12 (1961) 249-254.

[54] Yu M. Aleksandrova, L. N. Aleksandrov, V. D. Eliséeva, “Effect of Inert gases on the Recrystallization of Tungsten”, Fiziko Khimieheskaya Mekhanika Materialov, 2 (1966) 327-332.

[55] D. Klopp, R. Witzke, “Mechanical properties & recrystallization behavior of Electron-Beam-Melted Tungsten compared with Arc-Melted Tungsten. “, NASA TN D-3232, January 1966.

[56] Y. Yuan, H. Greuner, B. Böswirth, K. Krieger, G.-N. Luo, H.Y. Xu, B.Q. Fu, M. Li, W. Liu “Recrystallization & Grain growth of rolled tungsten under VDE-like short pulse high heat flux loads”, Journal of Nuclear Materials 433 (2013) 523-530.

[57] Zhang, Taiquan; Wang, Yujin; Zhou, Yu; Lei, Tingquan; Song, Guiming, " Model to determine recrystallization temperature of tungsten based dilute solid solution alloys", Journal of Materials Science 41 (2006) 7506-7508.

[58] J.W. Pugh, "On the Recovery and Recrystallization of Tungsten", Plansee Proc. 1958, F. Benesovsky, ed., 1959, pp. 97-107.

[59] D. William Klopp, Raffo, Peter L., "Effects of Purity and Structure on Recrystallization, Grain Growth, Ductility, Tensile, and Creep Properties of Arc-Melted Tungsten", NASA TR D-2503, 1964.

[60] J.N. Mundy, S.J. Rothman, N.Q. Lam, H.A. Hoff, and L.J. Nowicki, "Self-diffusion in tungsten" Phys. Rev. B (Solid State), 18 (1978) 6566.

[61] V.P. Vasil'ev, S.G. Chernomorchenko, "K Metodike Issledovaniya Samodiffuzii Volframa, Zavodskaya Laboratoriya 22 (1956) 688-691.

[62] W. Danneberg, "Selbstdiffusionsuntersuchungen an Wolfram", Metallurgy 15 (1961) 977-981.

[63] R.L. Andelin, J.D. Knight, M. Kahn, "Diffusion of tungsten and rhenium tracers in tungsten", Transactions of the metallurgical society of AIME 233 (1965) 19-24.

[64] W.V. Green, "Short-time creep-rupture behavior of tungsten at 2250 to 2800 C", Transactions of the metallurgical society of AIME 215 (1959) 1057-60.

[65] J.E. Dorn, "The Spectrum of Activation Energies for Creep", Creep and Recovery, American Society for Metals (1956) 255

[66] R.H. Schnitzel, "High temperature damping of Tantalum, Rhenium and Tungsten", Journal of Applied Physics 30 (1959) 2011-12.

[67] N.H. Nachtrieb, G.S. Handler, "A relaxed vacancy model for diffusion in crystalline metals" Acta Metallurgica 2 (1954) 797-802.

[68] J.A.M. van Liempt, "Die Diffusion in Wolfram mit Niedrigem Eisengehalt", Recueil des Travaux Chimiques des Pays Bas 64 (1945) 239-249.

[69] A.D. LeClaire, "Diffusion of Metals in Metals", Progress in Metal Physics 1 (1949) 306-79.

[70] O.D. Sherby, M.T. Simnad, "Prediction of atomic mobility in metallic systems", American Society for Metals, Transactions Quarterly 54 (1961) 227-240.

[71] M. Rühle, J. Almanstötter, “Grain growth phenomena in tungsten wire”, International Journal of Refractory Metals and Hard Materials, 15 (1997) 295-300.

[72] J. S. Lee, C. Minkwitz, and Ch. Herzig, “Grain Boundary Self-Diffusion in Polycrystalline Tungsten at Low Temperatures”, Phys. Stat. Sol., 202 (1997) 931-940.

[73] I. Kaur, W. Gust, L. Kozma, “Handbook of grain and interphase boundary diffusion data”, Vol. 2, Ziegler Press, Stuttgart, 1989.

[74] E. Laine, I. Lähteenmäki, “The energy dispersive X-ray diffraction method: annotated bibliography 1968–78”, Journal of Materials Science 15 (1980) 269-277.

[75] Y. Hatano, J. Shi, N. Yoshida, N. Futagami, Y. Oya, H. Nakamura, “Measurement of deuterium and helium by glow-discharge optical emission spectroscopy for plasma–surface interaction studies”, Fusion Engineering and Design, 87 (2012) 1091–1094.

[76] V. Hoffmann, A. Quentmeier, “Glow Discharge Optical Emission Spectroscopy (GD-OES)”, Surface and Thin Film Analysis: a Compendium of Principles, Instrumentation, and Applications, Second Edition, Wiley-VCH (2011), 329-344.

[77] T. Nelis, R. Payling, “Glow Discharge Optical Emission Spectroscopy: A Practical Guide”, Royal Society of Chemistry (RSC), 2003.

[78] W.F. Gale, T.C. Totemeier, Smithells “Metals Reference Book”, Elsevier Inc. (2033), 2033 p., U.S.

[79] J. Hammel “A Review of Acute Cyanide Poisoning With a Treatment Update”, Critical Care Nurse, 31 (2011) 72-82.

[80] F. J. Hunt, “Method for electropolishing tungsten filaments and baskets”, J. Phys. E. (Sci Instrum), 9 (1976) 921.

[81] V. Randle, O. Engler, “Introduction to Texture Analysis; Macrotexture, Microtexture & Orientation Mapping”, CRC PRESS (2000) 456 p., U.S.

[82] J.G. Wood, R.S. Marriner, “Measurement of Vickers hardness indentations”, Industrial Diamond Review 26 (1966) 159-163.

[83] D.S. Dugdale, “Vickers Hardness and Compressive Strength”, Journal of the Mechanics and Physics of Solids 6 (1958) 85-91.

[84] J.M. Schneider, M. Bigerelle, A. Iost, “Statistical analysis of the Vickers hardness”, Materials Science and Engineering A262 (1999) 256-263.

[85] P.P. Camus, J. Shapiro, S.V. Prikhodko, “An EBSD study of gallium arsenide nanopillars”, Materials Science Forum 702-703 (2012) 702-703.

[86] J. Schwartz, M. Kumar, B. Adams "Electron Backscatter Diffraction in Materials Science". Springer (2009) 403p., New York U.S.

[87] A.J. Wilkinson, T. Ben, "Strains, planes and EBSD in materials Science", Materials Today 15 (2012) 366-376.

[88] F.J. Humphreys, "Review Grain and subgrain characterisation by electronbackscatter diffraction", Journal of Materials Science 36 (2001) 3833 – 3854.

[89] T.B. Britton, A.J. Wilkinson, "Measurement of residual elastic strain and lattice rotations with high resolution electron backscatter diffraction", Ultramicroscopy 111 (2011) 1395–1404.

[90] G.M. Pennock, M. Coleman "Grain boundary plane populations in minerals: the example of wet NaCl after low strain deformation", Contributions to Mineralogy and Petrology 158 (2009) 53-67.

[91] B.C. Allen, "The interfacial free energies of solid chromium, molybdenum and tungsten", Journal of the Less-Common Metals, 29 (1972) 263-282.

[92] F.J. Humphreys, "Reconstruction of grains and subgrains from electron backscatter diffraction maps", Journal of Microscopy 213 (2004) 247-256.

[93] G.L. Wu, D. Juul Jensen, "Automatic determination of recrystallization parameters based on EBSD mapping". Mater. Charact., 59 (2008) 794-800.

[94] D. Kuhlmann, "Zur Theorie der Nachwirkungserscheinungen", Zeitschrift für Physik, 124 (1948) 468-481.

[95] D. Juul Jensen, N. Hansen, J. Kjems, T. Leffers, "In-Situ Texture Measurements by Neutron Diffraction used in a Study of Recrystallization Kinetics", in N.H. Andersen et al. (Eds.), Proc. 5th Risø Intern. Symp. Mater. Sci.: Microstructural Characterization of Materials by Non-Microscopical Techniques, Risø National Laboratory, Roskilde, 1984, pp. 325-332.

[96] N.X. Sun, X.D. Liu, K. Lu, "An explanation to the anomalous Avrami exponent", Scripta Materialia, 34 (1996) 1201-1207.

[97] F.-X. Lin, W. Pantleon, T. Leffers, D. Juul Jensen, "Effects of Initial Parameters on the Development of Cube Texture during Recrystallization of Copper", in: S. Fæster et al. (Eds.), Proc. 33rd Risø Intern. Symp. Mater. Sci.: Nanometals – Structures and Perspectives, DTU, Roskilde, 2012, pp. 398-401.

[98] Hesham E. Khalifa, Kenneth S. Vecchio, "Thermal stability and crystallization phenomena of low cost Ti-based bulk metallic glass", Journal of Non-Crystalline Solids, 357 (2011) 3393-3398.

[99] H. Tsukahara, A.M. Chaze, C. Levaillant, S. Hollard, "Static recrystallization and grain growth of a stainless austenitic steel", Journal de Physique IV, 5 (1995) 29-38.

[100] W. Wego. “Reverse engineering: technology of reinvention”, CRC Press (2011).

[101] S. Kobayashi, S. Zaefferer, A. Schneider, D. Raabe, G. Frommeyer, ”Effect of the degree of order and the deformation microstructure on the kinetics of recrystallisation in a Fe_3Al Ordered Alloy”, Materials Science Forum, 467-470 (2004) 153-158.

[102] J.Kwiecinski, J.W. Wyrzykowski, “Kinetics of recovery on grain-boundaries in polycrystalline aluminum”, Acta Metallurgica, 37 (1989) 1503-1507.

[103] J.W. Pugh, “Temperature dependence of preferred orientation in rolled tungsten” Trans. A.I.M.E., 212 (1958) 637-642.

[104] R. Stickler, W. Knabl, A. Lorich, S. Primig, H. Clemens, “Orientation dependent recovery and recrystallization behavior of hot-rolled molybdenum”, International Journal of Refractory Metals and Hard Materials, 48 (2015) 179-186.

[105] W. Pantleon, “Spatial Correlations of Disorientations in Deformation Substructures”, in: N. Hansen et al. (Eds.), Proc. 21st Risø Intern. Symp. Mater. Sci.: Recrystallization – Fundamental Aspects and Relations to Deformation Microstructure, DTU, Roskilde, 2000, pp. 497-504.

[106] W. Sung-Hyun, “Nanostructured metals and alloys: processing, microstructure, mechanical poperties and applications”, (2011) Woodhead Pub.

[107] S.V. Raj, G.M. Pharr, ”A compilation and analysis of data for the stress dependence of the subgrain size”, Materials Science and Engineering, 81(1986) 217-237.

[108] K.P. Mingard, B. Roebuck, E.G. Bennett, M. Thomas, B.P. Wynne, E.J. Palmiere, ”Grain size measurement by EBSD in complex hot deformed metal alloy microstructures”, Journal of Microscopy 227 (2007) 298-308.

[109] M. Thomas, B.P. Wynne, E.J. Palmiere, K.P. Mingard, B. Roebuck, E.G. Bennett, “Metrological aspects of Electron Backscattering Diffraction in characterising hot deformation grain structures”, Mapan-Journal of Metrology Society of India, 22 (2007) 177-200.

[110] S.S. Marchenko, V.S. Sysoeva, G.A. Chumak, “Recrystallization of cold worked structural steel”, Metal Science and Heat Treatment, 16 (1974) 732-735.

[111] R.A. Vandermeer, D. Juul Jensen “The migration of high angle grain boundaries during recrystallization”. Interf. Sci., 6 (1998) 95-104.

[112] R.A. Vandermeer, G.L. Wu, D. Juul Jensen, “Microstructural path model and strain dependence of recrystallization in commercial aluminium”. Mater. Sci. Technol., 25 (2009) 403-406.

[113] J.K. Mackenzie, ”Second Paper on Statistics Associated with the Random Disorientation of Cubes”, Biometrika 45 (1958) 229-240.

[114] D.N. Lee, “The evolution of recrystallization textures from deformed textures”. Scr. Metall. Mater. 32 (1995) 1689-1694.

[115] C.T. Necker, R.D. Doherty, A.D. Rollett, ”Cube texture generation dependence on deformation textures in cold-rolled of copper”, Materials Science Forum 157 (1994) 1021-1026.

[116] B. Hutchinson, ”The cube texture revisited”, Materials Science Forum 702-703 (2012) 3-10.

[117] J.K. Mackenzie, “Distribution of rotation axes in random aggregate of cubic crystals”, Acta Metallurgica, 12 (1964) 223-225.

[118] Cahn, J.W., and Hagel, W.C., “Divergent pearlite in a manganese eutectoid steel” Acta Metallurgica 11 (1963) 561-574.

[119] J.W. Cahn, W.C. Hagel, “In Decomposition of Austenite by Diffusional Processes”. Eds. V.F. Zackay and H.I. Aaronson, Interscience (1962) 131-196.

[120] Heinz-J., Stepper “Recrystallization of α particle irradiated tungsten”, Metallurgical Transactions A; Physical Metallurgy and Materials Science 3 (1972) 2293-2294

[121] V.A., Lavrenko, I. E., Shiyanovskaya, “Recrystallization of cold worked tungsten”, Metal Science and Heat Treatment of Metals 1 (1959) 45-46.

[122] J.W. Davis, V.R. Barabash, A. Makhankov, L. Plochl, K.T. Slattery, ”Assessment of tungsten for use in the ITER plasma facing components”, Journal of Nuclear Materials 258 (1998) 308-312.

[123] S.A. Golovanenko, A.B. Natapova, B.A. Klypin, T.M. Kesaev, ”Recrystallization of tungsten alloys”, Metal Science and Heat Treatment 18 (1976) 810-812.

[124] S. Hermsmeyer, P. Norajitra, L. Di Pace, L. Giancarli, R. Forrest, N.P. Taylor, I. Cook, D.J. Ward, P. Sardain, D. Maisonnier, “European fusion power plant studies”. Fusion Sci. Technol. 47 (2005) 384-392.

APPENDICES

Appendix I:

In this appendix, the hardness distributions on the outer and inner RD/TD surface, as well as the in-depth hardness distributions along the RD/ND surface, are presented for the plates W67 (Table 21) and W90 (Table 22).
It is shown that a good correspondence is found between the Vickers hardness of the internal RD/TD surface (6mm inside the plate, away from the contact surface with the rolls) and the Vickers hardness of the RD/ND surface for the plate W67. The outer RD/TD surface in direct contact with the rolls showed higher hardness values not used in this work, since these values were considered not representative of the sample.

Table 21. Through-thickness hardness values obtained for the as-received plate W67 (12 mm thick)

As-received W67	HV_{10}	Average Hardness ($\bar{X}$)
0mm (outer RD/TD surface)	454,449,446,446,446,446,446,444,444,441	**446**
6mm in-depth (inner RD/TD surface)	432,428,426,426,423,421,421,418,418,416	**423**
1mm in-depth (RD/ND surface)	432,430,430,427,427,427,422,422,422,422	**426**
2mm in-depth (RD/ND surface)	432,430,429,427,427,427,427,422,420,420	**426**
3mm in-depth (RD/ND surface)	428,428,425,425,423,423,420,418,418,413	**422**
4mm in-depth (RD/ND surface)	430,430,428,425,425,420,420,418,418,418	**423**
5mm in-depth (RD/ND surface)	432,428,427,427,425,423,423,420,420,418	**424**
6mm in-depth (RD/ND surface)	432,428,427,425,423,420,420,420,418,418	**423**

Table 22. Through-thickness hardness values obtained for the as-received plate W67 (4 mm thick)

As-received W90	HV_{10}	Average Hardness ($\bar{X}$)
0mm in-depth (outer RD/TD surface)	454,447,447,445,444,443,440,438,436,435 455,455,451,449,446,446,443,438,437,435	**444**
1mm in-depth (RD/ND surface)	439,439,436,434,434,434,434,434,422,420 441,439,437,436,436,432,430,428,426,424	**433**
2mm in-depth (RD/ND surface)	438,438,438,438,436,436,433,433,433,433, 433,433,431,431,429,429,426,426,424,424	**432**

Appendix II:

Additionally to the calculated growth rates for the plate W90 annealed at 1200 °C (Table 19), the growth rates for the plate W67 after annealing at 1150 °C and 1200 °C are also presented below (Table 23 and Table 24 respectively).

Table 23. Calculated growth rates at all annealing times for the plate W67 annealed at 1150 °C

Plate W67. Annealing time at 1150°C t (h)	X_{EBSD}	S_v (1/µm)	dX / dt	G (µm/s)	G (µm/h)
750	0.03	0.0032	0	0	0
950	0.15	0.0118	$2.99 \cdot 10^{-07}$	$2.53 \cdot 10^{-05}$	0.091
1213	0.41	0.0148	$2.48 \cdot 10^{-07}$	$1.68 \cdot 10^{-05}$	0.061
1373	0.44	0.0166	$2.07 \cdot 10^{-07}$	$1.25 \cdot 10^{-05}$	0.045
1582	0.69	0.0141	$1.59 \cdot 10^{-07}$	$1.13 \cdot 10^{-05}$	0.041
1900	0.86	0.0890	$1.03 \cdot 10^{-07}$	$1.15 \cdot 10^{-05}$	0.041
2200	0.99	0.0051	$6.64 \cdot 10^{-08}$	$1.30 \cdot 10^{-05}$	0.047

Table 24. Calculated growth rates at all annealing times for the plate W67 annealed at 1200 °C

Plate W67. Annealing time at 1200°C t (h)	X_{EBSD}	S_v (1/µm)	dX / dt	G (µm/s)	G (µm/h)
240	0.05	0.0065	$1.71 \cdot 10^{-06}$	$2.62 \cdot 10^{-04}$	0.942
300	0.32	0.0135	$1.35 \cdot 10^{-06}$	$1.00 \cdot 10^{-04}$	0.360
320	0.49	0.0157	$1.18 \cdot 10^{-06}$	$7.51 \cdot 10^{-05}$	0.270
359	0.58	0.0159	$8.85 \cdot 10^{-07}$	$5.55 \cdot 10^{-05}$	0.200
480	0.77	0.0101	$3.27 \cdot 10^{-07}$	$3.06 \cdot 10^{-05}$	0.117
600	0.97	0.0032	$1.12 \cdot 10^{-07}$	$3.75 \cdot 10^{-05}$	0.126

DTU Mechanical Engineering
Section of Materials and Surface Engineering
Technical University of Denmark

Produktionstorvet, Bld. 425
DK- 2800 Kgs. Lyngby
Denmark
Phone (+45) 4525 2205
Fax (+45) 4593 6213
www.mek.dtu.dk
ISBN: 978-87-7475-425-1